BWR SUBCHANNEL VOID PREDICTIONS

ACCURACY OF BOILING WATER REACTOR

SUBCHANNEL VOID DISTRIBUTION PREDICTIONS

By

KENNETH LEUNG, B.ENG.MGT

A Thesis

Submitted to the School of Graduate Studies

in Partial Fulfillment of the Requirements

for the Degree

Master of Applied Science

McMaster University

© Copyright by Kenneth Leung, June 2009

MASTER OF APPLIED SCIENCE (2009) McMaster University
(Engineering Physics) Hamilton, Ontario

TITLE: Accuracy of Boiling Water Reactor Subchannel Void Distribution Predictions

AUTHOR: Kenneth Leung, B.ENG.MGT (McMaster University)

SUPERVISOR: Dr. D. R. Novog

NUMBER OF PAGES: x, 205

ABSTRACT

The ability to accurately predict the void fraction in a nuclear reactor plays a vital role in the field of nuclear safety. Specifically, high volumetric fractions of vapour in a reactor core can lead to a severe degradation in the ability of the coolant to remove heat from the fuel. Unfortunately, the behaviour of two-phase flow is complex and not particularly well understood, making it infeasible to describe the fluid behaviour in the core analytically. Instead, computer codes which rely heavily on temporal and spatial averaging, as well as empirical correlations, are used to provide a 'best-estimate' of the core thermalhydraulic behaviour.

In this study, both the system code RELAP5-3D and the subchannel code ASSERT are used to simulate subchannel void fraction measurements conducted on full scale electrically heated BWR type bundles. RELAP was demonstrated to be capable of predicting the void fraction at the subchannel level to within ±0.10 of the reported value 82.6% of the time, while ASSERT was successful 95.6% of the time. When the accuracy levels are broken down by subchannel geometry, the corner and side subchannels tended to be the most inaccurately predicted, and this was determined to have been caused by the strong influence of subchannel mixing.

Uncertainty bands around the simulated points were predicted using the CIAU method developed at the University of Pisa. In the cases simulated with RELAP, the simulated uncertainty bounds enveloped a portion of the experimental uncertainty bounds 95.4% of the time while the ASSERT assessment saw coverage 85.4% of the time.

ACKNOWLEDGEMENTS

I am very grateful to those who have supported me over the past year while this work was completed. First and foremost, the guidance and patience afforded to me by my supervisor Dr. David Novog is most sincerely appreciated. The experiences that I have had over the last two years have truly been amazing.

Much of this work could not have been possible without the mentoring of Dr. Alessandro Petruzzi and Mr. Andriy Kovtonyuk. Their help, expertise, and advice are gratefully appreciated. Additionally, I would like to thank everyone else at the San Piero a Grado Nuclear Research Group for so warmly hosting me during my 6 month stay in Pisa.

I would also like to acknowledge "the boys in the lab": Fiend, Fang, Brad, Dan, Adam, Kurt, Justin, Ryan, Hummel, Jack and Mr. Banana. Whether it was for food, 10 p.m. coffee, shenanigans, or more food, your company always made those long days and late nights more tolerable.

Finally, and most importantly, I would like to thank my family for all their love and support. Even though you guys don't exactly know what I'm doing – you've always been there for me.

AUTHOR'S NOTE

An enormous amount of data has been generated during the course of the work required to complete this project. If printed, the input files, output files, data parsing scripts and CIAU code would fill thousands of pages (each input deck for RELAP is 627 pages long alone!). Although the author would be childishly amused at having this thesis fill an entire shelf, it is probably in everyone's best interest to simply supply an electronic copy of the resources used.

A DVD is archived in the Engineering Physics department office at McMaster University containing all of the input decks, output files (ASSERT), strip files (RELAP), CIAU code and custom scripts written.

The experimental data used in this thesis is the property of NUPEC, and was released under the OECD/NEA BFBT agreement. As such, it is NOT provided with the DVD.

Under certain conditions, the OECD/NEA Data Bank may at its discretion release the data under the titles "ZZ-BFBT-SPECS NEA-1731/002" and "ZZ-BFBT NEA-1731/006".

TABLE OF CONTENTS

1 INTRODUCTION & PROBLEM SCOPE 1

2 BACKGROUND & LITERATURE REVIEW 7
2.1 System Level Codes 7
2.2 Subchannel Level Codes 9
2.2.1 Subchannel Code Validation with the NUPEC Bundle Tests 11
2.3 Uncertainty Analysis 12
2.3.1 CIAU Method 14
2.3.2 Ordered Statistics Methods 17
2.3.3 Response Surface Method & Direct Monte Carlo Method 19
2.4 Flow Behaviour and Phenomena 20
2.4.1 Pressure Drop 20
2.4.2 Heat Transfer 21
2.4.3 Void Fraction 22
2.5 Experimental Studies on Two-Phase Flow in Vertical Bundles 24

3 THEORY 26
3.1 Single-Phase Thermalhydraulic Behaviour 26
3.2 Single-Phase Heat Transfer 28
3.3 Two Phase Thermalhydraulic Behaviour 30
3.3.1 Subchannel Mixing 33
3.4 Two-Phase Model Formulations 34
3.4.1 Reynolds Transport Theorem 34
3.4.2 The Two-Fluid Model 37
3.4.3 The Drift-Flux Model 37
3.5 Uncertainty 38
3.5.1 CIAU Method 38
3.5.2 Ordered Statistics 42

4 APPLICATION & METHODOLOGY 45
4.1 BFBT Facility Description 45
4.1.1 Case Matrices 48
4.2 Input Deck Description 50
4.2.1 Bundle Geometry 50
4.2.2 Fuel Rods 52
4.2.3 Code Implementation 53
4.2.4 Correlations Selected in RELAP 54
4.2.5 Correlations Selected in ASSERT 59
4.2.6 Boundary Conditions 64
4.3 CIAU Implementation 65

5 ACCURACY AND SENSITIVITY RESULTS 69
5.1 Accuracy 69
5.1.1 Pressure Drop Accuracy 70
5.1.2 Overall Void Fraction Accuracy 74
5.1.3 Accuracy Quantification 82
5.1.4 Comparison 87
5.2 Sensitivity to Boundary Condition Uncertainty 91
5.2.1 ASSERT Results 91

5.3 Influence of Subchannel Mixing 95
5.3.1 RELAP Results 96
5.3.2 ASSERT Results 97
5.4 Influence of User Effects 102
5.4.1 Nodalization Sensitivity 103
5.4.2 Model Selection Sensitivity 112

6 CIAU RESULTS 115
6.1 Uncertainty Band Prediction 115
6.1.1 Case Selection 115
6.1.2 RELAP Results 116
6.1.3 ASSERT Results 121
6.1.4 Comparison 125

7 CONCLUSIONS & EXTENSIONS 127
7.1 RELAP 127
7.2 ASSERT 128
7.3 CIAU 129
7.4 Recommendations for Future Work 130
7.4.1 Continued Participation in International Benchmarks 130
7.4.2 Mixing & Void Drift Model Refinement 130
7.4.3 Continued Development of Uncertainty Methods 131
7.4.4 CIAU Database Expansion & Sensitivity Studies 131
7.5 Contributions to Knowledge 132

REFERENCES 135

APPENDIX A NOMENCLATURE 142

APPENDIX B ABBREVIATIONS & ACRONYMS 143

APPENDIX C RELAP THEORY & EQUATIONS 145

APPENDIX D ASSERT THEORY & EQUATIONS 149

APPENDIX E SUBCHANNEL & JUNCTION DIMENSIONS 153

APPENDIX F MATERIAL PROPERTIES 157

APPENDIX G CIAU CODE DESCRIPTION 159

APPENDIX H RELAP INPUT DECK 164

APPENDIX I ASSERT INPUT DECK 190

APPENDIX J 1071-XX RESULT SUMMARY 203

LIST OF FIGURES

Figure 1 - Subchannel Definition 2
Figure 2 – Heat removal from a fuel rod 28
Figure 3 - Vertical Upward Two-Phase Flow Regimes. 31
Figure 4 - Vertical flow pattern map of Hewitt and Roberts 32
Figure 5 - "Current" Bundle Profile (left) and "High Burnup" Bundle Profile (right). 46
Figure 6 - Pressure tap and grid spacer locations. 47
Figure 7 - Relative Axial Power Profile 49
Figure 8 – Subchannel types for the "current" (left) and "high burnup" bundles (right). 51
Figure 9 - Heat contribution to the subchannel of adjacent fuel rods 53
Figure 10 - Prandtl Number Over Expected Conditions 57
Figure 11 - Viscosity Ratio over Experimental Pressures 61
Figure 12 - CIAU Data Flow for RELAP5-3D 68
Figure 13 - Two-phase bundle pressure distribution for case P60009 72
Figure 14 - Two-phase bundle pressure distribution for case P60026 72
Figure 15 - Effect of k-factor selection of the 2-phase pressure distribution for case P60009 73
Figure 16 - Effect of k-factor selection of the 2-phase pressure distribution for case P60026 73
Figure 17 – RELAP Subchannel Void Fraction Error Histogram for all 1071-XX Cases 75
Figure 18 – RELAP Void Fraction Error Distribution for 'Corner' Subchannels 76
Figure 19 – RELAP Void Fraction Error Distribution for 'Side' Subchannels 77
Figure 20 - RELAP Void Fraction Error Distribution for '1-Water' Subchannels 77
Figure 21 - RELAP Void Fraction Error Distribution for 'Typical' Subchannels 78
Figure 22 – ASSERT Subchannel Void Fraction Error Histogram for all 1071-XX Cases 79
Figure 23 – ASSERT Void Fraction Error Distribution for 'Corner' Subchannels 80
Figure 24 – ASSERT Void Fraction Error Distribution for 'Side' Subchannels 81
Figure 25 – ASSERT Void Fraction Error Distribution for '1Water' Subchannels. 81
Figure 26 – ASSERT Void Fraction Error Distribution for 'Typical' Subchannels 82
Figure 27 – Void Fraction Predictions for Case 4101-2 89
Figure 28 - Void Fraction Predictions for Case 4101-13 90
Figure 29 - Void Fraction Predictions for Case 4101-69 90
Figure 30 - Void Fraction Predictions for Case 4101-86 91
Figure 31 – Distribution of Boundary Conditions 92
Figure 32 - Subchannel Void Fraction Comparison for Case 1071-59 94
Figure 33 - Sensitivity of subchannel void distribution to boundary conditions 95
Figure 34 - Effect of Lateral Subchannel Junction Loss Factors 97
Figure 35 - Subchannel Averaged Void Fraction at Low Pressure 98
Figure 36 - Subchannel Averaged Void Fraction at High Pressure 98
Figure 37 - Corner (left) and Side (right) Subchannel Accuracy at 5% Outlet Mass Quality 100
Figure 38 - Corner (left) and Side (Right) Subchannel Accuracy at 12% Outlet Mass Quality 101
Figure 39 - Influence of the Incremental Mixing Parameter on the Mixing Rate 102
Figure 40 - Junction mass flow rate for two MULTI-D components connected in series 106
Figure 41 – Axial void distribution for a one MULTI-D Component bundle. 107
Figure 42 – Axial void distribution for a two MULTI-D Component bundle. 107
Figure 43 – Predicted vs. Measured void fraction for the two nodalizations 108
Figure 44 –Validity of the Quasi-Steady State Approach for Case 1071-59 109
Figure 45 - Bundle Averaged Void Fraction Dependence on Number of Nodes 111
Figure 46 - Subchannel Accuracy Dependence on Number of Nodes 111
Figure 47 - Application of CIAU on RELAP Results of Case 4101-02 118
Figure 48 - Application of CIAU on RELAP Results of Case 4101-13 119

Figure 49 - Application of CIAU on RELAP Results of Case 4101-69 119
Figure 50 - Application of CIAU on RELAP Results of Case 4101-86 120
Figure 51 - Application of CIAU on ASSERT Results of Case 4101-02 122
Figure 52 - Application of CIAU on ASSERT Results to Case 4101-13 123
Figure 53 - Application of CIAU on ASSERT Results to Case 4101-69 123
Figure 54 - Application of CIAU on ASSERT Results to Case 4101-02 124
Figure 55 - Junction Type: "1 Water - 1 Water" 153
Figure 56 - Junction Type: "Central - 1 Water" 153
Figure 57 - Junction Type: "Corner - Side" 154
Figure 58 - Junction Type: "Side - Side" 154
Figure 59 - Junction Type: "Side - Typical" 154
Figure 60 - Junction Type: "High Burnup Adjacent – High Burnup Diagonal" 155
Figure 61 - Junction Type: "High Burnup Adjacent - Typical" 155
Figure 62 - Junction Type: "High Burnup Diagonal - Typical" 156
Figure 63 - Thermal Conductivity of Fuel Rod Materials 157
Figure 64 - Specific Heat of Fuel Rod Materials 157
Figure 65 - Density of Fuel Rod Materials 158

LIST OF TABLES

Table 1 - Partial list of system codes in use 9
Table 2 - Partial list of subchannel codes in use 11
Table 3 - Sources of Uncertainty 13
Table 4 - Example of Input Uncertainty Parameters 18
Table 5 – Driving Mechanisms of Subchannel Mixing 33
Table 6 - General Transport Equation Terms [65]. 35
Table 7 - General Transport Equation Applications [65]. 36
Table 8 - Selected values for N. 44
Table 9 - Bundle Parameters. 46
Table 10 - Accuracy of Process Measurements. 48
Table 11 - Case Matrix for Test Series 1071-XX and 4101-XX 49
Table 12 - Subchannel Parameters 51
Table 13 – Subchannel Junction Properties 52
Table 14 - List of closure models selected 54
Table 15 - CIAU Method Summary 67
Table 16 - Hypercube boundaries 67
Table 17 - Boundary Conditions for the Two-Phase Pressure Distribution Tests 71
Table 18 – Effect of axial loss coefficients on void fraction predictions 74
Table 19 – RELAP5-3D Subchannel Void Fraction Prediction Accuracy 75
Table 20 – ASSERT Subchannel Void Fraction Prediction Accuracy 79
Table 21 - Definition of Accuracy Quantification Terms [73] 83
Table 22 - Selected Cases for Accuracy Analysis 85
Table 23 - Accuracy Analysis of Selected Cases in RELAP 86
Table 24 - Accuracy Analysis of Selected Cases in ASSERT 87
Table 25 - Overall result comparison 88
Table 26 - ASSERT Nodalization Sensitivity Test - Boundary Conditions 110
Table 27 - Boundary Conditions for the Heat Transfer Correlation Sensitivity Tests 112
Table 28 - Two Phase Heat Transfer Correlation Selection Effects 113

Table 29 - Effects of the Mixing & Void Drift Model on Accuracy at Low Pressure 114
Table 30 – Effect of Two-Phase Heat Transfer Model on the Average Subchannel Error 114
Table 31 - Statistics of hypercubes used for RELAP case 4101-86 120
Table 32 - Statistics of hypercubes used for ASSERT case 4101-86 124
Table 33 - CIAU Performance Evaluation 125
Table 34 - RELAP5 Mass Conservation Terms [8]. 145
Table 35 - RELAP5 Momentum Conservation Terms [8]. 147
Table 36 - RELAP5 Energy Conservation Terms [8]. 148
Table 37 - ASSERT Mass Conservation Terms [19] 150
Table 38 - ASSERT Momentum Conservation Terms [19] 150
Table 39 - ASSERT Energy Conservation Terms [19] 151
Table 40 - MATLAB Functions Created for CIAU 159
Table 41 - Data Structure explanation of inputData 160
Table 42 - Data structure explanation for expData 161
Table 43 - Data structure explanation for cube 162

1 INTRODUCTION & PROBLEM SCOPE

According to the IAEA, there were 439 operational nuclear power reactors in the world as of December 31, 2007, of which 21.4% or 94 were Boiling Water Reactors (BWR) [1]. These reactors had a rated capacity of 85.3 GW(e), representing 22.9% of the world's nuclear power capacity, with 7 Advanced BWRs being planned and 2 currently under construction [1]. The world's growing energy demands and the shift away from fossil fuel generated power has placed additional pressure to maintain and develop new nuclear power plants in a safe manner.

Safety analyses of Nuclear Power Plants (NPP) in the past have relied extensively on making conservative assumptions during accident scenarios. These assumptions include impairing the effectiveness of safety system trips or maximizing the size of hypothetical breaks in the cooling system. The rationale behind such assumptions was that analyzing the 'worst case' scenario could account for – or at least partially account for - some of the uncertainty in the available models at the time [2]. Advances in computational capabilities, as well as the increased availability of experimental data have allowed the shift towards 'best-estimate' codes and methodologies in safety analysis. These 'best-estimate' codes allow analysts to predict the flow, fuel and neutronic characteristics of reactors more accurately than with conservative assumptions.

The focus of this study is on predicting void formation in BWR fuel bundles on a subchannel level. BWR fuel consists of Low Enriched Uranium (LEU) oxide pellets which are encased in zircaloy-2 rods approximately 12 mm in diameter [3]. Fuel bundles are constructed from 62 or 63 fuel rods and 1 or 2 water rods arranged in an 8 × 8 grid. A 1200 MW(e) BWR core will employ 732 of these bundles containing a total of 45,384 fuel rods [3].

Fission events occur in the uranium, generating a large quantity of heat which must be removed by light water coolant flowing in the spaces between the rods. The spaces are illustrated in Figure 1 and constitute the subchannels which are of interest in this study.

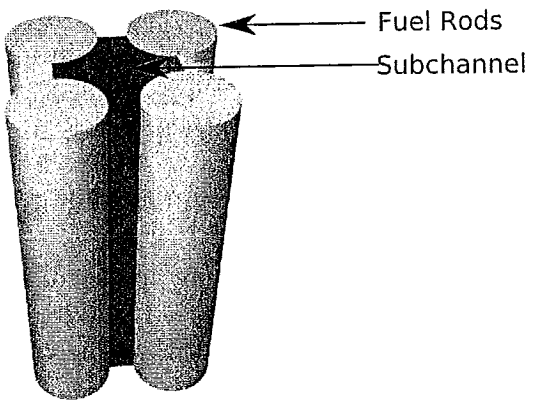

Figure 1 - Subchannel Definition

The coolant in a BWR enters the core from the bottom and flows upwards through the fuel bundles. As heat from the fuel is transferred to the coolant, the local enthalpy increases and eventually causes the water to undergo a phase

transition from liquid to vapour. The void fraction, α, of a fluid is defined as the fraction of a given volume which is occupied by vapour, and is provided as equation (1).

$$\alpha = \frac{V_{vapour}}{V_{total}} \tag{1}$$

The void fraction in a fuel bundle is a key quantity in core thermalhydraulics, and having accurate best-estimate predictions of it is essential when determining whether the fuel rods have sufficient cooling. A change in the subchannel void fraction will affect the heat transfer, pressure drop and neutron physics of the bundle.

In Light Water Reactors (LWRs), as void begins to form in the subchannels, the heat transport capability of the coolant is increased as a result of the turbulence caused by the bubbles. However, the heat transfer coefficient of vapour is much lower than water, so when the void fraction is increased to the point where vapour surrounds most of the fuel rod, the ability of the coolant to remove the heat generated by the rod is severely hampered. This is referred to as the Departure from Nucleate Boiling (DNB) or as the Critical Heat Flux (CHF) when referring to the heat flux at which it occurs.

Differences in the viscosity and density of the water and vapour suggest that the wall friction of each phase will be different. Although the exact nature of the two-phase friction is not yet completely understood, experimental studies

indicate that the addition of vapour to the flow of water in a channel will increase the frictional losses [4]. This phenomena implies that the pressure drop in a fuel channel or bundle will increase once the flow moves beyond the point of the Onset of Significant Void (OSV) [4].

The presence of vapour in the fuel bundles affects the neutronic behaviour of the reactor core. In LWRs, neutron thermalization is accomplished by using the water as a moderator. When the water is displaced by vapour, the number of neutrons being slowed enough to cause fission reactions is reduced. This in turn decreases the reactivity – or the fission reaction rate - of the core, and reduces the power of the fuel rods [5].

The ongoing BWR-Fine-mesh-full-size-Bundle-Test (BFBT) benchmark is being conducted under the Organization for Economic Cooperation and Development (OECD) and the Nuclear Energy Agency (NEA) [6]. One of the purposes of the benchmark is to document and compare the ability of available computer codes to predict the void fraction distribution in BWR fuel bundles. In this study two different codes – RELAP5-3D© and ASSERT-PV – are used to perform the void fraction simulations. RELAP5-3D© is a system-level code, and its application to determining subchannel behaviour has not been widely documented. ASSERT-PV is a Canadian subchannel code originally developed by Atomic Energy of Canada Limited (AECL), and although it is capable of

modeling vertical BWR style fuel bundles, its primary use is in modeling horizontal CANada Deuterium Uranium (CANDU) style bundles.

Regulatory bodies also demand uncertainty analyses of simulated results in order to account for user effects, code errors and input uncertainties. The BFBT benchmark provides a framework for participants to compare the application of uncertainty methods to experimental results [6]. In addition to simulating the void distribution and flow in a fuel bundle, part of this study is dedicated to exploring uncertainty and sensitivity analyses. Two methods will be examined: the Code for Internal Assessment of Uncertainty (CIAU) developed at the University of Pisa is used for the uncertainty analysis of the subchannel void fraction, while the ordered statistics method is used for the sensitivity analysis. Section 3.5 describes the theory behind both methods, while sections 5.2 and 6 present the results of the sensitivity and uncertainty analyses.

The results from the two codes will be compared against experimental data obtained by the Nuclear Power Engineering Corporation (NUPEC) of Japan. This dataset provides high resolution measurements of the void fraction in BWR bundles at the subchannel level. This dataset is notable since the experiments are done at full scale and at operating conditions encompassing what would be typically found in BWRs.

This study will present a brief overview of the codes available for performing such simulations as well as a review of past work which has been

conducted in the field. A theory section provides an overview of the theoretical basis of the key partial differential equations governing thermal-hydraulic behaviour and a brief discussion on how each of the codes implement it. The empirical models activated in the codes are also justified in this section. An examination of the theoretical basis of the uncertainty methods used is also provided.

The Application and Methodology section details the experimental facility as well as how it is represented in the ASSERT and RELAP simulations. The section also describes how the uncertainty methodology was adapted for this study. Finally, results, conclusions and recommendations for future work are provided.

To summarize, the objectives of this study are to:

- Evaluate the accuracy of ASSERT and RELAP in the prediction of the void fraction distribution in a BWR type bundle at the subchannel level.
- Study the sensitivity of code predictions to empirical correlation selection and nodalization.
- Apply ordered statistics methods to determine the sensitivity of the results to the uncertainty in the experimental boundary conditions.
- Adapt the CIAU method to the prediction of uncertainty bands at the subchannel level for void fraction estimates.

2 BACKGROUND & LITERATURE REVIEW

The two-phase flow behaviour of a fuel channel may be simulated through system level codes and subchannel level codes. This section provides background information on the former two types of codes, as well an introduction to the uncertainty methods available. A literature review of the work which has been conducted on void fraction behaviour in BWRs is also included.

2.1 *System Level Codes*

System level codes represent the most generic level of thermal-hydraulic modeling available. These codes are typically used to model the entire primary and/or secondary side loops of nuclear reactors. The one-dimensional nature of the code implies that the code relies heavily on the averaging of the equations describing the fluid characteristics so local effects may not always be properly represented. System codes are generally robust in nature and can be used to model complex components such as turbines, steam generators and pumps. The codes represent hydrodynamic components in one-dimension; although certain components of codes such as RELAP5-3D allow the three-dimensional mass and momentum conservation equations to be solved.

Since a typical application of a system code would be to model postulated accident scenarios such as a Loss Of Coolant Accident (LOCA), emergency coolant injections or pump trips [7,8], they are extensively validated against

experimental facilities. As part of the validation matrix for thermal-hydraulic system codes, the Nuclear Energy Agency's (NEA) Committee on (the) Safety of Nuclear Installations (CSNI) has identified 67 unique phenomena for which 2094 sets of test data spanning 187 experimental facilities are available [9].

In this study, the Reactor Excursion and Leak Analysis Program (RELAP) code will be employed. RELAP was developed by the United States Nuclear Regulatory Commission (USNRC) [8] and is extensively used in NPP analysis. It is currently managed under the Code Application and Maintenance Programme (CAMP), and plans are to gradually phase it out and replace it with the TRAC-RELAP Advanced Computational Engine (TRACE). Over decades of use and development, several specialized variants of the code have been spawned such as SCDAP/RELAP which is used in severe accident analysis [10] and RELAP5-3D which has a specialized component permitting three-dimensional modeling [8].

Studies involving LOCAs are frequently conducted using RELAP and are well documented in both conferences and published literature [11,12]. Part of the reason the code is so widely proliferated is because of its robustness. The RELAP family was originally designed for performing transient analyses on LWRs [8], but has since been adopted for the study of virtually all current commercial reactor types including VVERs [13], RBMKs [14] and CANDUs [15,16]. Additionally, there are documented cases of the code being successfully coupled to neutronics [17] and CFD codes [18].

Although RELAP is the code used in this study, other notable system codes in use are listed in Table 1.

Table 1 - Partial list of system codes in use

Code	Meaning	Origin
CATHARE	Code for Analysis of THermal-hydraulics during Accident of Reactor and safety Evaluation	CEA - France
TRACE	TRAC/RELAP Advanced Computational Engine	USNRC - USA
ATHLET	Analysis of THermal-hydraulics of LEaks and Transients	GRS - Germany
MARS	Multi-dimensional Analysis of Reactor Safety	KAERI - Korea
CATHENA	CANadian Algorithm for THErmalhydraulic Network Analysis	AECL - Canada
RELAP	Reactor Excursion and Leak Analysis Program	USNRC - USA
TUF	Two Unequal Fluids	OPG - Canada
SOPHT	Simulation Of Primary Heat Transport	OPG - Canada

2.2 *Subchannel Level Codes*

While a system code may represent a fuel channel as a one-dimensional component, results from the code represent spatially averaged values for the thermalhydraulic parameters. The drawback with this is that there are relevant local effects in fuel bundles which do not get represented. For example, in the NUPEC bundle tests, the fuel rods are operated at between 45% and 130% of the average rod power, so one would expect that the void fraction would be higher in subchannels adjacent to the hotter fuel rods. Subsequently, one of the subchannels may reach CHF at a lower power than the bundle average – underscoring the importance of being able to predict localized effects.

A subchannel code allows the fuel bundles to be modeled at a higher spatial resolution. In these codes, each subchannel and fuel rod in the assembly is

nodalized independently. The conservation equations of mass, momentum and energy are very similar to those found in the system codes, however, empirically derived source and sink terms are added to model the subchannel interactions [19,20,21]. These terms will typically represent phenomena such as turbulent mixing or void drift [19,20,21].

The subchannel codes are used exclusively for modeling the thermalhydraulic behaviour within a fuel bundle, and studies are commonly conducted to validate their ability to predict CHF [22], two-phase pressure losses [23], and of course void fraction distribution [24].

The Advanced Solution of Subchannel Equations in Reactor Thermalhydraulics (ASSERT) code is a subchannel code developed by Atomic Energy of Canada Limited (AECL). It is the successor to ASSERT-IV, which in turn traces its roots back to COBRA-IV, a subchannel code developed by Pacific Northwest Laboratories in the United States [19]. Although capable of modeling BWR and PWR subchannels, the ASSERT family of codes has primarily been used to examine subjects such as modeling flow behaviour in crept pressure tubes [25] and examining new fuel designs for CANDUs [26].

Some of the other subchannel codes currently in use are listed in Table 2.

Table 2 - Partial list of subchannel codes in use

Code	Meaning	Origin
MATRA	Multichannel Analyzer for steady states and Transients in Rod Arrays	KAERI - Korea
COBRA	COolant Boiling in Rod Arrays	PNL - USA
VIPRE	Versatile Internals and component Program for Reactors; EPRI	CSA - USA
ASSERT	Advanced Solution of Subchannel Equations in Reactor Thermalhydraulics	AECL - Canada
FIDAS	FIlm Dryout Analysis code in Subchannels	PNC – Japan

2.2.1 Subchannel Code Validation with the NUPEC Bundle Tests

In 1994, Inoue et. al. performed a study of the void fraction results obtained in the NUPEC tests using the COBRA/BWR and THERMIT-2 subchannel codes [24]. The authors found that both codes were capable of predicting the average void in the bundle to within 6%, however, they noted problems with both codes predicting large void gradients, suggesting that the code predictions at the subchannel level were not as accurate [24].

A 1999 study, Aounallah and Coddington used the NUPEC tests to validate VIPRE-02 and found that the code was generally over-predicting the bundle averaged void [27]. Additionally, they reported difficulties in obtaining accurate void fraction predictions under low flow and power scenarios [27].

Burns and Aumiller reported similar results in 2006 in their work modeling the tests with COBRA-IE [28]. They found that at low exit qualities,

the absolute error for the bundle void fraction average was as high as 0.10 void, although at higher exit qualities this problem diminished [28].

In 2006, Hwang, Jeong and In modeled the void distribution using MATRA and found that the code tended to under-predict the void fraction as when outlet quality was increased. They also determined that neither predicted nor measured void distributions were symmetric, and recommended against using symmetry planes in nodalizations [29].

Glück studied the ability of F-COBRA-TF to predict the void fraction in the NUPEC experiments in 2008 and had similar findings to Hwang et. al. The author suggested that over-prediction occurred when the flow was in the low-void bubbly regime and under-predicted as the void fraction increased and slug flows developed. He also suggested a correction to the densitometer measurements of the benchmark relating to the void distribution within a subchannel and where the beam actually scanned. The author determined that once the correction was applied to the experimental results, the simulation error was reduced overall [30].

2.3 *Uncertainty Analysis*

As part of 10 CFR 50.46 Appendix K, the USNRC explicitly requires uncertainty analyses to be performed on results obtained by best-estimate codes during scenarios involving LOCAs or Emergency Core Cooling System (ECCS) [31]. Although these codes may be constantly updated to include new

correlations and models, there always exists a certain degree of uncertainty in the simulated results. D'Auria has summarized the major components in Table 3 [32].

Table 3 - Sources of Uncertainty

Uncertainty Type	Stems from
Code Uncertainties	Uncertainty which may result from the empirical correlations selected or the numerical methods applied. Particular emphasis is placed on the choice of correlations since they are typically restricted to a particular range of validity and using them beyond this can have a significant impact on the result.
Plant or Process Uncertainties	Uncertainty resulting from the boundary or initial conditions either measured or supplied to the analyst being imperfect.
User Effects	Uncertainty stemming from the development of the nodalization or interpretation of the available information. Reference [32] suggests and demonstrates that it is unlikely that two independent analysts supplied the same information and using the same code for a problem will come up with the same results.

Swiler classifies the uncertainties as either epistemic or aleatory in nature. Epistemic uncertainties stem from an incomplete understanding of the phenomena or the physical processes involved and may be reduced by improving the models or measurement techniques used. Aleatory uncertainties are caused by the natural random fluctuations of the systems, and cannot be reduced [33]. Within the context of this study, the uncertainties related to the extensive use of empirical correlations in the codes and the measurement uncertainties are both classified as epistemic.

In 1989, the USNRC released NUREG/CR-5249 which was a report attempting to formalize the uncertainty assessment process with the Code Scaling, Applicability, and Uncertainty (CSAU) Evaluation methodology [34]. Since then, several different methods have been developed to assess the uncertainty of code predictions. Four methods commonly used are: the CIAU method, the Ordered Statistics Method, the Response Surface Method, and the Direct Monte Carlo Method.

The method used varies from group to group, and the pros and cons of each method are often vigorously debated. This study uses the CIAU method to predict void fraction uncertainty bands at the subchannel level and also make use of ordered statistics to demonstrate the sensitivity of the predictions to boundary condition uncertainties.

2.3.1 CIAU Method

The CIAU method was developed at the University of Pisa as a means of predicting the uncertainty bounds of parameters predicted by best-estimate codes based on existing comparisons with experimental data [32, 35]. This section briefly summarizes the principle of CIAU and some typical applications.

This method is based on simulating transients at test facilities and NPPs, comparing the code predictions with the measured results, compiling a large database of "accuracy quantities" which reflect the performance of the code under the particular scenarios, and then extrapolating this value when required in full

scale reactor analysis [36]. Once the accuracy database has been built, this method allows the near instantaneous prediction of uncertainty bands for plant transients. However, a considerable effort is required upfront to run each test case and construct the database. Furthermore, each new version of a code will require the entire database to be regenerated[1]. A thorough explanation of this method is provided in Section 3.5.1.

In a 2006 study, Salah et. al. assessed the CIAU method and one developed by Gesellschaft fur Anlagen- und Reaktorsicherheit (GRS) for predicting the uncertainty bounds on simulations of a Kozloduy (VVER-1000) pump trip transient [37]. The team analyzed the upper plenum pressure and clad temperature using the two methods and determined that the CIAU method predicted uncertainty bands about twice as wide as the GRS method for the pressure and five times as wide for the clad temperature [37]. The pressure predictions were compared to actual data from the Kozloduy test, and Salah determined that in order to generate bounds with the GRS method to fully envelop the experimental data, a large number of parameters needed to be varied [37].

De Crécy et. al. released the results of the Best Estimate Methods Uncertainty and Sensitivity Evaluation (BEMUSE) benchmark on the Loss of Fluid Test (LOFT) LBLOCA experiments in 2008 [38]. Part of the benchmark involved predicting the uncertainty bands around the clad temperature and upper

[1] This is not a unique characteristic of the CIAU method and may be true for any of the uncertainty assessment methods.

plenum pressure during the transients [38]. The study compared several methods for deriving the uncertainty bounds, and found that while the uncertainty bands predicted by CIAU on the pressure enveloped the experimental values, they were considerably larger than the bounds predicted by the other participants – spanning 5 MPa at some points in the transient [38].

Galetti reported in 2008 that the Brazilian nuclear regulatory body was examining the use of the CIAU method to predict the uncertainty bounds of fuel temperature during a hypothetical LBLOCA in the Angra-2 NPP [39]. The study presented the uncertainty bounds which were generated for the transient, however no comparison was made with experimental data [39].

In each of the three case studies above, the authors relied on a master CIAU database which is constantly being updated by the University of Pisa. A discussion on how accuracy quantities are defined, sorted and extrapolated is provided in section 3.5.1.

In addition to thermalhydraulic analyses, Petruzzi et. al. suggested that the basis behind the CIAU method could be extended and applied to other best-estimate reactor calculations [36]. The author demonstrates the feasibility of a modification of the CIAU code which allows the method to be applied to neutron kinetics measurements from the Peach Bottom NPP turbine trip transients [36].

2.3.2 Ordered Statistics Methods

Ordered statistics are a form of non-parametric statistics that allow the prediction of statistical tolerances without the need to know the Probability Distribution Function (PDF) of the sample [40]. This is crucial in the context of thermalhydraulic simulations since the output parameters of interest are typically non-linear functions of multiple inputs. With each input representing a degree of freedom, attempting to derive uncertainty bounds on code results using Monte Carlo methods to map the output probability distribution function is a computationally expensive task. Since the PDF of the output is irrelevant in ordered statistics, the number of samples or code runs required has been demonstrated to be significantly less [40]. A further theoretical discussion of ordered statistics – specifically the use of Wilks' formula in the nuclear industry – is presented in section 3.5.2. There is a significant body of work demonstrating the application of ordered statistics to the field of nuclear safety, with the majority of the papers dealing with predicting the Peak Cladding Temperature (PCT) of the fuel during a LBLOCA transient.

The GRS method is one of the more commonly cited methods based on ordered statistics. Glaser has documented the application of the GRS method to predict uncertainty bounds on the PCT during a simulated LBLOCA of a German PWR reference reactor, as well as predicting the bounds on containment pressure during a similar event. He concluded that GRS method was adequate for both

scenarios examined, and that the experimental PCT and pressure were both well within the predicted bands [41].

Avramova et. al. used the GRS method to analyze the uncertainty of void fraction predictions by COBRA-TF in the BFBT benchmark. In order to do so, the authors identified twelve relevant input uncertainty parameters which are reproduced in Table 4 [42]. The study presented preliminary results that indicated that the uncertainty of the pressure measurements and the single phase mixing coefficient had the strongest influence on the void fraction.

Table 4 - Example of Input Uncertainty Parameters

Input Parameter	Accuracy (2σ value)	PDF
Pressure	± 1.0%	Normal
Flow Rate	± 1.0%	Normal
Power	± 1.5%	Normal
Inlet Temperature	± 1.5 °C	Uniform
Subchannel Area	± 0.5%	Normal
Single Phase Mixing Coefficient	± 42.0%	Normal
Two-phase Multiplier of the Mixing Coefficient	± 24.0%	Normal
Equilibrium Distribution Weighting Factor in the Void Drift	± 14.0%	Normal
Nucleate Boiling Heat Transfer Coefficient	± 24.0%	Normal
Interfacial Drag Coefficient under Bubbly Flow	± 32.0%	Normal
Interfacial Drag Coefficient under Droplet Flow	± 26.0%	Normal
Interfacial Drag Coefficient under Film Flow	± 26.0%	Normal

As part of the LOFT L2-5 benchmark, eleven participating organizations were asked to simulate a LBLOCA transient and report on the PCT, time to accumulator injection and time to complete quenching [38]. Nine of the eleven organizations elected to use some form of ordered statistics in deriving the

uncertainty bands around their reported results and in every instance, the reported uncertainty bands enveloped the experimental result [38].

Srivastava et. al. generated uncertainty bands with ordered statistics for the simulated PCT during a LBLOCA in an Advanced Heavy Water Reactor (AHWR) using RELAP5 [43]. When compared to the uncertainty bounds generated using the response surface method for the same transient, the author found about a 15% difference in the predicted upper bound of the peak cladding temperature [43].

2.3.3 Response Surface Method & Direct Monte Carlo Method

The response surface method requires that the code be run for a given matrix of input variables, and that a polynomial or parametric surface is fit to the results [44]. A Monte Carlo simulation applied to the response surface then yields the expected distribution of outputs [44].

The direct Monte Carlo method is the brute force method, and involves running the code with varied inputs for as many times are required to generate the desired uncertainty bands [33, 44]. This is not typically used in large nodalizations due to the sheer number of code runs required, although it may be applicable for smaller scale tests or facilities. Recent advances in parallel and distributed computing have also renewed interest in this method.

2.4 *Flow Behaviour and Phenomena*

2.4.1 Pressure Drop

In single phase flow, one of the most widely used correlation for determining the pressure drop due to the friction of the liquid against the surface of the pipe is the Colebrook-White correlation [45]. The solution of this equation is iterative, and there have been many attempts at providing an explicit approximation. Moody [45], Zigrang-Sylvester [46], Chen [8], Haaland [47], and Churchill [48] are examples of the more widely known approximations. Romeo studied eleven such correlations and concluded that a modified version of the Zigrang-Sylvester correlation provided the best statistical fit to experimental data [49].

The pressure drop in two-phase flow may be determined either by assuming that the friction factor is the same as that in fluid phase only, or by applying a multiplier to the single-phase friction factor [50]. Lockhart-Martenelli first proposed a correlation for a two-phase multiplier in 1949, based on flow quality [50]. Martinelli and Nelson also proposed a steam-water correlation based on the absolute pressure and mass quality in 1948, which was subsequently adjusted by Thom in 1964 [50].

Barcozy proposed a correlation based on the fluid-gas viscosity and velocity ratios in 1965, while Chisholm introduced a several multipliers based on the velocity ratios and the roughness of the pipe [50]. Friedel suggested a

correlation based on the mass quality, density ratio and viscosity ratios of the fluid, in addition to the non-dimensional Froude and Weber numbers [50].

2.4.2 Heat Transfer

For single-phase forced convection flows, the Dittus-Boelter correlation, or some other similar correlation based on the dimensionless Reynolds and Prandtl numbers is typically used [3]. Petukhov's correlation includes both of these dimensionless numbers, as well as a modified version of the Darcy-Weisbach friction factor suggested by Filonenko [8].

Under two-phase flow conditions, the heat transfer capability of the fluid is dependent on factors such as the void fraction, flow regime and geometry, so many different correlations exist.

Chen proposed a correlation considering both the nucleate boiling (microscopic) and the bulk convective (macroscopic) contributions to the overall heat transfer coefficient [51]. The microscopic component was based on a corrected version of the Forster-Zuber correlation, while the macroscopic component is derived as an adjusted form of Dittus-Boelter [51,52].

The correlation proposed by Ahmad was originally intended to predict the heat transfer coefficients at the onset of bubble detachment [53]. Like many other heat transfer correlations, it is partly based on the dimensionless Reynolds and Prandtl numbers, however, it is suggests a dependence on the inlet enthalpy of the channel [53].

2.4.3 Void Fraction

Predicting the void fraction as the fluid undergoes phase transformation in a channel or pipe is a difficult task – and a motivation behind this study. In computer codes, the void fraction may be modeled using a homogenous, separated or drift-flux model [50].

The homogeneous model treats the flow as a single phase mixture with averaged fluid properties, and uses an Equal-Velocity-Equal-Temperature (EVET) assumption that assumes the vapour and liquid phases have the same velocity and are at thermal equilibrium. In this model, the treatment of two-phase friction requires a two-phase multiplier such as the ones proposed by McAdams, Cicchitti, or Dukler [50].

In the separated flow model, each phase is modeled individually, and is based on an Unequal-Velocity-Equal-Temperature (UVET) assumption. This assumes that the two phases are at thermal equilibrium, however, the momentum of each phase is modeled separately and may be different. Two phase friction multipliers such as Barcozy, Chisholm, or Friedel are still required, in addition to correlations relating the void fraction to an independent flow variable. Void correlations proposed by Lockhart-Martinelli, Thom, and Barcozy are associated with this model [50].

Drift-flux models are based upon the relative difference in velocity between the vapour and liquid phases in the flow. Additionally, since it is

assumed that the phases are not at thermal equilibrium, this model would be classified as having Relative-Velocity-Unequal-Temperature (RVUT). Empirical correlations are used in order to relate the void fraction of a system or channel to flow parameters such as the flow velocity, fluid density and pressure.

Coddington and Macian conducted a survey and found twenty-five different void fraction correlations for the drift-flux model, of which thirteen were determined to be accurate enough to warrant an in depth study. Each of the correlations were implemented in the RETRAN-3D code and compared against experimental data for vertical rod bundles and tubes from eight different facilities. The authors concluded that the Chexal-Lellouche correlation - which is used in RELAP - was among one of the 'best' performing, underpredicting the experimental void fraction by an average of only 0.017 [54]. The correlations which were examined in the study included those proposed by: Jowitt, Sonnenburg, Dix, Bestion, Chexal-Lellouche, Inoue, Zuber-Findlay, and Ishii [54].

Although BWR subchannel predictions have been investigated frequently, there have also been many studies conducted on different geometries and flows. Hibiki and Ishii have identified four scenarios where improvements to the current drift-flux void correlations can be made [55]. They suggest that further work is possible in areas of: low flow conditions, counter-current or downward flows, large diameter pipes and horizontal flows [55].

Hibiki and Ishii propose a drift flux void correlation for bubbly flows based on an extensive examination of bubble dynamics and incorporating the Sauter mean bubble diameter [55]. The authors compared the performance of their correlation against experimental data for pipes with an inner-diameter between 25.4 and 50.8 mm, and found that it had an average relative error between 8.90% and 23.1% depending on the location of the measurements [55].

Goda et. al. performed two-phase downward co-current flow experiments on pipes with inner-diameters of 25.4 and 50.8 mm [56]. A least squares fit was performed on the data and the subsequent correlation was then compared to results obtained at four other facilities. The investigators found that their correlation fit the data with "excellent agreement" with an average relative deviation of 15.4%.

2.5 *Experimental Studies on Two-Phase Flow in Vertical Bundles*

Lahey et. al. conducted a study on the pressure drop and heat transfer characteristics of a nine-rod bundle under two-phase conditions in 1970. The work concluded that the mass flux and quality of the corner and side subchannels was measured to be below the bundle average, while the center subchannel tended have measurements above the bundle average – although as the bundle averaged mass flux was increased, the differences between the perimeter subchannels and the central subchannels decreased. The study also attempted to model the bundle using the COBRA subchannel code, and concluded that while single-phase

predictions matched very well, the code had difficulty predicting the two-phase mass flux and quality of the side and corner subchannels. Also of interest was their observation that the two-phase pressure drop multiplier had little effect on the flow predictions and that measurements tended to be similar to the Martinelli-Nelson correlation [57].

A 2001 work by Kok, van der Hagen, and Mudde examined the void fraction measurements on a 6 × 6 electrically heated bundle and demonstrated that their results were best predicted by using a correlation for void fraction proposed by Dix in conjunction with the drift-flux model [58]. Additionally, they noted in their work that they saw no evidence of lateral void drift – which as identified in Section 3.3, is a key assumption of the drift-flux model [58].

In 2008, Yun et. al., used a partial vertical bundle consisting of 9 rods arranged in a 3 × 3 rectangular array to study the effects of heat flux and mass flow rates [59]. They concluded that the observed void fraction was best predicted by a correlation proposed by Bestion [59].

Shirai et. al. reported coupling the subchannel code NASCA to TRAC/BF1-ENTREE to simulate the turbine trip tests from Peach Bottom Unit 2 [60]. They noted that the cross flow between the subchannels affected their void distribution predictions by forcing void from the corner channels to the center channels [60]. They concluded that the driving force behind the redistribution of the void was the void drift term in NASCA [60].

3 THEORY

This section provides a brief overview of the fundamental equations and underlying principles describing the behaviour of single-phase flow in the subchannels, followed by a discussion on two-phase flow models. The code representations of these equations are then covered and any empirical correlations that have been selected for use in the code are explained and justified. Finally, the theory behind the uncertainty methods used in this study is described.

3.1 *Single-Phase Thermalhydraulic Behaviour*

Bernoulli's equation is one of the starting blocks when describing fluid behaviour. Equation (2) states that for a steady, invisicid and incompressible fluid, the sum of the static, hydrostatic and kinetic pressures is always constant along a streamline [45]. In the equation, P represents the local pressure, ρ is the density of the fluid, g is the gravitational acceleration, z is the relative height and v is the fluid velocity.

$$P + \rho g z + \frac{\rho v^2}{2} = \text{Constant along a streamline} \qquad (2)$$

Equation (3) is a modified version of Bernoulli's equation which is derived in reference [3] and is relevant to analyzing flows in a subchannel.

$$P_{out} - P_{in} + \frac{\rho\left(v_{out}^{\ 2} - v_{in}^{\ 2}\right)}{2} + \rho g\left(z_{out} - z_{in}\right) = -\rho g h_L \tag{3}$$

There are three major types of losses that must be accounted for: elevation losses, frictional losses and form losses. Elevational losses occur when moving up a vertical channel, and represent the work which must be exerted on the fluid in order to overcome gravity. This is represented by the third term of equation (3). The other two losses are represented in the right hand side term of (3) and the head loss term, h_L, may be broken down as (4):

$$h_L = \left(\sum \frac{fL}{D_h} + \sum K\right)\frac{v^2}{2g} \tag{4}$$

Frictional losses are incurred when the fluid passes over the microscopic imperfections of the fuel rod surface, and are proportional to the friction factor, f, length of the section, L, and the hydraulic diameter D_h. The friction factor in (3) may be extracted from Moody's friction factor chart, or solved using a correlation such as Swamee and Jain's version of the Colebrook-White equation (5) [45], noting that Re is the dimensionless Reynolds number defined in (6), k_s is the surface roughness in mm, and μ represents the dynamic viscosity of the fluid.

$$f = \frac{0.25}{\left[\log\left(\frac{k_s}{3.7D_h} + \frac{5.74}{\mathrm{Re}^{0.9}}\right)\right]^2} \tag{5}$$

$$\mathrm{Re} = \frac{\rho v D_h}{\mu} \tag{6}$$

Form losses account for head losses caused by abrupt changes in the flow area such as at the grid spacers. The loss coefficient K from equation (4), will vary depending on the geometry, and for this study has been provided by the benchmark organizers to be K = 1.2 for each grid spacer encountered by the flow [6].

3.2 *Single-Phase Heat Transfer*

The heat generated in the fuel rods is transferred to the fluid through conduction and convection. In the experiments, heat is generated by an electrical element at the center of fuel rods and conducted through the insulating Boron-Nitride to the sheath where it is removed by the coolant. This is illustrated in Figure 2.

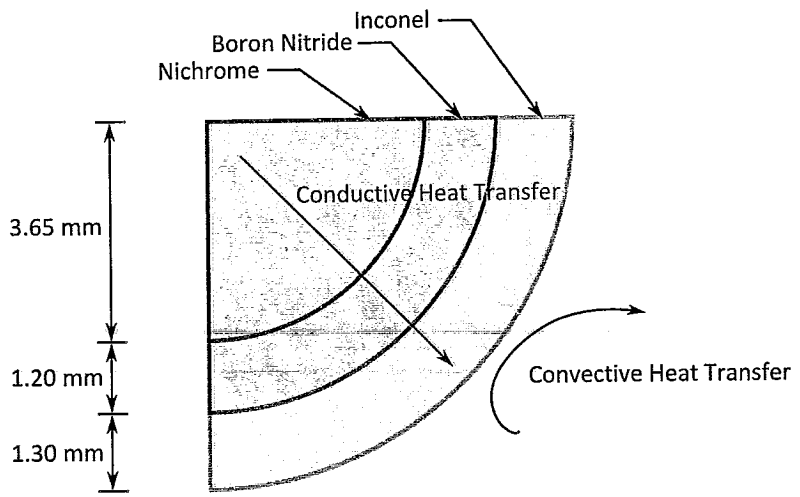

Figure 2 – Heat removal from a fuel rod

For a steady state, one-dimensional case, conduction is governed by Fourier's law given in equation (7) where k is the conductivity of a material.

$$\frac{q}{A} = q'' = -k\frac{dT}{dx} \tag{7}$$

Similarly, the heat removed from the sheath by the coolant is governed by equation (8).

$$q'' = h\frac{dT}{dx} \tag{8}$$

The heat transfer coefficient, h, is often expressed as part of the dimensionless Nusselt number given in equation (9). The Nusselt number by definition is the ratio of convective heat transfer to conductive heat transfer, and may be found through empirical correlations.

$$Nu = \frac{hD_h}{k} \tag{9}$$

It is often stated in terms of two other dimensionless numbers: the Prandtl number in equation (10) and the Reynolds number equation (6) [61]. The former describes the ratio of viscous to thermal diffusivity and is used to indicate as to whether convective or conductive heat transfer is expected to be dominant for a fluid [61]. The latter of the numbers represents the ratio of the inertial to viscous forces and is often used to characte1ize the level of turbulence in the flow [61]

$$\mathrm{Pr} = \frac{c_p \mu}{k} \tag{10}$$

These principles allow the formation of a rudimentary representation of the fluid and heat transfer behaviour which occurs in the subchannels. When a second phase – such as vapour – is introduced, the flow behaviour becomes much more complex.

3.3 Two Phase Thermalhydraulic Behaviour

The importance of being able to predict the void fraction cannot be understated as its presence in a flow will affect the heat transfer, pressure losses and general behaviour of the fluid. Since these parameters determine whether the fuel in the reactor can be kept cool, having accurate estimations is essential. Numerous studies have attempted to characterize both the formation of vapour as well as the hydrodynamic behaviour of two-phase flows. However complex phenomena such as turbulence, wall effects and interfacial interaction means that despite the effort, there is still no definitive model based entirely on first principles which fully describes all aspects of water-vapour flows. Instead, current modeling still requires the extensive use of empirical models and numerical methods to represent systems.

Collier and Thome divide co-current upward vertical two-phase flows into the four distinct, observable regimes illustrated in Figure 3 [50]. The driving factors which determine which regime that the flow falls in include: void fraction, mass flux and the relative velocity of the vapour and liquid.

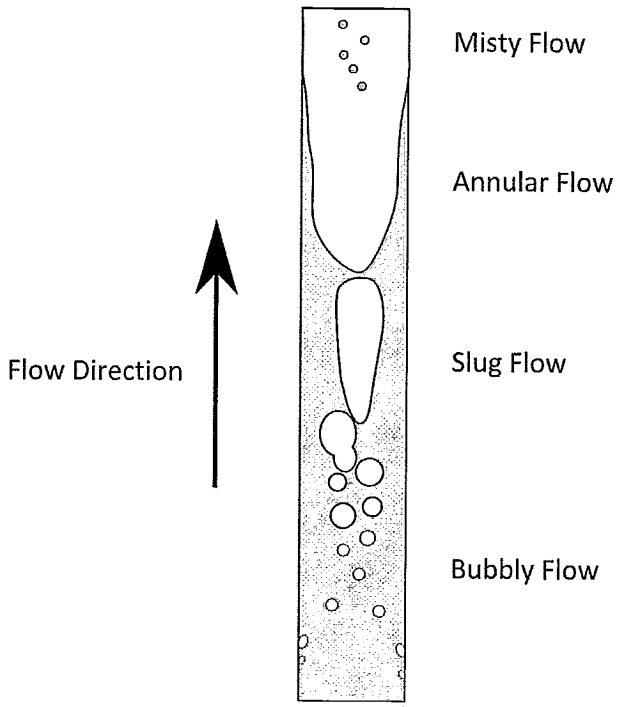

Figure 3 - Vertical Upward Two-Phase Flow Regimes.

Nucleation theory holds that when a fluid is heated vapour bubbles will begin to form on defects and imperfections on a surface [62]. As the liquid is heated to a temperature several degrees below saturation, the bubbles begin to grow. The vapour in the bubble has a density an order of magnitude lower than the fluid causing a buoyant force to be exerted upwards. When this force exceeds the adhesion force of the bubbles, they begin to detach from the surface and interact with the liquid flow, marking the beginning of the bubbly flow regime. Additional heat applied brings the flow to saturation temperature, increasing the frequency and size of the bubbles, to the point where they begin coalescing and forming intermittent vapour slugs. At higher void fractions, the slugs eventually begin merging with one another and the flow is characterized by a vapour core surrounded by a thin liquid layer on the walls of the channel. This region is

known as the annular flow regime. Increasing the void fraction further drives the flow into the misty flow regime where in the peripheral liquid layer has vapourized and the flow is dominated by steam containing small liquid droplets.

The flow regime of the channel is not based entirely on the void fraction, as both the liquid and vapour mass flux will also affect it. The flow regime of Hewitt and Roberts for vertical two phase flows is illustrated as an example in Figure 4 [50]. RELAP uses a modified version of the flow regime maps proposed by Taitel, Dukler and Ishii while ASSERT determines it based only on the void fraction [8,19].

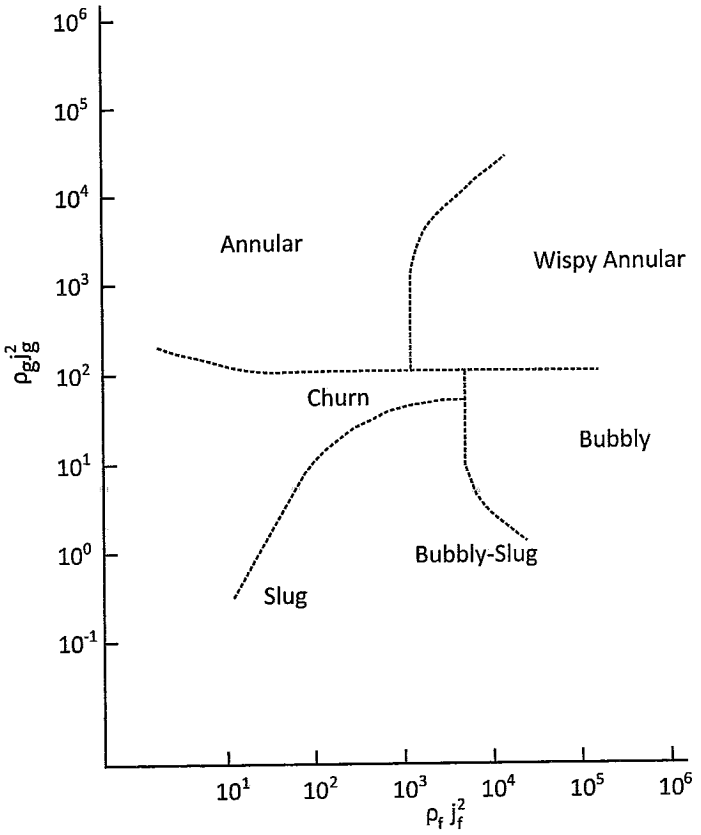

Figure 4 - Vertical flow pattern map of Hewitt and Roberts

3.3.1 Subchannel Mixing

Subchannel mixing is a phenomena caused by the unequal heating, geometry and mass fluxes across adjacent subchannels. Mass, momentum and energy interactions across the inter-subchannel junctions are predicted empirically by subchannel codes, while system codes do not typically include these correlations. Lahey and Moody identify four driving mechanisms behind subchannel mixing which are listed in Table 5 [63]. In the present study, only the void diffusion mechanism is modelled since it is the most significant. The diversion cross flow is assumed to be negligible while the spacer grids are modelled simply as axial form losses with little effect on the turbulent mixing. The buoyancy drift is insignificant since the bundle is vertical.

Table 5 – Driving Mechanisms of Subchannel Mixing

Mechanism	Cause
Diversion Cross Flow	A difference in the local pressure of two adjacent subchannels will cause a lateral driving force across the common junction.
Turbulent Mixing	Mixing which is caused by chaotic and random fluctuations in the subchannel pressure and flow, or by obstacles such as spacer grids.
Void Diffusion	The tendency for the void to migrate to an "equilibrium void distribution".
Buoyancy Drift	Void migration caused gravitational forces. Only of significance in horizontal channels where the void tends to migrate to the top of the bundles [64].

The void diffusion phenomena is not particularly well understood and is based more on observed trends than physics. Lahey and Moody indicate that the

equilibrium void distribution represents the tendency of void to migrate from subchannels which are small or have low flow rates to those which are larger or have higher flow rates [63].

3.4 Two-Phase Model Formulations

In Thermo-Fluid Dynamics of Two-Phase Flow, Ishii derives two models representing two-phase flow behaviour: the drift-flux or mixture model and the two-fluid model [65]. Both ASSERT-PV and RELAP base its constitutive equations on the drift-flux model [8, 19].

3.4.1 Reynolds Transport Theorem

3.4.1.1 Conservation Equations

Solving for the flow variables for every point in time and space is impractical for engineering applications, as not only would the computational requirements significantly outweigh the benefits, but many of the physical phenomena involved are not yet well understood. To this end, Ishii uses the concept of control volumes which divide the system under investigation into a manageable series of connected nodes [65]. The flow variables are solved for each node and the solutions represent the temporal and spatial averages. The underlying concept of the conservation equations is that any transportable quantity such as mass, momentum or energy must be conserved for over the entire

series of control volumes. Equation (11) is Reynolds transport theorem, a general equation for any transportable quantity [65].

$$\frac{\partial \rho_k \psi_k}{\partial t} + \nabla \cdot \left(\rho_k v_k \psi_k \right) = -\nabla \cdot J_k + \rho_k \phi_k \tag{11}$$

In the equation, the transportable quantity in phase k – such as mass or energy – is represented by ψ, while J represents the "current" of ψ through a given control volume, and φ represents sources and sinks of ψ. Table 6 explains each term in equation (11), which forms the basis of both the two-fluid and drift-flux models.

Table 6 - General Transport Equation Terms [65].

Term	Meaning
$\frac{\partial \rho_k \psi_k}{\partial t}$	This term is the storage of ψ per unit volume.
$\nabla \cdot \left(\rho_k v_k \psi_k \right)$	This term represents net quantity of ψ being advected into or out of the control volume by the fluid.
$-\nabla \cdot J_k$	The diffusive transport of ψ is represented as the gradient of the current.
$\rho_k \phi_k$	This term represents the sources and sinks of ψ per unit volume.

Ishii applies equation (11) to uphold the conservation of mass, momentum and energy using Table 7, yielding equations (12), (13) and (14) [65].

Table 7 - General Transport Equation Applications [65].

	ψ_k	$\mathbf{J}_k$	ϕ_k
Mass	1	0	0
Momentum	v_k	$p_k - \tau_k$	g_k
Energy	$u_k + \frac{v^2}{2}$	$q_k - T_k \cdot v_k$	$g_k \cdot v_k + \frac{\dot{q}}{\rho_k}$

$$\frac{\partial \rho_k}{\partial t} + \nabla \cdot (\rho_k v_k) = 0 \tag{12}$$

$$\frac{\partial \rho_k v_k}{\partial t} + \nabla \cdot (\rho_k v_k v_k) = -\nabla P_k + \nabla \cdot \tau_k + \rho_k g_k \tag{13}$$

$$\frac{\partial \rho_k \left(u_k + \frac{v_k^2}{2} \right)}{\partial t} + \nabla \cdot \left(\rho_k \left[u_k + \frac{v_k^2}{2} \right] v_k \right) = -\nabla \cdot q_k + \nabla \cdot (T_k \cdot v_k) + \rho_k g_k \cdot v_k + \dot{q}_k \tag{14}$$

The P in equation (13) represents pressure, while τ represents viscous stresses and g represents a general body force acting on the fluid such as gravity [65]. In equation (14), u represents the internal energy, while q is the heat flux, T is a surface stress tensor, and $\dot{q}$ represents the body heating [65]. Typically however, the energy equation is represented in terms of enthalpy, and equation (14) is modified accordingly. Together they form the fundamental basis upon which the two-fluid and drift-flux models are derived.

3.4.1.2 Jump Conditions

When two phases are modeled, the transfer of mass, momentum and energy between the phases must be modeled in such a way that the transported

quantities are conserved for the entire system. Ishii gives the jump conditions as equations (15), (16) and (17).

$$\sum \Gamma_k = 0 \tag{15}$$

$$\sum M_{ik} = 0 \tag{16}$$

$$\sum \left(\Gamma_k h_{fg} + a_i q'' \right) = 0 \tag{17}$$

Equation (15) simply states that the rate of mass created in phase k, represented as Γ_k, must be balanced by an equivalent rate of destruction of mass in the other phase. Equation (16) indicates that the interfacial drag forces of each phase must be equal and opposing, while equation (17) indicates that the enthalpy transferred to or away from phase k must consist of the enthalpy of vapourization and the heat flux applied to the interfacial area, a_i [65].

3.4.2 The Two-Fluid Model

The underlying principle behind the two-fluid model is that each phase may be represented with its own set of conservation equations [65]. This means that the two-fluid model consists of six total equations which describe the mass, momentum and energy conservation of each phase, with interactions being modeled by the jump conditions.

3.4.3 The Drift-Flux Model

The drift-flux model represents a simplification of the two-fluid model, and thus is, in theory, computationally more tractable. The underlying principle

behind the drift-flux model is that the entire system is considered as a mixture rather than as two independent phases, with additional modeling of the relative motion of the vapour phase to the mixture phase. This therefore captures both the mixture behaviour as well as the momentum and velocity differences in the phases. This is particularly important since the vapour velocity is typically greater than the bulk. Ishii derives a version of the drift-flux model containing four equations: mass, momentum and energy for the mixture, as well as a vapour mass continuity equation [65].

3.5 *Uncertainty*

3.5.1 CIAU Method

A Code (with the capability of) Internal Assessment of Uncertainty (CIAU) was developed at the University of Pisa as a means of estimating the uncertainty bands in NPP transients by a qualified system code. In the context of the BFBT benchmark, a code based on the core concepts of the CIAU methodology was developed in order to estimate the uncertainty of the simulated void fraction in the BWR fuel bundles.

The CIAU methodology assumes that all operational states of a NPP may be characterized as a combination of selected 'driving quantities' or critical parameters. These parameters form the basis of a hypercube in n-dimensional Euclidian-space, and it is postulated that different combinations of driving quantities will have inherently different uncertainties during the simulated

transients. In simulations of BWR transients, the CIAU methodology has established the driving quantities to be: the upper plenum pressure, primary circuit mass inventory, cladding temperature, core power, downcomer level [35].

Since this portion of the BFBT benchmark focuses solely on the behaviour of a single fuel bundle at steady state, a different set of driving quantities must be derived. Four parameters are selected for characterizing the accuracy of the void in the BFBT simulations. They are: the subchannel power to mass flux ratio, inlet pressure, inlet subcooling and the simulated void fraction in the subchannel. These driving quantities are normalized, subdivided into appropriate intervals and form the bases of the new hypercubes.

In order to take advantage of the quantity of available data, a calculation of the subchannel void fraction was performed for each available set of experimental conditions. The void prediction for each subchannel is treated as an individual data point, with each case in the BFBT simulation providing up to 80 points for the database.

An Accuracy Quantity (AQ) is defined in equation (18) and calculated for each data point. In the equation, Y_E and Y_S represent the experimental and simulated void fraction at the top of the active portion of each fuel bundle, while $\varepsilon = \pm 0.03 Y_E$ and represents the experimental uncertainty provided in the BFBT specifications.

$$AQ = \begin{cases} \dfrac{Y_S - \left(Y_E + \varepsilon^+\right)}{Y_S} & \left(Y_E + \varepsilon^+\right) < Y_S \\ \dfrac{\left(Y_E - \varepsilon^-\right) - Y_S}{Y_S} & Y_S < \left(Y_E - \varepsilon^-\right) \\ 0 & \left(Y_E - \varepsilon^-\right) \le Y_S \le \left(Y_E + \varepsilon^+\right) \end{cases} \tag{18}$$

Each hypercube may contain the results of several tests, however, data points from one test can be spread over several hypercubes as the subchannels at the sides and corners of the bundle have different power to mass flux ratios than those in the center.

The dispersion of data points belonging to the same test in a hypercube is accounted for using equations (19) to (23). In the subsequent equations, superscript i denotes the index of the hypercube while subscripts j and k represent a specific test and subchannel within hypercube i. When N_k points from one test are classified into a hypercube, the average and standard deviation to test average ratio are found for each test using equations (19) and (20).

$$\overline{AQ_j^i} = \sum_{k=1}^{N_k} \frac{AQ_{j,k}^i}{N_k} \tag{19}$$

$$S_j^i = \frac{1}{\overline{AQ_j^i}} \sqrt{\frac{\sum_{k=1}^{N_k} \left(AQ_{j,k}^i - \overline{AQ_j^i}\right)^2}{N_k - 1}} \tag{20}$$

A weighting factor P_j for each test in a hypercube is derived in equations (21) and (22). Pd represents experimental uncertainty in the test data, Pk is a weighting factor that accounts for the scaling of the test facility, and Ps is the weighting factor which accounts for the dispersion of points in each test as calculated in equation (21). In the BFBT benchmark cases, Pd = 0.03 as provided by the specifications, and Pk = 1 since the tests were conducted at full scale.

$$Ps_j^i = \begin{cases} 1.0 - 0.9S_j^i & \text{if } 0.0 < S_j^i < 1.0 \\ 0.1 & \text{if } S_j^i \geq 1.0 \end{cases} \tag{21}$$

$$P_j^i = \frac{\left(Pd_j^i\right)\left(Pk_j^i\right)\left(Ps_j^i\right)}{\sum_{J=1}^{N_J}\left(Pd_J^i\right)\left(Pk_J^i\right)\left(Ps_J^i\right)} \tag{22}$$

The dispersion of the tests in a hypercube is accounted for using equations (23) and (24) that are the average and weighted standard deviations calculated over N_j tests in a hypercube.

$$\overline{AQ^i} = \sum_{j=1}^{N_j} \frac{\overline{AQ_j^i}}{N_j} \tag{23}$$

$$\sigma^i = \sqrt{\frac{\sum_{j=1}^{N_j}\left(P_j N_j \left|\overline{AQ_j^i}\right| - \overline{AQ^i}\right)^2}{N_j - 1}} \tag{24}$$

When a simulation with no corresponding experimental data is performed, an estimate of the uncertainty band is made by using the statistical information

contained in the corresponding hypercubes. Equation (25) predicts the bounds of a two-tailed 95% uncertainty band for the simulated void fraction α_{sim}.

$$\alpha_{band} = \alpha_{sim} \pm \alpha_{sim}\left(\overline{AQ^i} + \left(\sum_{j=1}^{N_j} 2P_j^i S_j^i \overline{AQ_j^i}\right) + \left(1.96\sigma^i\right)\right) \tag{25}$$

3.5.2 Ordered Statistics

Wilks' formula is commonly used in the nuclear industry in order to reduce the number of code runs required to predict uncertainty bands around simulated values. The method is also referred to as ordered statistics and is based on the principle that when a randomly sampled set of results are placed in ascending order, the distribution of the original set may be estimated from the sample [66]. Within the context of this study, Wilks' method is used to examine the sensitivity of the nodalization to the uncertainty of the measured boundary conditions.

Wilks demonstrated that ordered statistics may be used to find the tolerance limits of a sample such that it fulfills equation (26). In the equation, L and M are the lower and upper tolerance limits, f(t) is an unknown probability distribution function, γ is the coverage level, and β is the confidence level [67].

$$P\left(\int_L^M f(t)\,dt \geq \gamma\right) = \beta \tag{26}$$

Wilks also proved that if X_1, X_2, … X_N are a set of observations arranged in increasing order of magnitude and drawn randomly from a sample for which the probability distribution function is unknown, then the distribution of values in equation (27), where r is any positive integer between 1 and N, is independent of the PDF [68].

$$\int_{X_r}^{X_{N-r+1}} f(t)\,dt \tag{27}$$

Through further manipulation, Guba and Wald both demonstrate ways that the left hand side of equation (26) reduces to a statement of the binomial theorem since each sampled point has only two outcomes: either it is within the tolerance limits, or it is outside of them [40,69]. This is represented by equation (28) where r and s are the indices of the values representing the lower and upper tolerance limits in the ordered set.

$$\sum_{j=0}^{s-r-1}\binom{N}{j}(\gamma)^j(1-\gamma)^{N-j}=\beta \tag{28}$$

Solving equation (28) for r = 1 and s = N yields equation (29), which is the expression relating the number of code runs, N, to the desired coverage and confidence levels for a two-tailed distribution. Values for N are typically given in a tabular form such as in Table 8 [40].

$$1-\gamma^{N}-(N-1)(1-\gamma)\gamma^{N-1}=\beta \tag{29}$$

Table 8 - Selected values for N.

N	γ		
	β = 0.90	**β = 0.95**	**β = 0.99**
10	0.66315	0.60584	0.49565
20	0.81904	0.78389	0.71127
50	0.92443	0.9086	0.87448
100	0.96166	0.95344	0.93554
150	0.97432	0.96877	0.95658
300	0.98710	0.98429	0.97809

4 APPLICATION & METHODOLOGY

This section explains the layout of the test facility and provides a summary of the conditions at which the experiments were performed. An explanation of the how the facility was modeled in RELAP and ASSERT is provided, along with an explanation and justification of the empirical correlations selected. Additionally, a description of the implementation of the CIAU method is also provided.

4.1 BFBT Facility Description

BWR fuel bundles are simulated at full scale using an 8 × 8 array of electrically heated fuel rods, each with an outer diameter of 12.3 mm. The bundle is 3704 mm in length and sits vertically along a test loop containing demineralised water. Rods are held in place by a series of axially positioned grid spacers, and key bundle parameters are listed in Table 9 [6]. Two styles of bundles are used – a "current" design consisting of 62 fuel rods and 2 water rods, and a "high burnup" design which is characterized by one large water rod in the center. Both of the bundle configurations are illustrated along with the relative fuel rod powers in Figure 5.

Table 9 - Bundle Parameters.

Parameter	Quantity
Maximum Power [MW]	12
Maximum Mass Flux [kg / m^2s]	2130
Maximum Pressure [MPa]	10.3
Number of Fuel Rods	62 (current), 60 (high burnup)
Rod Pitch [mm]	16.2
Fuel Rod Diameter [mm]	12.3
Number of Water Rods	2 (current), 1 (high burnup)
Water Rod Diameter [mm]	34.0 (current), 15.0 (high burnup)
Heated Length [mm]	3708

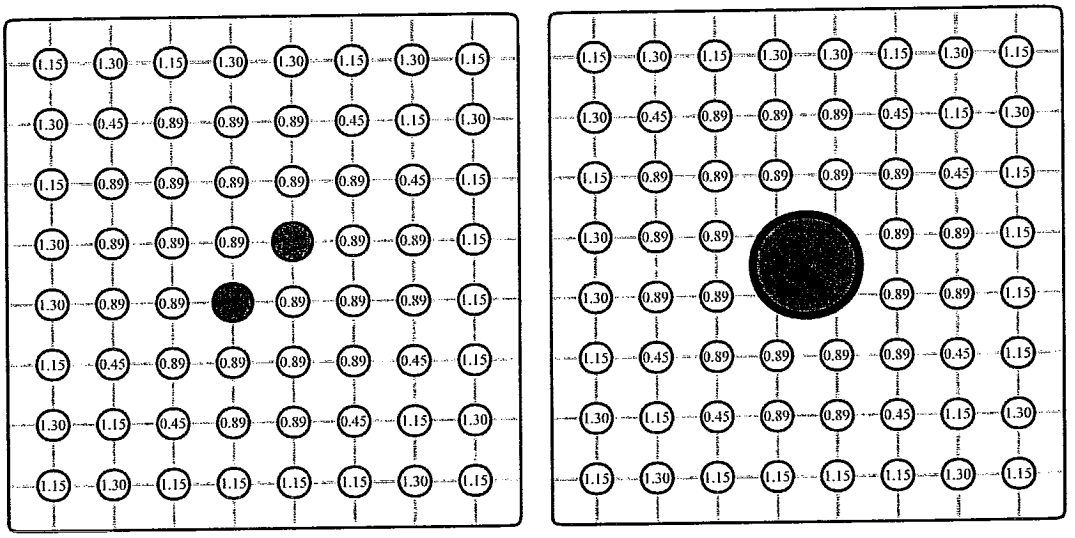

Figure 5 - "Current" Bundle Profile (left) and "High Burnup" Bundle Profile (right).

Three X-ray densitometers recorded the chordal averaged void fraction at different locations along the axial length of the bundle, while one high-resolution X-ray CT scanner measures the average void fraction on a subchannel level at the top of the heated test section. Unless otherwise explicitly specified, the void fraction measurements being compared in this study are those obtained by the X-ray CT scanner.

Mass flow in the test loop is governed by three parallel control valves located after a circulation pump. The experimental mass flows are set to a value between 2.78 to 19.44 kg/s, and are measured using a turbine flow meter.

A system preheater maintains the fluid temperature at the inlet of the test section and the temperature is set to a value reflecting the desired inlet subcooling. The inlet subcooling in the experiment ranges between 20.0 and 130.0 kJ/kg, and the inlet temperature is monitored using two thermocouples. The system pressure is controlled by a pressurizer, and the experiments are conducted at operating pressures between 0.98 to 8.72 MPa. Pressure tap and grid spacer locations are illustrated in Figure 6.

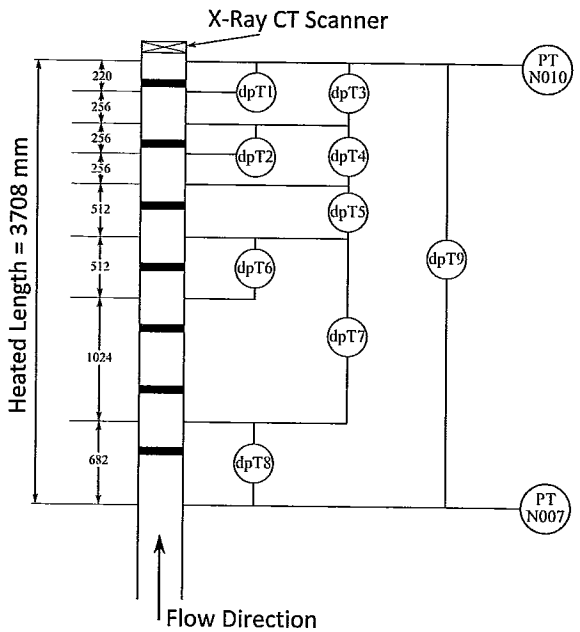

Figure 6 - Pressure tap and grid spacer locations.

Each of the measured quantities has an associated uncertainty. The uncertainty distributions for the measured parameters have been assessed by the experimenters and are provided in Table 10 [6]. It is assumed that each accuracy value provided represents the 95% / 95% bounds of the distribution.

Table 10 - Accuracy of Process Measurements.

Quantity	Accuracy (2σ value)	Distribution
Pressure	1.00%	Normal
Mass Flow Rate	1.00%	Normal
Power	1.50%	Normal
Inlet Temperature	1.50 C	Uniform
Subchannel Void Fraction	3.00%	Normal

4.1.1 Case Matrices

In this study, two sets of experiments from the BFBT tests are used. The 1071-XX series of experiments were conducted on the 62 fuel pin bundle with a cosine relative power profile in the axial direction as illustrated in Figure 7.

The 4101-XX series of experiments were conducted on the "high-burnup" bundle with a uniform power profile in the axial direction. Both bundles were run using the boundary conditions listed in Table 11, where X's denote a set of boundary conditions where experimental data was taken. The thermo-equilibrium quantity referred to in the table is defined in equation (30) as the ratio of the

difference between the vapour and fluid enthalpy to the latent heat of vapourization.

$$x = \frac{h_g - h_f}{h_{fg}} \tag{30}$$

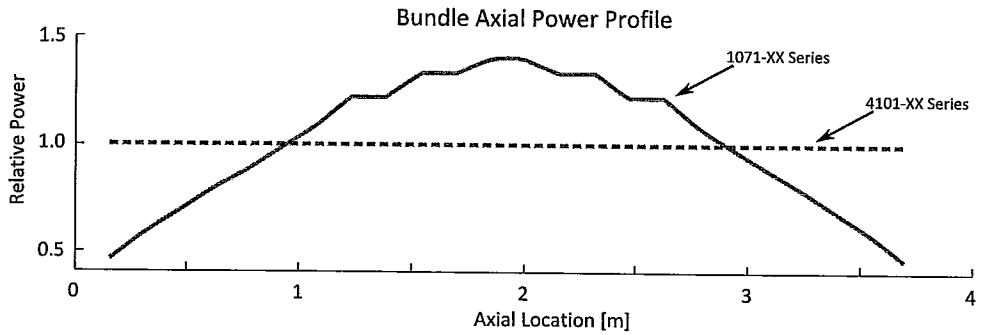

Figure 7 - Relative Axial Power Profile

Table 11 - Case Matrix for Test Series 1071-XX and 4101-XX

Pressure [MPa]	Inlet Subcooling [kJ/kg]	Mass Flow Rate [kg/s]	Exit Quality (Thermo-equilibrium) [%]					
			2	5	8	12	18	25
1.0	50.2	2.78	X	X	X	X		
		8.33	X	X	X	X		
		15.3	X	X	X	X		
3.9	50.2	2.78	X	X	X	X	X	X
		8.33	X	X	X	X	X	X
		15.3	X	X	X	X	X	X
7.2	20.9	12.5		X		X		
	50.2	2.78	X	X	X	X	X	X
		5.56	X	X	X	X	X	X
		8.33	X	X	X	X	X	X
		15.3	X	X	X	X	X	X
		19.4	X	X	X	X	X	

	126	15.3	X	X		X		
8.6	50.2	2.78	X	X	X	X	X	X
		8.33	X	X	X	X	X	X
		15.3	X	X	X	X	X	

4.2 *Input Deck Description*

4.2.1 Bundle Geometry

4.2.1.1 RELAP

The geometry of the active portion of the fuel bundle is modeled using RELAP's multi-dimensional (MULTI-D) component of the code, which represents a three-dimensional array of volumes. The nodalization of the bundle represents the 81 subchannels as a 9 × 9 array in the planar direction with 12 axial levels, each 0.309 m in length. The flow areas in both the planar and axial directions are preserved. Code limitations with RELAP5-3D prevent a finer nodalization from being used, and the implications of this are examined in detail in section 5.4.1.1.

4.2.1.2 ASSERT

ASSERT allows users to model the bundle as an array of interconnected subchannels. For the 1071-XX bundle configuration, five types of subchannels are identified and illustrated in the left half of Figure 8, while their characteristics are listed in Table 12. Two additional types of subchannels unique to only the

"high burnup" style bundle are illustrated in the right half of Figure 8. Based on these values, the centroid-to-centroid distance and angle, as well as the gap width of each junction type are calculated. These values are summarized in Table 13, and illustrated in detail in Appendix E.

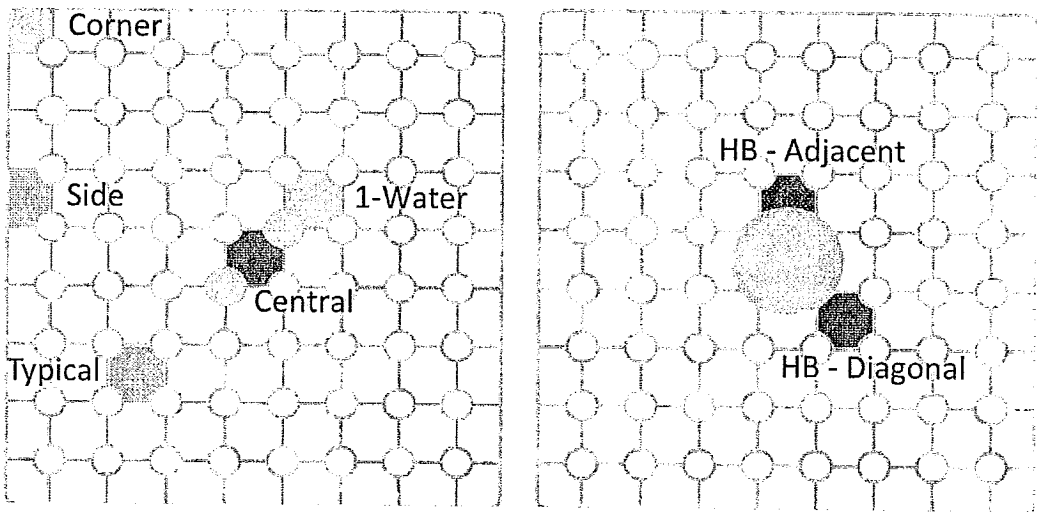

Figure 8 – Subchannel types for the "current" (left) and "high burnup" bundles (right).

Table 12 - Subchannel Parameters

	Corner	Side	Typical	Central	1-Water	HB - Adjacent	HB - Diagonal
Flow Area [m^2]	4.78E-05	9.53E-05	1.44E-04	1.15E-04	1.29E-04	6.97E-05	1.45E-04
Wetted Perimeter [m]	0.0242	0.0355	0.0386	0.0429	0.0408	0.03621	0.0388
Hydraulic Diameter [m]	0.0079	0.0107	0.0149	0.0107	0.0127	0.0077	0.0150
Centroid X [mm]	5.1411	3.3925	3.0000	8.1000	8.3631	8.1000	8.1500
Centroid Y [mm]	5.1411	8.1000	8.1000	8.1000	8.3631	10.960	8.0500

Table 13 – Subchannel Junction Properties

Junction Type	Relative Centroid Angle [deg]	Centroid Distance [cm]	Gap Width [cm]
"1 Water - 1 Water"	0.000	1.672	0.255
"Central - 1 Water"	0.904	1.646	0.255
"Corner - Side"	4.405	1.328	0.340
"Side - Side"	0.000	1.620	0.340
"Side - Typical"	0.000	1.426	0.390
"Typical - 1 Water"	0.934	1.594	0.390
"HB - Adjacent - Diagonal"	10.21	1.615	0.320
"HB - Adjacent - Typical"	0.000	1.334	0.390
"HB - Diagonal - Typical"	0.351	1.625	0.390

4.2.2 Fuel Rods

The rods used in the experiment consist of a Nichrome electric heater and a Boron Nitride insulator all enclosed within an Inconel-600 cladding. The BFBT specifications provide the temperature dependence of the density, specific heat and thermal conductivity of these materials, and they are incorporated into the fuel rod models of both ASSERT and RELAP.

Modelling the thermal properties of the materials is relevant for the RELAP nodalization since simulations in the code are run in quasi-steady state and heat is being applied only to the Nichrome layer. The properties are illustrated in Appendix F. In RELAP, each fuel rod is modeled as four heat individual heat structures each consisting of a layer of Nichrome, Inconel and Boron-Nitride. Each heat structure is connected to only one subchannel via the Inconel layer. In order to make the heat structures dependent on one another, a radiation enclosure is created to encompass each group heat structures belonging to the same fuel rod.

The ASSERT model differs in that it has 'fuel rod' objects which can be employed instead of the generic heat structures in RELAP. This object allows the three materials in the fuel rod to be nodalized radially and connected together. Each fuel rod is in contact with four different subchannels, and it is assumed in the nodalization that the heat is evenly distributed between each. Figure 9 illustrates how each rod contributions 25% of its power to an adjacent subchannel.

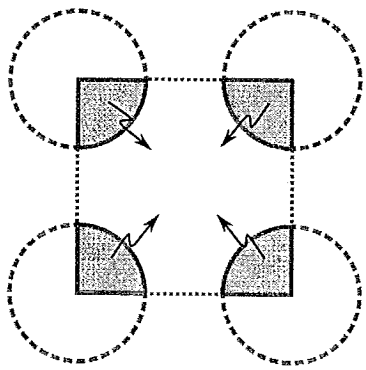

Figure 9 - Heat contribution to the subchannel of adjacent fuel rods

4.2.3 Code Implementation

The actual implementation of mass, momentum and energy equations in ASSERT and RELAP are located in Appendices C and D, while the input decks used are located in Appendices H and I. Table 14 lists the empirical correlations selected, while sections 4.2.4 and 4.2.5 justify their use.

Table 14 - List of closure models selected

Phenomena	RELAP	ASSERT
Single Phase Friction	Zigrang-Sylvester (approx. of Colebrook-White)	Colebrook-White
Two Phase Multiplier	Barcozy	Friedel
Single Phase Heat Transfer	Dittus-Boelter	Dittus-Boelter
Two Phase Heat Transfer	Chen	Ahmad
Equilibrium Void & Mixing Rate	----	Carlucci-Carlucci

4.2.4 Correlations Selected in RELAP

4.2.4.1 Single Phase Friction Factor

The single phase friction factor is computed using the Zigrang-Sylvester approximation to the Colebrook-White correlation [70]. Equation (31) is the approximation used in the code, while the justification for the use of the Colebrook-White correlation has already been provided in section 4.2.5.1 [46].

$$\frac{1}{\sqrt{f}} = -2\log\left\{\frac{\varepsilon/D_h}{3.7} - \frac{5.02}{\mathrm{Re}}\log\left[\frac{\varepsilon/D_h}{3.7} - \frac{5.02}{\mathrm{Re}}\log\left(\frac{\varepsilon/D_h}{3.7} + \frac{13}{\mathrm{Re}}\right)\right]\right\} \qquad (31)$$

Based on the experimental flow rates and the flow area, the minimum flow velocity expected is 0.4 m/s, and using equation (6), the Reynolds number is estimated to be around 43,000 which indicates that the fluid is definitively in the turbulent regime, justifying the use of this correlation.

4.2.4.2 Two-Phase Friction Multiplier

No user selectable two-phase friction options are available in RELAP5-3D. The two correlations for this term are hard-coded, and so this section is included only for completeness.

The two-phase friction in RELAP is calculated using the modified Barcozy two-phase multiplier on the Lockhart-Martinelli parameter [70]. The Lockhart-Martinelli parameter is given in equation (34) as the ratio of the liquid to vapour pressure gradient in equations (32) and (33). In the equations, f represents the friction factor.

$$\left(\frac{dP}{dx}\right)_g = \frac{f_g \mathrm{Re}_g \left(\alpha \rho_g v_g A\right)^2}{2 D_h \rho_g A^2} \tag{32}$$

$$\left(\frac{dP}{dx}\right)_f = \frac{f_f \mathrm{Re}_f \left(\alpha \rho_f v_f A\right)^2}{2 D_h \rho_f A^2} \tag{33}$$

$$\chi^2 = \frac{\left(\frac{dP}{dx}\right)_f}{\left(\frac{dP}{dx}\right)_g} \tag{34}$$

The two-phase multiplier for each phase is then defined in equations (35) and (36), with C being the coefficient specified in equation (37). G in equation (37) represents the mass flux in kg/m^2s.

$$\phi_f^2 = 1 + \frac{C}{\chi} + \frac{1}{\chi^2} \tag{35}$$

$$\phi_g^2 = \chi^2 + C\chi + 1 \tag{36}$$

$$C = -2 + \left(28 - 0.3\sqrt{G}\right)\left[\exp\left(-\frac{\left[\log_{10}\left(\frac{\rho_g \mu_f^{0.2}}{\rho_f \mu_g^{0.2}}\right) + 2.5\right]^2}{2.4 - G\left(10^{-4}\right)}\right)\right] \quad (37)$$

4.2.4.3 Single Phase Heat Transfer

In RELAP, the single and two-phase heat transfer correlations are not explicitly selected by the user – instead they are determined by the code based on the geometry models activated. For the BFBT bundles, the default geometry model was used, which activates the Dittus-Boelter correlation for the single phase heat transfer [70].

The Dittus-Boelter correlation was selected to determine the single phase heat transfer coefficient between the rods and the fluid. It is given in equation (38) [70] and the valid range of the correlation according to reference [3] is Re > 10,000 and 0.7 < Pr < 120.

$$Nu = \left(\frac{h_{dittus} D_h}{k_f}\right) = 0.023\,\mathrm{Re}^{0.8}\,\mathrm{Pr}^{0.4} \quad (38)$$

Section 4.2.4.1 already demonstrated that the expected Reynolds number will be above 10,000, satisfying the first criteria. The Prandtl number is defined in equation (10), while Figure 10 illustrates that it is expected to be within the

range of validity over the expected operating conditions thus, its use in the model is justified.

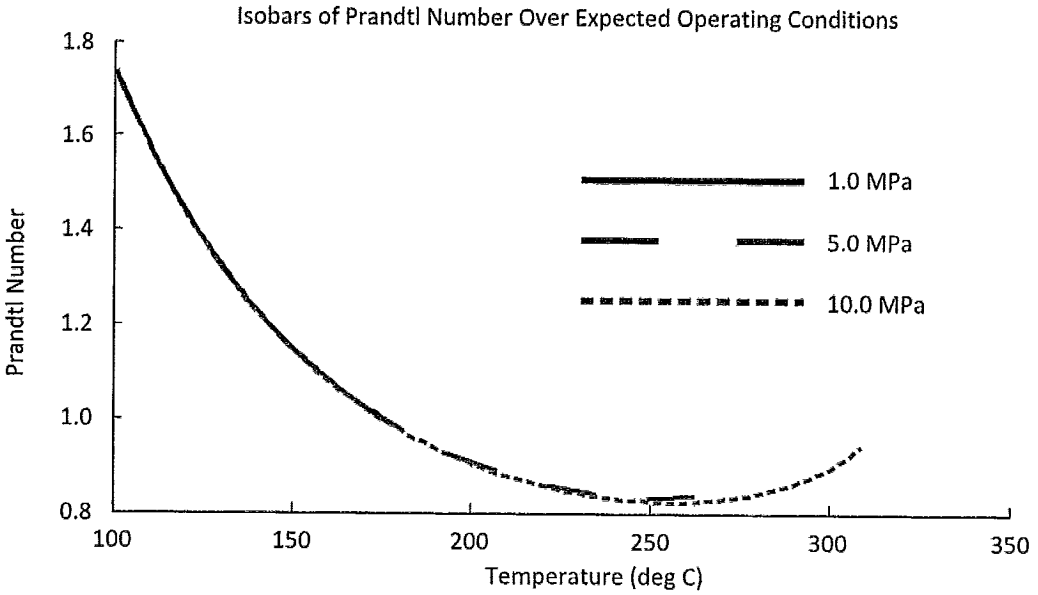

Figure 10 - Prandtl Number Over Expected Conditions

4.2.4.4 Two-Phase Heat Transfer

The Chen correlation (39) is the default two-phase heat transfer model for RELAP and it is used in the nodalization [70]. The model assumes the two phase heat transfer coefficient is comprised of two parts: the macroscopic convective heat transfer portion, h_{mac} (40) and the heat transfer due to microscopic bubble nucleation h_{mic} (42) [52].

$$q'' = h_{mac}\Delta T_w F + h_{mic}\Delta T_w S \tag{39}$$

$$\left(Nu_{mac}\right)\left(\frac{k}{D_h}\right)=h_{mac}=h_{dittus} \tag{40}$$

$$F=\left(2.35\right)\left[\left(\frac{G_g}{G_f}\right)^{0.9}\left(\frac{\rho_f}{\rho_g}\right)^{0.5}\left(\frac{\mu_g}{\mu_f}\right)^{0.1}+0.213\right]^{0.736} \tag{41}$$

The macroscopic heat transfer coefficient is comprised of a multiplier to the heat transfer coefficient found using the Dittus-Boelter correlation based on the Reynolds number, with h_{dittus} given in equation (38) [52]. In equation (39), ΔT_w is the difference between the temperature of the wall and the temperature of the bulk liquid and in equation (41) G_g and G_f represent the mass flux of the vapour and liquid phases respectively [70].

The microscopic coefficient is given in equation (42), and the suppressing factor, S, is provided as equation (43) [70]. The exact formulation of S is dependent on the Reynolds number of the flow, however, for brevity and simplicity, it is assumed that all flows in the study are fully turbulent.

$$\left(Nu_{mic}\right)\left(\frac{k}{D_h}\right)=h_{mic}=\left(0.00122\right)\left(\frac{k_f^{0.79}C_{pf}^{0.45}\rho_f^{0.49}}{\sigma^{0.5}\mu_f^{0.29}h_{fg}^{0.24}\rho_g^{0.24}}\right)\left(\Delta\bar{T}_w^{0.24}\Delta P^{0.75}\right) \tag{42}$$

$$S=0.0797 \tag{43}$$

Although the correlation is recommended by Collier and Thome for vertical flows, it is worth mentioning that corrections to this correlation have been proposed by authors such as Inayatov [50].

Equations (44) and (45) represent the Chen-Inayatov correlation, which was specifically derived for two-phase heat transfer in vertical bundles [70]. The model postulates that the heat transfer coefficient in bundles is higher than that of tubes due to the effects of the turbulent cross flow. Equation (45) provides a Nusselt number to account for the cross flows, and it is summed into equation (44). Comparisons between the results of the two models are made in Section 5.4.2.1. In equation (45), D_o represents the outer diameter of the rods.

$$h_{total} = \left(h_{Chen}^2 + h_{cross}^2 \right)^{0.5} \tag{44}$$

$$Nu_{cross} = 0.21 \left(\frac{GD_o}{\mu} \right)^{0.62} \Pr^{0.4} \tag{45}$$

A further study by Aounallah suggests that the extension of the Chen correlation from the annular flow regime – which the original data was based – to subcooled and saturated nucleate boiling [71] as done in many best-estimate thermalhydraulics codes has not been sufficiently scrutinized. In light of this study, a through analysis of this issue is supplied in Section 5.4.2.1.

4.2.5 Correlations Selected in ASSERT

4.2.5.1 Single Phase Friction Factor

In order to model the effects of friction, the iterative Colebrook-White correlation (46) was used to determine the friction factor of the subchannels. It is valid in the turbulent flow regime, which is typically defined as a fluid characterized by $Re > 10^4$ [45].

$$\frac{1}{f}=\left[-2\log\left(\frac{\varepsilon/D_h}{3.7}+\frac{2.51}{\mathrm{Re}\sqrt{f}}\right)\right]^2 \tag{46}$$

In equation (46), ε/D_h represents the relative roughness of the surface as compared to the hydraulic diameter. Section 4.2.4.1 demonstrated that the bundle is expected to be fully turbulent, justifying the use of this correlation.

4.2.5.2 Two-Phase Friction Multiplier

The Friedel correlation in equation (47) was selected to compute the two-phase friction factor. In Collier and Thome's restatement of the correlation, x represents the vapour quality, while Fr and We represent the Froude and Weber dimensionless numbers defined in (48) and (49) in terms of mass velocity, G [50].

$$\phi_{fo}^2=(1-x)^2+x^2\left(\frac{\rho_f f_{go}}{\rho_g f_{fo}}\right)+\frac{(3.24)\left(x^{0.78}\right)(1-x)^{0.224}\left(\frac{\rho_f}{\rho_g}\right)^{0.91}\left(\frac{\mu_g}{\mu_f}\right)^{0.19}\left(1-\frac{\mu_g}{\mu_f}\right)^{0.7}}{Fr^{0.045}We^{0.035}} \tag{47}$$

$$Fr=\frac{G^2}{gD\rho} \tag{48}$$

$$We=\frac{G^2D}{\rho\sigma} \tag{49}$$

Valid pressure and mass flux ranges for the Friedel correlation are 0.2 – 21.2 [MPa] and 0.2 – 10.33 [Mg/m^{2}s] respectively [19], and both of these encompass the test conditions in the bundle.

Finally, the correlation is valid for fluid-vapour viscosity ratios where $\mu_f/\mu_g < 1000$ [50]. The viscosity ratios at saturation temperature over the entire range of experimental pressure are plotted in Figure 11, and it is evident that the ratio is two orders of magnitude below the threshold where the correlation becomes invalid and so the usage of it is accepted.

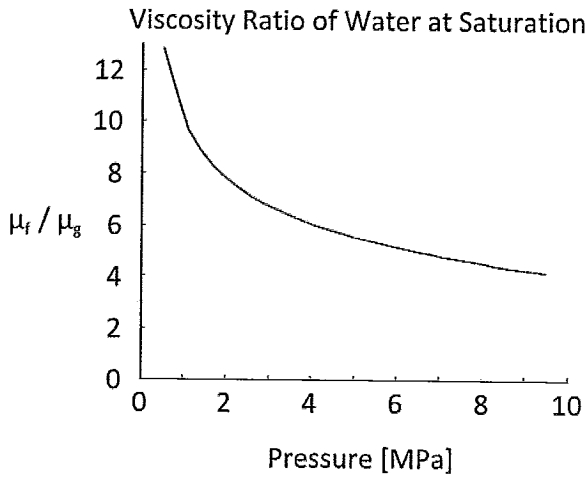

Figure 11 - Viscosity Ratio over Experimental Pressures

4.2.5.3 Single Phase Heat Transfer

The Dittus-Boelter correlation was selected to model the single phase heat transfer in ASSERT. The justification for the use of this correlation has already been done in section 4.2.4.3.

4.2.5.4 Two-Phase Heat Transfer

The Ahmad empirical correlation was selected to model the heat transfer between the wall and the fluid under two-phase flow conditions, and is based on steam-water data. It is dependent on the dimensionless Reynolds and Prandtl

numbers as well as the inlet and local fluid enthalpies, and the latent heat of vapourization [53].

$$Nu = 2.44\,\mathrm{Re}^{0.5}\,\mathrm{Pr}^{0.33}\left(\frac{h_{in}}{h_f}\right)^{0.33}\left(\frac{h_{fg}}{h_f}\right)^{0.5} \tag{50}$$

The correlation has been found to be applicable over the pressure range of 1.0 -13.8 MPa and between mass fluxes of 0.50 – 3.63 Mg/m^{2}s [19]. This covers most of the experimental range of conditions which are given as between 0.95 - 8.65 MPa and 0.28 – 1.98 Mg/m^{2}s [6]. Although part of the low-pressure, low mass-flux data is not covered by the correlation, no ASSERT options are available covering the entire range of experimental conditions. Sensitivity studies are performed in 5.4.2.3.

4.2.5.5 Equilibrium Void Distribution and Mixing Rate

There are two relevant correlations used to determine the mixing rate in ASSERT. The void drift is modelled by determining how far the void distribution is from an "equilibrium" state. This equilibrium state is determined empirically using a correlation proposed by Rowe, which Carlucci provides as equation (51) [72]. In the equation, $\alpha_{eq,i}$ and $d_{h,i}$ represent the local subchannel level void fraction and hydraulic diameter respectively, while $\overline{\alpha}$ and $\overline{d}_h$ represent the void and hydraulic diameter averaged over the entire cross section of the bundle.

$$\alpha_{eq,i} = \overline{\alpha} + (0.85)\left(F_{G,P}\right)\left(\overline{\alpha}\right)\left(1-\overline{\alpha}\right)\left(1-\frac{\overline{d_h}}{d_{h,i}}\right) \tag{51}$$

The coefficient $F_{G,P}$ represents a correction factor for the mass flux and system pressure as it is postulated that increasing mass flux and pressure reduces the void drift [72]. The value of $F_{G,P}$ is given in equation (52), where d_C is the maximum stable bubble size required to maintain dispersed bubbly flow, d_{CD}^{Br} is Brodkey's expression for the size required for the bubble to deform, and d_{CB} is the bubble size required for buoyancy effects to be present.

$$F_{G,P} = \exp\left[-11.0\left(0.9-\min\left(0.9,\frac{d_C}{\min\left(d_{CD}^{Br},d_{CB}\right)}\right)^2\right)\right] \tag{52}$$

The rate at which the void migrates towards this equilibrium distribution is determined in ASSERT via Carlucci's correlation given in equation (53) [72]. Carlucci proposed that the void drift, ε_α is comprised of a homogeneous term representing the mixing which would occur under single phase flow conditions, and incremental term which is the additional mixing caused by the addition of the second phase.

The term Ω is an 'adjustment factor' deliberately left by Carlucci et. al. in anticipation of efforts to fine tune the correlation [72]. Based on the data at the time, the authors suggest an appropriate value of Ω to be 3. The other parameters

in the equation are the density ρ, centroid to centroid distance between the two subchannels Δy, and the gap distance, S.

$$\varepsilon_\alpha = \left[\left(\frac{w_{v,\text{hom}} + w_{l,\text{hom}}}{\rho}\right) + \Omega\left(\frac{w_{v,inc} + w_{l,inc}}{\rho}\right)\right]\left[\frac{\Delta y}{S}\right] \quad (53)$$

4.2.6 Boundary Conditions

4.2.6.1 RELAP

Boundary conditions are modelled in the RELAP input deck using time-dependent volumes and junctions below and above the active portion of the bundle. Inlet and outlet pressures are specified at these locations, as is the mass flow rate and inlet temperature. The fuel rods are modelled as heat structures and act as a heat source, while the outer walls of the bundle are adiabatic.

The RELAP simulations are run in quasi-steady state, meaning that the boundary conditions are set to the experimental values, but rather than running one large time step to obtain steady-state values, an extended transient is run. In this study, transient times of between 80 – 100 seconds are used, and this is justified in Section 5.4.1.2.

4.2.6.2 ASSERT

The flow boundary conditions in ASSERT are modeled using an inlet and outlet plenum. The outlet pressure, inlet mass flux and the inlet temperature are

all calculated and implemented into the input deck. The heat flux is also imposed as the energy boundary conditions.

4.3 CIAU Implementation

One method to estimate the uncertainty bands around the predicted subchannel void fractions is using the CIAU method. In order to facilitate this, a series of scripts were written in MATLAB to handle the data and perform the necessary calculations. This section gives an overview of the code, while further details may be found in Appendix G.

CIAU is based on the extrapolation of a pre-existing database of known accuracy quantities, and as such, prior to running the CIAU code the simulations making up this database must be performed. The uncertainty portion of this study is conducted on the tests from the 4101-XX series of experiments which consists of 86 different sets of boundary conditions applied to the "high-burnup" bundle. Each of one of these tests is simulated, and the CIAU code constructs an error database by comparing the simulated and experimental results. Cases for which the uncertainty bands are being predicted are excluded from this database.

The accuracy of each subchannel prediction is quantified using equation (18), and then classified to a hypercube according to: the subchannel power to mass flux ratio, outlet pressure, predicted void fraction and inlet subcooling.

After the error database is constructed, the CIAU code takes the simulated values for which the uncertainty bands are being predicted and extracts the void fraction for each subchannel. Based on the local conditions of each simulated point, the code looks up the corresponding hypercube in the database and extrapolates uncertainty bands based on the accuracy quantities in that hypercube.

That data flow of this process is illustrated in Figure 12 for the RELAP code, however the procedure to apply CIAU to ASSERT predictions is identical. A summary of the data flow is provided in Table 15, while the partitioning of the hypercubes is provided in Table 16.

Although the pressure range of the tests, for example, spans 0.95 to 8.70 MPa, this does not mean that pressures were selected at uniform intervals along this range and experiments conducted. The outlet pressures selected in the tests were centered at 1.0, 3.7, 7.1 and 8.6 MPa, hence the pressure hypercube boundaries reflect this. A similar situation exists with the power to mass flux ratio and the inlet subcooling. The void fraction is loosely based on the flow regime map found in RELAP5-3D, although the term loosely is emphasized since the flow regime is also a function of mass flux.

Table 15 - CIAU Method Summary

Step	Task
1	A nodalization is developed and frozen.
2	The code is run to simulate each set of available experimental conditions using the nodalization.
3	Cases for which the uncertainty bounds are to be applied to are removed from the group of simulations.
4	For the remaining cases, each subchannel void fraction prediction is compared to the experimental result and Accuracy Quantities are computed.
5	Each Accuracy Quantity is classified to a hypercube based on the driving quantities
6	Parameters are calculated to account for the scatter of the data within one hypercube and within the same tests of the hypercube.
7	The cases from step 3 are reintroduced. The corresponding hypercubes for each of the predicted subchannel void fractions in these cases is determined.
8	Using the hypercubes selected, uncertainty bands are generated each code prediction based in the existing Accuracy Quantities in the hypercube.

Table 16 - Hypercube boundaries

Upper bound of hypercube	Pressure [MPa]	Power to Mass Flux Ratio [W / kg/m^{2}s]	Inlet Subcooling [kJ/kg]	Void Fraction [%]
1	2.0	10.25	42.5	5
2	5.0	19.57	58.8	32
3	8.0	24.23	128.4	53
4	8.77	93.20		68
5				100

Finally, it is noted that the RELAP and ASSERT databases are completely independent. Specifically, uncertainty predictions for a RELAP simulation are based only on the RELAP database.

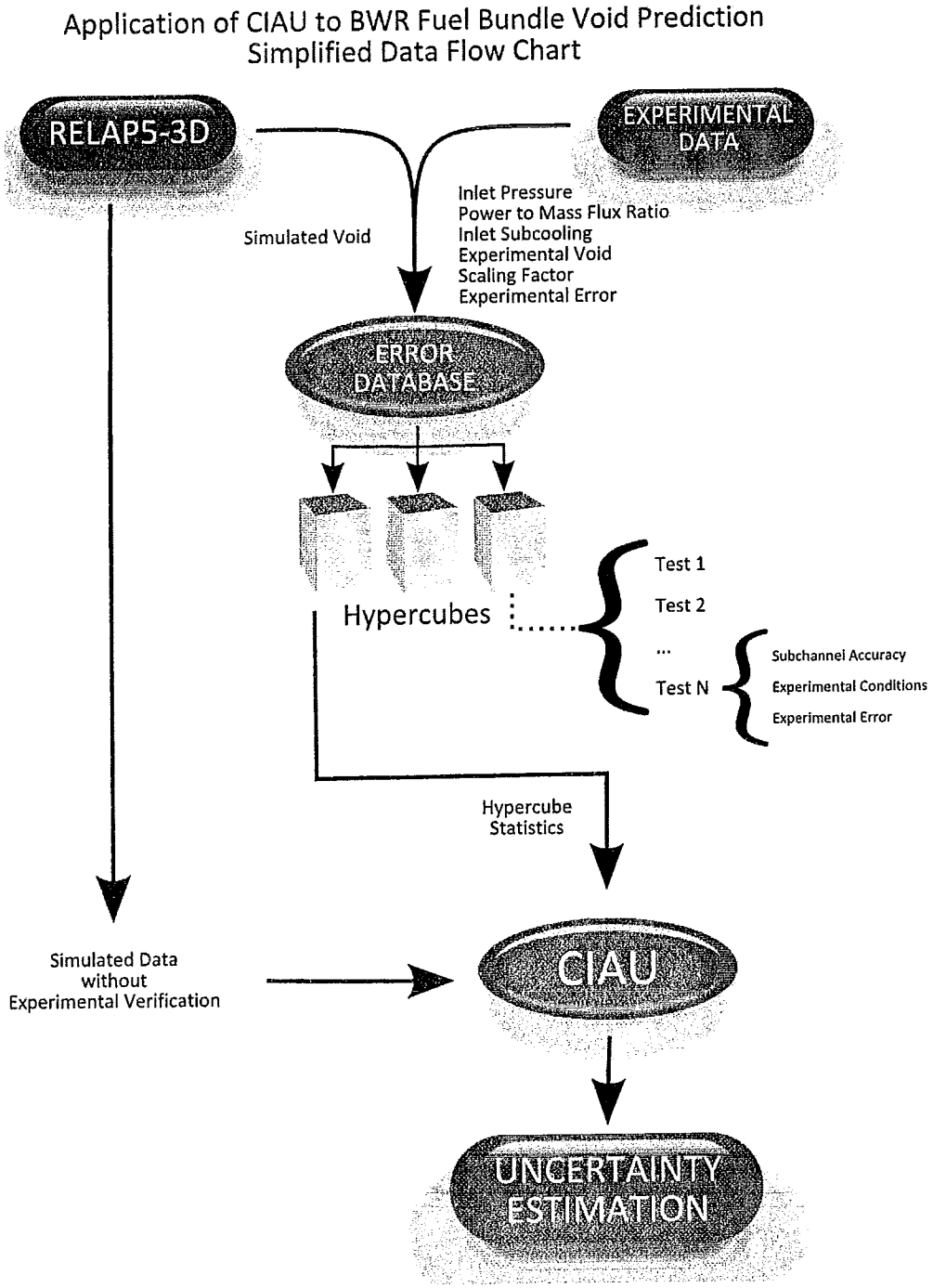

Figure 12 - CIAU Data Flow for RELAP5-3D

5 ACCURACY AND SENSITIVITY RESULTS

5.1 Accuracy

The accuracy of a simulation is defined in the simplest of terms as being how close a predicted data point is to an experimental value. The large library of data from the BFBT benchmark allows a thorough comparison of the accuracy of both codes. In this section, simulations of the steady state void fraction in the subchannels of BWR fuel bundles are conducted using RELAP and ASSERT, and compared to the measured values. Additionally, the two-phase axial pressure distribution predicted by both codes is compared against the experimental data. A full set of results for the void fraction comparison is available in Appendix J. In the discussion, the reported void fraction refers to the steady state, subchannel averaged void fraction measured at the top of the active portion of the bundle.

Accuracy is assessed both on the aggregate level and in detail using the defined quantities in Section 5.1.3. The aggregate analysis is performed on the results obtained for the 1071-XX bundle, while four cases are selected from the 4101-XX bundle dataset for detailed analysis. The cases selected for detailed analysis cover the extremes of the available experimental data and represent off-normal bundle states.

The uncertainty of the input boundary conditions must also be accounted for when examining the accuracy of the code. With that in mind, the sensitivity of

the results to uncertainties in the boundary conditions is assessed for a representative case using Wilks' formula.

5.1.1 Pressure Drop Accuracy

The void fraction in the bundle is a function of the pressure, hence the ability of the code to predict the correct pressure distribution is of importance. Diaphragm transducers located along the length of the bundle provide differential pressure measurements, and are illustrated in Figure 6 Two cases were selected from the available data, and the axial pressure distributions for both codes are illustrated in Figure 13 and Figure 14. Boundary conditions for the cases are listed in Table 18, and all reported code predictions represent the average pressure across all subchannels at the indicated axial location.

In both of the cases examined, ASSERT tends to over-predict the pressure losses, while RELAP over-predicts the pressure for case P60009 and is within experimental error for case P60026.

Gluck reported that in calculations conducted using COBRA-TF, using the loss coefficient of 1.2 resulted in a predicted pressure loss which was higher than observed in experiment [23]. Furthermore, calculations conducted by the author using a loss coefficient derived by the method proposed by Shiralkar and Radcliffe improved the accuracy of the pressure drop results. The Shiralkar and Radcliffe axial loss coefficient was reported by Gluck to be 0.94, and the pressure

drop predictions by ASSERT using this value are included for comparison in Figure 15 and Figure 16.

Although pressure drop results using the modified axial loss coefficient are more accurate using Gluck's proposed coefficient, for the purposes of this study the original k-factor specified by the benchmark is used. Since the pressure at the outlet is one of the input boundary conditions, the difference in the simulated void fraction at the top of the bundle between the two k-factors is negligible. Table 18 compares the void fraction for case P60009 for both k = 1.20 and k = 0.94, and demonstrates that the average subchannel void fraction difference between the two cases is 0.00011 which is insignificant.

Table 17 - Boundary Conditions for the Two-Phase Pressure Distribution Tests

Case	Outlet Pressure [MPa]	Mass Flow Rate [kg/s]	Inlet Subcooling [kJ/kg]	Power [MW]
P60009	7.17	5.56	50.8	2.366
P60026	8.64	15.31	53	3.975

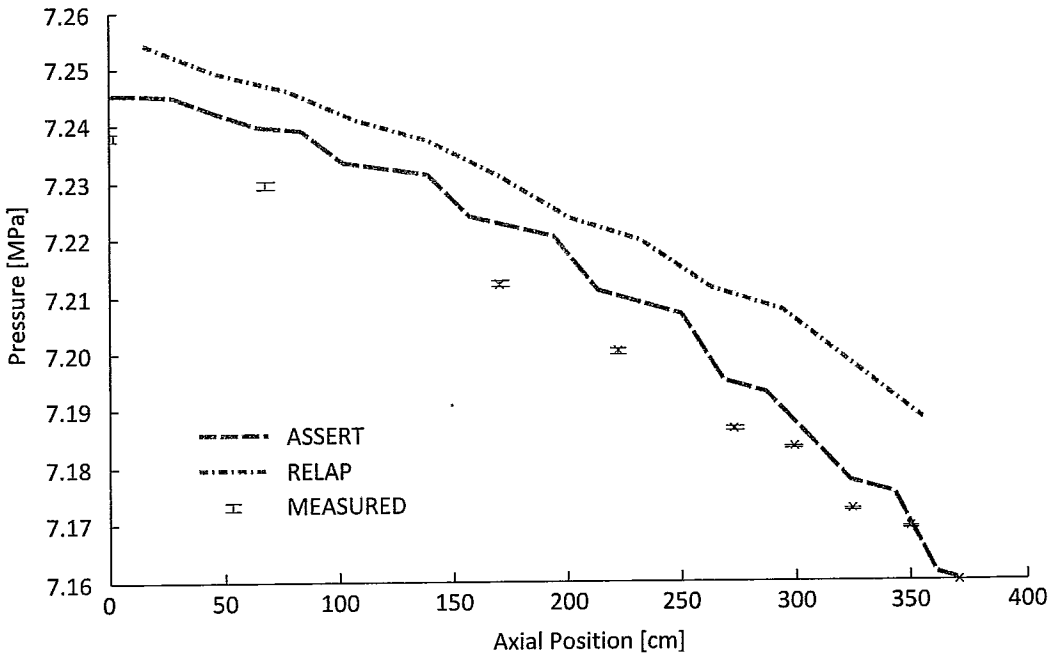

Figure 13 - Two-phase bundle pressure distribution for case P60009

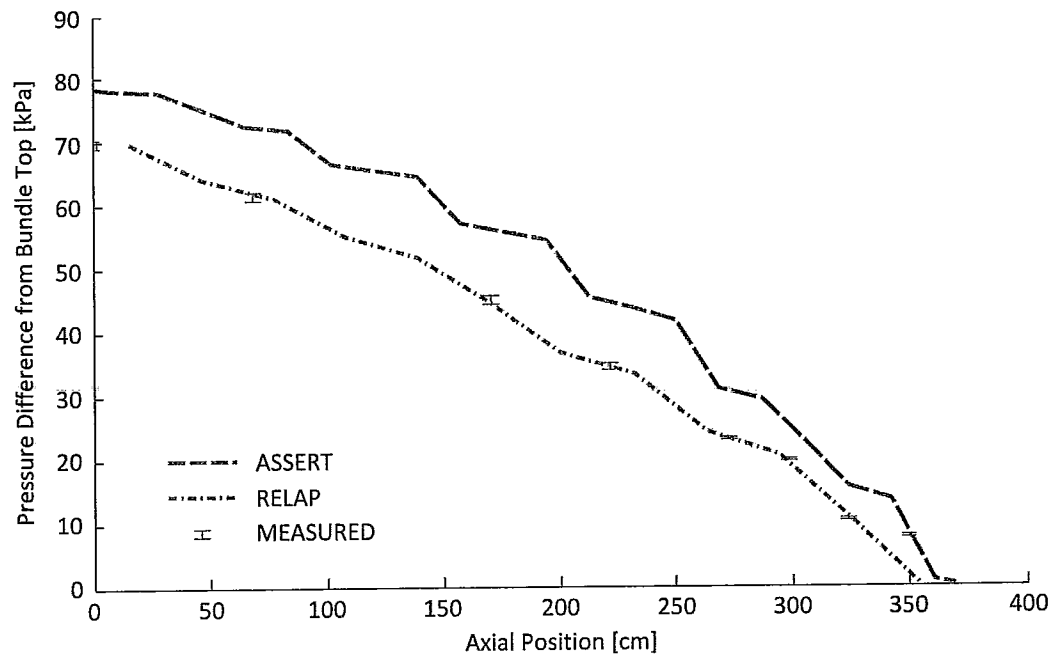

Figure 14 - Two-phase bundle pressure distribution for case P60026

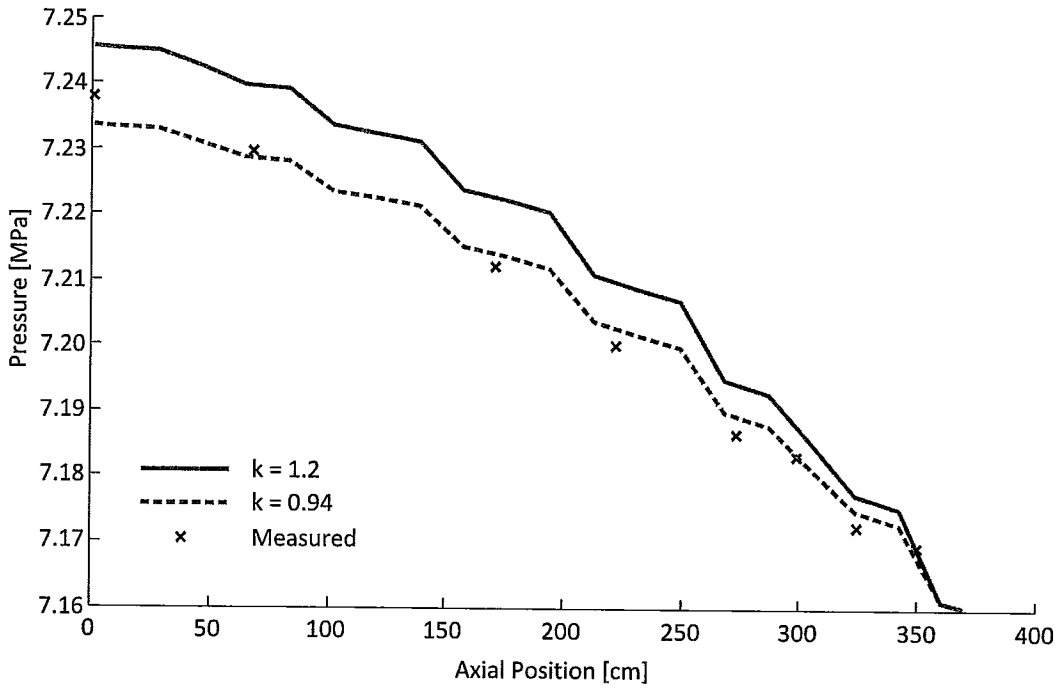

Figure 15 - Effect of k-factor selection of the 2-phase pressure distribution for case P60009.

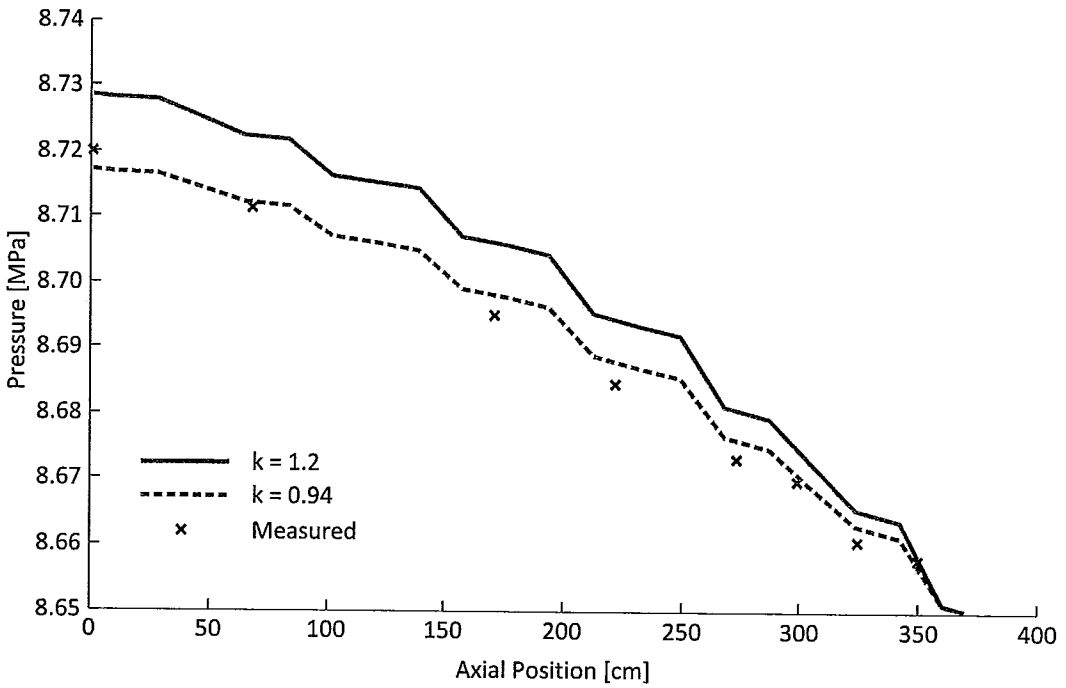

Figure 16 - Effect of k-factor selection of the 2-phase pressure distribution for case P60026.

Table 18 – Effect of axial loss coefficients on void fraction predictions

	k = 1.20	k = 0.94
Average Void at Outlet	0.673021	0.673132
Standard Deviation	0.042045	0.042209

5.1.2 Overall Void Fraction Accuracy

The assessment of the overall accuracy of the code and model is conducted by simulating the entire test matrix for the 1071-XX series of tests shown in Table 11.

For both codes, the subchannel accuracy analysis in this section is based on δ in equation (54) which is the difference between the simulated and experimental void fraction value.

$$\delta = \alpha_{SIM} - \alpha_{EXP} \tag{54}$$

5.1.2.1 RELAP Results

Of 86 steady state cases attempted with RELAP, 74 were successfully run to completion, yielding 5832 datapoints. The remaining 12 cases failed to converge numerically, and are not included in the analysis. In total, 30.9% of the simulated points fell within the experimental uncertainty of ±0.03, while 82.6% of the predictions were within ±0.10 of the measured value. Most of the failed cases were attempted at low pressure range (1.0 MPa). As shown in Figure 17, about 95% of the points fell within ±0.20 of the measured value, with the code having a

slight tendency to overpredict – as indicated in Table 19. In the worst case, one of the corner subchannel void fractions was over predicted by 0.62.

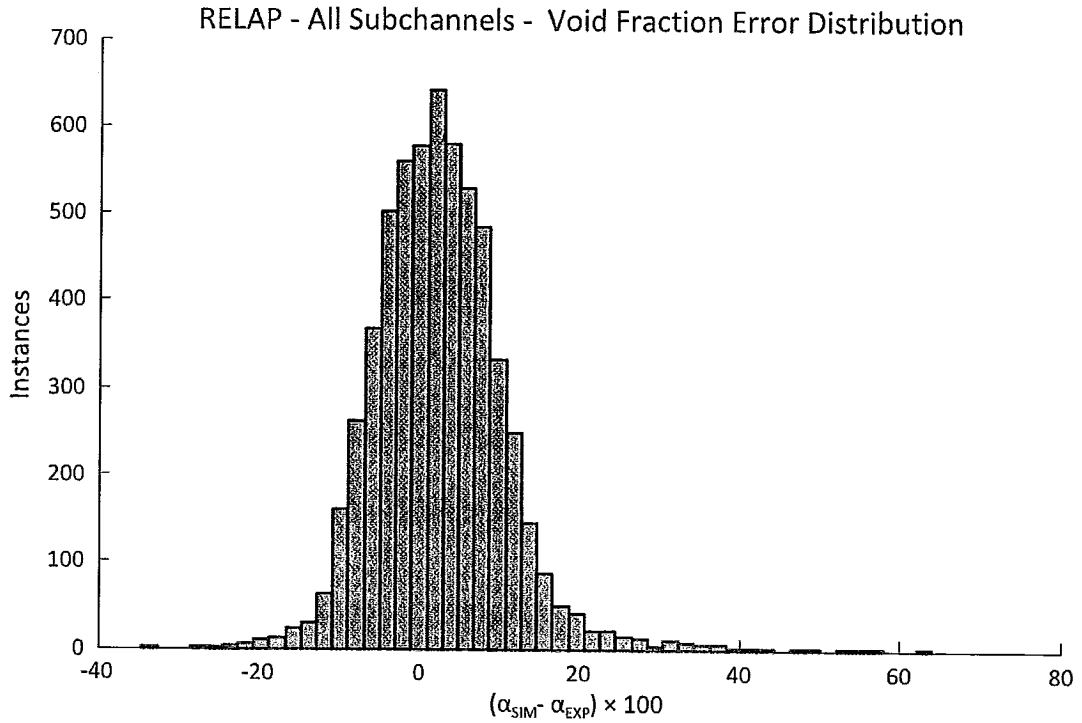

Figure 17 – RELAP Subchannel Void Fraction Error Histogram for all 1071-XX Cases

Table 19 – RELAP5-3D Subchannel Void Fraction Prediction Accuracy

Subchannel Type	Number of points where $\lvert\delta\rvert \le 0.03$		Number of points where $\lvert\delta\rvert \le 0.10$		$\bar{\delta}\times100$	$\sigma_\delta \times100$	N_{Points}
Typical	1202	(39.7%)	2766	(91.5%)	-0.4029	6.1131	3024
Side	493	(41.2%)	1588	(78.8%)	3.9048	7.9765	2016
1-Water	64	(14.8%)	276	(63.8%)	8.2268	6.2784	432
Corner	45	(15.6%)	160	(55.6%)	9.8146	13.399	288
Central	1	(1.4%)	29	(40.3%)	11.341	5.0401	72
All Subchannel Types	1805	(30.9%)	4819	(82.6%)	2.3750	8.0338	5832

The performance of RELAP in predicting the subchannel void fraction varied depending on the location of the subchannel. Although the overall average difference between the predicted and measured values was 0.024. Figure 18 to Figure 21 reveal that the central and corner subchannels were over predicted by an average of 0.113 and 0.098 respectively – well outside of the experimental error – indicating that the error is highly subchannel dependent. Subsequently the "typical" style subchannels were underpredicted by an average of 0.004. Also of note is a severe bias in the predictions of the 1-Water type subchannels illustrated in Figure 20 where approximately 85% of all predictions were greater than the measured values. Section 5.1.4 explores these issues in further detail.

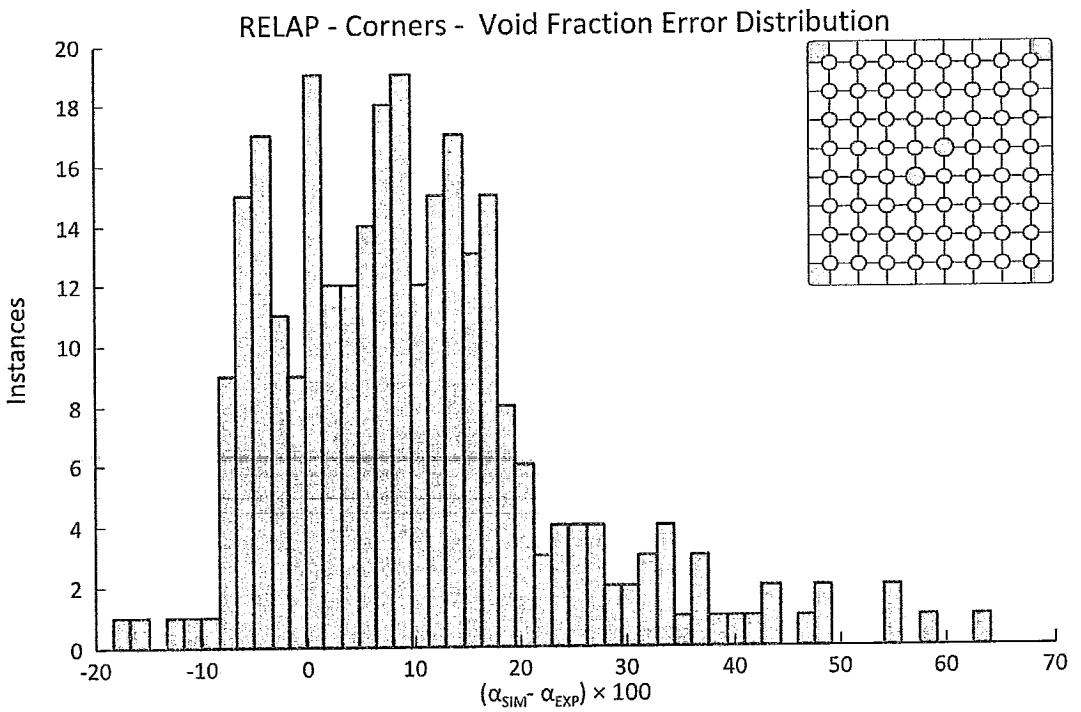

Figure 18 – RELAP Void Fraction Error Distribution for 'Corner' Subchannels

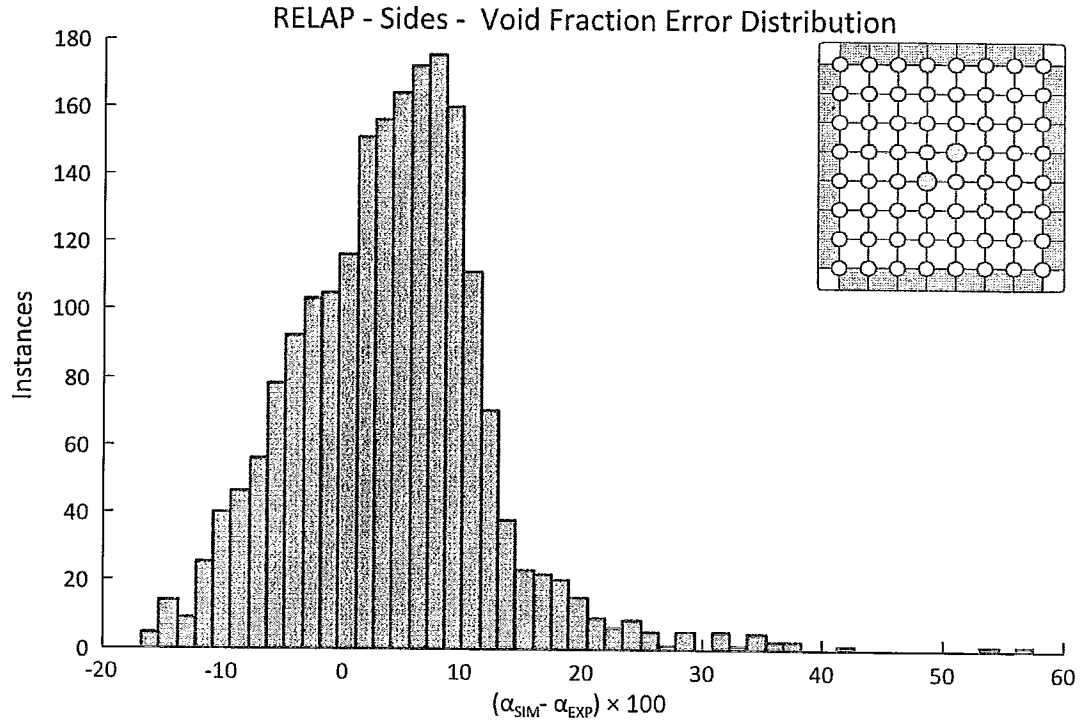

Figure 19 – RELAP Void Fraction Error Distribution for 'Side' Subchannels

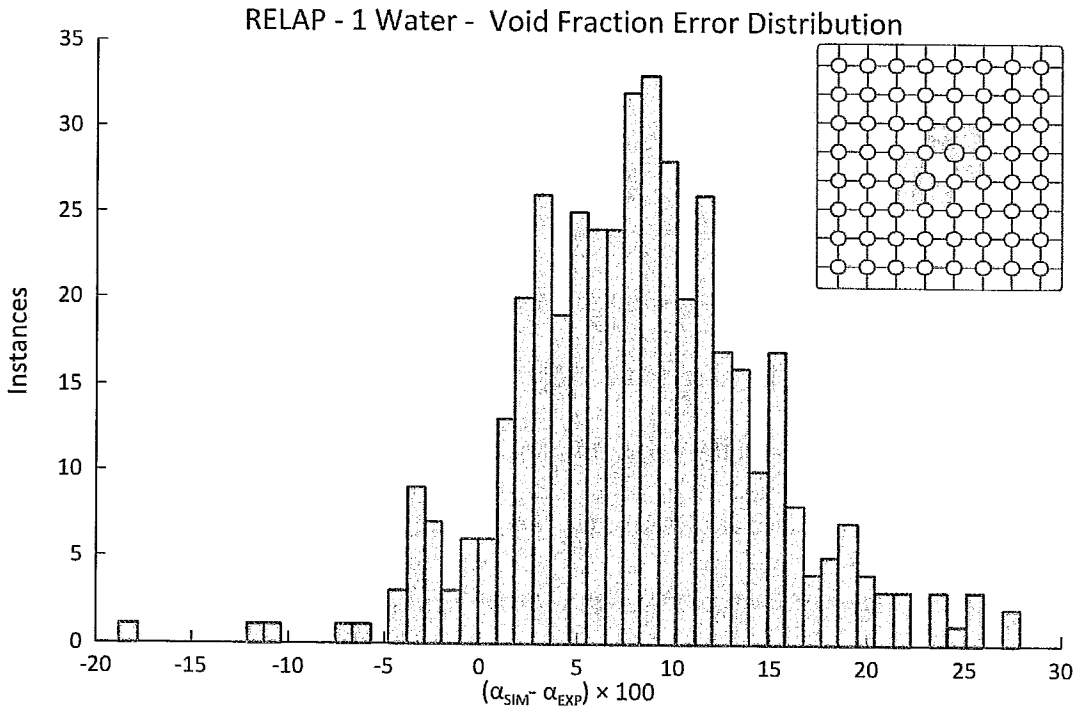

Figure 20 - RELAP Void Fraction Error Distribution for '1-Water' Subchannels

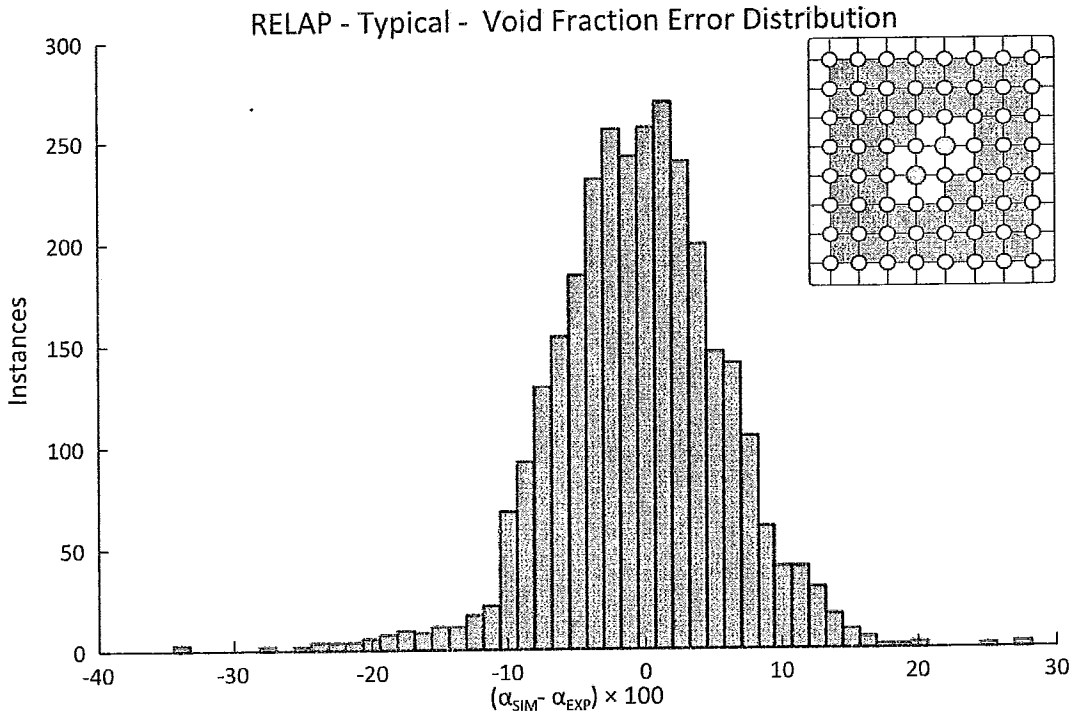

Figure 21 - RELAP Void Fraction Error Distribution for 'Typical' Subchannels

5.1.2.2 ASSERT Results

Overall, the ASSERT results are in excellent agreement with the experiments. There were two simulations that failed to converge, and they were characterized by low pressure (0.98 MPa), low flow (2.80 kg/s) and low power (0.23 – 0.32 MW) boundary conditions. The void fraction in each of the subchannels of the successfully run cases are compared against the experimental data, and as Figure 22 illustrates, approximately 95% of the simulated data fell within the bounds $-0.10 \leq \delta \leq 0.10$.

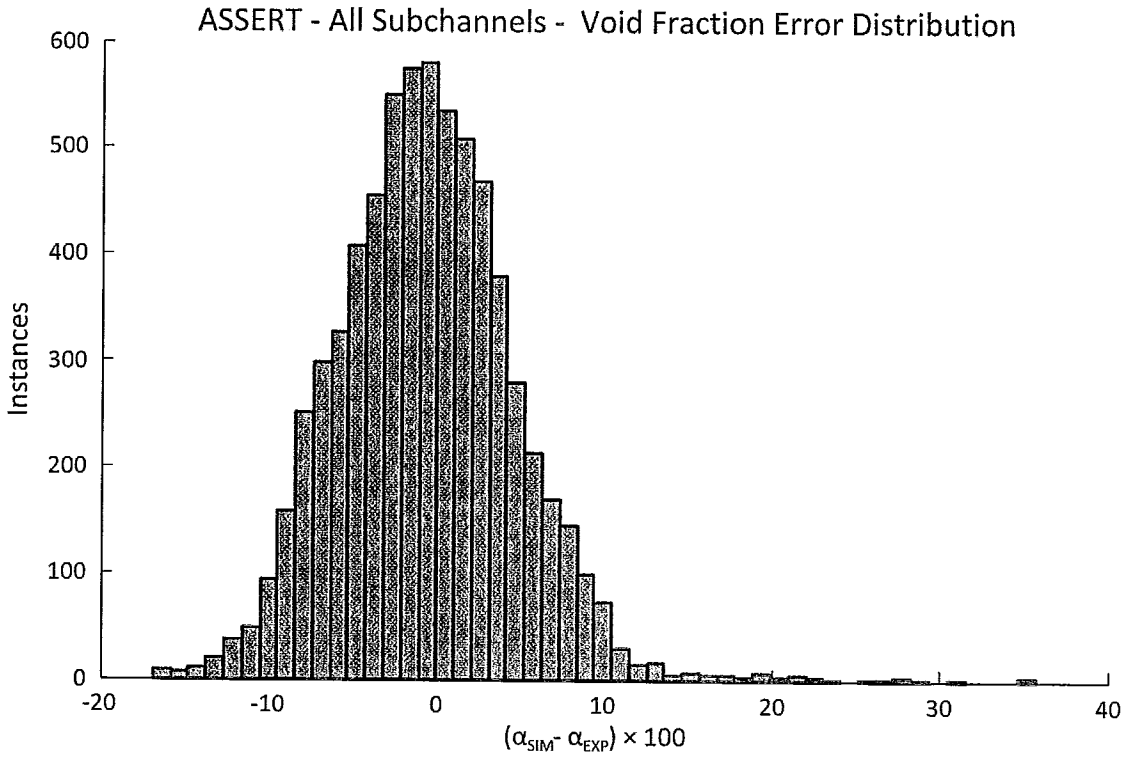

Figure 22 – ASSERT Subchannel Void Fraction Error Histogram for all 1071-XX Cases

Table 20 – ASSERT Subchannel Void Fraction Prediction Accuracy

Subchannel Type	Number of points where $\lvert\delta\rvert \le 0.03$		Number of points where $\lvert\delta\rvert \le 0.10$		$\bar{\delta}\times 100$	$\sigma_\delta \times 100$	N_{Points}
Typical	1676	(47.5%)	3472	(98.4%)	-1.6337	4.2749	3528
Side	970	(41.2%)	2204	(93.7%)	0.6052	5.5472	2352
1-Water	286	(56.7%)	501	(99.4%)	-0.2909	3.8668	504
Corner	101	(30.1%)	233	(69.3%)	0.7924	9.7107	336
Central	43	(51.2%)	81	(96.4%)	-1.4446	4.5193	84
All Types	3076	(45.2%)	6491	(95.4%)	-0.6382	5.2245	6804

Table 20 demonstrates that the ASSERT code accuracy is also dependent on the location of the subchannel within the bundle. Positive values of $\bar{\delta}$ in the side and corner subchannel types suggest that the code may have a tendency to

overpredict the void fraction in these regions. Although the $\overline{\delta}$ values are less than the measurement error, the large σ_δ values imply that a substantial number of the points fall outside of experimental uncertainty. Only 69.3% of the corner subchannels simulated fell within $|\delta| \leq 0.10$, which together with the high standard deviation suggest that the code has difficulty predicting the void fraction in the corners.

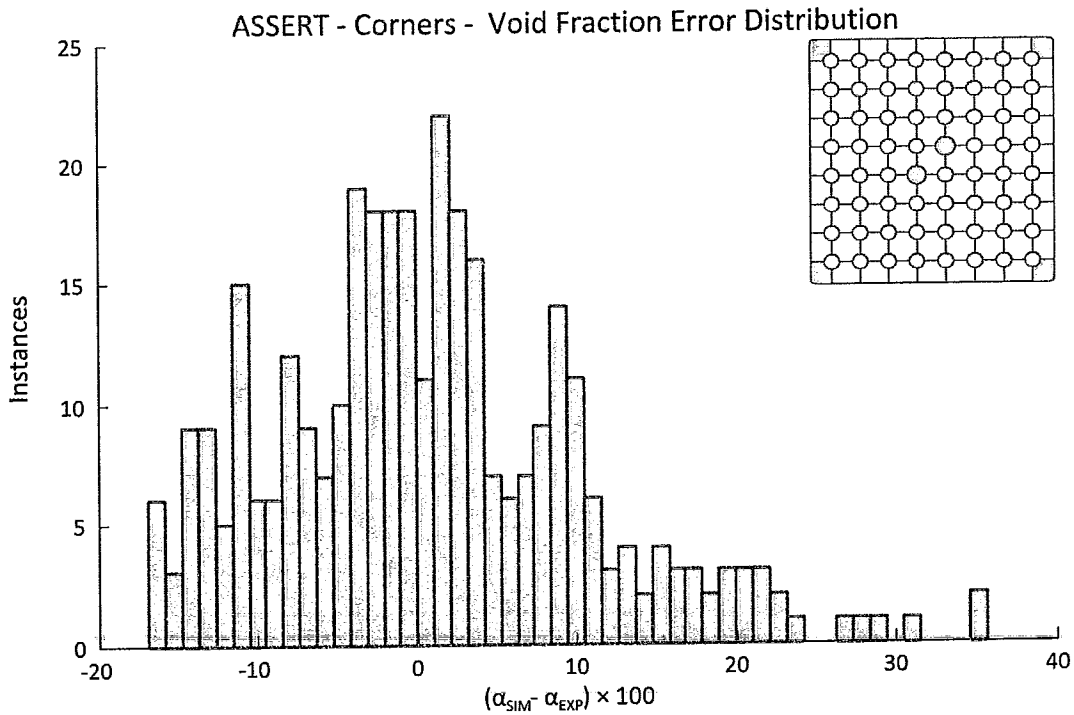

Figure 23 – ASSERT Void Fraction Error Distribution for 'Corner' Subchannels

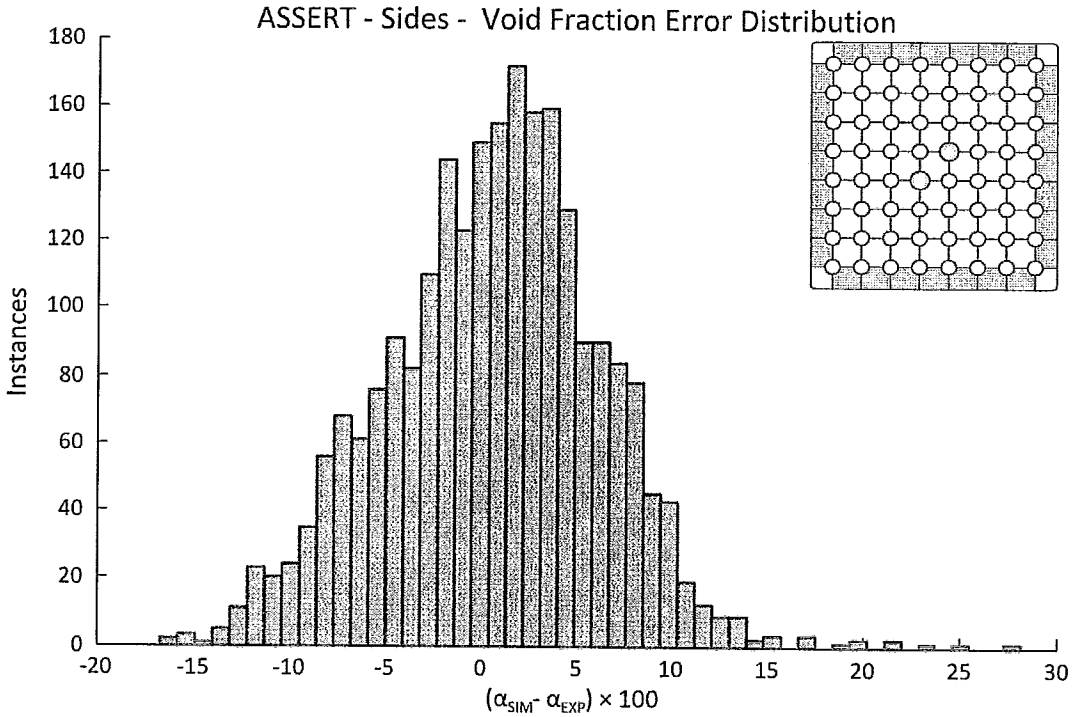

Figure 24 – ASSERT Void Fraction Error Distribution for 'Side' Subchannels

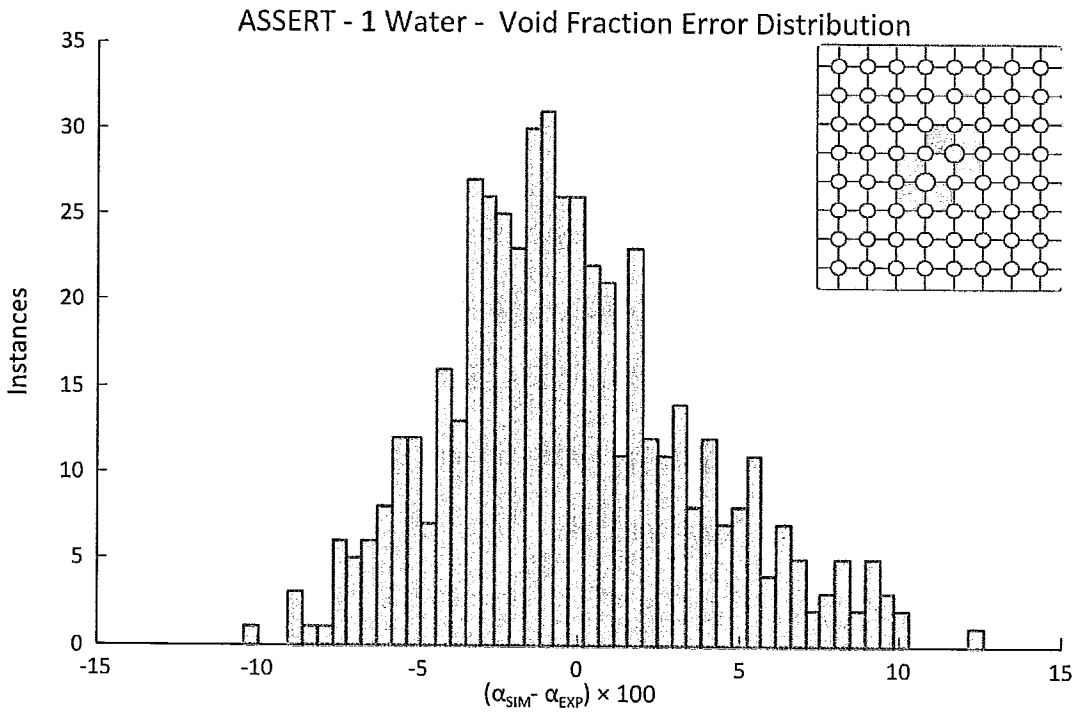

Figure 25 – ASSERT Void Fraction Error Distribution for '1Water' Subchannels.

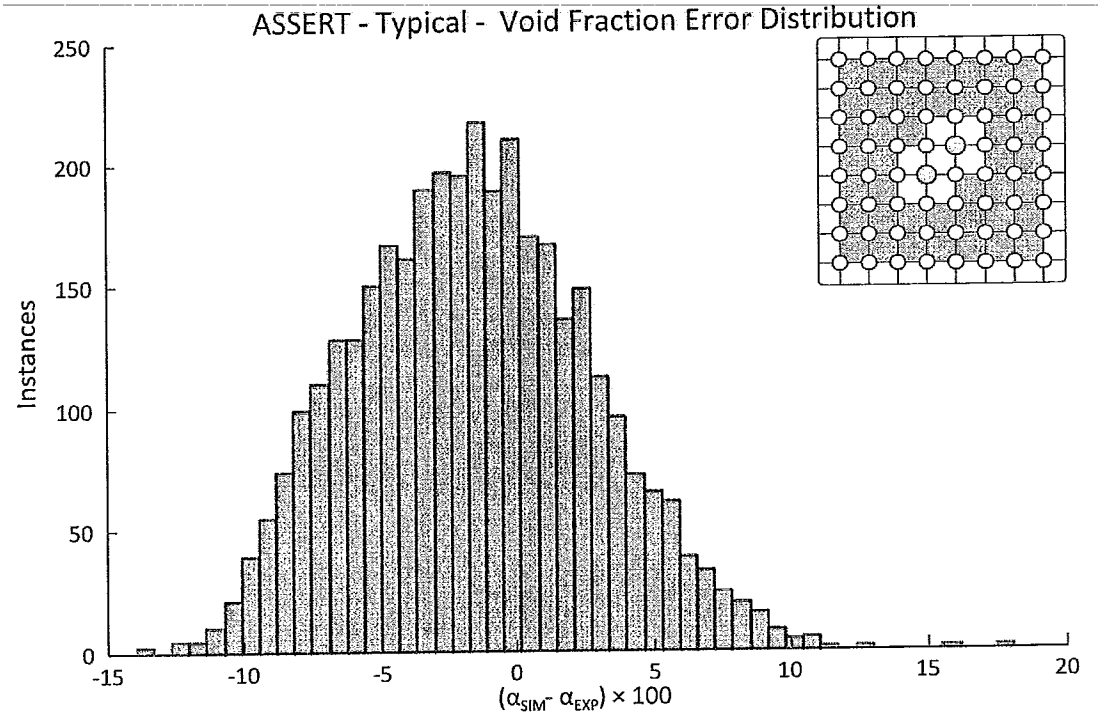

Figure 26 – ASSERT Void Fraction Error Distribution for 'Typical' Subchannels

5.1.3 Accuracy Quantification

5.1.3.1 Definitions

In order to assess the accuracy of the simulations, several quantities are defined by the Nuclear Energy Agency working group on uncertainty methods, and these are listed in Table 21 [73]. Since the simulated values often straddle the experimental value causing the value of the bias error to be misleadingly small, the absolute bias error is also included.

Table 21 - Definition of Accuracy Quantification Terms [73]

Quantity	Definition
Planar Averaged Void Distribution	$\bar{\alpha}^{sim} = \frac{1}{N}\sum_{n=1}^{N}\alpha_n^{sim}$
Sample Averaged Bias Error	$\bar{\delta}^{sim} = \frac{1}{N}\sum_{n=1}^{N}\frac{\alpha_n^{sim}-\alpha_n^{exp}}{\alpha_n^{exp}}$
Sample Averaged Absolute Bias Error	$\left\|\bar{\delta}\right\|^{sim} = \frac{1}{N}\sum_{n=1}^{N}\frac{\left\|\alpha_n^{sim}-\alpha_n^{exp}\right\|}{\alpha_n^{exp}}$
Maximum Bias Error	$\varepsilon^{sim} = \max\left(\frac{\alpha_n^{sim}-\alpha_n^{exp}}{\alpha_n^{exp}}\right)$
Standard Deviation	$\sigma^{sim} = \sqrt{\frac{1}{N}\sum_{n=1}^{N}\left(\alpha_n^{sim}-\bar{\alpha}^{sim}\right)^2}$
Absolute Coverage Ratio	$\frac{\#\text{ of points where: } \left(\alpha_n^{sim}-\alpha_n^{exp}\right)\le\varepsilon^{exp}}{N}$
Relative Coverage Ratio	$\frac{\#\text{ of points where: } \left(\frac{\alpha_n^{sim}-\alpha_n^{exp}}{\alpha_n^{exp}}\right)\le\varepsilon^{exp}}{N}$

The planar averaged void distribution represents the bundle averaged void fraction at the top of the test section. The considerable time and effort spent in developing and refining both codes means that at the very least, it can be expected that this value falls within the experimental error.

The sample averaged bias error quantity reveals either systemic errors or issues with the model or code. This value is presented both in terms of the averaged and absolute averaged values since the former reveals whether the code

under-predicts or over-predicts the measurements, while the latter provides information on the magnitude of the under or over prediction. The standard deviation is a typical statistical measure which provides an indication of the scatter of the error of the points.

The coverage ratio is a quantity for assessing the accuracy of the simulation simply by counting the number of predictions that fell within experimental error. It should be noted that the BFBT benchmark specifications define the coverage ratio in terms of the relative error rather than the absolute error. Subsequently, this means that the estimated experimental uncertainty of the void fraction measurements is unreasonably small at low voids. While the validity of this assumption for the benchmark can be debated, for simplicity this study includes both the absolute and relative coverage ratios.

5.1.3.2 Selected Cases

Four experimental cases from the 4101-XX series of tests were selected for detailed analysis and the boundary conditions imposed on the nodalization are listed in Table 22. The choice of cases represent extremes of the available data in terms of both pressure, power and mass flux. This is done deliberately since the closure relationships of both codes use empirical correlations which often are derived or developed based on data taken at "normal" conditions. For example, the Carlucci mixing correlations in ASSERT are derived using data from tests conducted at 6.9 MPa [72]. Similarly, the Chen two phase heat transfer

correlation used by RELAP was originally derived using saturated water data from between 0.29 – 3.48 MPa, although recent efforts have adjusted the maximum pressure in this database to 7.0 MPa [52, 70]. In addition to providing for a more interesting analysis, by selecting cases which push the limits and of the range of validity of these correlations, weaknesses or deficiencies in the current models can be exposed, which is consistent with the stated objectives of this study.

Table 22 - Selected Cases for Accuracy Analysis

	4101-02	4101-13	4101-69	4101-86
Inlet Pressure (MPa)	1.03	1.22	8.66	8.77
Mass Flux (kg/m^2-s)	297.1	1614.7	395.8	1602.4
Power (MW)	0.32	4.46	0.23	4.62
Inlet Subcooling (kJ/kg)	53.3	92.5	52.5	54.2

Cases 4101-02 and 4101-13 are run at low pressure with the former experiment being conducted at low power and mass flux, while the latter is run under high power and mass flux conditions. Two additional cases are run at a higher pressure and again, one is run at low power and mass flux, while the other is run at a higher power and mass flux.

5.1.3.3 RELAP Results for Selected Cases

The accuracy quantities of the RELAP simulations of the four cases are listed in Table 23. The planar averaged void fractions are in close agreement with the experimentally reported values, which should be expected for a mature system

code. The averaged absolute bias error was found to be significantly larger in the cases run at low power and flow, implying that the code performance under these conditions is not as good as under higher power and flux conditions. Sample standard deviations for all four cases were higher in the experimentally reported values than in the RELAP predictions, which may indicate that the code has difficulty predicting the void fraction gradients that may exist between two adjacent subchannels.

Table 23 - Accuracy Analysis of Selected Cases in RELAP

	4101-02	4101-13	4101-69	4101-86
Predicted Planar Void Fraction Average	0.5886	0.8865	0.1684	0.6932
Experimental Planar Void Fraction Average	0.5409	0.8626	0.1736	0.6972
Sample Averaged Bias Error	0.1910	0.0293	0.0433	0.0027
Sample Averaged Absolute Bias Error	0.3374	0.0361	0.2400	0.0805
Maximum Bias Error	1.8524	0.2295	1.3231	0.4472
Predicted Void Fraction Standard Deviation	0.0748	0.0144	0.0093	0.0165
Experimental Void Fraction Standard Deviation	0.1267	0.0254	0.0349	0.0365
Relative Coverage Ratio	0.1000	0.5875	0.0500	0.2500
Absolute Coverage Ratio	0.1500	0.6625	0.4250	0.3125

5.1.3.4 ASSERT Results for Selected Cases

Accuracy quantities derived from the ASSERT results are presented in Table 24. Predictions for the planar void fraction average were within experimental error for the high pressure cases, while the code tended to over-predict this value for both low pressure cases. Like the RELAP assessment, the void fraction standard deviation for the simulated values is lower than the experiment.

Table 24 - Accuracy Analysis of Selected Cases in ASSERT

	4101-02	4101-13	4101-69	4101-86
Predicted Planar Void Fraction Average	0.6187	0.9193	0.1520	0.6828
Experimental Planar Void Fraction Average	0.5409	0.8626	0.1736	0.6972
Sample Averaged Bias Error	0.2311	0.0669	-0.0780	-0.0179
Sample Averaged Absolute Bias Error	0.2726	0.0669	0.1895	0.0469
Maximum Bias Error	1.7296	0.2172	0.4829	0.1116
Predicted Void Fraction Standard Deviation	0.0254	0.0116	0.0112	0.0253
Experimental Void Fraction Standard Deviation	0.1267	0.0254	0.0349	0.0365
Relative Coverage Ratio	0.1500	0.1250	0.0375	0.4125
Absolute Coverage Ratio	0.2375	0.1500	0.5000	0.5375

5.1.4 Comparison

In terms of the overall accuracy, the results in Section 5.1.1 indicate the ASSERT void fraction predictions are in better agreement with experiments as compared to RELAP. This is no surprise since ASSERT is a dedicated subchannel code with empirical mixing and void drift models, while RELAP is a system code which is not typically used in these applications.

Overall, both codes tended to predict the "typical" style subchannels fairly well, with 91.5% of all RELAP predictions and 98.3% of the ASSERT values falling within ±0.10 of the measured void fraction. However, both codes could not accurately simulate the differences between the void in the typical subchannels and that in the corner and side subchannels. The void fraction in these subchannels tended to be overpredicted with both codes, and although the average error in the ASSERT predictions was within the experimental error, the standard deviation of the values was 0.097 – in terms of void fraction – indicating a wide distribution of values. This effect may be caused by the code predicting

the flow regime on a subchannel level as opposed to on a bundle level. The measured void fraction profiles suggest that for some of the cases, at the bundle-level, the flow is in the annular regime, and vapour is concentrated in the central subchannels. Without a bundle-level flow map, both codes predict that the void is distributed more evenly among the subchannels, causing the vapour in the corner and sides to be over-predicted, while the central subchannels are under-predicted.

Table 25 provides four figures of merit which may be used to compare the two codes in this aspect, and in every case the performance of ASSERT is better than that of RELAP. A similar trend is found when the set of results is sorted by subchannel type as again, the accuracy of ASSERT is better than that for RELAP, with the exception of the "typical" style subchannel accuracy.

Table 25 - Overall result comparison

	RELAP	ASSERT
% of total points where $\delta \leq 0.03$	30.9 %	45.2 %
$\overline{\delta} \times 100$ (All Cases)	2.375	-0.638
$\sigma_\delta \times 100$ (All Cases)	8.034	5.225

Predicted versus measured graphs are presented in Figure 27 to Figure 30 in order to assess the ability of the code to predict the trends of the void fraction distribution. The solid line in these figures represents situations where the predicted value is exactly the value reported in experiment. The dashed and dotted lines denote the measurement uncertainty of ±0.03 and an arbitrary difference of ±0.10 respectively. The predictions of the low pressure, high power and flow case (4101-13) in Figure 28 are noteworthy as the positive bias in the

ASSERT results compared to the RELAP results is clearly visible. In the high pressure cases where the two codes are generally more accurate, the points on the far left of Figure 29 and Figure 30 represent the predictions for the subchannels adjacent to the large water rod in the center of the bundle. In both cases, it is clear that the ASSERT predictions for these subchannels is closer to the experimental values than the RELAP predictions.

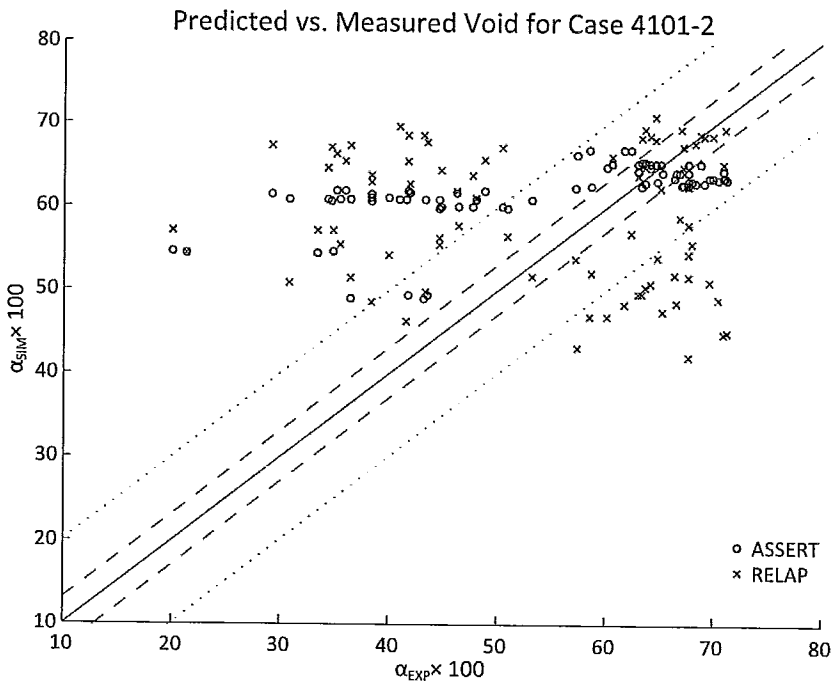

Figure 27 – Void Fraction Predictions for Case 4101-2

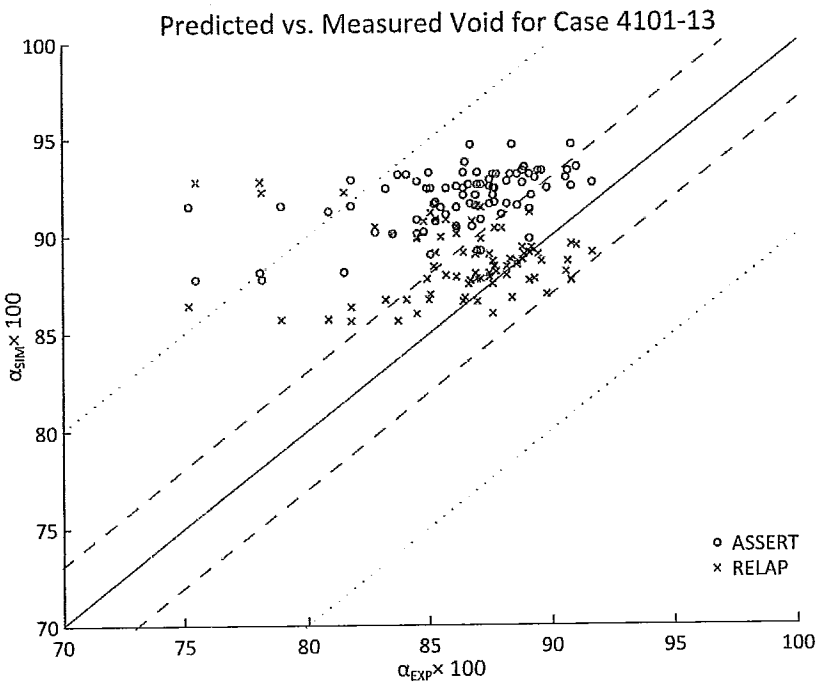

Figure 28 - Void Fraction Predictions for Case 4101-13

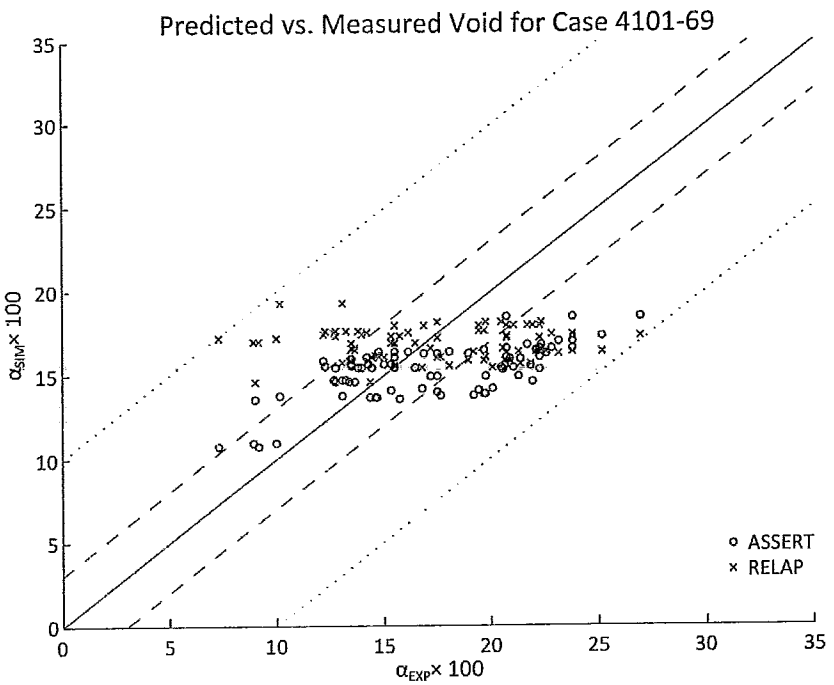

Figure 29 - Void Fraction Predictions for Case 4101-69

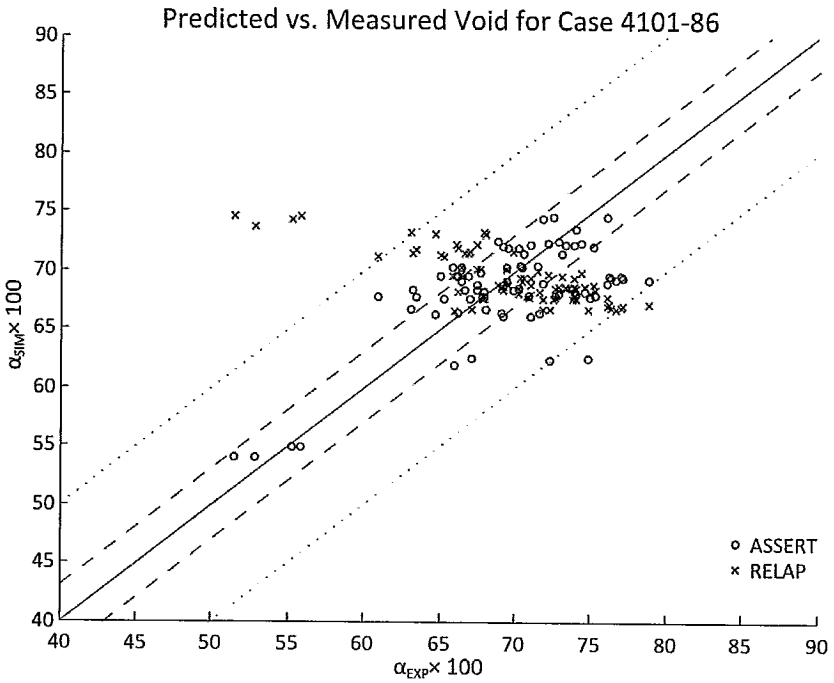

Figure 30 - Void Fraction Predictions for Case 4101-86

5.2 *Sensitivity to Boundary Condition Uncertainty*

5.2.1 ASSERT Results

The sensitivity of the code predictions to the boundary condition uncertainty may be assessed using Wilks' formula. In the study, 93 sets of boundary conditions are randomly selected for the inlet temperature, outlet pressure, mass flow rate and bundle power based on the distributions indicated in Table 10. The variation of these conditions is illustrated in Figure 31.

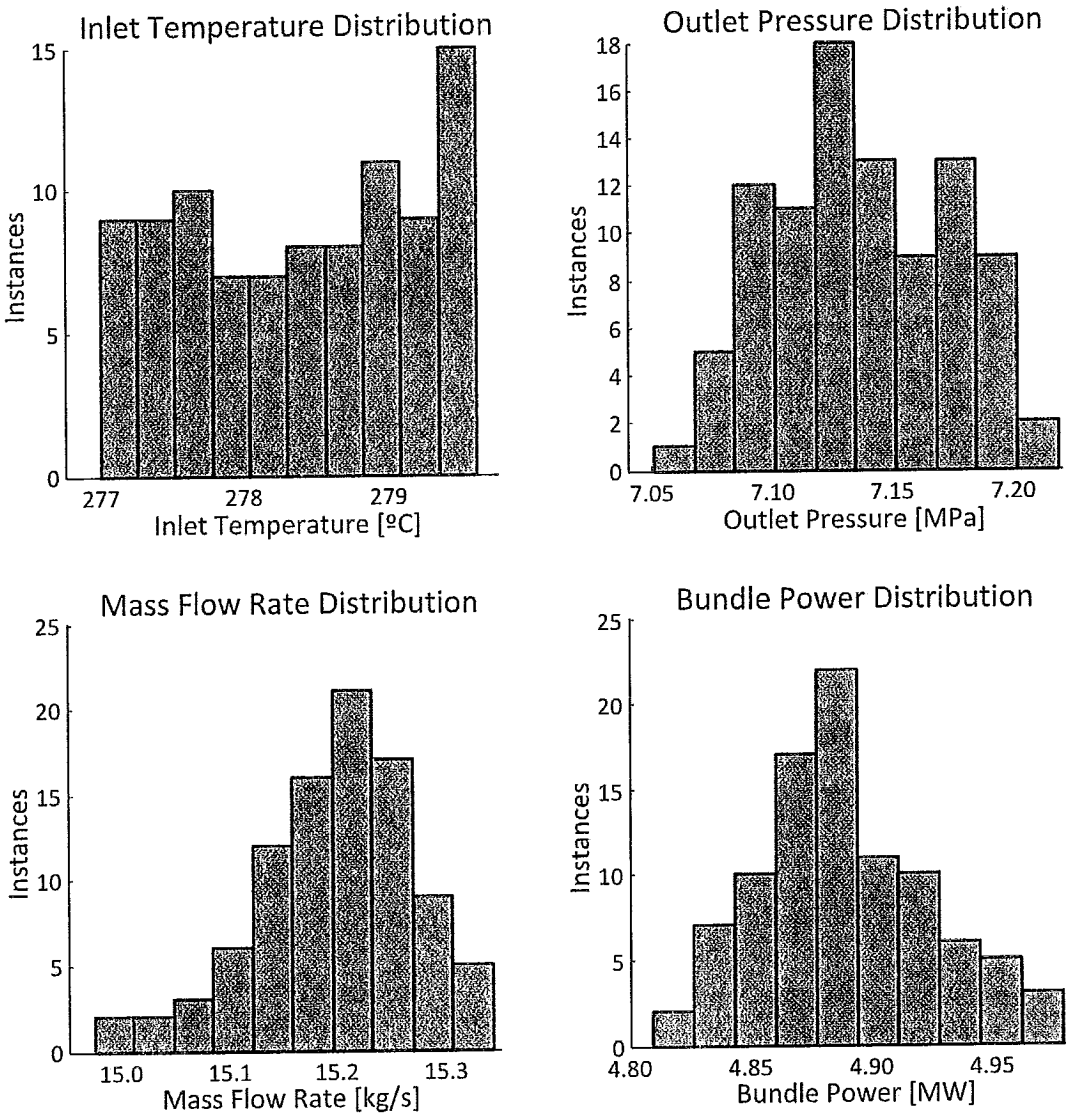

Figure 31 – Distribution of Boundary Conditions

Although the inlet pressure was measured in the experiment and has the same uncertainty as the outlet pressure, it was assumed that the reported value was the actual value. This must be done since in some cases, the reported pressure difference between the outlet and inlet is on the order of 10 – 20 kPa. Varying both boundary conditions leads to certain situations where the inlet

pressure is less than the outlet pressure, causing the flow to reverse. To avoid this, the flow measurement uncertainty for this section is applied only to the mass flow at the inlet and the pressure at the outlet.

A subchannel-by-subchannel comparison of the experimental and ASSERT results for this case are provided in Figure 32. In the figure, the reported values are denoted by the blue dots, surrounded by the void fraction measurement uncertainty. The red bars represent the possible range of simulated values, and they are derived by running the code for each of the boundary condition sets generated. The results for each subchannel are then placed in numerical order such that $\alpha_1 < \alpha_2 < \ldots \alpha_N$. α_2 and α_{N-1} are then plotted as the lower and upper bounds for the void fraction of that particular subchannel. On average, the size of each of the uncertainty due to boundary condition is 0.023.

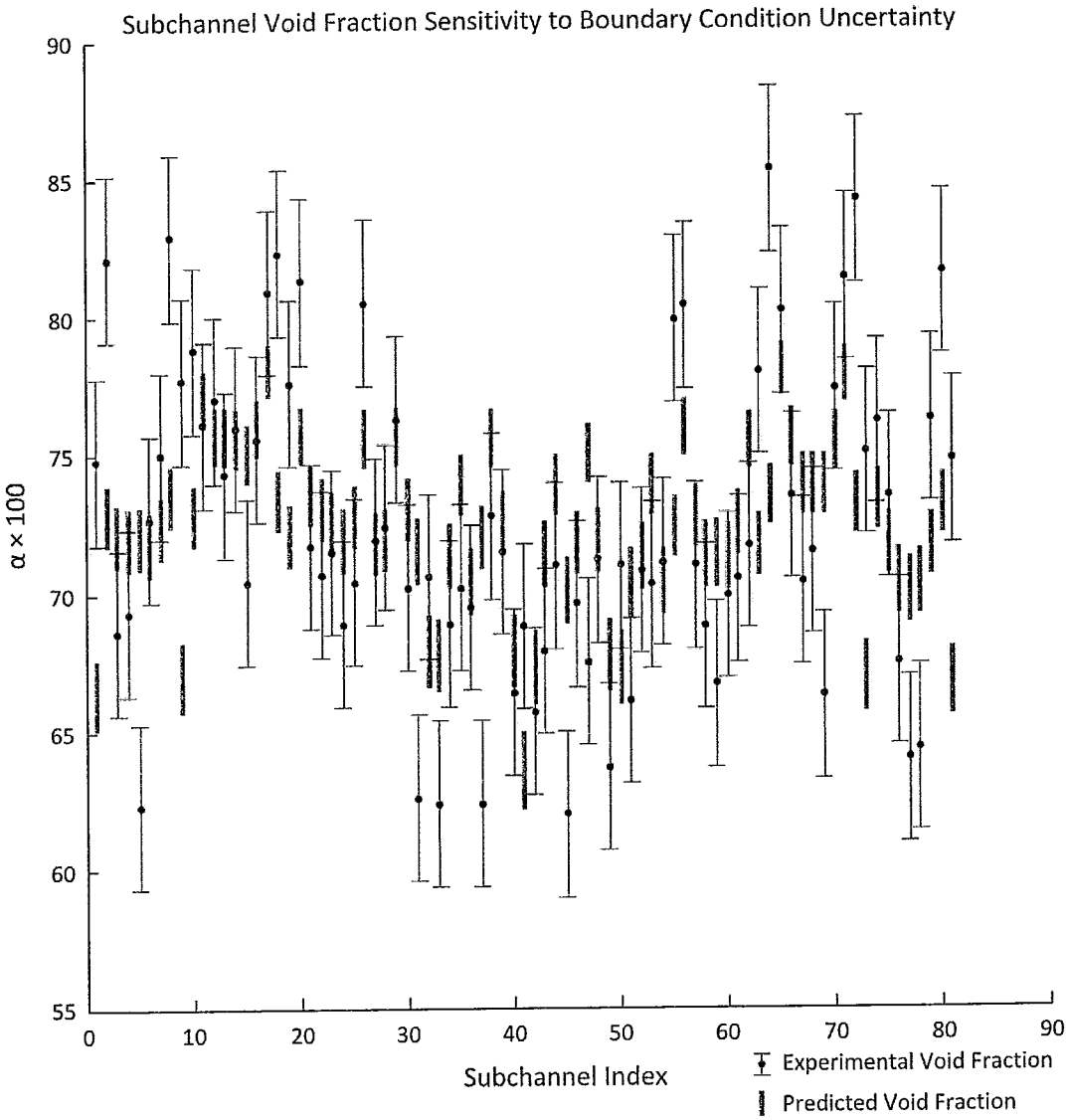

Figure 32 - Subchannel Void Fraction Comparison for Case 1071-59

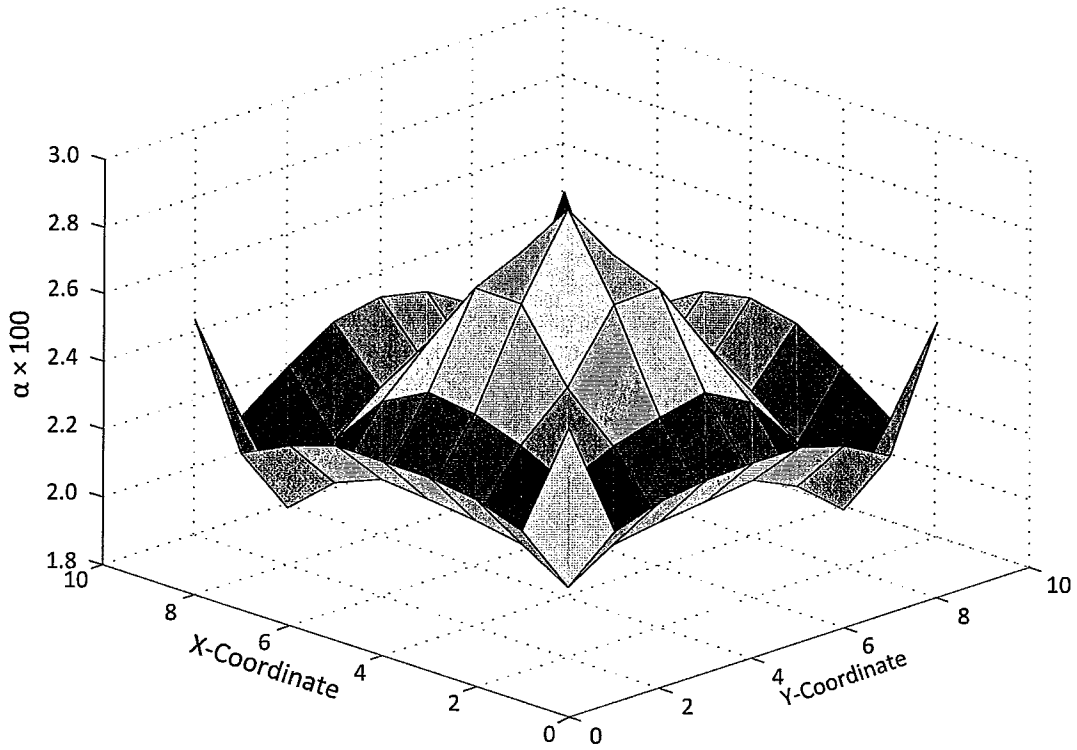

Figure 33 - Sensitivity of subchannel void distribution to boundary conditions

Figure 33 plots the size of each of the sensitivity bands as a function of their position within the bundle. The subchannels near the center of the bundle are the most sensitive to the boundary condition variations, while subchannels adjacent to the side subchannels are least sensitive.

5.3 *Influence of Subchannel Mixing*

Although the constituent equations of both codes are based on the same principles, the most significant difference between the two codes is the presence of a mixing and void drift model in ASSERT. As the results in Table 23 and

Table 24 indicate, RELAP actually predicts the planar averaged void fraction better than ASSERT does. However, the lack of a proper mixing model in the MULTI-D component means that the distribution of the void in the subchannels is not as accurate as that in ASSERT. The aim of this section is to examine the effects of subchannel mixing on the accuracy of the void fraction predictions of both of the codes used.

5.3.1 RELAP Results

The RELAP code does not have an empirical correlation for mixing, and laterally adjacent subchannels are connected with a lossless junction in the default nodalization. This assumption prevents "tweaking" the nodalization to get the desired results, even though it is clear that this is incorrect. From a cross-flow perspective, fluid passing from one subchannel to an adjacent one will "see" a reduction in the flow area as it approaches the junction, and then an expansion after passing through due to the grid arrangement of the fuel rods. This means that form loss, or 'k-factor' should be applied to the junctions.

Figure 34 illustrates the impact that this assumption has on the results, as one case with the 1071-XX bundle was taken and the transverse junction form loss factors were incremented. From the figure, it is evident that altering the loss coefficients between k = 0 and k = 2 has the greatest impact on the accuracy of the simulations – especially in the corner subchannels.

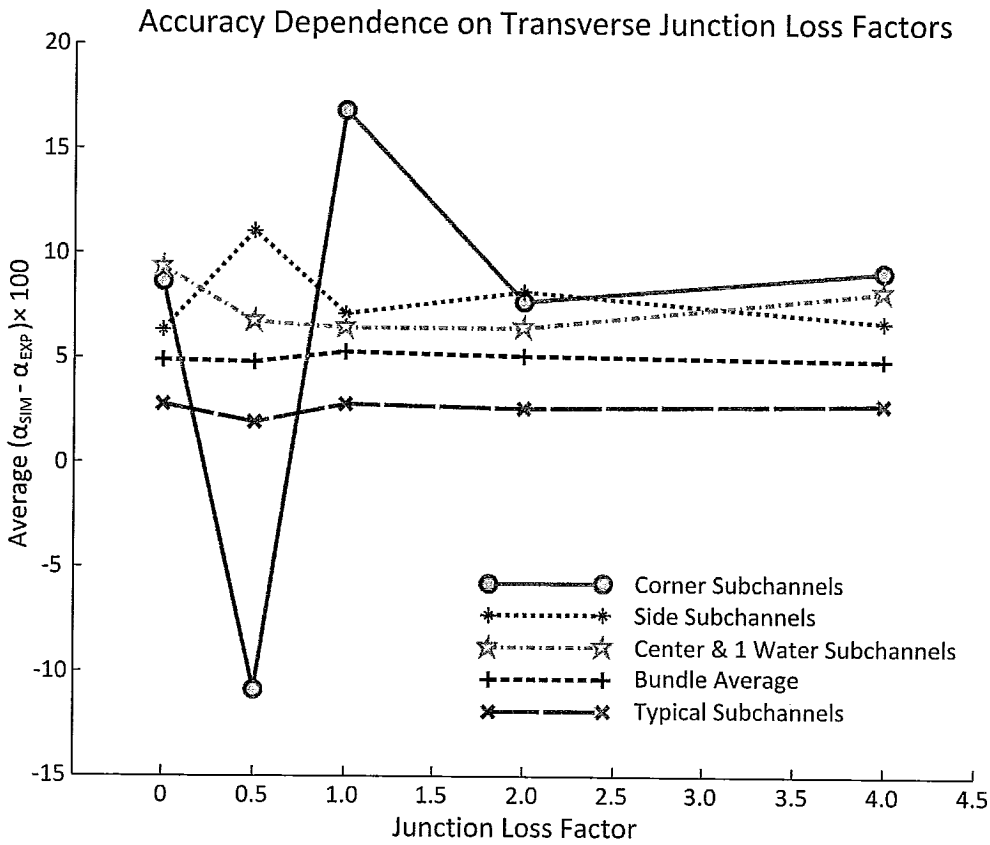

Figure 34 - Effect of Lateral Subchannel Junction Loss Factors

5.3.2 ASSERT Results

A single, isolated subchannel was simulated in ASSERT in order to assess the impact of the presence of the mixing model. The results in Figure 35 indicate that a model consisting of a single subchannel and a single fuel rod would predict a void fraction higher than a model of the full bundle. This implies that the mixing correlation is causing void to be advected out of the side and corner channels, and into the central channels. This is consistent with Lahey and Moody's theory that the "equilibrium void distribution" drives the void to move towards larger subchannels and those with higher flow rates.

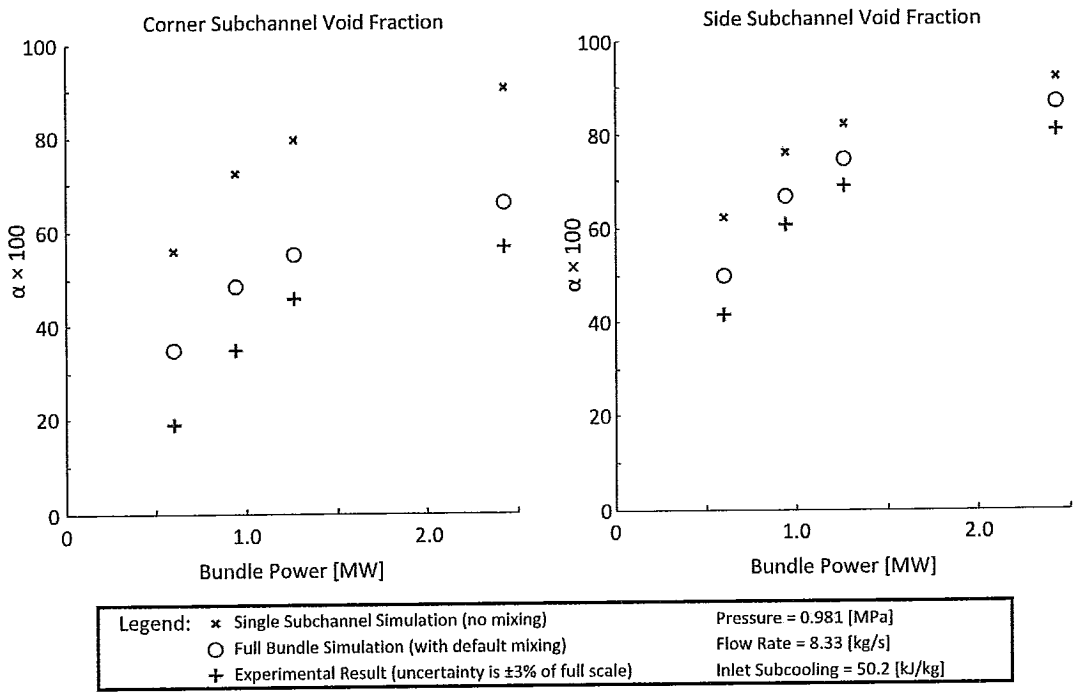

Figure 35 - Subchannel Averaged Void Fraction at Low Pressure

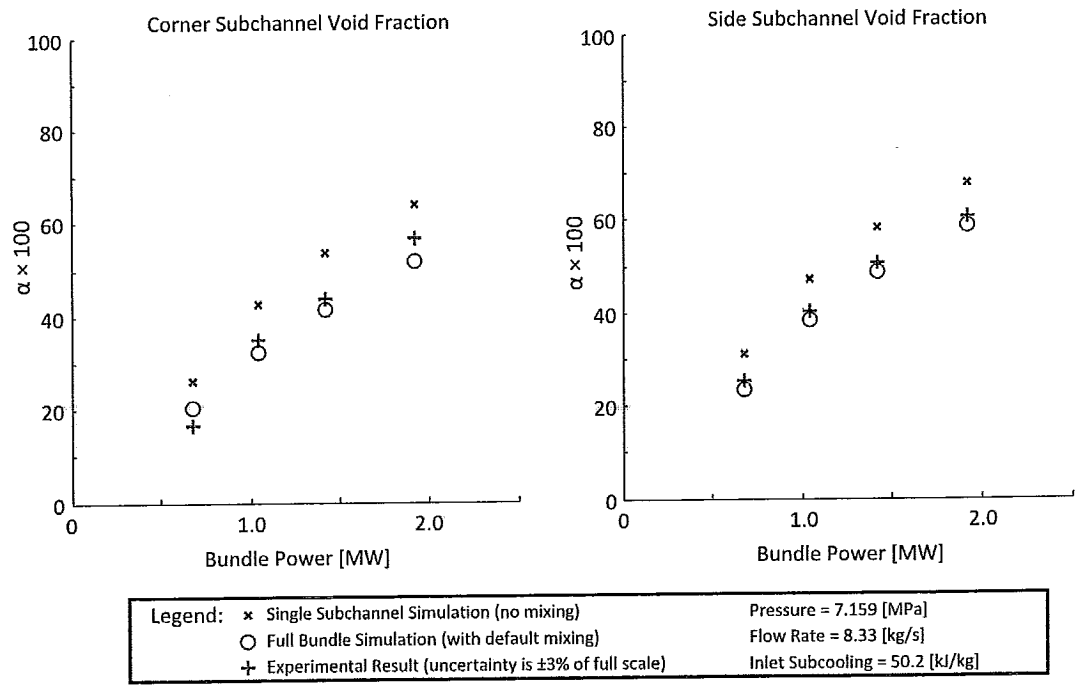

Figure 36 - Subchannel Averaged Void Fraction at High Pressure

The data in Figure 35 indicates that the problem with the simulations appears to be that the mixing rates in the corner and side subchannels at low pressure is under predicted. The plot in Figure 36 illustrates the effect of increasing the pressure to 7.159 MPa - typical of what would be found in a BWR under normal operations. With the increased pressure, the isolated subchannel still over-predicts the experimental void fraction. However in every case, the void fraction in the subchannels of the full bundle simulation is within the experimental uncertainty of the measured value. This demonstrates that the mixing correlation is correct when used at high pressure, but does not adequately reflect the experimental results when used at low pressure. Since the Carlucci mixing and void drift correlations are primarily functions of mass flow rate, local void fraction and viscosity, the model is not particularly sensitive to pressure, despite the current evidence that there should be a pressure dependency.

The incremental mixing factor, Ω from equation 53, allows the mixing rate in the model to be adjusted. In Figure 37 and Figure 38, 8 cases have been simulated for values of Ω between 0 and 10. Cases in the same figure have the same flow rate, inlet subcooling and outlet mass quality, and only the outlet pressure is varied. In each instance, increasing the incremental mixing coefficient decreases the void in the corner and side subchannels, and at low pressures, decreases the error. At higher pressures, the void fraction in these channels seems to be under-predicted, and the "optimal" value for the incremental mixing coefficient should be set close to 0.

It is interesting to note that Carlucci recommends a value of $\Omega = 3.0$ for his correlation which is based on steam-water data from a 3 × 3 bundle at 6.9 MPa. In the present simulations of the cases at 7.16 MPa (green crosses), an incremental mixing factor multiplier of $\Omega = 3.0$ causes ASSERT to slightly underpredict the void in the corner and side subchannels – suggesting that the mixing is already too strong.

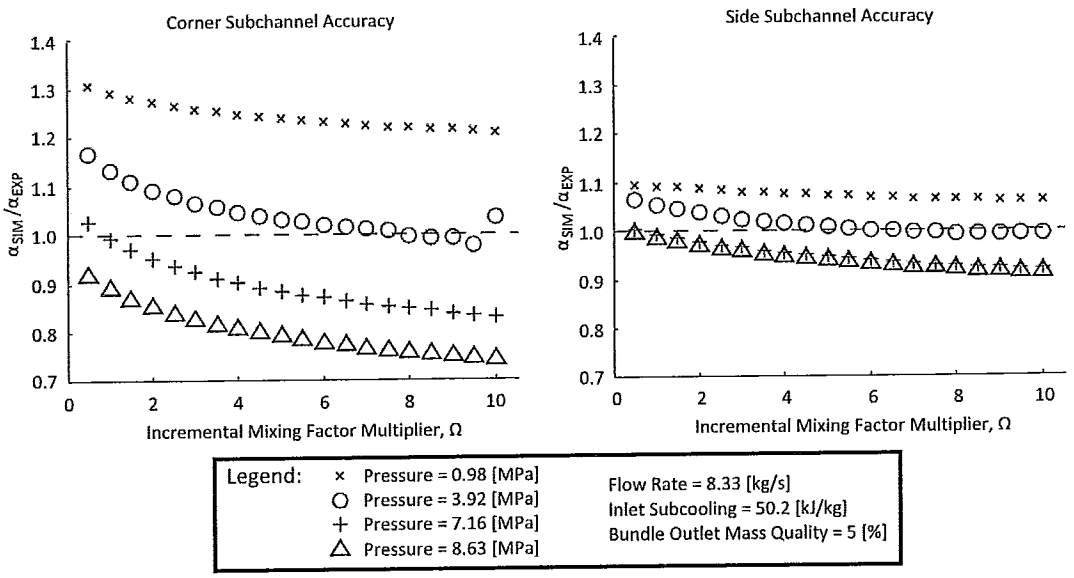

Figure 37 - Corner (left) and Side (right) Subchannel Accuracy at 5% Outlet Mass Quality

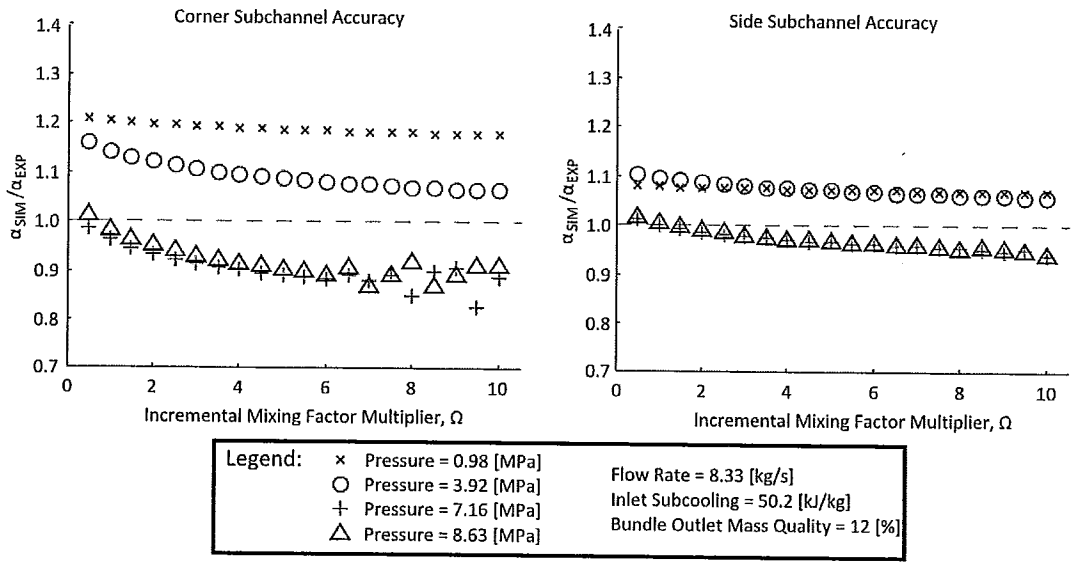

Figure 38 - Corner (left) and Side (Right) Subchannel Accuracy at 12% Outlet Mass Quality

From a theoretical point of view, the net mixing term is dominated by the homogeneous component, which is justifiable since one would expect that in a vertical bundle, grid spacers and other obstructions would be the primary source of diversionary flows. For the 0.98 MPa case examined in Figure 37, the lateral mass flow rate at the top node of the corner subchannel (junction 1-2 according to Figure 5) is plotted against the incremental mixing factor in Figure 39. Increasing Ω from the default value of 3 to 8 causes a 5.8% increase in the actual mixing rate of this node and corresponds to a 3.9% increase in accuracy.

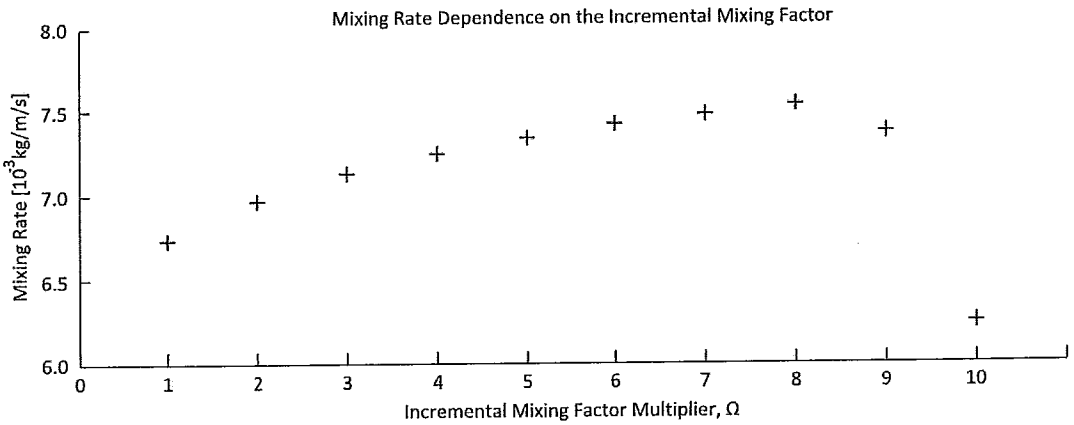

Figure 39 - Influence of the Incremental Mixing Parameter on the Mixing Rate

According to Carlucci's description of the experimental data obtained by Rowe and Angle, the two-phase mixing rate in a junction 2.1 mm in size, at 2.8 MPa pressure and 1356 kg/m^{2}s mass flux should be between 0.02 – 0.08 kg/m/s [72]. Since the subchannel mixing rate increases with an increasing junction size, and the size of the corner junction in the test bundle being examined is 3.4 mm, it would be reasonable to expect simulated mixing rate to be higher than that reported by Rowe and Angle. However, this is not the case, as even with using $\Omega = 9$, the simulated results predict a total mixing rate one order of magnitude lower than expected, strengthening the claim that the mixing in the simulated bundle corners is under-predicted.

5.4 *Influence of User Effects*

During the development of the nodalizations, decisions made in terms of model selection, node size and convergence criteria will affect the predictions,

and are referred to as the user effects. The philosophy behind the development of the ASSERT and RELAP nodalizations was to use default or general models whenever possible, and the results presented in the preceding sections are based on this. This section examines the impact that user decisions on the nodalization development can have.

5.4.1 Nodalization Sensitivity

5.4.1.1 RELAP Node Size Sensitivity

All 81 of the subchannels in the bundle are modelled in RELAP using a MULTI-D component containing 12 axial layers. A code limitation restricts a single MULTI-D component to a maximum of 999 nodes, which means that a finer nodalization is only possible if more than one MULTI-D component were connected in series. A study by Kovtonyuk et. al. demonstrated problems with connecting two MULTI-D components together – specifically large lateral mass flow rate increases at the connecting junctions [74]. As demonstrated by Section 5.3 the magnitude of the subchannel mixing present has a significant impact on the void distribution of the bundle.

This sensitivity test demonstrates what may be a significant flaw with the RELAP5-3D code when the MULTI-D components are used. Simulations were conducted of a 1071-XX type bundle at a pressure, power and mass flow of 7.180 MPa, 1.90 MW and 15.0 kg/s respectively. Data from the 0011-XX series of tests were used since they were conducted with uniform power profiles in both the

axial and planar directions – in other words, each rod has the same power in both the flow and lateral directions. A "fine" nodalization was built by connecting two MULTI-D components connected end to end, thus the bundle is represented with 24 layers of nodes in the axial direction, each 0.1545 m in length. The results of this test are compared to the results obtained using the "coarse" nodalization used in the previous sections.

Figure 40, plots the average junction mass flow rate in both the planar and axial directions for the test using the "fine" nodalization. The problem with connecting the two MULTI-D components end to end can be seen between axial nodes 12 and 13 where a large jump in the average lateral mass flow rate is observed. The effects of this jump can be observed by comparing Figure 41 and Figure 42 which represent the axial void distribution for both the coarse and fine mesh simulations.

In the case of the "coarse" mesh (Figure 41), the void fraction monotonically increases as the flow moves up the bundle. This is a result which makes sense since once the flow enters the active portion of the bundle, energy is being added at each subsequent node. However, this characteristic was not observed in the "fine" mesh results in Figure 42. The void fraction in the flow through the first MULTI-D component increases consistently, however at the node just downstream of the connection between the two components, the void fraction in the side and corner subchannels suddenly decreases. This is mirrored

by a sudden increase in the void fraction in the central subchannels, and when this is considered with the mass flow rate increase, it seems to imply that the vapour is being driven into the middle of the bundle.

The effect of this unexplained vapour migration on the overall subchannel prediction accuracy can be seen in Figure 43, a predicted versus measured graph for the void fraction at the top of the bundle. In the "coarse" mesh case without the faux-mixing, the void fraction profile is relatively flat, reflecting on the uniform power profile of the bundle. However, in the "fine" mesh case, the void simulation is over-predicted in the center of the bundle, and under predicted towards the edges.

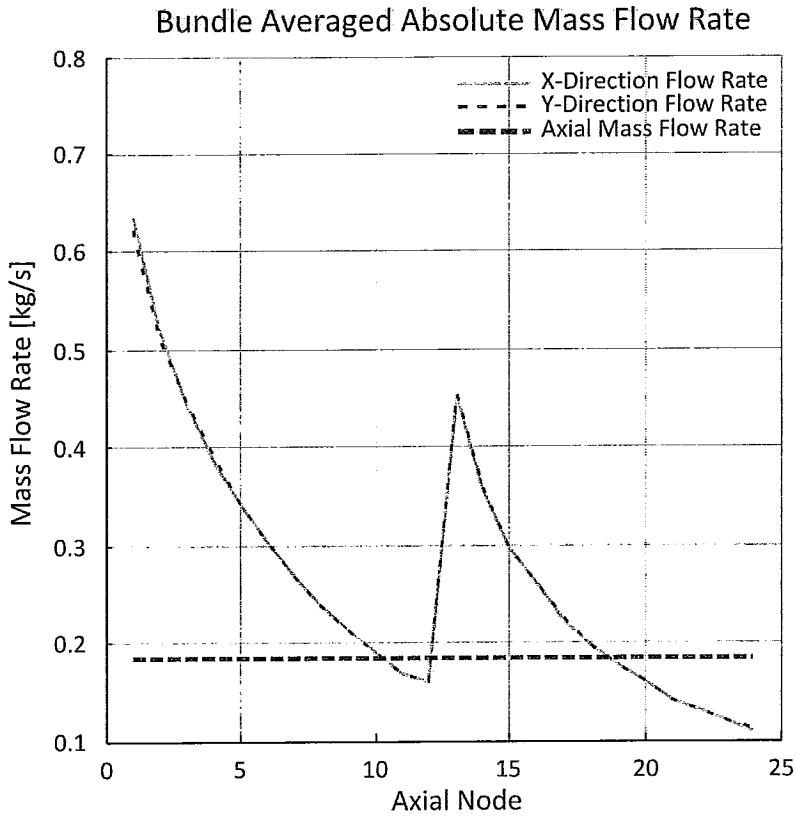

Figure 40 - Junction mass flow rate for two MULTI-D components connected in series.

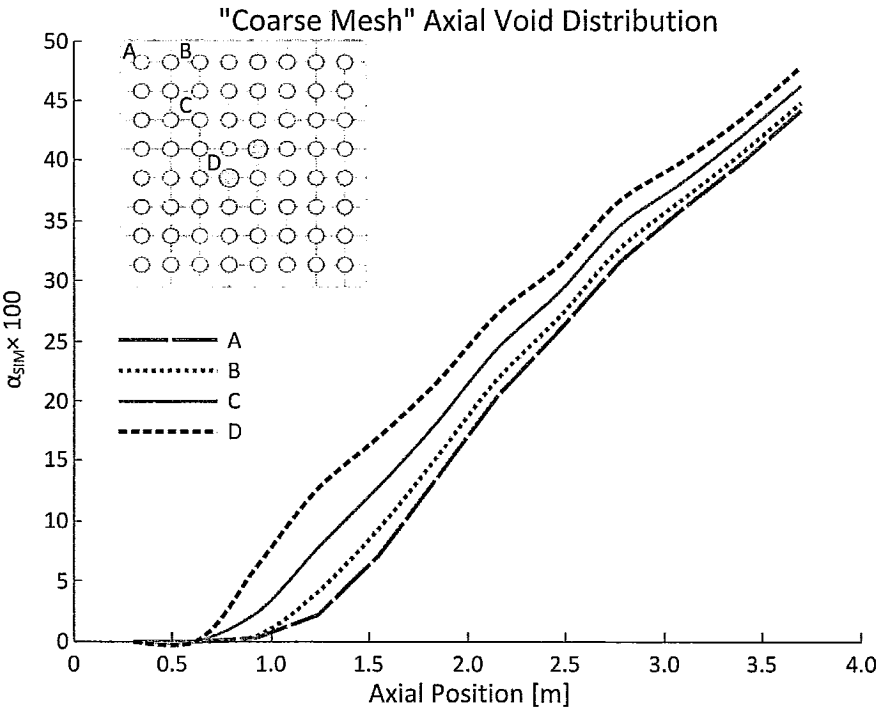

Figure 41 – Axial void distribution for a one MULTI-D Component bundle.

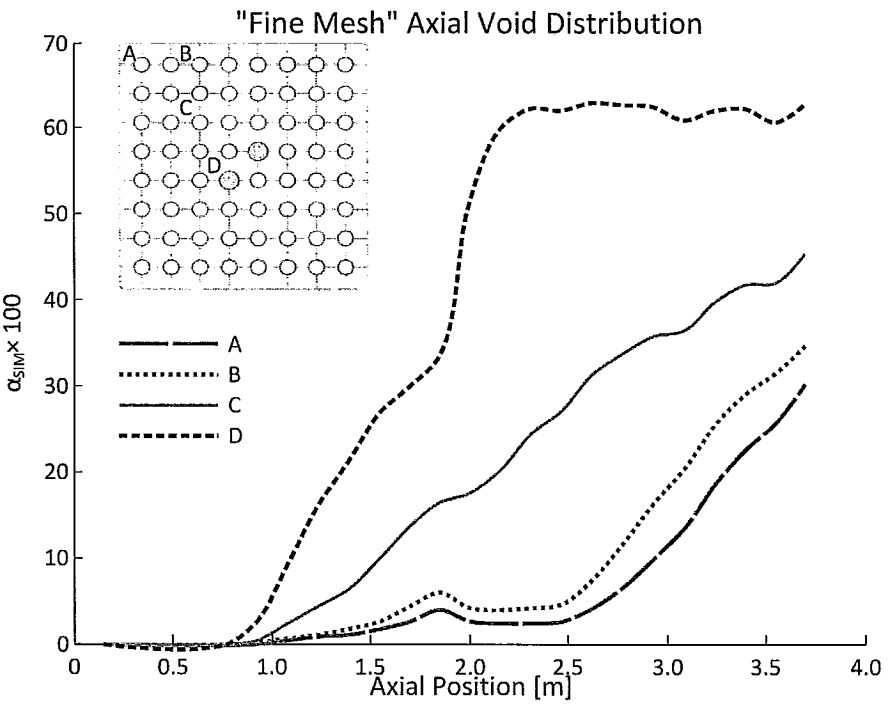

Figure 42 – Axial void distribution for a two MULTI-D Component bundle.

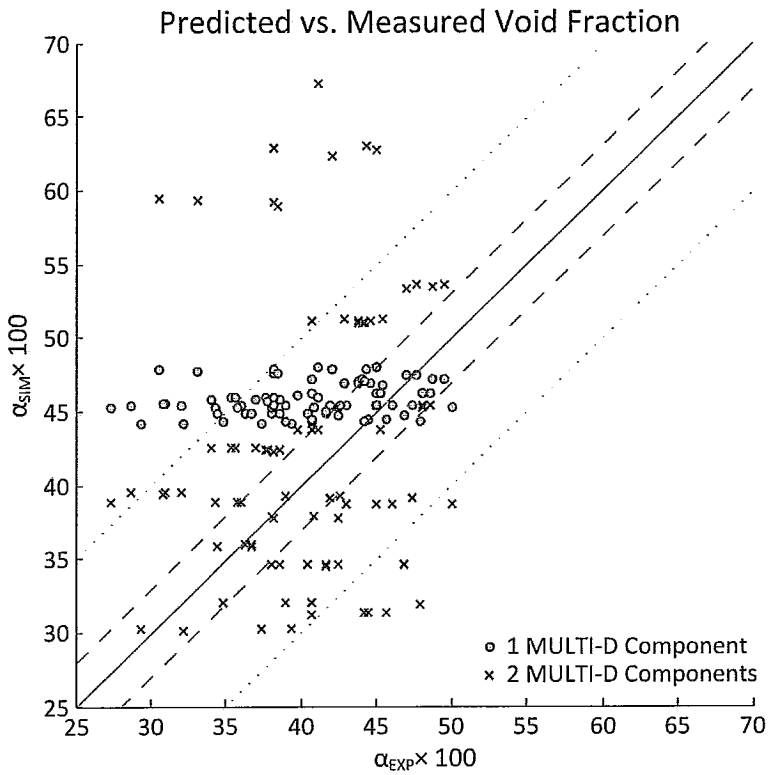

Figure 43 – Predicted vs. Measured void fraction for the two nodalizations

5.4.1.2 RELAP Quasi-Steady State Approach

Although the RELAP code may be run for either transient or steady state scenarios, both numerical stability issues and for simplicity, the experiments were simulated as extended transients. In the steady-state mode, the code is normally run over one large time step selected so that any transient effects are simply "averaged" into the result.

Figure 44 demonstrates that a quasi-steady state can also be achieved when the code is run in transient mode for a sufficient number of time steps. In

the figure at t = 0 seconds, the heat structures are set to the same temperature as the flow from the inlet junction, and no power is applied. Single phase steady state flow conditions are assumed to have been established 20 seconds into the transient, at which point the bundle power is increased instantaneously to the experimentally reported value. After the power increase, no other changes to the boundary conditions are made. In the case analyzed, after t = 50 seconds, the void fraction in the selected subchannels levels out and for the purposes of the study, the void fraction reported 100 seconds after the start of the simulation is considered the steady-state value. Fluctuations in the void fraction values are present, however the magnitude of these fluctuations is at most 0.003.

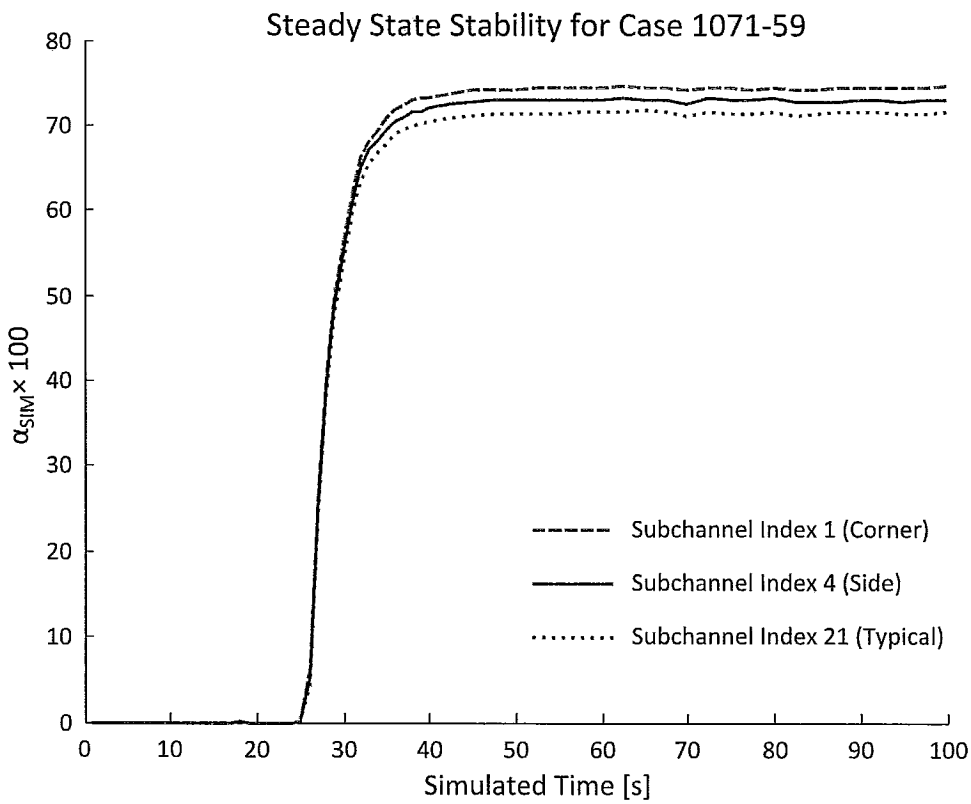

Figure 44 –Validity of the Quasi-Steady State Approach for Case 1071-59

5.4.1.3 ASSERT Node Size Sensitivity

The sensitivity of the ASSERT model to the number of axial nodes used was determined by setting the boundary conditions of the nodalization to the values in Table 26, and varying the value for NHTDX in the deck. Results in Figure 45 show the bundle averaged void fraction as a function of the number of nodes used in the axial direction in the input deck. The difference between using 5 and 40 nodes resulted in a 0.0013 increase in the predicted value, and can be considered insignificant.

Twenty nodes were used for the input decks in the accuracy assessment, and this value is justified since Figure 45 demonstrates that in this case, the predicted void fraction converges beyond this point. The accuracy of this case was found to be almost independent to the number of nodes used. Figure 46 demonstrates that in the worst case, the accuracy of the corner subchannels varied by 0.003 void fraction between using 5 nodes and 40 nodes.

Table 26 - ASSERT Nodalization Sensitivity Test - Boundary Conditions

Condition	Quantity
Outlet Pressure [MPa]	7.177
Mass Flow Rate [kg/s]	15.21
Inlet Subcooling [kJ/kg]	51.30
Bundle Power [MW]	4.88

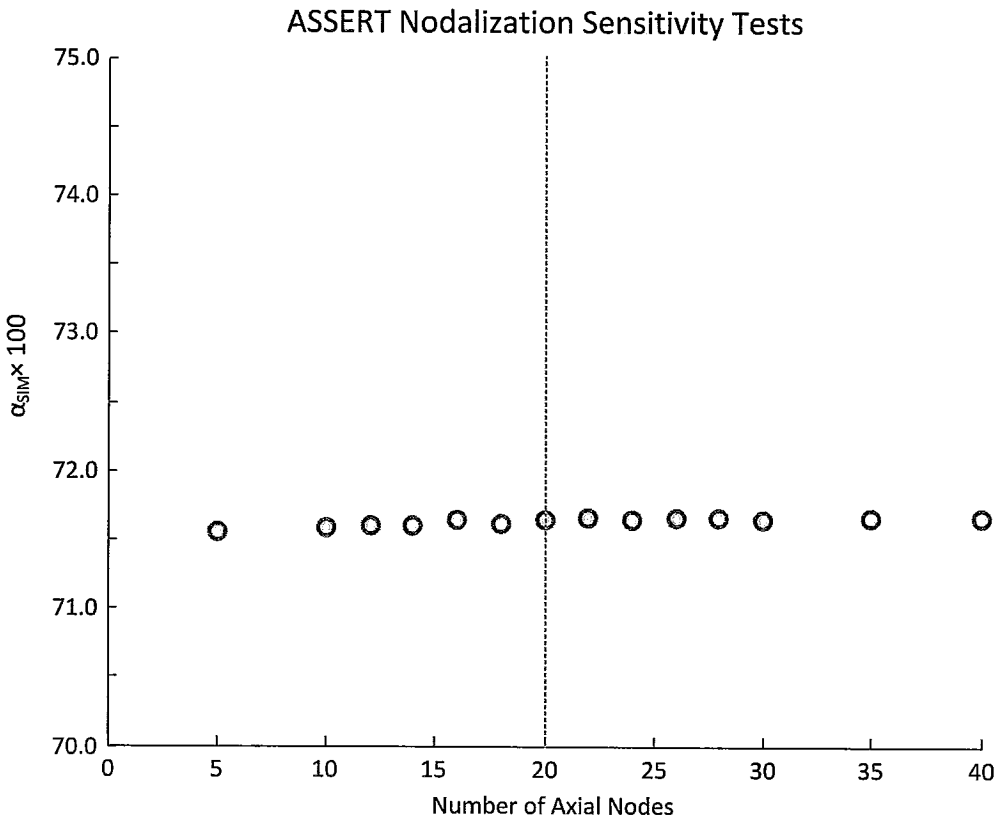

Figure 45 - Bundle Averaged Void Fraction Dependence on Number of Nodes

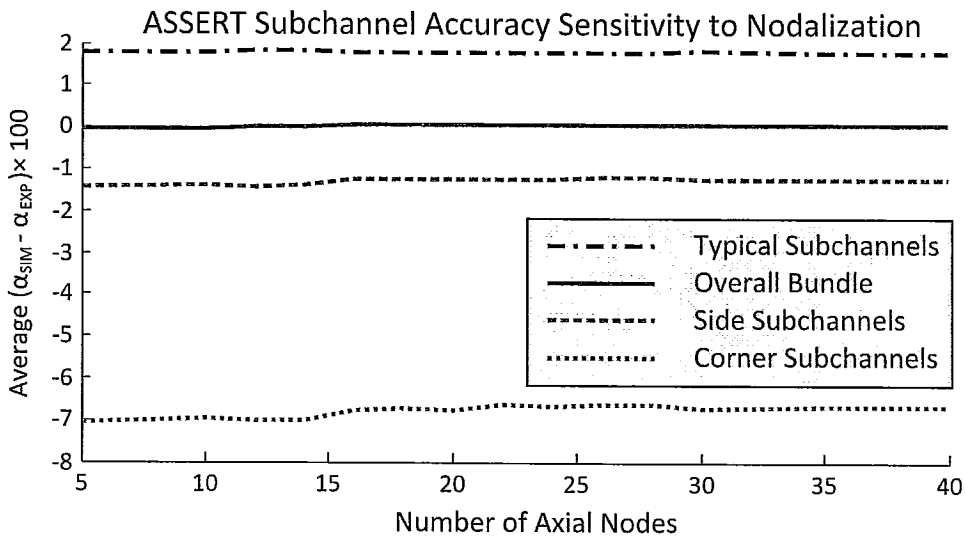

Figure 46 - Subchannel Accuracy Dependence on Number of Nodes

5.4.2 Model Selection Sensitivity

5.4.2.1 RELAP Two-Phase Heat Transfer Model Sensitivity

In RELAP, the Chen two-phase heat transfer model was selected by default and used for the assessment of the benchmark cases, although Aounallah indicates that this may not be the ideal correlation for vertical bundle geometries or nucleate boiling flows. The Chen-Inayatov correlation was implemented in RELAP specifically to model these types of geometries with the intention to collapse the fuel bundle into one hydrodynamic component and heat structure rather than model each rod separately.

This section provides a comparison between the results obtained with both of the models in terms of the subchannel void fraction accuracy. Four experimental cases from the "high burnup" database have been selected for this sensitivity assessment, and the boundary conditions of each are listed in Table 27.

Table 27 - Boundary Conditions for the Heat Transfer Correlation Sensitivity Tests

Case	Outlet Pressure [MPa]	Flow Rate [t/h]	Inlet Subcooling [kJ/kg]	Power [MW]
4101-82	8.636	15.15	52.9	1.85
4101-83	8.666	15.17	53.2	2.49
4101-84	8.680	15.18	53.2	3.35
4101-86	8.705	15.16	54.2	4.62

Table 28 indicates, there is no significant change in the accuracy of the predictions between using the Chen and the Chen-Inayatov correlation.

Table 28 - Two Phase Heat Transfer Correlation Selection Effects

Power	Chen		Chen-Inayatov		Difference	
	Subchannel Average $\alpha_{SIM} / \alpha_{EXP}$	Sample Standard Deviation	Subchannel Average $\alpha_{SIM} / \alpha_{EXP}$	Sample Standard Deviation	Subchannel Average $\alpha_{SIM} / \alpha_{EXP}$	Sample Standard Deviation
1.85	1.08833	0.25975	1.08831	0.25972	2.073E-05	2.972E-05
2.49	1.04499	0.18084	1.04459	0.18038	4.056E-04	4.567E-04
3.35	1.01642	0.13249	1.01669	0.13226	-2.689E-04	2.246E-04
4.62	1.00269	0.11453	1.00234	0.11352	3.484E-04	1.014E-03

5.4.2.2 ASSERT Mixing & Void Drift Models

In Table 29, 11 experimental cases at a pressure of 0.981 MPa, with varying power, flow rate and subcooling, were analyzed in order to examine the effects of model selection on the accuracy of the void fraction predictions. The data presented in the table represents the average error over the cases run for the particular subchannel being examined. At first glance, it appears the Carlucci-Carlucci model is the most accurate, however it is noted that the experimental uncertainty is ±0.03, and so the differences are insignificant. Although the bundle averaged error is small, and within experimental uncertainty, the fact that the error in the corner subchannels is about 6 times the experimental uncertainty indicates that the mixing correlation at low pressures should be improved.

Table 29 - Effects of the Mixing & Void Drift Model on Accuracy at Low Pressure

Mixing Model	Carlucci	Carlucci	Carlucci	Rogers-Rosehart	N_{Points}
Void Drift Model	Carlucci	Rowe	Shoukri	Shoukri	
Average Corner Subchannel Error	.1755	.1888	.1850	.1856	44
Average Side Subchannel Error	.0702	.0734	.0697	.0700	308
All Other Subchannels	-.0063	-.0082	-.0058	-.0060	539
Bundle Average Error	.0291	.0297	.0297	.0297	891

5.4.2.3 ASSERT Two-Phase Heat Transfer Model

It was noted in section 4.2.5.4 that the Ahmad two-phase heat transfer correlation did not cover the entire range of the experimental data. The cases from Table 22 are used to examine the sensitivity of the nodalization to the two-phase heat transfer model selection. In addition to the Ahmad model, three others are considered. The Ahmad and the Rouhani & Axelsson models are empirical, while the Maroti and Lahey & Moody models are derived from theory [19]. Table 30 presents the average subchannel error for the four cases, and while the Maroti model is slightly more accurate than the other models, the differences are less than the experimental uncertainty and are considered insignificant.

Table 30 – Effect of Two-Phase Heat Transfer Model on the Average Subchannel Error

Case	Heat Transfer Model			
	Ahmad	Rouhani & Axelsson	Maroti	Lahey & Moody
4101-2	0.0751	0.0751	0.0737	0.0720
4101-13	0.0551	0.0551	0.0536	0.0506
4101-69	-0.0215	-0.0164	-0.0133	-0.0213
4101-86	-0.0131	-0.0131	-0.0127	-0.0135

6 CIAU RESULTS

6.1 Uncertainty Band Prediction

Every measurement taken is subject to uncertainty, and as such, the boundary conditions for each test run in this study can never be truly known. Additionally, the extensive use of empirical correlations in thermalhydraulics and user effects means that codes can only estimate the value of a parameter. This creates the need to develop a method to quantify the uncertainty of the code predictions. To accomplish this, the CIAU method has been applied to the results generated by both RELAP and ASSERT.

In this section, the CIAU code builds an accuracy database by comparing simulated to experimental results, and based on that, predicts a set of uncertainty bands covering 95% of the expected range of values with a 95% confidence level.

6.1.1 Case Selection

The four cases used for the uncertainty analysis portion of the BFBT benchmark are identical to those used in the accuracy quantification portion. Boundary conditions for these cases have been previously listed in Table 22 in Section 5.1.3.2.

6.1.2 RELAP Results

An accuracy database for RELAP was created by simulating all 86 of the test cases from the 4101-XX series of tests. Simulations were performed on two 1.86 GHz Dual-Quad core computers each with 8.0 GB of RAM. Each case required between 2.5 hours to 35 hours to run. All cases were completed successfully yielding 6880 sets of data points – although three of the cases required modification of the time steps to avoid transient failures. The four cases which uncertainty bounds are generated for are not included the database.

Figure 47 to Figure 50 illustrate the RELAP results for each subchannel along with the uncertainty band predicted by CIAU. The uncertainty of the measured value is represented by the superimposed red bar.

Case 4101-02 is characterized by a set of boundary conditions with low pressure, power and flow. The experimental void fraction in this case ranges between 0.20 to 0.71, and both Figure 27 and Figure 47 illustrate that the RELAP model developed has difficulty predicting the void fraction under these conditions. The sample averaged bias error was 0.19 for this particular case. The large uncertainty bounds represent the fact that the inaccurate predictions are common among cases run under similar conditions using the current nodalization and code.

In cases 4101-13 and 4101-86 – illustrated in Figure 48 and Figure 50 respectively, the uncertainty bands in subchannels 1, 9, 72 and 81 (corner

channels) are noticeably larger. These subchannels are only adjacent to one-quarter of one of the fuel rods meaning that the subchannel power to mass flux ratio is lower, forcing the data points from those subchannels to be classified in a different hypercube.

In the same two cases, subchannels 32, 40, 42 and 50 also stand out as they are only adjacent to two fuel rods with a relative power factor of 0.89. This puts them in a different hypercube than surrounding subchannels. Since the code is consistent in over-predicting the void in these channels, the accuracy quantities associated with these channels is higher, which in turn causes the uncertainty bands to be larger.

In both of the high power cases, 4101-13 and 4101-86, all experimental points fell within the predicted uncertainty bounds. In case 4101-69 - the low power, high pressure test in Figure 49 - the uncertainty bounds encompassed all but one of the experimental points. In case 4101-02 - low power, flow and pressure - 87.5% of the experimental points fell within the predicted bounds, although very large uncertainty bands were present due to the hypercube selected for these conditions. Additionally, two points from this case were classified to empty hypercubes, thus no uncertainty bands were predicted.

A breakdown of the contents of the hypercubes used to estimate the uncertainty bounds of case 4101-86 is provided in Table 31.

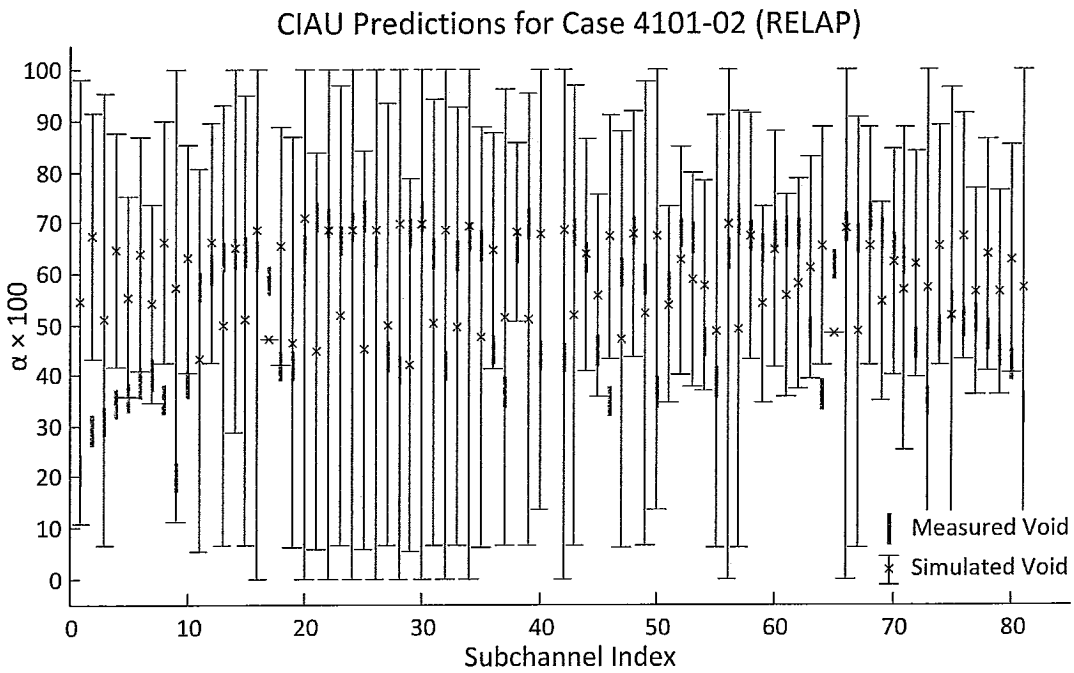

Figure 47 - Application of CIAU on RELAP Results of Case 4101-02

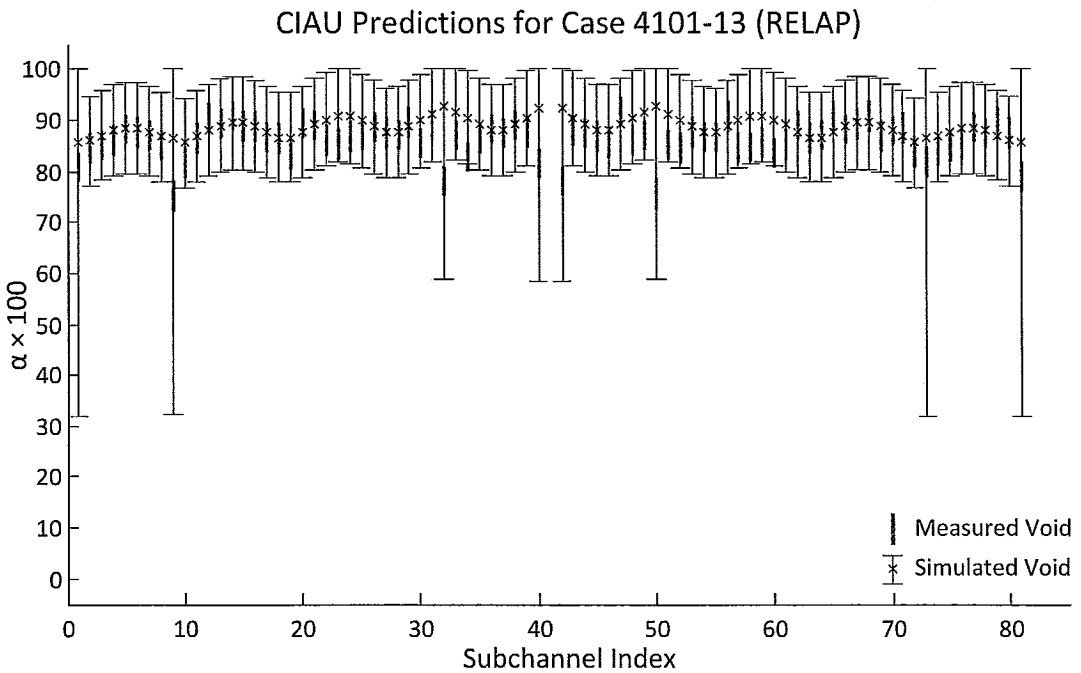

Figure 48 - Application of CIAU on RELAP Results of Case 4101-13

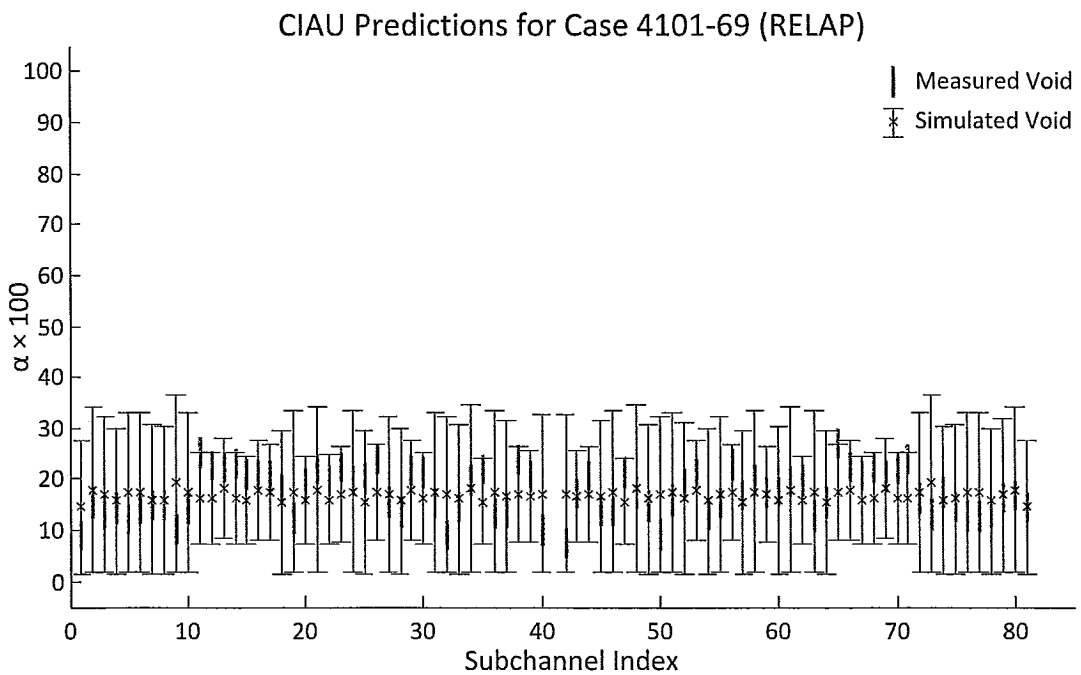

Figure 49 - Application of CIAU on RELAP Results of Case 4101-69

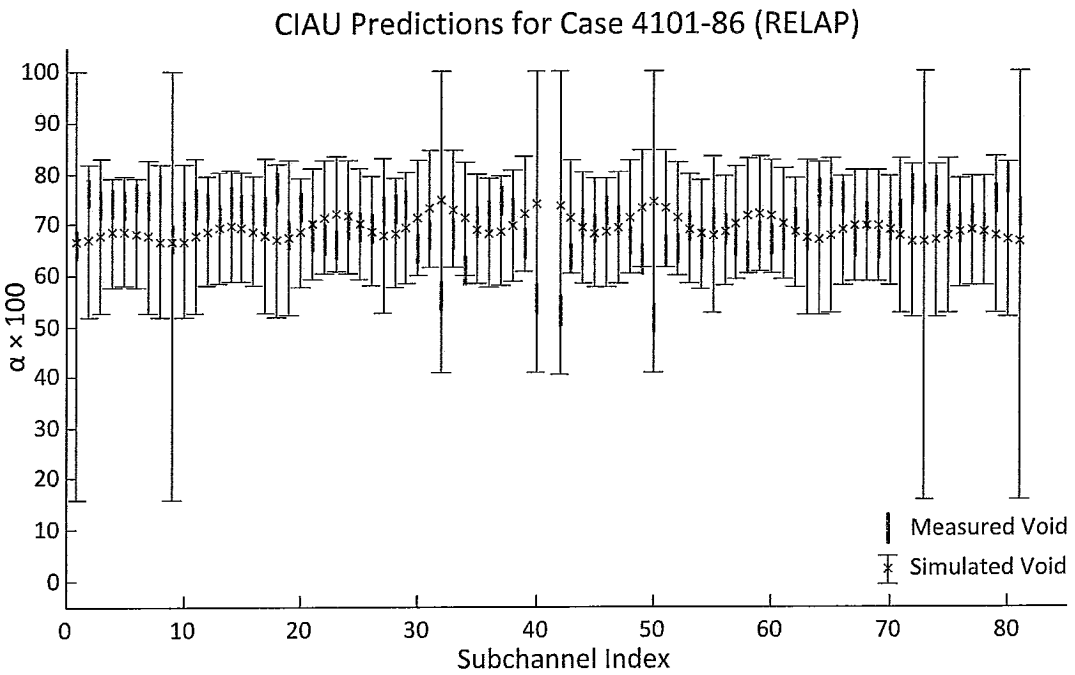

Figure 50 - Application of CIAU on RELAP Results of Case 4101-86

Table 31 - Statistics of hypercubes used for RELAP case 4101-86

Hypercube ID	Coordinates (Pressure, Power/Mass Flux, Inlet Subcooling, Void Fraction)	Subchannels from 4101-86 Classified to this hypercube	$\overline{AQ^i}$	σ^i	Data points in hypercube
264	(4,3,2,4)	1, 9, 73, 81	0.238	0.125	34
294	(4,5,2,4)	2, 3, 7, 8, 10, 11, 17, 18, 19, 27, 55, 63, 64, 65, 71, 72, 74, 75, 79, 80	0.065	0.045	209
295	(4,5,2,5)	4, 5, 6, 12, 13, 14, 15, 16, 20, 21, 22, 23, 24, 25, 26, 28, 29, 30, 31, 33, 34, 35, 36, 37, 38, 39, 43, 44, 45, 46, 47, 48, 49, 51, 52, 53, 54, 56, 57, 58, 59, 60, 61, 62, 66, 67, 68, 69, 70, 76, 77, 78	0.05	0.042	252
280	(4,4,2,5)	32, 40, 42, 50	0.247	0.052	8

6.1.3 ASSERT Results

The entire 4101-XX case matrix was attempted in ASSERT to create the CIAU accuracy database. It total 79 of the 86 cases were completed successfully, and after isolating the cases used for the uncertainty study, 6000 'accuracy quantities' were available for use in the database. Uncertainty bands are predicted for the four isolated cases in Figure 51 to Figure 54.

The large uncertainty bands in the low pressure, power and flow case in Figure 51 reflect the expected accuracy of the subchannel void fraction predictions for these conditions. In case 4101-2, four subchannels were classified to hypercubes with no existing data and three of the measured values fell outside the predicted uncertainty bounds. Additionally, the uncertainty bounds around the predictions of the four subchannels adjacent to the large central water rod span the entire range.

In case 4101-13 - the low pressure, high power and flow test depicted in Figure 52 - 79 out of the 80 predicted uncertainty bands encompass the measured value. Figure 53 and Figure 54 show the CIAU results for the two cases at high pressure, where the predicted uncertainty bounds cover all of the measured values.

In Figure 53, the uncertainty predictions around the side and corner subchannels are much smaller than those for the "typical" type subchannels. The CIAU code is predicting uncertainty band sizes of between ±0.04 to ±0.06 around the simulated values in the sides and corners, while the "typical" subchannels

have uncertainties of up to ±0.25. This is the opposite of what has been observed in every other case analyzed in both RELAP and ASSERT, and this trend is attributed to accuracy of the predictions in these hypercubes. In this case, there are 32 "side" and "corner" type subchannels, and ASSERT predicts the void fraction within experimental error in 27 of these. This indicates that the code is accurate for the high pressure, low flow and power conditions in these subchannels, resulting in smaller uncertainty bands.

A breakdown of the contents of the hypercubes used to estimate the uncertainty bounds of case 4101-86 is provided in Table 32.

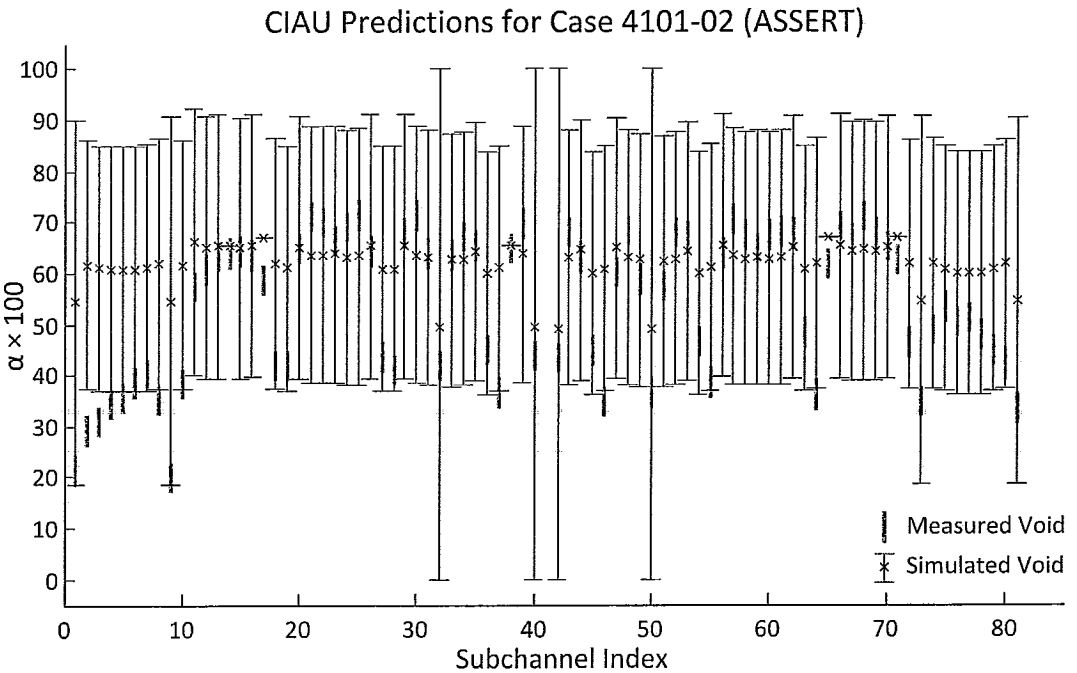

Figure 51 - Application of CIAU on ASSERT Results of Case 4101-02

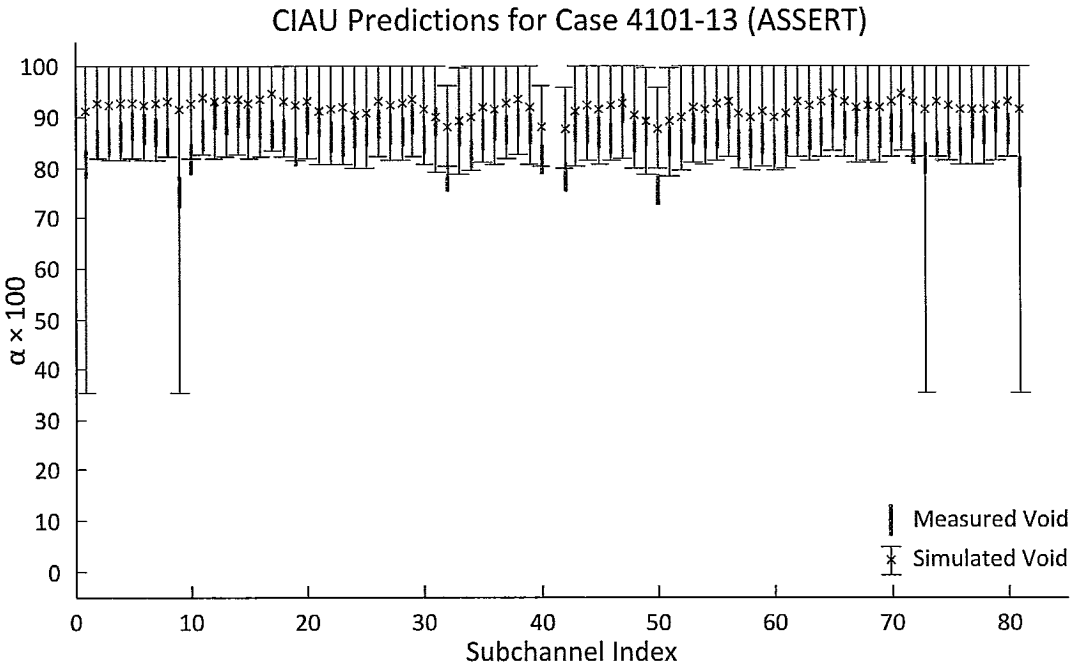

Figure 52 - Application of CIAU on ASSERT Results to Case 4101-13

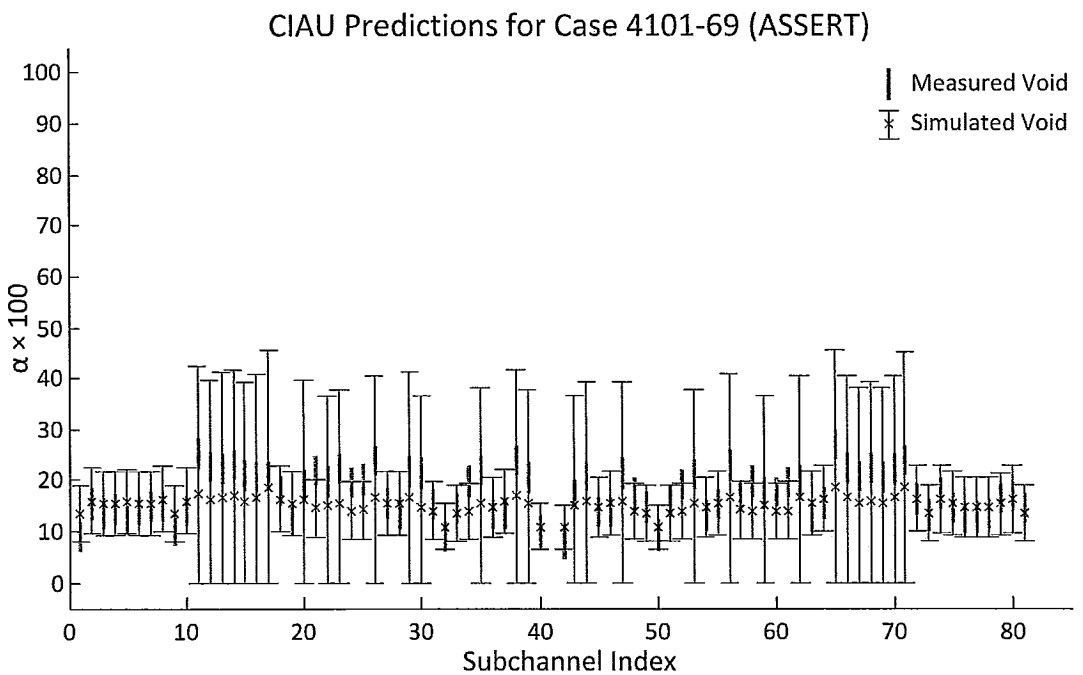

Figure 53 - Application of CIAU on ASSERT Results to Case 4101-69

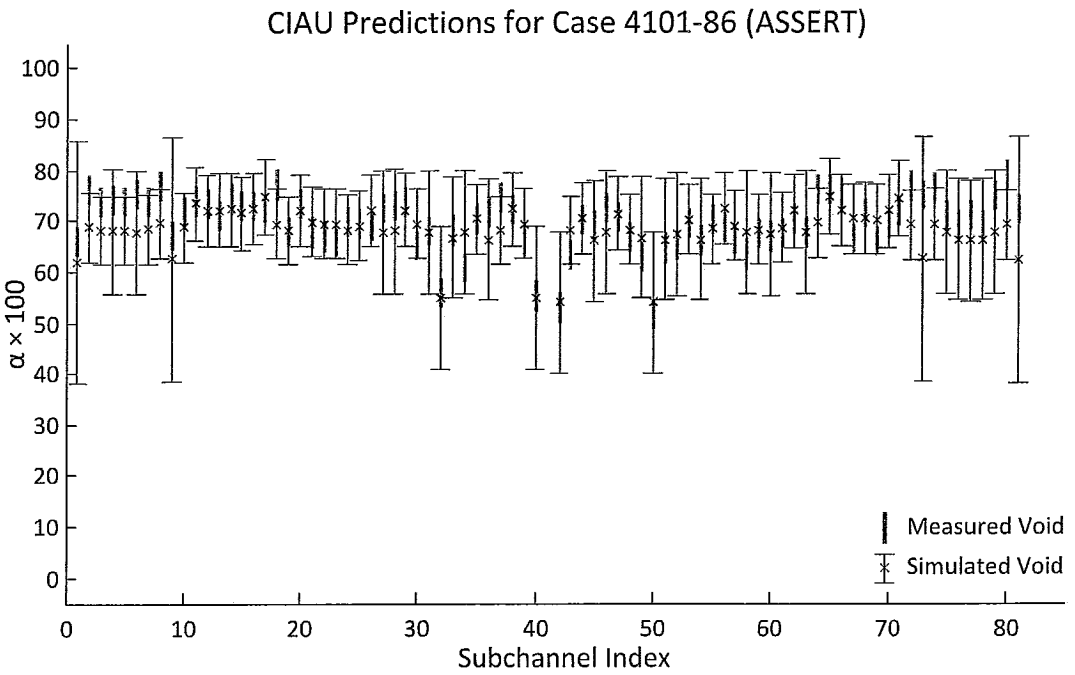

Figure 54 - Application of CIAU on ASSERT Results to Case 4101-02

Table 32 - Statistics of hypercubes used for ASSERT case 4101-86

Hypercube ID	Coordinates (Pressure, Power/Mass Flux, Inlet Subcooling, Void Fraction)	Subchannels from 4101-86 classified to this hypercube	$\overline{AQ^i}$	σ^i	Data points in hypercube
264	(4,3,2,4)	1, 9, 73, 81	0.086	0.066	8
294	(4,5,2,4)	4, 6, 9, 27, 28, 31, 33, 34, 36, 40, 45, 46, 49, 51, 52, 54, 58, 60, 63, 75, 76, 77, 78, 79	0.050	0.037	227
295	(4,5,2,5)	2, 3, 5, 7, 8, 10, 11, 12, 13, 14, 15, 16, 17, 18, 19, 20, 21, 22, 23, 24, 25, 26, 29, 30, 35, 37, 38, 39, 43, 44, 47, 48, 53, 55, 56, 57, 59, 61, 62, 64, 65, 66, 67, 68, 69, 70, 71, 72, 74, 80	0.032	0.026	149
279	(4,4,2,4)	32, 42, 50	0.07	0.045	70

6.1.4 Comparison

The most noticeable difference between the RELAP and ASSERT predictions is that the uncertainty bands CIAU predicts for the ASSERT results are small than those of RELAP. Since the ASSERT void predictions are closer to the experimental values than the RELAP ones, the 'accuracy quantities' are generally lower, and therefore cause smaller uncertainty bands to be predicted.

Two figures of merit may be used to assess the effectiveness of the CIAU code performance. The first is simply the number of points where any portion of the predicted uncertainty band falls within the measurement uncertainty. The second is the number of points where the CIAU predicted uncertainty bands cover at least 95% of the measured uncertainty bands, assuming that the latter follows a two-tailed normal distribution. The two figures are presented in Table 33, and for both of the codes, 97.81% of the points in the cases examined had some portion of the measurement uncertainty fall within the CIAU predicted bounds.

Table 33 - CIAU Performance Evaluation

	RELAP		ASSERT	
	Number of Points with any Coverage	Number of Points with 95% Coverage	Number of Points with any Coverage	Number of Points with 95% Coverage
4101-02	73 (91.25%)	68 (85.00%)	74 (92.50%)	63 (78.75%)
4101-13	80 (100.0%)	79 (98.75%)	79 (98.75%)	72 (90.00%)
4101-69	80 (100.0%)	74 (92.50%)	80 (100.0%)	66 (82.50%)
4101-86	80 (100.0%)	78 (97.50%)	80 (100.0%)	66 (82.50%)
All 4 Cases	313 (97.81%)	299 (93.44%)	313 (97.81%)	267 (83.44%)

Under the more stringent of the two criteria, the CIAU code uncertainty bands covered 10% more of the points in RELAP than in ASSERT. This is again the result of the ASSERT uncertainty bands being smaller as the predictions themselves are generally more accurate.

7 CONCLUSIONS & EXTENSIONS

7.1 RELAP

The RELAP5-3D system code was used in this study to model a full-scale BWR bundle at the subchannel level. Although this may be regarded as pushing a system code beyond its intended capabilities, reasonable results compared to those from a dedicated subchannel code have been obtained.

Of seventy-four cases successfully simulated with RELAP, 30.9% of all predicted subchannel void fractions fell within ±0.10 of the measurement uncertainty of the experiments. A breakdown of the results by subchannel type revealed that the subchannels next to the central water rod, and those in the corner and sides of the bundle were generally poorly predicted, while the "typical" style subchannel simulations were much better.

Examination of the void fraction profile at the top of the bundle revealed that RELAP was incapable of predicting large differences in void fraction values between two adjacent subchannels, typically leading to "flat" profiles. This was attributed to the lack of a proper mixing model in the code, and as a result, the subchannel mixing was too strong. Artificially restricting the subchannel flows by applying a form loss factor between adjacent subchannels did not have a significant impact on the overall accuracy of the results, although the corner subchannels were found to be highly sensitive to varying the form loss factors.

One severe problem was demonstrated with the use of multiple MULTI-D components in an effort to refine the nodalization. It was determined that connecting two MULTI-D components caused a large increase in the lateral mass flow which in turn had a large impact on the void fraction predictions.

7.2 ASSERT

An analysis of eighty-four cases with ASSERT determined that 95.4% of the points fell within ±0.10 of the measured value, while 45.2% of the comparisons were within experimental error. The void fraction in the subchannels at the bundle side and corners were over predicted, while cases run at low pressure, power and mass fluxes either failed to converge or yielded generally poor predictions. In one particular case run, the void fraction was over-predicted in one of the corner subchannels by over 0.35, and this implies that in such cases there further study is required on the phenomena present. This is expected since the void mixing relationships inherent in ASSERT were derived from higher pressure data, hence further work to develop low pressure mixing models, or alternatively a more universally applicable correlation may be needed.

Boundary condition uncertainty contributes about 0.023 to the code void fraction uncertainty for one particular case. The boundary condition uncertainties have the greatest effects on the corner and central subchannels, which is where a majority of the void fraction inaccuracy takes place. Again, this may be linked to the void mixing models.

Void fraction over prediction for low pressure cases in the corner subchannels is caused by the under-prediction of the mixing rate within these regions at these conditions. Code predictions for the mixing rate at low pressures is about one order of magnitude less than expected in the corner subchannel junction. By increasing the incremental mixing coefficient, Ω, the mixing rate was artificially increased, and the accuracy of the low pressure predictions was improved.

An analysis of eleven experimental cases using the four different void drift and mixing models available in ASSERT demonstrated no significant effect of the accuracy of the simulation. The Carlucci-Carlucci mixing and void drift model was determined to be the most accurate of the four models tested – although by a small margin.

7.3 CIAU

The study has demonstrated that the CIAU method can be adapted for use in predicting the subchannel void fraction uncertainty bands. Accuracy databases were generated for both the ASSERT and RELAP codes, and uncertainty estimates were generated for four selected cases. For both codes the estimated uncertainty bands covered some portion of experimental uncertainty band over 97% of the time. The code performance on the "95% coverage" metric was not as good however, and it was noted that several points in the low pressure case were classified to empty hypercubes.

7.4 *Recommendations for Future Work*

The present study has identified several areas in which further work would be beneficial.

7.4.1 Continued Participation in International Benchmarks

International activities such as the BFBT benchmark provide a forum for participants to assess the performance of thermalhydraulic codes. Deficiencies or areas where code improvements are possible can be identified as a direct result of benchmarking activities, and therefore continued participation in these international benchmarks is recommended. Specifically, the Pressurized Water Reactor Subchannel Bundle Tests (PSBT) is an upcoming subchannel thermalhydraulics benchmark sponsored by the OECD/NEA, and participation in it would be beneficial.

7.4.2 Mixing & Void Drift Model Refinement

In ASSERT, the accuracy of the code in predicting the subchannel void fraction of vertical bundles is linked to the estimated lateral mixing rate. The present study has identified that the accuracy of the empirical Carlucci model may be improved by considering dependencies on pressure or other flow parameters. Further experimental work, including high resolution flow measurements, is recommended to determine the exact nature of the relationship.

7.4.3 Continued Development of Uncertainty Methods

The present study demonstrated how ordered statistics can be used to determine the sensitivity of the subchannel void fraction predictions to input boundary condition uncertainties. The result is two sets of uncertainties, one representing the measurement uncertainty and one for the code predictions. This raises questions during the assessment of code accuracy as it is not clear how much overlap these two uncertainties require before a result can be deemed as adequate. Further work should be conducted in order to create either a metric to assess code accuracy under these circumstances or a single uncertainty value which encompasses both the code and measurement uncertainties.

7.4.4 CIAU Database Expansion & Sensitivity Studies

While CIAU estimated uncertainty bands on the code predictions encompassed most of the experimental void fractions, there were instances where points fell into empty hypercubes. This indicates the need for additional data to fully populate the CIAU database. Furthermore, data from other facilities should be used where possible in order to account for differences in scaling or measurement uncertainty.

Additionally, further work should be done to determine the sensitivity of the uncertainty bands to the hypercube boundaries. Specifically, the number of hypercubes as well as the division of the boundaries needs to be studied further.

7.5 Contributions to Knowledge

Papers Submitted to Refereed Journals

Leung, K. H., Kovtonyuk, A., Petruzzi, A., Parisi, C., D'Auria, F., Novog, D.R., RELAP5-3D Analysis of the BFBT Benchmark, *submitted to Nuclear Engineering and Design*, 2009.

Novog, D. R., and Leung, K., Benchmark of numerical CFD studies of phase distribution in two-phase boiling in a swirl-flow channel against experimental heat transfer and phase distribution data, *submitted to the Journal of Heat Transfer Engineering,* 2008.

Refereed Conference Proceedings

Leung, K. H. and Novog, D.R., Evaluation of ASSERT-PV V3R1 void fraction predictions against the OECD/NED BFBT benchmark data, *30th Annual Conference of the Canadian Nuclear Society*, Calgary, Canada , 2009.

Leung, K., Kovtonyuk, A., Petruzzi, A, D'Auria, F., and Novog, D. R., Prediction of void fraction uncertainty bands in BWR fuel bundles using the CIAU methodology, *International Conference on Mathematics, Computational Methods & Reactor Physics*, Saratoga Springs, United States of America, 2009.

Novog, D.R. and Leung, K., Comparisons of numerical CFD studies and experimental heat transfer and phase distribution data for high-heat flux swirl-flow in cylindrical tubes, *Proceedings of the International Conference on Transport Phenomena in Multi-Phase Systems*, Bailystok, Poland, 2008.

Non-Refereed Conference Proceedings & Presentations

Leung, K. H., Effects of two-phase mixing and void drift models on subchannel void fraction predictions in vertical bundles, *33rd Canadian Nuclear Society / Canadian Nuclear Association Student Conference*, Calgary, Canada, 2009.

Leung, K. H., Hummel, D. W., Muhana, A., Spencer, J. H., Ball, M. R., Morreale, A. C., Statham, B. A., Bao, F., McDonald, M. H. and Novog, D. R., Thermal-Hydraulics & Safety Analysis Research, *Poster Presentation to the CANDU Owners Group*, Ottawa, Canada, 2009.

Hummel, D. W., Leung, K. H., and Novog, D. R., Code Validation and Verification, *Poster Presentation to the CANDU Owners Group*, Ottawa, Canada, 2009.

Leung, K. H, Kovtonyuk, A., Petruzzi, A., D'Auria, F., and Novog D. R., UNIPI BFBT Benchmark Result Submissions, *BFBT-6*, State College, United States of America, 2009.

Technical Reports

Leung K., Petruzzi, A., D'Auria, F., *UNIPI BFBT Phase I – Ex 4 Submission*, GRNSPG NT, Pisa, Italy, 2009.

Leung K., Petruzzi, A., D'Auria, F., *Application of CIAU to BFBT Benchmark: Phase 1 – Ex 4*, GRNSPG NT 641, Pisa, Italy, 2008.

REFERENCES

[1] International Atomic Energy Agency, Nuclear Power Reactors in the World – 2008 Edition, International Atomic Energy Agency, Vienna, Austria, 2008.

[2] Luxat, J.C., Safety Analysis Technology: Evolution, Revolution and the Drive to Re-Establish Margins. Proc. 21st Annual Conference of the Canadian Nuclear Society, Toronto, Canada, 2000.

[3] Luxat, J.C., Engineering Physics 4NE3 Notes, McMaster University, Hamilton, Canada, 2007.

[4] Leung, L. K. H., Engineering Physics UN0804 Notes, McMaster University, Whitby, Canada, 2004.

[5] Duderstadt, J. and Hamilton, L., Nuclear Reactor Analysis, John Wiley & Sons, New York, 1976.

[6] Neykov, B., et. al., NUPEC BWR Full-Size Fine-Mesh Bundle Test (BFBT) Benchmark Volume I: Specifications, Organization for Economic Cooperation and Development / Nuclear Energy Agency, Paris, France, 2005.

[7] Hanna, B. N., CATHENA: A thermalhydraulic code for CANDU analysis. *Nuc. Eng. Des.*,180, pp. 113-131, 1998.

[8] RELAP5-3D© Code Manual Volume I: Code Structure, System Models and Solution Methods. Idaho National Laboratories, Idaho Falls, USA, 1999.

[9] Aksan, N., Overview of CSNI Separate Effects Test Facility Matrices for Validation of Best Estimate Thermal-Hydraulic Computer Codes. Proc. THICKET-2008, Pisa, Italy, 2008.

[10] SCDAP/RELAP/MOD3.2 Code Manual Volume II: Damage Progression Model Theory. Idaho National Laboratory, Idaho Falls, USA, October 1997.

[11] Lessons Learned From OECD/CSNI ISP on Small Break LOCA. Paris, France, 1997.

[12] Intercomparison and validation of computer codes for thermalhydraulic safety analysis of heavy water reactors. International Atomic Energy Agency Tecdoc 1395, Vienna, Austria, 2004.

[13] Shkarupa, A., et. al., Comparative RELAP5-3D analysis in support of the NPP DBA analysis in Ukraine. *Prog. Nucl. Energy*, 48, pp. 891-911, 2006.

[14] D'Auria, F., et. al., Deterministic Safety Technology for RBMK Reactors, *Science and Technology of Nuclear Installations*, vol. 2008, 2008.

[15] Mladin, M., Dupleac, D., Prisecaru, I., SCDAP/RELAP5 application to CANDU6 fuel channel analysis under postulated LLOCA/LOECC conditions, *Nuc. Eng. Des.*, 239, pp. 353-364, 2009.

[16] Kim, M., et. al., Enhancement of safety analysis capability for a CANDU-6 reactor using RELAP-CANDU/SCAN coupled code system, *Nuc. Tech.*, 156, pp. 159-167, 2006.

[17] Aragones, J. M., Basis for coupled 3-D neutronics and thermal-hydraulics, Proc. THICKET-2008, Pisa, Italy, 2008.

[18] Aumiller, D. L., Tomlinson, E. T., Weaver, W. L., An integrated RELAP5-3D and multiphase CFD code system utilizing a semi-implicit coupling technique, *Nuc. Eng. Des.*, 216, pp. 77-87, 2002.

[19] ASSERT-PV V3R1 Theory Manual. Atomic Energy of Canada Limited, Mississauga, Canada, 2007.

[20] Stewart, C. W., Wheeler, C. L. et. al., Cobra-IV: The Model and the Method. Battelle Pacific Northwest Laboratories, Richland, United States of America, July 1977.

[21] Yoo, Y., et. al., Development of a Subchannel Analysis Code MATRA Applicable to PWRs and ALWRs. *Journal of the Korean Nuclear Society*, 31, no. 3, pp. 314-327, 1999.

[22] Glück, M., Sub-channel analysis with F-COBRA-TF – Code validation and approaches to CHF prediction, *Nuc. Eng. Des.*, 237, pp. 655-667, 2007.

[23] Glück, M., Validation of the sub-channel code F-COBRA-TF Part I. Recalculation of single-phase and two-phase pressure loss measurements, *Nuc. Eng. Des.*, 238, pp. 2308-2316, 2008.

[24] Inoue, A., et. al., Void fraction distribution in BWR fuel assembly and evaluation of subchannel code, *J. Nuc. Sci. Tech.*, 32, pp. 629-640, 1995.

[25] ASSERT-PV V3R1 Program Abstract. Atomic Energy of Canada Limited, Mississauga, Canada, 2007.

[26] Park, J. W., A subchannel analysis of DUPIC fuel bundle for the CANDU reactor, *Annals of Nuclear Energy*, 26, pp. 29-46, 1999.

[27] Aounallah, Y. and Coddington, P., VIPRE-02 subchannel validation against NUPEC BWR void fraction data, *Nuc. Tech.*, 128, pp. 225-232, 1999.

[28] Burns, C. J. and Aumiller D. L., COBRA-IE evaluation by simulation of the NUPEC BWR full-size fine-mesh bundle tests (BFBT), Proc. BFBT-3, 16 pages, Pisa, Italy, 2006.

[29] Hwang, D. H., et al., Activities of KAERI BFBT benchmark team using MATRA, MARS(COBRA-TF) and CFX, Proc. BFBT-3, 16 pages, Pisa, Italy, 2006.

[30] Glück, M., Validation of the sub-channel code F-COBRA-TF Part II. Recalculation of void measurements, *Nuc. Eng. Des.*, 238, pp. 2317-2327, 2008.

[31] Acceptance Criteria for Emergency Core Cooling Systems for Light-Water Nuclear Power Reactors, 10 CFR 50.46, U.S. Federal Register.

[32] D'Auria, F., et. al., State of the art in using best estimate calculation tools in nuclear technology, *Nuc. Eng. Tech.*, 38, pp. 11-36, 2006.

[33] Swiler, L. P., Paez, T., and Mayes, R., Epistemic Uncertainty Quantification Tutorial, *Proc.* IMAC XXVII Conference and Exposition on Structural Dynamics, Orlando, United States of America, 2009.

[34] Boyack, B., Duffey, R., Griffith, P., Lelouche, G., Levy, S., Rohatgi, R., Wilson, G., Wulff, W., and Zuber, N., Quantifying Reactor Safety Margins, Application of Code Scaling, Applicability, and Uncertainty Evalution Methodology to a Large-Break, Loss-of-Coolant Accident, NUREG/CR-5249, United States Nuclear Regulatory Commission, Washington, United States of America, 1989.

[35] D'Auria, F., and Giannotti, W., Development of a code with the capability of internal assessment of uncertainty, *Nuc. Tech.*, 131, pp. 159 – 196, 2000.

[36] Petruzzi A., et. al., Methodology of internal assessment of uncertainty and extension to neutron kinetics/thermal-hydraulics coupled codes, *Nuc. Sci. Eng.*, 149, pp.211-236 (2005).

[37] Salah, A. B., et. al., Uncertainty and sensitivity analyses of the Kozloduy pump trip test using coupled thermal-hydraulic 3D kinetics code, *Nuc. Eng. Des.*, 236, pp 1240-1255, 2006.

[38] de Crécy, A., et. al., Uncertainty and sensitivity analysis of the LOFT L2-5 test: Results of the BEMUSE programme, *Nuc. Eng. Des.*, 238, pp. 3561-3578, 2008.

[39] Galetti, M. R., Regulatory scenario for the acceptance of uncertainty analysis methodologies for the LB-LOCA and the Brazilian approach, *Science and Technology of Nuclear Installations*, 2008, 7 pages, 2008.

[40] Guba, A., Makai, M., and Pal, L., Statistical aspects of best estimate method – I, *Reliability Engineering & System Safety*, 80, pp. 217-232, 2003.

[41] Glaser, H., GRS method of uncertainty and sensitivity evaluation of code results and applications, *Science and Technology of Nuclear Installations*, vol 2008, 7 pages, 2008.

[42] Avramova, M., Ivanov, K., Krzyakacz-Hausmann, B., Velkov, K., Pautz, A., and Perin, Y., Uncertainty analysis of COBRA-TF void distribution predictions for the OECD/NRC BFBT benchmark, Proceedings of the International Conference of Mathematics, Computational Methods & Reactor Physics, Saratoga Springs, United States of America, 2009.

[43] Srivastava, A., Lele, H. G., Ghosh, A. K., and Kushwaha, H. S., Uncertainty analysis of LBLOCA for advanced heavy water reactor, *Annals of Nuclear Energy*, 35, pp. 323-334, 2008.

[44] Frepoli, C., An overview of Westinghouse realistic large break LOCA evaluation model, *Science and Technology of Nuclear Installations*, vol 2008, 15 pages, 2008.

[45] Crowe, T. C., Elger, D. F., Roberson, J. A., Engineering Fluid Mechanics. 7th Edition, John Wiley and Sons, Toronto, 2001.

[46] Zigrang, D. J., and Sylvester, N. D., Explicit approximations to the solution of Colebrook's friction factor equation, *AIChE Journal*, 28, pp. 514-515, 1982.

[47] Haaland, S. E., Simple and explicit formulas for the friction factor in turbulent pipe flow, *Journal of Fluids Engineering*, 105, pp. 89-90, 1983.

[48] Churchill, S. W. and Usagi, R., A general expression for the correlation of rates of transfer and other phenomena, *AIChE Journal*, 18, pp. 1121-1128, 1972.

[49] Romeo, E., Royo, C., and Monzon, A., Improved explicit equations for estimation of the friction factor in rough and smooth pipes, *Chemical Engineering Journal*, 86, pp. 269-374, 2002.

[50] Collier, J. G., and Thome, J. R., Convective Boiling and Condensation, Oxford Science Publications, New York, United States of America, 2001.

[51] Carey, V. P., Liquid-Vapor Phase Change Phenomena, Hemisphere Publications, United States of America, 1992.

[52] Chen, J. C., Correlation for boiling heat transfer to saturated fluids in convective flow, *Ind. Eng. Chem. Process Des. Dev.*, 5, pp. 322-329, 1966.

[53] Ahmad, S. Y., Axial distribution of bulk temperature and void fraction in a heated channel with inlet subcooling, *Journal of Heat Transfer*, 92, pp 595-609, 1970.

[54] Coddington, P., and Macian, R., A study of the performance of void fraction correlations used in the context of drift-flux two-phase flow models, *Nuc. Eng. Des.*, 215, pp 199-216, 2002.

[55] Hibiki, T., and Ishii, M., Distribution parameter and drift velocity of drift-flux model in bubbly flow, *International J. of Heat and Mass Transfer*, 45, pp 702-721, 2002.

[56] Goda, H., et. al., Drift-flux model for downward two-phase flow, *International J. of Heat and Mass Transfer*, 46, pp 4835-4844, 2003.

[57] Lahey, R. T., Shiralkar, B. S., Radcliffe, D. W., Two-Phase Flow and Heat Transfer in Multirod Geometries: Subchannel and Pressure Drop Measurements in a Nine-Rod Bundle for Diabetic and Adiabatic Conditions, General Electric Company, San Jose, United States of America, 1970.

[58] Kok, H. V., et. al., Subchannel void-fraction measurements in a 6 × 6 rod bundle using a simple gamma-transmission method, *Intl. J. of Multiphase Flow*, 27, pp. 147-170, 2001.

[59] Yun, B. J., et. al., Flow structure of subcooled boiling water flow in a subchannel of 3 × 3 rod bundles, *J. Nuc. Sci. Tech.*, 45, no. 5, pp 402-422, 2008.

[60] Shirai, H., ,et. al., Analytical study on detailed void distributions inside BWR fuel bundle under turbine trip event considering time-dependent pin power distributions, *J. Nuc. Sci. Tech.*, 39, no. 11, pp 1152-1161, 2002.

[61] Incropera, F. P. and DeWitt, D. P., Introduction to Heat Transfer, John Wiley and Sons, Toronto, Canada, 1996.

[62] Blander, M., Bubble nucleation in liquids, *Advances in Colloid and Interface Science,* 10, pp. 1-32, 1979.

[63] Lahey, R. T. and Moody, J. F., The Thermal-hydraulics of a Boiling Water Nuclear Reactor, American Nuclear Society, New York, United States of America, 1979.

[64] Tye, P., Teyssedou, A., Tapucu, A., An investigation of the constitutive relations for intersubchannel transfer mechanisms in horizontal flows as applied in the ASSERT-4 subchannel code, *Nuc. Eng. Des.*, 149, pp. 207-220, 1994.

[65] Ishii, M. and Hibiki, T., Thermo-Fluid Dynamics of Two-Phase Flow, Springer Science, New York, USA, 2006.

[66] Wilks, S. S., Determination of sample sizes for setting tolerance limits, *The Annals of Mathematical Statistics*, 12, pp. 91-96, 1941.

[67] Wilks, S. S., Statistical prediction with special reference to the problem of tolerance limits, *The Annals of Mathematical Statistics*, 13, pp. 400-409, 1942.

[68] Wilks, S. S., Order Statistics, *Bulletin of the American Mathematical Society*, 54, pp. 6–50, 1948.

[69] Wald, A., An extension of Wilks' method for setting tolerance limits, *The Annals of Mathematical Statistics*, 14, pp.45-55, 1943.

[70] The RELAP5-3D© Code Development Team, RELAP5-3D© Code Manual Volume IV: Models and Correlations. Idaho National Laboratories, Idaho Falls, USA, 1999.

[71] Aounallah, Y., A separate-effect-based new appraisal of convective boiling and its suppression, *J. Nuc. Sci. and Tech.*, 45, pp. 149-159, 2008.

[72] Carlucci, L. N., Hammouda, N., and Rowe, D. S., Two-phase turbulent mixing and buoyancy drift in rod bundles,*Nuc. Eng. Des.*, 227, pp 64-84, 2004.

[73] F. Aydogan, L. Hochreiter, K. Ivanov, M. Martin, H. Utsuno, E. Satori, *NUPEC BWR Full-Size Fine-Mesh Bundle Test (BFBT) Benchmark. Volume II:*

Uncertainty and Sensitivity Analyses of Void Distribution and Critical Power - Specification, NEA/NSC/DOC(2007)21.

[74] Kovtonyuk, A., Petruzzi, A., D'Auria, F., RELAP5-3D Analysis of OECD-NEA/NRC BFBT, *Gruppo di Ricerca Nucleare San Piero a Grado*, GRNSPG NT 640, Pisa, Italy, 2007.

APPENDIX A NOMENCLATURE

General

Symbol	Meaning	Symbol	Meaning
A	Area [m^2]	μ	Viscosity [Pas]
a_i	Interfacial Area [m^2]	P	Pressure [Pa]
β	Confidence Level [%]	Ψ	Transport Quantity
χ	Lockhart-Martinelli Parameter	φ	Flux
c_p	Heat Capacity [J/kg]	φ	Two Phase Friction Multiplier
d_h	Hydraulic Diameter [m]	q"	Heat Flux [W/m^2]
g	Gravitational Acceleration [m/s^2]	q	Power [W]
G	Mass Flux [kg/m^2s]	ρ	Density [kg/m^3]
γ	Coverage Level [%]	σ	Surface Tension [N/m]
Γ	Mass Transfer Rate [kg/s]	t	Time [s]
f	Friction Factor	T	Temperature [K] or [°C]
h_{fg}	Latent heat of vapourization [kJ/kg]	τ	Viscous Stress Tensor
h_L	Head Loss	u	Internal Energy [J]
J	Current [Ψ/s]	v	Velocity [m/s]
K	Loss Coefficient	x	Distance [m]
k	Conductivity [W/mK]	z	Elevation [m]

Dimensionless Numbers

Dimensionless Numbers	
Re	Measure of flow turbulence
Pr	Ratio of viscous to thermal diffusion rates
Nu	Ratio of convective to conductive heat transfer rate
Fr	Ratio of inertial to gravitational forces
We	Ratio of inertia to surface tension

APPENDIX B ABBREVIATIONS & ACRONYMS

Acronym	Meaning	Definition
-----	Rostechnadzor	Russian Regulatory Body
AECL	Atomic Energy of Canada Limited	Canadian NPP Vendor / R&D Organization
ANL	Argonne National Laboratory	US DoE Lab - Near Chicago
ANS	American Nuclear Society	-----
ASSERT	Advanced Solution of Subchannel Equations in Reactor Thermalhydraulics	Canadian Subchannel Code
ATHLET	Analysis of Thermal-Hydraulics LEaks and Transients	German TH System Code
BWR	Boiling Water Reactor	Reactor Type
CAMP	Code Application and Maintenance Programme	International Group - Codes
CANDU	CANada Deuterium Uranium	Reactor Brand
CATHARE	Code for Analysis of Thermal-Hydraulics during Accident of Reactor safety Evaluation	French TH System Code
CATHENA	Canadian Algorithm for THErmal-hydraulic Network Analysis	Canadian TH System Code
CCFL	Counter Current Flow Limiting	-----
CFD	Computational Fluid Dynamics	Branch of fluid dynamics… involving computers.
CFX	-----	Commercial CFD Code
CHF	Critical Heat Flux	TH Phenomena
CNS	Canadian Nuclear Society	-----
COBRA	COolant Boiling in Rod Arrays	US Subchannel Code
CSNI	Committee on the Safety of Nuclear Installations	International Organization
DNB	Departure from Nucleate Boiling	TH Phenomena
ECC	Emergency Core Coolant	-----
FIREBIRD	-----	Canadian TH System Code
FLUENT	-----	Commercial CFD Code
GRS	Gesellschaft fur Anlagen- und Reaktorsicherheit	German Company
HEU	Highly Enriched Uranium	Uranium with > 20 wt% ^{235}U.
IAEA	International Atomic Energy Agency	International Organization
ICONE	International Conference on Nuclear Engineering	Conference
IETF	Integral Effects Test Facility	Experimental Facility Type
ISP	International Standard Problem	-----
JAEA	Japan Atomic Energy Agency	Japanese R&D Organization

KAERI	Korea Atomic Energy Research Institute	Korean R&D Organization
KINS	Korean Institute of Nuclear Safety	Korean Consulting Company
LBLOCA	Large Break Loss of Coolant Accident	A Large LOCA
LEU	Low Enriched Uranium	Uranium at < 20 wt% ^{235}U.
LMFBR	Liquid Metal Fast Breeder Reactor	Reactor Type
LOCA	Loss of Coolant Accident	Reactor "Event"
LORC	Loss of Reactor Control	Reactor "Event"
LWR	Light Water Reactor	Reactor Type
MANTRA	Multichannel ANalyzer for steady states and Transients in Rod Arrays	Korean Subchannel Code
MARS	Multi-dimensional Analysis of Reactor Safety	Korean TH System Code based on RELAP
MNR	McMaster Nuclear Reactor	Research Reactor
MODTURC-CLAS	MODerator-TURbulent Circulation - Co-Located Advanced Solution	Canadian CFD Code
NEA	Nuclear Energy Agency	International Organization
NPP	Nuclear Power Plant	-----
NURETH	NUclear REactor Thermal-Hydrulics	Conference
PARCS	Purdue Advanced Reactor Core Simulator	Reactor Physics Code
PHWR	Pressurized Heavy Water Reactor	Reactor Type
PSA	Probabilistic Safety Analysis	-----
PWR	Pressurized Water Reactor	Reactor Type
RELAP	Reactor Excursion and Leak Analysis Program	TH System Code
SBLOCA	Small Break Loss of Coolant Accident	A Small LOCA
SETF	Separate Effects Test Facility	Experimental Facility Type
SEU	Slightly Enriched Uranium	Uranium at 0.9 - 2.0wt% ^{235}U
SMIRT	Structural Mechanics in Reactor Technology	Conference
SOPHT	Simulation of Primary Heat Transport	Canadian System Code
THICKET	-----	Seminar
TRAC	Transient Reactor Analysis Code	TH System Code
TRACE	TRAC/RELAP Advanced Computational Engine	TH System Code
VIPRE	Versatile Internals and Component Program for Reactors	US Subchannel Code
VVER	Vodo-Vodyanoi Energetichesky Reactor	Russian PWR Type
WIMS	-----	Reactor Physics Code
WWER	See VVER.	-----

APPENDIX C RELAP THEORY & EQUATIONS

The RELAP code family is built upon the two-fluid model, and solves the six equations as described in Section 3.4.2. The following sections summarize as briefly as possible the formulation of the two-fluid model which RELAP uses.

Mass Conservation Equations

The one-dimensional mass conservation equations for RELAP are provided as equations (1) and (2), while the mass jump condition is equation (3) [8]. The one-dimensional mass conservation equations consist of three terms for each phase which are briefly explained in

Table 34. The three-dimensional equations are only applicable to the multidimensional component, and will not be stated here for the sake of brevity.

$$\frac{\partial}{\partial t}\left(\alpha_g \rho_g\right)+\frac{1}{A}\frac{\partial}{\partial x}\left(\alpha_g \rho_g v_g A\right)=\Gamma_g \tag{1}$$

$$\frac{\partial}{\partial t}\left(\alpha_f \rho_f\right)+\frac{1}{A}\frac{\partial}{\partial x}\left(\alpha_f \rho_f v_f A\right)=\Gamma_f \tag{2}$$

$$\Gamma_f=-\Gamma_g \tag{3}$$

Table 34 - RELAP5 Mass Conservation Terms [8].

Term	Meaning
$\frac{\partial}{\partial t}\left(\alpha_k \rho_k\right)$	Accounts for the rate at which mass which accumulates or depletes in the control volume.

$\frac{1}{A}\frac{\partial}{\partial x}(\alpha_k \rho_k v_k A)$	Net mass advection term into the control volume of phase k.
Γ_k	Volumetric rate of mass generation or destruction of phase k from condensation or evaporation.

Momentum Conservation Equations

The momentum conservation equations are provided for the vapour (4) and fluid (5) phases, as is the inter-phasic jump equation (6) [8].

$$\begin{aligned}\alpha_g \rho_g A\frac{\partial v_g}{\partial t}+\frac{1}{2}\alpha_g \rho_g \frac{\partial v_g^2}{\partial x} = &-\alpha_g A\frac{\partial P}{\partial x}+\alpha_g \rho_g B_x A-(\alpha_g \rho_g A)FWG(v_g)\\ &+\Gamma_g A(v_{gI}-v_g)-(\alpha_g \rho_g A)FIG(v_g-v_f)\\ &-C\alpha_g \alpha_f \rho_m A\left[\frac{\partial(v_g-v_f)}{\partial t}+v_f\frac{\partial v_g}{\partial x}-v_g\frac{\partial v_f}{\partial x}\right]\end{aligned} \tag{4}$$

$$\begin{aligned}\alpha_f \rho_f A\frac{\partial v_f}{\partial t}+\frac{1}{2}\alpha_f \rho_f \frac{\partial v_f^2}{\partial x} = &-\alpha_f A\frac{\partial P}{\partial x}+\alpha_f \rho_f B_x A-(\alpha_f \rho_f A)FWG(v_f)\\ &+\Gamma_g A(v_{fI}-v_f)-(\alpha_f \rho_f A)FIF(v_f-v_g)\\ &-C\alpha_f \alpha_g \rho_m A\left[\frac{\partial(v_f-v_g)}{\partial t}+v_g\frac{\partial v_f}{\partial x}-v_f\frac{\partial v_g}{\partial x}\right]\end{aligned} \tag{5}$$

$$\begin{aligned}&\Gamma_g A v_{gI}-(\alpha_g \rho_g A)FIG(v_g-v_f)-C\alpha_g \alpha_f \rho_m A\left(\frac{\partial(v_g-v_f)}{\partial t}\right)\\ &=\Gamma_g A v_{fI}+(\alpha_f \rho_f A)FIF(v_f-v_g)+C\alpha_f \alpha_g \rho_m A\left(\frac{\partial(v_f-v_g)}{\partial t}\right)\end{aligned} \tag{6}$$

Table 35 - RELAP5 Momentum Conservation Terms [8].

Term	Meaning
$\alpha_k \rho_k A \frac{\partial v_k}{\partial t}$	Rate of momentum change.
$\frac{1}{2}\alpha_k \rho_k \frac{\partial v_k^2}{\partial x}$	Net momentum advection term into the control volume in phase k.
$-\alpha_k A \frac{\partial P}{\partial x}$	Force exerted per unit length due to the pressure gradient.
$\alpha_k \rho_k B_x A$	Body forces – e.g. gravity.
$(\alpha_k \rho_k A) FWG(v_k)$	Wall friction induced on phase k – Momentum sink.
$\Gamma_g A(v_{gI} - v_g)$	Momentum transfer to/from the other phase.
$(\alpha_g \rho_g A) FIG(v_g - v_f)$	Interfacial drag – Momentum sink.
$C\alpha_g \alpha_f \rho_m A\left[\frac{\partial(v_g - v_f)}{\partial t} + v_f \frac{\partial v_g}{\partial x} - v_g \frac{\partial v_f}{\partial x}\right.$	Force due to virtual mass; is flow regime dependent.

Energy Conservation Equations

Energy conservation equations are listed for both the vapour (7) and fluid (8) phases, as is the jump equation (9) [8].

$$\frac{\partial}{\partial t}(\alpha_g \rho_g U_g) + \frac{1}{A}\frac{\partial}{\partial x}(\alpha_g \rho_g U_g v_g A) = -P\frac{\partial \alpha_g}{\partial t} - \frac{P}{A}\frac{\partial}{\partial x}(\alpha_g v_g A) + Q_{wg} + Q_{ig} + \Gamma_{ig} h_g^* + \Gamma_w h_g + DISS_g \quad (7)$$

$$\frac{\partial}{\partial t}(\alpha_f \rho_f U_f) + \frac{1}{A}\frac{\partial}{\partial x}(\alpha_f \rho_f U_f v_f A) = -P\frac{\partial \alpha_f}{\partial t} - \frac{P}{A}\frac{\partial}{\partial x}(\alpha_f v_f A) + Q_{wf} + Q_{if} + \Gamma_{ig} h_f^* + \Gamma_w h_f + DISS_f \quad (8)$$

$$Q_{ig} + Q_{if} + \Gamma_{ig}\left(h_g^* - h_f^*\right) + \Gamma_w\left(h_g - h_f\right) = 0 \tag{9}$$

Table 36 - RELAP5 Energy Conservation Terms [8].

Term	Meaning
$\frac{\partial}{\partial t}\left(\alpha_g \rho_g U_g\right)$	Time rate of change of the internal energy.
$\frac{1}{A}\frac{\partial}{\partial x}\left(\alpha_g \rho_g U_g v_g A\right.$	Net internal energy advection term into the control volume in phase k.
$-P\frac{\partial \alpha_g}{\partial t}$	Work done for void formation.
$-\frac{P}{A}\frac{\partial}{\partial x}\left(\alpha_g v_g A\right)$	Interfacial energy
Q_{wg}	Wall heat transfer rate per unit volume.
Q_{ig}	Heat transferred across the fluid-vapour interface.
$\Gamma_{ig} h_g^*$	Enthalpy term from vapour generation in the bulk portion of the fluid.
$\Gamma_w h_g$	Enthalpy term from vapour generation in the near-wall region.
$DISS_k$	Represents the energy dissipated in phase k due to friction.

APPENDIX D ASSERT THEORY & EQUATIONS

The ASSERT codes were developed by AECL to analyze the unique two-phase flow phenomena found in horizontal orientation of CANDU fuel channels. ASSERT-PV is a specialized subchannel code and uses a heavily modified formulation of the drift-flux model containing mass, momentum and energy equations for a mixture, as well as energy equations for both the vapour and liquid phases [19]. The representation of the subchannels is done using individual equations for the axial and lateral momentum terms which are linked [19].

Mass Conservation Equations

ASSERT represents the mass conservation equation in terms of a mixture, hence only one equation (1) is required [19]. Attention should be drawn to equation (2), as F is defined as the total mixture flow rate, and is referred to again subsequently.

$$\frac{\partial}{\partial t}\left(A\Delta x\rho_m\right)+\frac{\partial}{\partial x}\left(\Delta xF\right)+\sum_k W_k=0 \tag{1}$$

$$F=\left(1-\alpha_g\right)A\rho_f v_f+\alpha_g A\rho_g v_g \tag{2}$$

Table 37 - ASSERT Mass Conservation Terms [19]

Term	Meaning
$\frac{\partial}{\partial t}(V\rho_m)$	Mass storage term.
$\frac{\partial}{\partial x}(\Delta x F)$	Net mass advected into / out of the control volume axially.
$\sum_k W_k$	Net mass flow entering / exiting the control volume from lateral connections.

Momentum Conservation Equations

Two sets of momentum conservation equations are used by ASSERT: one mixture equation (3) for the axial flow and one mixture equation (4) for the lateral flows [19].

$$\frac{\partial}{\partial t}(\Delta x F)+\frac{\partial}{\partial x}\left[\Delta x\left(F_f U_f + F_g U_g\right)\right] = -A\Delta x\frac{\partial P}{\partial x} - \sum_k\left[W_f U_f + W_g U_g\right]_k + \sum_k\left[W_f' \Delta U_f + W_g' \Delta U_g\right]_k - AK_U|F|F + \rho A\Delta x g_x \quad (3)$$

Table 38 - ASSERT Momentum Conservation Terms [19]

Term	Meaning
$\frac{\partial}{\partial t}(\Delta x F)$	Momentum storage term.
$\frac{\partial}{\partial x}\left[\Delta x\left(F_f U_f + F_g U_g\right)\right]$	Net mixture momentum advected into / out of the control volume axially.
$-A\Delta x\frac{\partial P}{\partial x}$	Momentum source due to the force applied as a result the pressure gradient.
$-\sum_k\left[W_f U_f + W_g V_g\right]_k$	Lateral momentum transfer.
$\sum_k\left[W_f' \Delta U_f + W_g' \Delta U_g\right]_k$	Lateral momentum advected into cell.

$-AK_U\|F\|F$	Axial momentum form losses.
$\rho A\Delta x g_x$	Body forces – e.g. gravity.

The lateral momentum equation is given as:

$$A\Delta x\rho\frac{\partial}{\partial t}(V)+\frac{\partial}{\partial x}(\Delta xFV)-V\frac{\partial}{\partial x}(\Delta xF)=-A\Delta x\frac{\partial P}{\partial y}+\bar{S}\Delta xK_Y|W|W + \frac{\partial}{\partial x}\left(A\Delta x\frac{W_f'\Delta U_f+W_g'\Delta U_g}{S\Delta x}\right)+\rho A\Delta x g_y \quad (4)$$

Energy Conservation Equations

$$\Delta xA\rho_m\frac{\partial h}{\partial t}+\Delta x\frac{\partial\left(F_fh_f+F_gh_g\right)}{\partial x}-\Delta xh\left[\frac{\partial F_f}{\partial x}+\frac{\partial F_g}{\partial x}\right]+\sum_k\left[W_gh_g+W_fh_f\right]_k - h\sum_k(W)_k-\sum_k\left(W_g'\Delta h_g+W_f'\Delta h_f\right)_k-\Psi_{i,n}q_{wn}=0 \quad (5)$$

Table 39 - ASSERT Energy Conservation Terms [19]

Term	Meaning
$\Delta xA\rho_m\frac{\partial h}{\partial t}$	Energy storage term.
$\Delta x\frac{\partial\left(F_fh_f+F_gh_g\right)}{\partial x}$	Axial energy advection
$-\Delta xh\left[\frac{\partial F_f}{\partial x}+\frac{\partial F_g}{\partial x}\right]$	Axial energy advection

$\sum_k \left[W_g h_g + W_f h_f \right]_k$	Lateral energy advection.
$-h \sum_k \left(W \right)_k$	Lateral energy advection.
$-\sum_k \left(W_g' \Delta h_g + W_f' \Delta h_f \right)_k$	Lateral energy advection.
$-\Psi_{i,n} q_{wn}$	Heat source/sink term.

APPENDIX E SUBCHANNEL & JUNCTION DIMENSIONS

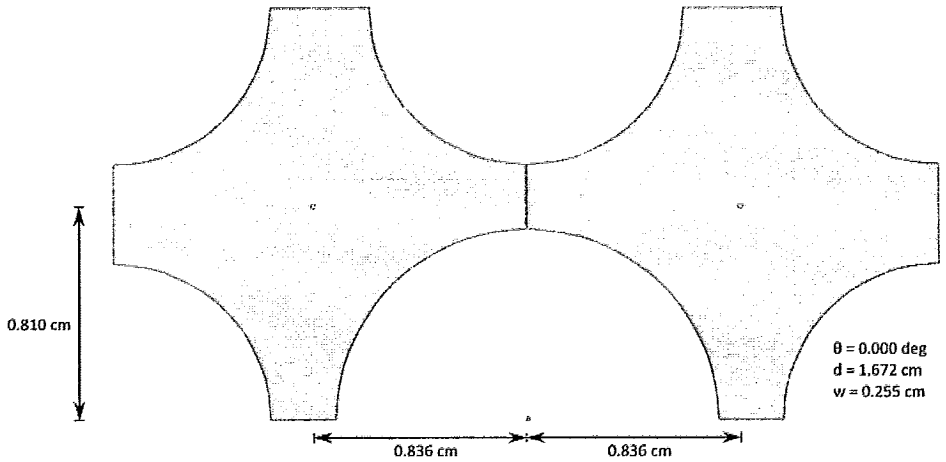

Figure 55 - Junction Type: "1 Water - 1 Water"

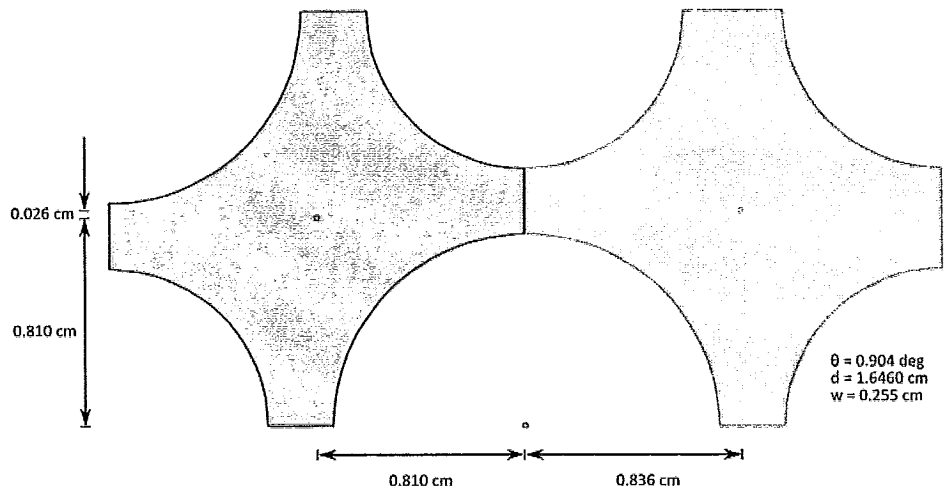

Figure 56 - Junction Type: "Central - 1 Water"

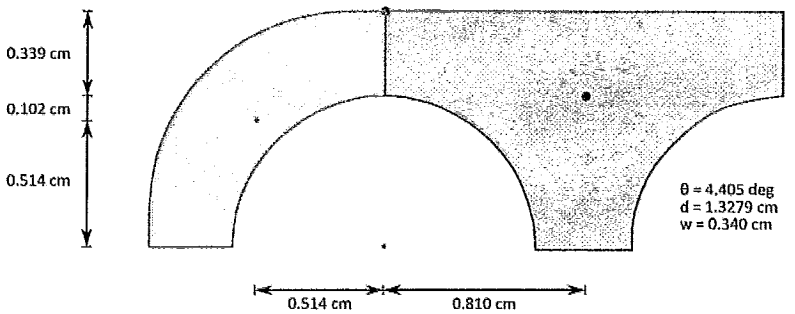

Figure 57 - Junction Type: "Corner - Side"

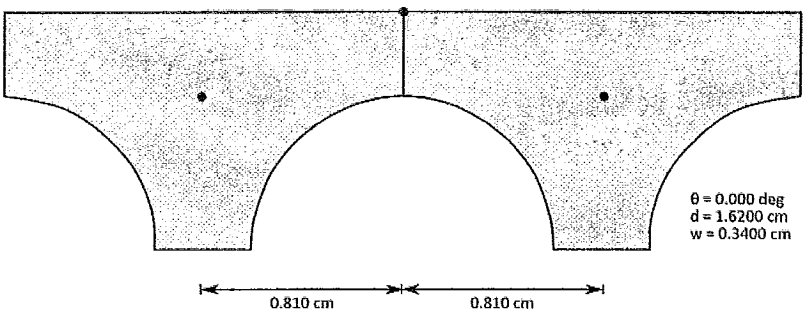

Figure 58 - Junction Type: "Side - Side"

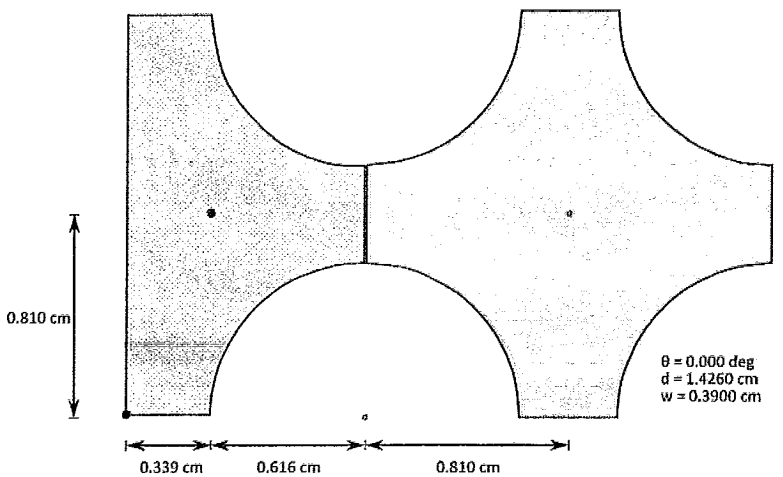

Figure 59 - Junction Type: "Side - Typical"

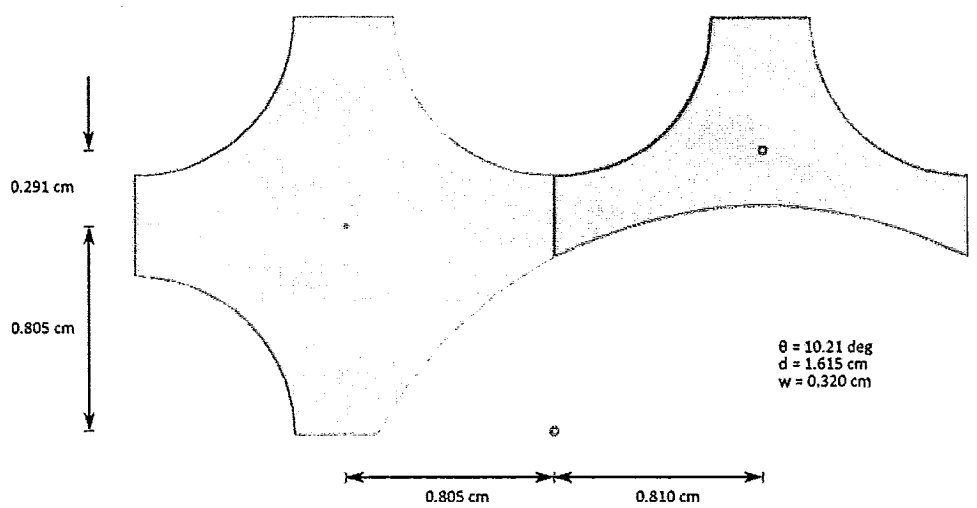

Figure 60 - Junction Type: "High Burnup Adjacent – High Burnup Diagonal"

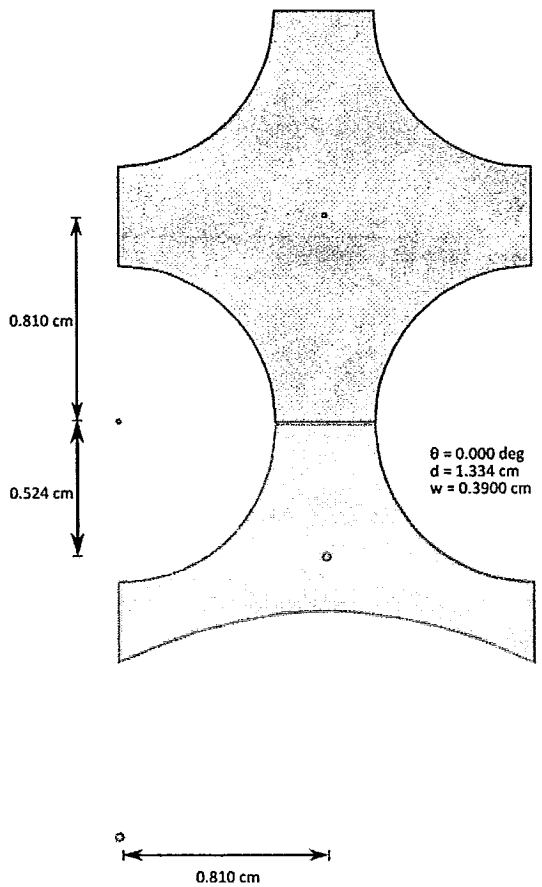

Figure 61 - Junction Type: "High Burnup Adjacent - Typical"

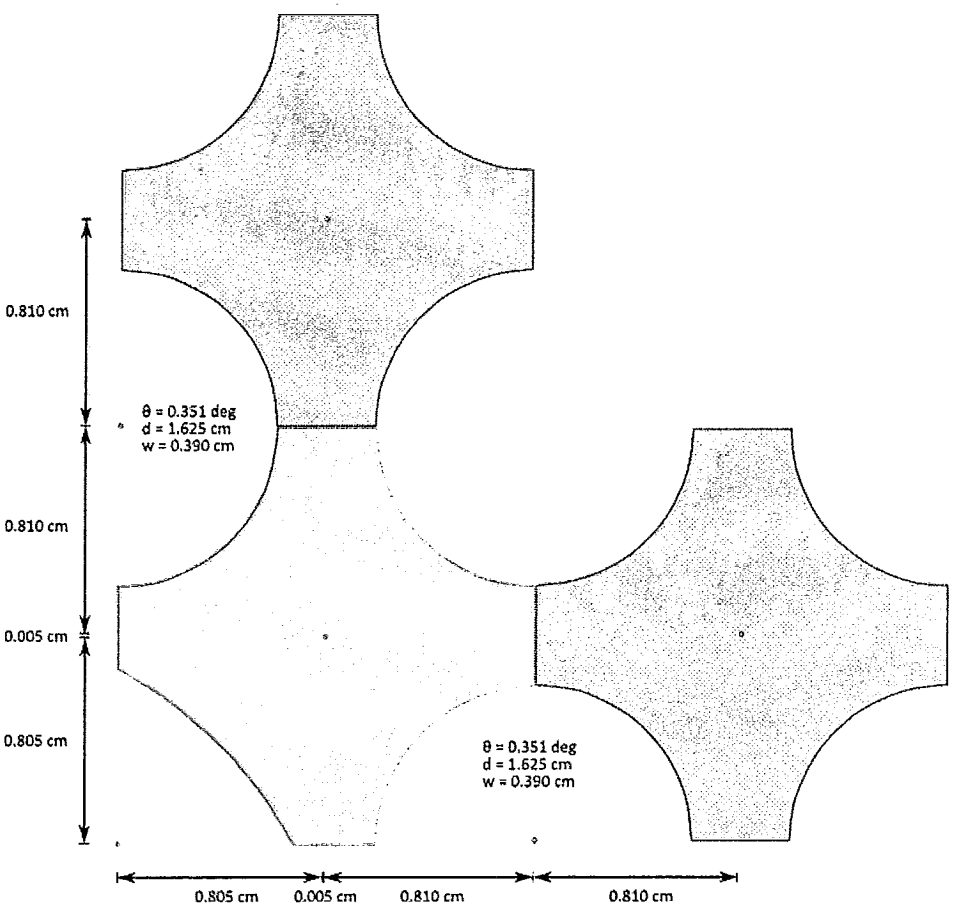

Figure 62 - Junction Type: "High Burnup Diagonal - Typical"

APPENDIX F MATERIAL PROPERTIES

Fuel Rod Properties

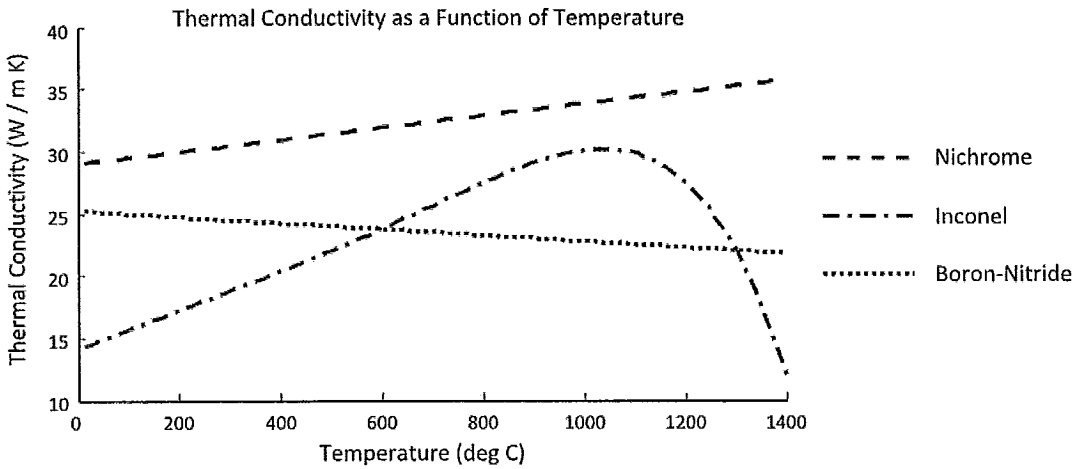

Figure 63 - Thermal Conductivity of Fuel Rod Materials

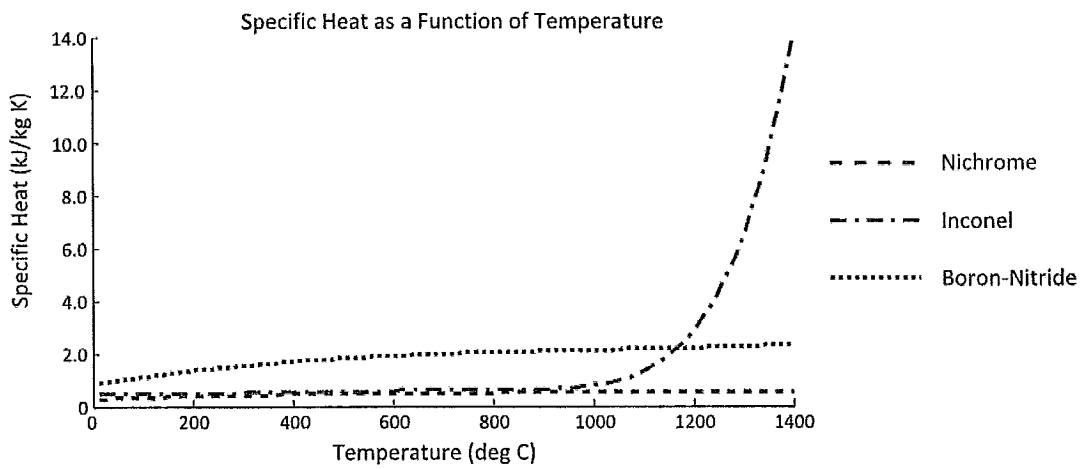

Figure 64 - Specific Heat of Fuel Rod Materials

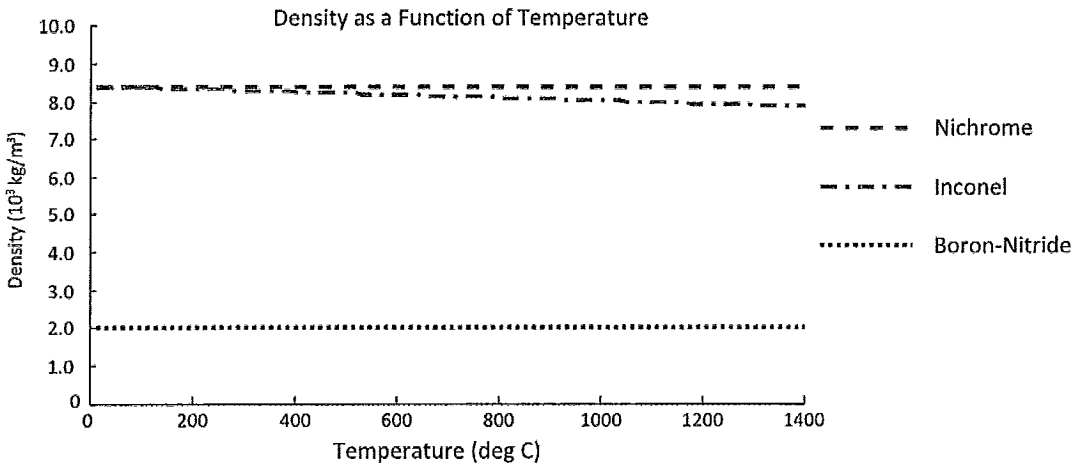

Figure 65 - Density of Fuel Rod Materials

APPENDIX G CIAU CODE DESCRIPTION

Rather than provide a meaningless appendix with the code used for the application of the CIAU method, this section provides a summary of the functions written in Table 40 and three of the important data structures being passed in Table 41, Table 42, and Table 43. For interested parties, a copy of the code is available from the Department of Engineering Physics at McMaster University.

Table 40 - MATLAB Functions Created for CIAU

File	Purpose
addPoint.m	Adds a single subchannel/experimental pair to a hypercube.
buildCubes.m	Creates a 1D array of hypercubes based on the cube boundaries read.
calcCubeStats.m	Calculates the statistical measures used by the CIAU method for each hypercube to generate uncertainty bounds.
calcPowerDist.m	Calculates the power to a single subchannel by summing the contributions of one-quarter of all adjacent rods.
CIAU.m	Builds and error database and applies the CIAU method to a set of simulated results. Main Program.
determineCubeID.m	Determines the index of the hypercube which a datapoint belongs to.
dumpLine.m	Prints a line to the screen and the output file.
newExpData.m	Builds a structure for a single set of experimental conditions.
newHyperCube.m	Builds a structure for a single hypercube with empty/default values.
normalize.m	Normalizes a parameter.
parse_strip.m	Reads a RELAP strip file (voidg) and returns an array with the void fraction at each subchannel.
readASSERTOut.m	Reads a single ASSERT output file and returns an array with the void fraction of each subchannel.
readCubeBoundaries.m	Reads a text file containing the hypercube subdivisions (normalized). Returns a structure containing the boundaries.
readExp.m	Reads in all experimental files in the specified directory. Returns an array containing the experimental void fraction for each subchannel for each test found.

readExpConditions.m	Reads the experimental conditions for one experiment from the files provided by the benchmark team.
readExpVoid.m	Reads a single experimental void fraction file.
readNormBoundaries.m	Reads a text file containing the boundaries containing the range of experimental conditions. Used to normalize the boundaries of the hypercubes.
readPowerProfile.m	Reads a text file containing the relative power distribution of the bundle.
readSim.m	Reads in all simulated files in the specified directory. Returns an array containing the simulated void fraction for each subchannel for each test found.

Table 41 - Data Structure explanation of inputData

Structure Name	Purpose
inputData	Stores/Passes Run-time options
testDir	Directory where the simulated data is located (relative)
expDir	Directory where the BFBT experimental data files are located (relative)
testFile	Root Name of the file containing the simulated data. The program will search for testFileXX in the testDir directory, where XX is an integer between 1 and numExpFiles
expFile	Root Name of the file containing the experimental data. The program will search for expFileXX in the expDir directory, where XX is an integer between 1 and numExpFiles
markedSimFile	Simulated File to apply the uncertainty bounds to.
markedExpFile	Corresponding experimental file to markedSimFile. Used to compare if simulated uncertainty bounds encompass experimental points.
normalizeFile	Name of the file with the normalization parameters.
powerFile	Name of the file containing the planar power profile
cubeFile	Name of the file containing the cube boundaries.

numExpFiles	The number of experimental files to search for. Integer values from 1 to numExpFiles.
flowArea	Flow area in [m^2]
activeRods	Number of active rods in the bundle.
doStats	Flag for alpha & beta stats. Set to 1 to perform statistical analysis; 0 otherwise.
exp_pos_err	Experimental error in the positive direction.
exp_neg_err	Experimental error in the negative direction.
boundMethod	Method to bound simulated points. Set to 'v4'
dataType	Flag to determine whether RELAP or ASSERT files are read. ['RELAP' | 'ASSERT']

Table 42 - Data structure explanation for expData

Structure Name	Purpose
expData	Stores/Passes Contents of 1 Experimental Case
P_IN	Inlet Pressure [MPa]
P_OUT	Outlet Pressure [MPa]
SUBCOOL	Inlet Subcooling [kJ/kg]
MASSFLUX	Inlet Mass Flux [kg/m^2s]
POWER	Bundle Power [MW]
VOID	Experimental Subchannel Void Fraction. 9 x 9 array

power_profile	Subchannel Power Distribution.
massflux_profile	Mass flux profile distribution. Not used.
fileName	Name of file read.
P_NORM	Not used.
SUBCOOL_NORM	Not used.
POWERMASS_NORM	Not used.

Table 43 - Data structure explanation for cube

Structure Name	Purpose
cube	Stores/Passes data from 1 hypercube.
pressureIndex	Pressure bin (coordinate) which the hypercube belongs to
powerIndex	Power bin (coordinate) which the hypercube belongs to
subCoolIndex	Subcooling bin (coordinate) which the hypercube belongs to
voidIndex	Void Fraction bin (coordinate) which the hypercube belongs to
testPointExp	Experimental Subchannel Void Fraction (1D array from 1 to numData)
testPointSim	Simulated Subchannel Void Fraction (1D array from 1 to numData)
testPointList	Coordinate Map for each test point. In the format AAXY, where AA is the experiment #, X is the x-coordinate and Y is the y-coordinate.
testPointAQ	Accuracy Quantity of the test point. Does NOT account for experimental error.

testPointAQv4	Accuracy Quantity of the test point. Accounts for experimental error.
avgAQ	Average of testPointAQ in the hypercube.
avgAQv4	Average of testPointAQv4 in the hypercube.
sdAQ	Sample standard deviation of testPointAQ in the hypercube.
sdAQv4	Sample standard deviation of testPointAQv4 in the hypercube.
Sj	Standard Deviation to test average ratio
Psj	Weighting Factor accounting for the dispersion of points.
Pj	Weighting factor accounting for experimental uncertainty & scaling.
AY	Term for calculating the uncertainty band size.
ES	Term for calculating the uncertainty band size.
ESIGMA	Term for calculating the uncertainty band size.
linearIndex	Index of the hypercube.
numTests	Number of different tests classified to this hypercube. Counter
testIndex	Index of the tests in the hypercube. Counter.
numDataFromTest	Array of data points from a specific test.
numData	Total number of data points in the hypercube

APPENDIX H RELAP INPUT DECK

```
= BFBT Nodalization
* Test 4101-86
*
*
* nodalization developed by Andriy Kovtonyuk October 2007
* modified by Ken Leung October 2008
*
100 new transnt
101 run * inp-chk
*
* 105 5. 6.
* 110 air
* 115 0.4 0.6
*
*
* TIME STEPS TABLE
*
* min mj re
201 0.00010 1.00E-14 0.00001 7003 100 10 10
202 0.00100 1.00E-14 0.0001 7003 100 10 10
203 0.01000 1.00E-14 0.001 7003 1000 10 10
204 0.10000 1.00E-14 0.005 7003 1000 20 20
205 1.00000 1.00E-14 0.01 7003 1000 20 20
206 10.00000 1.00E-14 0.01 7003 100 200 200
207 30.00000 1.00E-14 0.05 7003 10 40 100
208 40.00000 1.00E-14 0.1 7003 10 20 50
209 80.00000 1.00E-14 0.1 7003 10 20 100
* 208 100.00000 1.00E-14 0.1 7003 100 500 5000
* 203 1000000 5.00E-07 0.01 7003 500 2500 2500
*
* MINOR EDIT REQUEST
*
*
*
* TRIPs TABLE
*
* triggering for core inlet flow == Start problem
410 time 0 ge null 0 0. 1 -1.0
*
* power control Start
420 time 0 gt null 0 20.0 1 -1.0
*
* end program
* 430 time 0.0 gt null 0 100. 1 -1.0
* 440 430
*
*
* Hydraulics Components
*
*
* * * * * * * * * * * * *
* CORE INLET TANK (600)
* * * * * * * * * * * * *
*
6000000 coreita1 tmdpvol
6000101 1.00E+01 0.5 0.0 0.0 90.0 0.5 0.0 0.0 10
6000200 3
6000201 0.0 8.819E+06 564.65
*
* * * * * * * * * * * * *
* CORE INLET FLOW (625)
```

```
* * * * * * * * * * * * *
*
6250000 coreiju tmdpjun
6250101 600000000 650000000 0.0 0
6250200 1 410
6250201 -1.0 0.0 0.0 0.0
6250202 5.0 0.0 0.0 0.0
6250203 10.0 15.28 0.0 0.0
6250204 1.00E+06 15.28 0.0 0.0
*
* * * * * * * * * * * * *
* * * * * * * * * * * * * *
* SNGVOL (650)
* * * * * * * * * * * * *
*
6500000 invol snglvol
6500101 0.0097809 0.25 0.0 0.0 90.0 0.25 0.0 0.0 0
6500200 3 8.814E+06 564.65
*
* * * * * * * * * * * * *
* MULTIJUNCTION TMDVOL TO LOWER PLENUM FUEL BUNDLE (700)
* * * * * * * * * * * * *
*
7000000 lp-bt-jn mtpljun
7000001 80 1
7000011 650000000 750101015 0.0 0.001 0.001 0 1.0 1.0 1.0 0 100000 0 9
7000021 650000000 750102015 0.0 0.001 0.001 0 1.0 1.0 1.0 0 100000 0 18
7000031 650000000 750103015 0.0 0.001 0.001 0 1.0 1.0 1.0 0 100000 0 27
7000041 650000000 750104015 0.0 0.001 0.001 0 1.0 1.0 1.0 0 100000 0 36
7000051 650000000 750105015 0.0 0.001 0.001 0 1.0 1.0 1.0 0 100000 0 40
7000061 650000000 750605015 0.0 0.001 0.001 0 1.0 1.0 1.0 0 100000 0 44
7000071 650000000 750106015 0.0 0.001 0.001 0 1.0 1.0 1.0 0 100000 0 53
7000081 650000000 750107015 0.0 0.001 0.001 0 1.0 1.0 1.0 0 100000 0 62
7000091 650000000 750108015 0.0 0.001 0.001 0 1.0 1.0 1.0 0 100000 0 71
7000101 650000000 750109015 0.0 0.001 0.001 0 1.0 1.0 1.0 0 100000 0 80
7001011 0.0 0.0 9
7001021 0.0 0.0 18
7001031 0.0 0.0 27
7001041 0.0 0.0 36
7001051 0.0 0.0 45
7001061 0.0 0.0 54
7001071 0.0 0.0 63
7001081 0.0 0.0 72
7001091 0.0 0.0 80
*
*
* * * * * * * * * * * * *
* LOWER PLENUM FUEL BUNDLE (750)
* * * * * * * * * * * * *
*
7500000 lpplenFB multid
7500001 9 9 6 1 0 0.0 0
7500101 0.00955 1
7500102 0.0162 8
7500103 0.00955 9
7500201 0.00955 1
7500202 0.0162 8
7500203 0.00955 9
7500301 0.25 6
7501001 1 9 1 9 1 6 0.615982 100 0 0 0
7501002 1 1 1 1 1 6 0.523695 100 0 0 0
7501003 9 9 1 1 1 6 0.523695 100 0 0 0
7501004 1 1 9 9 1 6 0.523695 100 0 0 0
7501005 9 9 9 9 1 6 0.523695 100 0 0 0
7501006 2 8 2 8 1 6 0.547238 100 0 0 0
7501007 4 6 4 6 1 6 0.564218 100 0 0 0
7501008 4 4 5 5 1 6 0.254946 100 0 0 0
```

```
7501009 6 6 5 5 1 6 0.254946 100 0 0 0
7501010 5 5 4 4 1 6 0.254946 100 0 0 0
7501011 5 5 6 6 1 6 0.254946 100 0 0 0
7502001 1 9 1 9 1 6 0.0 0.01295 0.0 0.0201 0.0 0.01073
7502002 1 9 2 8 1 6 0.0 0.0201 0.0 0.01295 0.0 0.01073
7502003 1 1 1 1 1 6 0.0 0.00968 0.0 0.00968 0.0 0.00754
7502004 9 9 1 1 1 6 0.0 0.00968 0.0 0.00968 0.0 0.00754
7502005 9 9 9 9 1 6 0.0 0.00968 0.0 0.00968 0.0 0.00754
7502006 1 1 9 9 1 6 0.0 0.00968 0.0 0.00968 0.0 0.00754
7502007 2 8 2 8 1 6 0.0 0.0201 0.0 0.0201 0.0 0.01487
7502008 4 5 4 5 1 6 0.0 0.01728 0.0 0.01728 0.0 0.01267
7502009 5 6 5 6 1 6 0.0 0.01728 0.0 0.01728 0.0 0.01267
7502010 5 5 5 5 1 6 0.0 0.01446 0.0 0.01446 0.0 0.0107
7503001 1 8 1 9 1 6 2 0.356021 0.0 0.0 0 0.0068
7503002 1 8 2 8 1 6 2 0.240741 0.0 0.0 0 0.0078
7503003 4 5 4 6 1 6 2 0.197778 0.0 0.0 0 0.0051
7503004 4 5 5 5 1 6 2 0.000000 0.0 0.0 0 0.0051
7503005 1 9 1 8 1 6 4 0.356021 0.0 0.0 0 0.0068
7503006 2 8 1 8 1 6 4 0.240741 0.0 0.0 0 0.0078
7503007 4 6 4 5 1 6 4 0.197778 0.0 0.0 0 0.0051
7503008 5 5 4 5 1 6 4 0.000000 0.0 0.0 0 0.0051
7503009 1 9 1 9 1 4 6 0.615982 0.0 0.0 0 0.01073
7503010 1 9 1 9 5 5 6 0.615982 0.0 0.0 0 0.01073
7503011 1 1 1 1 1 4 6 0.52369464 0.0 0.0 0 0.00754
7503012 1 1 1 1 5 5 6 0.52369464 0.0 0.0 0 0.00754
7503013 9 9 1 1 1 4 6 0.52369464 0.0 0.0 0 0.00754
7503014 9 9 1 1 5 5 6 0.52369464 0.0 0.0 0 0.00754
7503015 9 9 9 9 1 4 6 0.52369464 0.0 0.0 0 0.00754
7503016 9 9 9 9 5 5 6 0.52369464 0.0 0.0 0 0.00754
7503017 1 1 9 9 1 4 6 0.52369464 0.0 0.0 0 0.00754
7503018 1 1 9 9 5 5 6 0.52369464 0.0 0.0 0 0.00754
7503019 2 8 2 8 1 4 6 0.54723789 0.0 0.0 0 0.01487
7503020 2 8 2 8 5 5 6 0.54723789 0.0 0.0 0 0.01487
7503021 4 5 4 5 1 4 6 0.492090334 0.0 0.0 0 0.01267
7503022 4 5 4 5 5 5 6 0.492090334 0.0 0.0 0 0.01267
7503023 5 6 5 6 1 4 6 0.492090334 0.0 0.0 0 0.01267
7503024 5 6 5 6 5 5 6 0.492090334 0.0 0.0 0 0.01267
7503025 5 5 5 5 1 4 6 0.436942778 0.0 0.0 0 0.0107
7503026 5 5 5 5 5 5 6 0.436942778 0.0 0.0 0 0.0107
7506001 1 9 1 9 1 3 3 8.800E+06 564.65
7506002 1 9 1 9 4 6 3 8.780E+06 564.65
7507001 1 8 1 9 1 6 2 0.0 0.0
7507002 1 9 1 8 1 6 4 0.0 0.0
7507003 1 9 1 9 1 5 6 0.0 0.0
*
*
* * * * * * * * * * * * *
* MULTIJUNCTION LOWER PLENUM TO ACTIVE FUEL BUNDLE (775)
* * * * * * * * * * * * *
*
7750000 lp-bt-jn mtpljun
7750001 81 1
7750011 750101066 800101015 0.0 0.001 0.001 0 1.0 1.0 1.0 100000 100000 0 9
7750021 750102066 800102015 0.0 0.001 0.001 0 1.0 1.0 1.0 100000 100000 0 18
7750031 750103066 800103015 0.0 0.001 0.001 0 1.0 1.0 1.0 100000 100000 0 27
7750041 750104066 800104015 0.0 0.001 0.001 0 1.0 1.0 1.0 100000 100000 0 36
7750051 750105066 800105015 0.0 0.001 0.001 0 1.0 1.0 1.0 100000 100000 0 45
7750061 750106066 800106015 0.0 0.001 0.001 0 1.0 1.0 1.0 100000 100000 0 54
7750071 750107066 800107015 0.0 0.001 0.001 0 1.0 1.0 1.0 100000 100000 0 63
7750081 750108066 800108015 0.0 0.001 0.001 0 1.0 1.0 1.0 100000 100000 0 72
7750091 750109066 800109015 0.0 0.001 0.001 0 1.0 1.0 1.0 100000 100000 0 81
7751011 0.0 0.0 9
7751021 0.0 0.0 18
7751031 0.0 0.0 27
7751041 0.0 0.0 36
7751051 0.0 0.0 45
7751061 0.0 0.0 54
```

```
7751071 0.0 0.0 63
7751081 0.0 0.0 72
7751091 0.0 0.0 81
*
*
* * * * * * * * * * * * *
* ACTIVE FUEL BUNDLE (800)
* * * * * * * * * * * * *
*
8000000 acFB multid
8000001 9 9 12 1 0 0.0 0
8000101 0.00955 1
8000102 0.0162 8
8000103 0.00955 9
8000201 0.00955 1
8000202 0.0162 8
8000203 0.00955 9
8000301 0.309 12
8001001 1 9 1 9 1 12 0.615982 100 0 0 0
8001002 1 1 1 1 1 12 0.523695 100 0 0 0
8001003 9 9 1 1 1 12 0.523695 100 0 0 0
8001004 1 1 9 9 1 12 0.523695 100 0 0 0
8001005 9 9 9 9 1 12 0.523695 100 0 0 0
8001006 2 8 2 8 1 12 0.547238 100 0 0 0
8001007 4 6 4 6 1 12 0.564218 100 0 0 0
8001008 4 4 5 5 1 12 0.254946 100 0 0 0
8001009 6 6 5 5 1 12 0.254946 100 0 0 0
8001010 5 5 4 4 1 12 0.254946 100 0 0 0
8001011 5 5 6 6 1 12 0.254946 100 0 0 0
8002001 1 9 1 9 1 12 0.0 0.01295 0.0 0.0201 0.0 0.01073
8002002 1 9 2 8 1 12 0.0 0.0201 0.0 0.01295 0.0 0.01073
8002003 1 1 1 1 1 12 0.0 0.00968 0.0 0.00968 0.0 0.00754
8002004 9 9 1 1 1 12 0.0 0.00968 0.0 0.00968 0.0 0.00754
8002005 9 9 9 9 1 12 0.0 0.00968 0.0 0.00968 0.0 0.00754
8002006 1 1 9 9 1 12 0.0 0.00968 0.0 0.00968 0.0 0.00754
8002007 2 8 2 8 1 12 0.0 0.0201 0.0 0.0201 0.0 0.01487
8002008 4 5 4 5 1 12 0.0 0.01728 0.0 0.01728 0.0 0.01267
8002009 5 6 5 6 1 12 0.0 0.01728 0.0 0.01728 0.0 0.01267
8002010 5 5 5 5 1 12 0.0 0.014460 0.0 0.01446 0.0 0.0107
8003001 1 8 1 9 1 12 2 0.356021 0.0 0.0 0 0.0068
8003002 1 8 2 8 1 12 2 0.240741 0.0 0.0 0 0.0078
8003003 4 5 4 6 1 12 2 0.197778 0.0 0.0 0 0.0051
8003004 4 5 5 5 1 12 2 0.000000 0.0 0.0 0 0.0051
8003005 1 9 1 8 1 12 4 0.356021 0.0 0.0 0 0.0068
8003006 2 8 1 8 1 12 4 0.240741 0.0 0.0 0 0.0078
8003007 4 6 4 5 1 12 4 0.197778 0.0 0.0 0 0.0051
8003008 5 5 4 5 1 12 4 0.000000 0.0 0.0 0 0.0051
8003009 1 9 1 9 1 11 6 0.615982 0.0 0.0 0 0.01073
8003010 1 9 1 9 1 1 6 0.615982 1.6 1.6 0 0.01073
8003011 1 9 1 9 3 3 6 0.615982 1.6 1.6 0 0.01073
8003012 1 9 1 9 5 5 6 0.615982 1.6 1.6 0 0.01073
8003013 1 9 1 9 6 6 6 0.615982 1.6 1.6 0 0.01073
8003014 1 9 1 9 8 8 6 0.615982 1.6 1.6 0 0.01073
8003015 1 9 1 9 10 10 6 0.615982 1.6 1.6 0 0.01073
8003016 1 9 1 9 11 11 6 0.615982 1.6 1.6 0 0.01073
8003017 1 1 1 1 1 11 6 0.52369464 0.0 0.0 0 0.00754
8003018 1 1 1 1 1 1 6 0.52369464 1.6 1.6 0 0.00754
8003019 1 1 1 1 3 3 6 0.52369464 1.6 1.6 0 0.00754
8003020 1 1 1 1 5 5 6 0.52369464 1.6 1.6 0 0.00754
8003021 1 1 1 1 6 6 6 0.52369464 1.6 1.6 0 0.00754
8003022 1 1 1 1 8 8 6 0.52369464 1.6 1.6 0 0.00754
8003023 1 1 1 1 10 10 6 0.52369464 1.6 1.6 0 0.00754
8003024 1 1 1 1 11 11 6 0.52369464 1.6 1.6 0 0.00754
8003025 9 9 1 1 1 11 6 0.52369464 0.0 0.0 0 0.00754
8003026 9 9 1 1 1 1 6 0.52369464 1.6 1.6 0 0.00754
8003027 9 9 1 1 3 3 6 0.52369464 1.6 1.6 0 0.00754
8003028 9 9 1 1 5 5 6 0.52369464 1.6 1.6 0 0.00754
```

```
8003029 9 9 1 1 6 6 6 0.52369464 1.6 1.6 0 0.00754
8003030 9 9 1 1 8 8 6 0.52369464 1.6 1.6 0 0.00754
8003031 9 9 1 1 10 10 6 0.52369464 1.6 1.6 0 0.00754
8003032 9 9 1 1 11 11 6 0.52369464 1.6 1.6 0 0.00754
8003033 9 9 9 9 1 11 6 0.52369464 0.0 0.0 0 0.00754
8003034 9 9 9 9 1 1 6 0.52369464 1.6 1.6 0 0.00754
8003035 9 9 9 9 3 3 6 0.52369464 1.6 1.6 0 0.00754
8003036 9 9 9 9 5 5 6 0.52369464 1.6 1.6 0 0.00754
8003037 9 9 9 9 6 6 6 0.52369464 1.6 1.6 0 0.00754
8003038 9 9 9 9 8 8 6 0.52369464 1.6 1.6 0 0.00754
8003039 9 9 9 9 10 10 6 0.52369464 1.6 1.6 0 0.00754
8003040 9 9 9 9 11 11 6 0.52369464 1.6 1.6 0 0.00754
8003041 1 1 9 9 1 11 6 0.52369464 0.0 0.0 0 0.00754
8003042 1 1 9 9 1 1 6 0.52369464 1.6 1.6 0 0.00754
8003043 1 1 9 9 3 3 6 0.52369464 1.6 1.6 0 0.00754
8003044 1 1 9 9 5 5 6 0.52369464 1.6 1.6 0 0.00754
8003045 1 1 9 9 6 6 6 0.52369464 1.6 1.6 0 0.00754
8003046 1 1 9 9 8 8 6 0.52369464 1.6 1.6 0 0.00754
8003047 1 1 9 9 10 10 6 0.52369464 1.6 1.6 0 0.00754
8003048 1 1 9 9 11 11 6 0.52369464 1.6 1.6 0 0.00754
8003049 2 8 2 8 1 11 6 0.54723789 0.0 0.0 0 0.01487
8003050 2 8 2 8 1 1 6 0.54723789 1.6 1.6 0 0.01487
8003051 2 8 2 8 3 3 6 0.54723789 1.6 1.6 0 0.01487
8003052 2 8 2 8 5 5 6 0.54723789 1.6 1.6 0 0.01487
8003053 2 8 2 8 6 6 6 0.54723789 1.6 1.6 0 0.01487
8003054 2 8 2 8 8 8 6 0.54723789 1.6 1.6 0 0.01487
8003055 2 8 2 8 10 10 6 0.54723789 1.6 1.6 0 0.01487
8003056 2 8 2 8 11 11 6 0.54723789 1.6 1.6 0 0.01487
8003057 4 5 4 5 1 11 6 0.492090334 0.0 0.0 0 0.01267
8003058 4 5 4 5 1 1 6 0.492090334 1.6 1.6 0 0.01267
8003059 4 5 4 5 3 3 6 0.492090334 1.6 1.6 0 0.01267
8003060 4 5 4 5 5 5 6 0.492090334 1.6 1.6 0 0.01267
8003061 4 5 4 5 6 6 6 0.492090334 1.6 1.6 0 0.01267
8003062 4 5 4 5 8 8 6 0.492090334 1.6 1.6 0 0.01267
8003063 4 5 4 5 10 10 6 0.492090334 1.6 1.6 0 0.01267
8003064 4 5 4 5 11 11 6 0.492090334 1.6 1.6 0 0.01267
8003065 5 6 5 6 1 11 6 0.492090334 0.0 0.0 0 0.01267
8003066 5 6 5 6 1 1 6 0.492090334 1.6 1.6 0 0.01267
8003067 5 6 5 6 3 3 6 0.492090334 1.6 1.6 0 0.01267
8003068 5 6 5 6 5 5 6 0.492090334 1.6 1.6 0 0.01267
8003069 5 6 5 6 6 6 6 0.492090334 1.6 1.6 0 0.01267
8003070 5 6 5 6 8 8 6 0.492090334 1.6 1.6 0 0.01267
8003071 5 6 5 6 10 10 6 0.492090334 1.6 1.6 0 0.01267
8003072 5 6 5 6 11 11 6 0.492090334 1.6 1.6 0 0.01267
8003073 5 5 5 5 1 11 6 0.436942778 0.0 0.0 0 0.0107
8003074 5 5 5 5 1 1 6 0.436942778 1.6 1.6 0 0.0107
8003075 5 5 5 5 3 3 6 0.436942778 1.6 1.6 0 0.0107
8003076 5 5 5 5 5 5 6 0.436942778 1.6 1.6 0 0.0107
8003077 5 5 5 5 6 6 6 0.436942778 1.6 1.6 0 0.0107
8003078 5 5 5 5 8 8 6 0.436942778 1.6 1.6 0 0.0107
8003079 5 5 5 5 10 10 6 0.436942778 1.6 1.6 0 0.0107
8003080 5 5 5 5 11 11 6 0.436942778 1.6 1.6 0 0.0107
8006001 1 9 1 9 1 2 3 8.770E+06 564.65
8006002 1 9 1 9 3 4 3 8.750E+06 564.65
8006003 1 9 1 9 5 6 3 8.730E+06 564.65
8006004 1 9 1 9 7 8 3 8.710E+06 564.65
8006005 1 9 1 9 9 10 3 8.690E+06 564.65
8006006 1 9 1 9 11 12 3 8.670E+06 564.65
8007001 1 8 1 9 1 12 2 0.0 0.0
8007002 1 9 1 8 1 12 4 0.0 0.0
8007003 1 9 1 9 1 11 6 0.0 0.0
*
*
* * * * * * * * * * * * *
* MULTIJUNCTION ACTIVE FUEL BUNDLE TO UPPER PLENUM (875)
* * * * * * * * * * * * *
*
```

```
8750000 tp-up-jn mtpljun
8750001 81 1
8750011 800101126 900101015 0.0 0.001 0.001 0 1.0 1.0 1.0 100000 100000 0 9
8750021 800102126 900102015 0.0 0.001 0.001 0 1.0 1.0 1.0 100000 100000 0 18
8750031 800103126 900103015 0.0 0.001 0.001 0 1.0 1.0 1.0 100000 100000 0 27
8750041 800104126 900104015 0.0 0.001 0.001 0 1.0 1.0 1.0 100000 100000 0 36
8750051 800105126 900105015 0.0 0.001 0.001 0 1.0 1.0 1.0 100000 100000 0 45
8750061 800106126 900106015 0.0 0.001 0.001 0 1.0 1.0 1.0 100000 100000 0 54
8750071 800107126 900107015 0.0 0.001 0.001 0 1.0 1.0 1.0 100000 100000 0 63
8750081 800108126 900108015 0.0 0.001 0.001 0 1.0 1.0 1.0 100000 100000 0 72
8750091 800109126 900109015 0.0 0.001 0.001 0 1.0 1.0 1.0 100000 100000 0 81
8751011 0.0 0.0 9
8751021 0.0 0.0 18
8751031 0.0 0.0 27
8751041 0.0 0.0 36
8751051 0.0 0.0 45
8751061 0.0 0.0 54
8751071 0.0 0.0 63
8751081 0.0 0.0 72
8751091 0.0 0.0 81
*
* * * * * * * * * * * * *
* UPPER PLENUM FUEL BUNDLE (900)
* * * * * * * * * * * * *
*
9000000 upplenFB multid
9000001 9 9 6 1 0 0.0 0
9000101 0.00955 1
9000102 0.0162 8
9000103 0.00955 9
9000201 0.00955 1
9000202 0.0162 8
9000203 0.00955 9
9000301 0.15 1
9000302 0.25 6
9001001 1 9 1 9 1 6 0.615982 100 0 0 0
9001002 1 1 1 1 1 6 0.523695 100 0 0 0
9001003 9 9 1 1 1 6 0.523695 100 0 0 0
9001004 1 1 9 9 1 6 0.523695 100 0 0 0
9001005 9 9 9 9 1 6 0.523695 100 0 0 0
9001006 2 8 2 8 1 6 0.547238 100 0 0 0
9001007 4 6 4 6 1 6 0.564218 100 0 0 0
9001008 4 4 5 5 1 6 0.254946 100 0 0 0
9001009 6 6 5 5 1 6 0.254946 100 0 0 0
9001010 5 5 4 4 1 6 0.254946 100 0 0 0
9001011 5 5 6 6 1 6 0.254946 100 0 0 0
9002001 1 9 1 9 1 6 0.0 0.01295 0.0 0.0201 0.0 0.01073
9002002 1 9 2 8 1 6 0.0 0.0201 0.0 0.01295 0.0 0.01073
9002003 1 1 1 1 1 6 0.0 0.00968 0.0 0.00968 0.0 0.00754
9002004 9 9 1 1 1 6 0.0 0.00968 0.0 0.00968 0.0 0.00754
9002005 9 9 9 9 1 6 0.0 0.00968 0.0 0.00968 0.0 0.00754
9002006 1 1 9 9 1 6 0.0 0.00968 0.0 0.00968 0.0 0.00754
9002007 2 8 2 8 1 6 0.0 0.0201 0.0 0.0201 0.0 0.01487
9002008 4 5 4 5 1 6 0.0 0.01728 0.0 0.01728 0.0 0.01267
9002009 5 6 5 6 1 6 0.0 0.01728 0.0 0.01728 0.0 0.01267
9002010 5 5 5 5 1 6 0.0 0.01446 0.0 0.01446 0.0 0.0107
9003001 1 8 1 9 1 6 2 0.356021 0.0 0.0 0 0.0068
9003002 1 8 2 8 1 6 2 0.240741 0.0 0.0 0 0.0078
9003003 4 5 4 6 1 6 2 0.197778 0.0 0.0 0 0.0051
9003004 4 5 5 5 1 6 2 0.000000 0.0 0.0 0 0.0051
9003005 1 9 1 8 1 6 4 0.356021 0.0 0.0 0 0.0068
9003006 2 8 1 8 1 6 4 0.240741 0.0 0.0 0 0.0078
9003007 4 6 4 5 1 6 4 0.197778 0.0 0.0 0 0.0051
9003008 5 5 4 5 1 6 4 0.000000 0.0 0.0 0 0.0051
9003009 1 9 1 9 1 5 6 0.615982 0.0 0.0 0 0.01073
9003010 1 1 1 1 1 5 6 0.523695 0.0 0.0 0 0.00754
9003011 9 9 1 1 1 5 6 0.523695 0.0 0.0 0 0.00754
```

```
9003012 9 9 9 9 1 5 6 0.52369464 0.0 0.0 0 0.00754
9003013 1 1 9 9 1 5 6 0.52369464 0.0 0.0 0 0.00754
9003014 2 8 2 8 1 5 6 0.54723789 0.0 0.0 0 0.01487
9003015 4 5 4 5 1 5 6 0.492090334 0.0 0.0 0 0.01267
9003016 5 6 5 6 1 5 6 0.492090334 0.0 0.0 0 0.01267
9003017 5 5 5 5 1 5 6 0.436942778 0.0 0.0 0 0.0107
9006001 1 9 1 9 1 4 3 8.660E+06 564.65
9006002 1 9 1 9 5 6 3 8.640E+06 564.65
9007001 1 8 1 9 1 6 2 0.0 0.0
9007002 1 9 1 8 1 6 4 0.0 0.0
9007003 1 9 1 9 1 5 6 0.0 0.0
*
*
* * * * * * * * * * * * *
* DOME 1 LEVEL 1 (921): 101-108-157-164
* * * * * * * * * * * * *
*
9210000 d1-lvl1 branch
9210001 4 1
9210101 0.000191049 0.2 0.0 0.0 90.0 0.2 0.0 0.007543364 0
9210200 3 8.637E+06 564.65
9211101 900101066 921000000 0.0 0.001 10000.0 0
9212101 900109066 921000000 0.0 0.001 10000.0 0
9213101 900901066 921000000 0.0 0.001 10000.0 0
9214101 900909066 921000000 0.0 0.001 10000.0 0
9211201 0.0 0.0 0.0
9212201 0.0 0.0 0.0
9213201 0.0 0.0 0.0
9214201 0.0 0.0 0.0
*
*
* * * * * * * * * * * * *
* DOME 2 LEVEL 1 (931): 201-202-203-204-205-206-207
* * * * * * * * * * * * *
*
9310000 d2-lvl1 branch
9310001 7 1
9310101 0.00066709 0.2 0.0 0.0 90.0 0.2 0.0 0.0107316 0
9310200 3 8.637E+06 564.65
9311101 900209066 931000000 0.0 0.001 10000.0 0
9312101 900309066 931000000 0.0 0.001 10000.0 0
9313101 900409066 931000000 0.0 0.001 10000.0 0
9314101 900509066 931000000 0.0 0.001 10000.0 0
9315101 900609066 931000000 0.0 0.001 10000.0 0
9316101 900709066 931000000 0.0 0.001 10000.0 0
9317101 900809066 931000000 0.0 0.001 10000.0 0
9311201 0.0 0.0 0.0
9312201 0.0 0.0 0.0
9313201 0.0 0.0 0.0
9314201 0.0 0.0 0.0
9315201 0.0 0.0 0.0
9316201 0.0 0.0 0.0
9317201 0.0 0.0 0.0
*
*
* * * * * * * * * * * * *
* DOME 3 LEVEL 1 (932): 258-259-260-261-262-263-264
* * * * * * * * * * * * *
*
9320000 d3-lvl1 branch
9320001 7 1
9320101 0.00066709 0.2 0.0 0.0 90.0 0.2 0.0 0.0107316 0
9320200 3 8.637E+06 564.65
9321101 900201066 932000000 0.0 0.001 10000.0 0
9322101 900301066 932000000 0.0 0.001 10000.0 0
9323101 900401066 932000000 0.0 0.001 10000.0 0
9324101 900501066 932000000 0.0 0.001 10000.0 0
```

```
9325101 900601066 932000000 0.0 0.001 10000.0 0
9326101 900701066 932000000 0.0 0.001 10000.0 0
9327101 900801066 932000000 0.0 0.001 10000.0 0
9321201 0.0 0.0 0.0
9322201 0.0 0.0 0.0
9323201 0.0 0.0 0.0
9324201 0.0 0.0 0.0
9325201 0.0 0.0 0.0
9326201 0.0 0.0 0.0
9327201 0.0 0.0 0.0
*
*
* * * * * * * * * * * * *
* DOME 4 LEVEL 1 (933): 209-217-225-233-241-249-267
* * * * * * * * * * * * *
*
9330000 d4-lvl1 branch
9330001 7 1
9330101 0.00066709 0.2 0.0 0.0 90.0 0.2 0.0 0.0107316 0
9330200 3 8.637E+06 564.65
9331101 900102066 933000000 0.0 0.001 10000.0 0
9332101 900103066 933000000 0.0 0.001 10000.0 0
9333101 900104066 933000000 0.0 0.001 10000.0 0
9334101 900105066 933000000 0.0 0.001 10000.0 0
9335101 900106066 933000000 0.0 0.001 10000.0 0
9336101 900107066 933000000 0.0 0.001 10000.0 0
9337101 900108066 933000000 0.0 0.001 10000.0 0
9331201 0.0 0.0 0.0
9332201 0.0 0.0 0.0
9333201 0.0 0.0 0.0
9334201 0.0 0.0 0.0
9335201 0.0 0.0 0.0
9336201 0.0 0.0 0.0
9337201 0.0 0.0 0.0
*
*
* * * * * * * * * * * * *
* DOME 5 LEVEL 1 (934): 208-216-224-232-240-248-256
* * * * * * * * * * * * *
*
9340000 d5-lvl1 branch
9340001 7 1
9340101 0.00066709 0.2 0.0 0.0 90.0 0.2 0.0 0.0107316 0
9340200 3 8.637E+06 564.65
9341101 900902066 934000000 0.0 0.001 10000.0 0
9342101 900903066 934000000 0.0 0.001 10000.0 0
9343101 900904066 934000000 0.0 0.001 10000.0 0
9344101 900905066 934000000 0.0 0.001 10000.0 0
9345101 900906066 934000000 0.0 0.001 10000.0 0
9346101 900907066 934000000 0.0 0.001 10000.0 0
9347101 900908066 934000000 0.0 0.001 10000.0 0
9341201 0.0 0.0 0.0
9342201 0.0 0.0 0.0
9343201 0.0 0.0 0.0
9344201 0.0 0.0 0.0
9345201 0.0 0.0 0.0
9346201 0.0 0.0 0.0
9347201 0.0 0.0 0.0
*
*
* * * * * * * * * * * * *
* DOME 6 LEVEL 1 (941): 410-411-412-413-414-415-416
* * * * * * * * * * * * *
*
9410000 d6-lvl1 branch
9410001 7 1
9410101 0.001005319 0.2 0.0 0.0 90.0 0.2 0.0 0.0148666 0
```

```
9410200 3 8.637E+06 564.65
9411101 900208066 941000000 0.0 0.001 10000.0 0
9412101 900308066 941000000 0.0 0.001 10000.0 0
9413101 900408066 941000000 0.0 0.001 10000.0 0
9414101 900508066 941000000 0.0 0.001 10000.0 0
9415101 900608066 941000000 0.0 0.001 10000.0 0
9416101 900708066 941000000 0.0 0.001 10000.0 0
9417101 900808066 941000000 0.0 0.001 10000.0 0
9411201 0.0 0.0 0.0
9412201 0.0 0.0 0.0
9413201 0.0 0.0 0.0
9414201 0.0 0.0 0.0
9415201 0.0 0.0 0.0
9416201 0.0 0.0 0.0
9417201 0.0 0.0 0.0
*
*
* * * * * * * * * * * * *
* DOME 7 LEVEL 1 (942): 458-459-460-461-462-463-464
* * * * * * * * * * * * *
*
9420000 d7-lvl1 branch
9420001 7 1
9420101 0.001005319 0.2 0.0 0.0 90.0 0.2 0.0 0.0148666 0
9420200 3 8.637E+06 564.65
9421101 900202066 942000000 0.0 0.001 10000.0 0
9422101 900302066 942000000 0.0 0.001 10000.0 0
9423101 900402066 942000000 0.0 0.001 10000.0 0
9424101 900502066 942000000 0.0 0.001 10000.0 0
9425101 900602066 942000000 0.0 0.001 10000.0 0
9426101 900702066 942000000 0.0 0.001 10000.0 0
9427101 900802066 942000000 0.0 0.001 10000.0 0
9421201 0.0 0.0 0.0
9422201 0.0 0.0 0.0
9423201 0.0 0.0 0.0
9424201 0.0 0.0 0.0
9425201 0.0 0.0 0.0
9426201 0.0 0.0 0.0
9427201 0.0 0.0 0.0
*
*
* * * * * * * * * * * * *
* DOME 8 LEVEL 1 (943): 418-426-434-442-450
* * * * * * * * * * * * *
*
9430000 d8-lvl1 branch
9430001 5 1
9430101 0.000718085 0.2 0.0 0.0 90.0 0.2 0.0 0.0148666 0
9430200 3 8.637E+06 564.65
9431101 900207066 943000000 0.0 0.001 10000.0 0
9432101 900206066 943000000 0.0 0.001 10000.0 0
9433101 900205066 943000000 0.0 0.001 10000.0 0
9434101 900204066 943000000 0.0 0.001 10000.0 0
9435101 900203066 943000000 0.0 0.001 10000.0 0
9431201 0.0 0.0 0.0
9432201 0.0 0.0 0.0
9433201 0.0 0.0 0.0
9434201 0.0 0.0 0.0
9435201 0.0 0.0 0.0
*
*
* * * * * * * * * * * * *
* DOME 9 LEVEL 1 (944): 424-432-440-448-456
* * * * * * * * * * * * *
*
9440000 d9-lvl1 branch
9440001 5 1
```

```
9440101 0.000718085 0.2 0.0 0.0 90.0 0.2 0.0 0.0148666 0
9440200 3 8.637E+06 564.65
9441101 900807066 944000000 0.0 0.001 10000.0 0
9442101 900806066 944000000 0.0 0.001 10000.0 0
9443101 900805066 944000000 0.0 0.001 10000.0 0
9444101 900804066 944000000 0.0 0.001 10000.0 0
9445101 900803066 944000000 0.0 0.001 10000.0 0
9441201 0.0 0.0 0.0
9442201 0.0 0.0 0.0
9443201 0.0 0.0 0.0
9444201 0.0 0.0 0.0
9445201 0.0 0.0 0.0
*
*
* * * * * * * * * * * * *
* DOME 10 LEVEL 1 (951): 419-420-421-422-423-431-439-447
* * * * * * * * * * * * *
*
9510000 d10-lvl1 branch
9510001 8 1
9510101 0.001148936 0.2 0.0 0.0 90.0 0.2 0.0 0.0148666 0
9510200 3 8.637E+06 564.65
9511101 900307066 951000000 0.0 0.001 10000.0 0
9512101 900407066 951000000 0.0 0.001 10000.0 0
9513101 900507066 951000000 0.0 0.001 10000.0 0
9514101 900607066 951000000 0.0 0.001 10000.0 0
9515101 900707066 951000000 0.0 0.001 10000.0 0
9516101 900706066 951000000 0.0 0.001 10000.0 0
9517101 900705066 951000000 0.0 0.001 10000.0 0
9518101 900704066 951000000 0.0 0.001 10000.0 0
9511201 0.0 0.0 0.0
9512201 0.0 0.0 0.0
9513201 0.0 0.0 0.0
9514201 0.0 0.0 0.0
9515201 0.0 0.0 0.0
9516201 0.0 0.0 0.0
9517201 0.0 0.0 0.0
9518201 0.0 0.0 0.0
*
*
* * * * * * * * * * * * *
* DOME 11 LEVEL 1 (952): 427-435-443-451-452-453-454-455
* * * * * * * * * * * * *
*
9520000 d11-lvl1 branch
9520001 8 1
9520101 0.001148936 0.2 0.0 0.0 90.0 0.2 0.0 0.0148666 0
9520200 3 8.637E+06 564.65
9521101 900306066 952000000 0.0 0.001 10000.0 0
9522101 900305066 952000000 0.0 0.001 10000.0 0
9523101 900304066 952000000 0.0 0.001 10000.0 0
9524101 900303066 952000000 0.0 0.001 10000.0 0
9525101 900403066 952000000 0.0 0.001 10000.0 0
9526101 900503066 952000000 0.0 0.001 10000.0 0
9527101 900603066 952000000 0.0 0.001 10000.0 0
9528101 900703066 952000000 0.0 0.001 10000.0 0
9521201 0.0 0.0 0.0
9522201 0.0 0.0 0.0
9523201 0.0 0.0 0.0
9524201 0.0 0.0 0.0
9525201 0.0 0.0 0.0
9526201 0.0 0.0 0.0
9527201 0.0 0.0 0.0
9528201 0.0 0.0 0.0
*
*
* * * * * * * * * * * * *
```

```
* DOME 12 LEVEL 1 (961): 428-429-430-438-446
* * * * * * * * * * * * *
*
9610000 d12-lvl1 branch
9610001 5 1
9610101 0.000718085 0.2 0.0 0.0 90.0 0.2 0.0 0.0148666 0
9610200 3 8.637E+06 564.65
9611101 900406066 961000000 0.0 0.001 10000.0 0
9612101 900506066 961000000 0.0 0.001 10000.0 0
9613101 900606066 961000000 0.0 0.001 10000.0 0
9614101 900605066 961000000 0.0 0.001 10000.0 0
9615101 900604066 961000000 0.0 0.001 10000.0 0
9611201 0.0 0.0 0.0
9612201 0.0 0.0 0.0
9613201 0.0 0.0 0.0
9614201 0.0 0.0 0.0
9615201 0.0 0.0 0.0
*
*
* * * * * * * * * * * * *
* DOME 13 LEVEL 1 (962): 436-437-444-445
* * * * * * * * * * * * *
*
9620000 d13-lvl1 branch
9620001 3 1
9620101 0.000574468 0.2 0.0 0.0 90.0 0.2 0.0 0.0148666 0
9620200 3 8.637E+06 564.65
9621101 900405066 962000000 0.0 0.001 10000.0 0
* 9622101 900505066 962000000 0.0 0.001 10000.0 0
9622101 900404066 962000000 0.0 0.001 10000.0 0
9623101 900504066 962000000 0.0 0.001 10000.0 0
9621201 0.0 0.0 0.0
9622201 0.0 0.0 0.0
9623201 0.0 0.0 0.0
* 9624201 0.0 0.0 0.0
*
*
* * * * * * * * * * * * *
* DOME 1 LEVEL 2 (971): 921
* * * * * * * * * * * * *
*
9710000 d1-lvl2 branch
9710001 1 1
9710101 0.000191049 0.2 0.0 0.0 90.0 0.2 0.0 0.007543364 0
9710200 3 8.634E+06 564.65
9711101 921010000 971000000 0.0 0.001 10000.0 0
9711201 0.0 0.0 0.0
*
*
* * * * * * * * * * * * *
* DOME 2 LEVEL 2 (972): 931-932-933-934
* * * * * * * * * * * * *
*
9720000 d2-lvl2 branch
9720001 4 1
9720101 0.002668358 0.2 0.0 0.0 90.0 0.2 0.0 0.0107316 0
9720200 3 8.634E+06 564.65
9721101 931010000 972000000 0.0 0.001 10000.0 0
9722101 932010000 972000000 0.0 0.001 10000.0 0
9723101 933010000 972000000 0.0 0.001 10000.0 0
9724101 934010000 972000000 0.0 0.001 10000.0 0
9721201 0.0 0.0 0.0
9722201 0.0 0.0 0.0
9723201 0.0 0.0 0.0
9724201 0.0 0.0 0.0
*
*
```

```
* * * * * * * * * * * * *
* DOME 3 LEVEL 2 (973): 941-942-943-944
* * * * * * * * * * * * *
*
9730000 d3-lvl2 branch
9730001 4 1
9730101 0.003446808 0.2 0.0 0.0 90.0 0.2 0.0 0.0148666 0
9730200 3 8.634E+06 564.65
9731101 941010000 973000000 0.0 0.001 10000.0 0
9732101 942010000 973000000 0.0 0.001 10000.0 0
9733101 943010000 973000000 0.0 0.001 10000.0 0
9734101 944010000 973000000 0.0 0.001 10000.0 0
9731201 0.0 0.0 0.0
9732201 0.0 0.0 0.0
9733201 0.0 0.0 0.0
9734201 0.0 0.0 0.0
*
*
* * * * * * * * * * * * *
* DOME 4 LEVEL 2 (974): 951-952
* * * * * * * * * * * * *
*
9740000 d4-lvl2 branch
9740001 2 1
9740101 0.002297872 0.2 0.0 0.0 90.0 0.2 0.0 0.0148666 0
9740200 3 8.634E+06 564.65
9741101 951010000 974000000 0.0 0.001 10000.0 0
9742101 952010000 974000000 0.0 0.001 10000.0 0
9741201 0.0 0.0 0.0
9742201 0.0 0.0 0.0
*
*
* * * * * * * * * * * * *
* DOME 5 LEVEL 2 (975): 961-962
* * * * * * * * * * * * *
*
9750000 d5-lvl2 branch
9750001 2 1
9750101 0.001292553 0.2 0.0 0.0 90.0 0.2 0.0 0.0148666 0
9750200 3 8.634E+06 564.65
9751101 961010000 975000000 0.0 0.001 10000.0 0
9752101 962010000 975000000 0.0 0.001 10000.0 0
9751201 0.0 0.0 0.0
9752201 0.0 0.0 0.0
*
*
* * * * * * * * * * * * *
* DOME 1 LEVEL 3 (981): 971-972-973-974-975
* * * * * * * * * * * * *
*
9810000 d1-lvl3 branch
9810001 6 1
9810101 0.009951585 0.2 0.0 0.0 90.0 0.2 0.0 0.0148666 0
9810200 3 8.632E+06 564.65
9811101 971010000 981000000 0.0 0.001 10000.0 0
9812101 972010000 981000000 0.0 0.001 10000.0 0
9813101 973010000 981000000 0.0 0.001 10000.0 0
9814101 974010000 981000000 0.0 0.001 10000.0 0
9815101 975010000 981000000 0.0 0.001 10000.0 0
9816101 981010000 990000000 0.0 0.001 10000.0 0
9811201 0.0 0.0 0.0
9812201 0.0 0.0 0.0
9813201 0.0 0.0 0.0
9814201 0.0 0.0 0.0
9815201 0.0 0.0 0.0
9816201 0.0 0.0 0.0
*
```

```
*
* * * * * * * * * * * * *
* CORE OUTLET TANK (990)
* * * * * * * * * * * * *
*
9900000 coreota tmdpvol
9900101 1.00E+01 0.5 0.0 0.0 90.0 0.5 0.0 0.0 10
9900200 2
9900201 0.0 8.629E+06 1.0
*
*
* * * * * * * * * * * * *
* HEAT STRUCTURES
* * * * * * * * * * * * *
*
* ROD # 1 side 1
*
10011000 12 7 1 1 0.0
10011100 0 1
10011101 1 5.71E-04 1 1.08E-03 2 1.91E-03 2 3.08E-03
10011201 2 1
10011202 1 2
10011203 2 4
10011204 3 6
10011301 0.0 1
10011302 1.0 2
10011303 0.0 6
10011400 0
10011401 700.0 3
10011402 600.0 5
10011403 573.0 7
10011501 000000000 00000 0 1 0.0029850 12
10011601 800109011 10 1 1 0.0029850 12
10011701 100 0.0003993056 0.0 0.0 1
10011702 100 0.0003993056 0.0 0.0 2
10011703 100 0.0003993056 0.0 0.0 3
10011704 100 0.0003993056 0.0 0.0 4
10011705 100 0.0003993056 0.0 0.0 5
10011706 100 0.0003993056 0.0 0.0 6
10011707 100 0.0003993056 0.0 0.0 7
10011708 100 0.0003993056 0.0 0.0 8
10011709 100 0.0003993056 0.0 0.0 9
10011710 100 0.0003993056 0.0 0.0 10
10011711 100 0.0003993056 0.0 0.0 11
10011712 100 0.0003993056 0.0 0.0 12
10011900 0
10011901 0.019777 100.0 100.0 0.0 0.0 0.0 0.0 1.0 12
*
* ROD # 1 side 2
*
10012000 12 7 1 1 0.0
10012100 0 1
10012101 1 5.71E-04 1 1.08E-03 2 1.91E-03 2 3.08E-03
10012201 2 1
10012202 1 2
10012203 2 4
10012204 3 6
10012301 0.0 1
10012302 1.0 2
10012303 0.0 6
10012400 0
10012401 700.0 3
10012402 600.0 5
10012403 573.0 7
10012501 000000000 00000 0 1 0.0029850 12
10012601 800108011 10 1 1 0.0029850 12
10012701 100 0.0003993056 0.0 0.0 1
```

```
10012702 100 0.0003993056 0.0 0.0 2
10012703 100 0.0003993056 0.0 0.0 3
10012704 100 0.0003993056 0.0 0.0 4
10012705 100 0.0003993056 0.0 0.0 5
10012706 100 0.0003993056 0.0 0.0 6
10012707 100 0.0003993056 0.0 0.0 7
10012708 100 0.0003993056 0.0 0.0 8
10012709 100 0.0003993056 0.0 0.0 9
10012710 100 0.0003993056 0.0 0.0 10
10012711 100 0.0003993056 0.0 0.0 11
10012712 100 0.0003993056 0.0 0.0 12
10012900 0
10012901 0.019730 100.0 100.0 0.0 0.0 0.0 0.0 1.0 12
*
* ROD # 1 side 3
*
10013000 12 7 1 1 0.0
10013100 0 1
10013101 1 5.71E-04 1 1.08E-03 2 1.91E-03 2 3.08E-03
10013201 2 1
10013202 1 2
10013203 2 4
10013204 3 6
10013301 0.0 1
10013302 1.0 2
10013303 0.0 6
10013400 0
10013401 700.0 3
10013402 600.0 5
10013403 573.0 7
10013501 000000000 00000 0 1 0.0029850 12
10013601 800208011 10 1 1 0.0029850 12
10013701 100 0.0003993056 0.0 0.0 1
10013702 100 0.0003993056 0.0 0.0 2
10013703 100 0.0003993056 0.0 0.0 3
10013704 100 0.0003993056 0.0 0.0 4
10013705 100 0.0003993056 0.0 0.0 5
10013706 100 0.0003993056 0.0 0.0 6
10013707 100 0.0003993056 0.0 0.0 7
10013708 100 0.0003993056 0.0 0.0 8
10013709 100 0.0003993056 0.0 0.0 9
10013710 100 0.0003993056 0.0 0.0 10
10013711 100 0.0003993056 0.0 0.0 11
10013712 100 0.0003993056 0.0 0.0 12
10013900 0
10013901 0.014867 100.0 100.0 0.0 0.0 0.0 0.0 1.0 12
*
* ROD # 1 side 4
*
10014000 12 7 1 1 0.0
10014100 0 1
10014101 1 5.71E-04 1 1.08E-03 2 1.91E-03 2 3.08E-03
10014201 2 1
10014202 1 2
10014203 2 4
10014204 3 6
10014301 0.0 1
10014302 1.0 2
10014303 0.0 6
10014400 0
10014401 700.0 3
10014402 600.0 5
10014403 573.0 7
10014501 000000000 00000 0 1 0.0029850 12
10014601 800209011 10 1 1 0.0029850 12
10014701 100 0.0003993056 0.0 0.0 1
10014702 100 0.0003993056 0.0 0.0 2
```

```
10014703 100 0.0003993056 0.0 0.0 3
10014704 100 0.0003993056 0.0 0.0 4
10014705 100 0.0003993056 0.0 0.0 5
10014706 100 0.0003993056 0.0 0.0 6
10014707 100 0.0003993056 0.0 0.0 7
10014708 100 0.0003993056 0.0 0.0 8
10014709 100 0.0003993056 0.0 0.0 9
10014710 100 0.0003993056 0.0 0.0 10
10014711 100 0.0003993056 0.0 0.0 11
10014712 100 0.0003993056 0.0 0.0 12
10014900 0
10014901 0.019730 100.0 100.0 0.0 0.0 0.0 0.0 1.0 12
*
* RADIATION ENCLOSURE
*
60000000 60
*
* ROD # 1
*
60100000 -48
60101001 0011001 1 2000.0
60102001 0011002 1 2000.0
60103001 0011003 1 2000.0
60104001 0011004 1 2000.0
60105001 0011005 1 2000.0
60106001 0011006 1 2000.0
60107001 0011007 1 2000.0
60108001 0011008 1 2000.0
60109001 0011009 1 2000.0
60110001 0011010 1 2000.0
60111001 0011011 1 2000.0
60112001 0011012 1 2000.0
60113001 0012001 1 2000.0
60114001 0012002 1 2000.0
60115001 0012003 1 2000.0
60116001 0012004 1 2000.0
60117001 0012005 1 2000.0
60118001 0012006 1 2000.0
60119001 0012007 1 2000.0
60120001 0012008 1 2000.0
60121001 0012009 1 2000.0
60122001 0012010 1 2000.0
60123001 0012011 1 2000.0
60124001 0012012 1 2000.0
60125001 0013001 1 2000.0
60126001 0013002 1 2000.0
60127001 0013003 1 2000.0
60128001 0013004 1 2000.0
60129001 0013005 1 2000.0
60130001 0013006 1 2000.0
60131001 0013007 1 2000.0
60132001 0013008 1 2000.0
60133001 0013009 1 2000.0
60134001 0013010 1 2000.0
60135001 0013011 1 2000.0
60136001 0013012 1 2000.0
60137001 0014001 1 2000.0
60138001 0014002 1 2000.0
60139001 0014003 1 2000.0
60140001 0014004 1 2000.0
60141001 0014005 1 2000.0
60142001 0014006 1 2000.0
60143001 0014007 1 2000.0
60144001 0014008 1 2000.0
60145001 0014009 1 2000.0
60146001 0014010 1 2000.0
60147001 0014011 1 2000.0
```

```
60148001 0014012 1 2000.0
* * * * * * * * * * * * *
* VIEW FACTORS
* ROD 001 SET 1 GROUP 1
* * * * * * * * * * * * *
60101101 0.00 12
60101102 0.50 13
60101103 0.00 36
60101104 0.50 37
60101105 0.00 48
60102101 0.00 13
60102102 0.50 14
60102103 0.00 37
60102104 0.50 38
60102105 0.00 48
60103101 0.00 14
60103102 0.50 15
60103103 0.00 38
60103104 0.50 39
60103105 0.00 48
60104101 0.00 15
60104102 0.50 16
60104103 0.00 39
60104104 0.50 40
60104105 0.00 48
60105101 0.00 16
60105102 0.50 17
60105103 0.00 40
60105104 0.50 41
60105105 0.00 48
60106101 0.00 17
60106102 0.50 18
60106103 0.00 41
60106104 0.50 42
60106105 0.00 48
60107101 0.00 18
60107102 0.50 19
60107103 0.00 42
60107104 0.50 43
60107105 0.00 48
60108101 0.00 19
60108102 0.50 20
60108103 0.00 43
60108104 0.50 44
60108105 0.00 48
60109101 0.00 20
60109102 0.50 21
60109103 0.00 44
60109104 0.50 45
60109105 0.00 48
60110101 0.00 21
60110102 0.50 22
60110103 0.00 45
60110104 0.50 46
60110105 0.00 48
60111101 0.00 22
60111102 0.50 23
60111103 0.00 46
60111104 0.50 47
60111105 0.00 48
60112101 0.00 23
60112102 0.50 24
60112103 0.00 47
60112104 0.50 48
* ROD 001 SET 1 GROUP 2
60113101 0.50 1
60113102 0.00 24
```

```
60113103 0.50 25
60113104 0.00 48
60114101 0.00 1
60114102 0.50 2
60114103 0.00 25
60114104 0.50 26
60114105 0.00 48
60115101 0.00 2
60115102 0.50 3
60115103 0.00 26
60115104 0.50 27
60115105 0.00 48
60116101 0.00 3
60116102 0.50 4
60116103 0.00 27
60116104 0.50 28
60116105 0.00 48
60117101 0.00 4
60117102 0.50 5
60117103 0.00 28
60117104 0.50 29
60117105 0.00 48
60118101 0.00 5
60118102 0.50 6
60118103 0.00 29
60118104 0.50 30
60118105 0.00 48
60119101 0.00 6
60119102 0.50 7
60119103 0.00 30
60119104 0.50 31
60119105 0.00 48
60120101 0.00 7
60120102 0.50 8
60120103 0.00 31
60120104 0.50 32
60120105 0.00 48
60121101 0.00 8
60121102 0.50 9
60121103 0.00 32
60121104 0.50 33
60121105 0.00 48
60122101 0.00 9
60122102 0.50 10
60122103 0.00 33
60122104 0.50 34
60122105 0.00 48
60123101 0.00 10
60123102 0.50 11
60123103 0.00 34
60123104 0.50 35
60123105 0.00 48
60124101 0.00 11
60124102 0.50 12
60124103 0.00 35
60124104 0.50 36
60124105 0.00 48
* ROD 001 SET 1 GROUP 3
60125101 0.00 12
60125102 0.50 13
60125103 0.00 36
60125104 0.50 37
60125105 0.00 48
60126101 0.00 13
60126102 0.50 14
60126103 0.00 37
60126104 0.50 38
```

```
60126105 0.00 48
60127101 0.00 14
60127102 0.50 15
60127103 0.00 38
60127104 0.50 39
60127105 0.00 48
60128101 0.00 15
60128102 0.50 16
60128103 0.00 39
60128104 0.50 40
60128105 0.00 48
60129101 0.00 16
60129102 0.50 17
60129103 0.00 40
60129104 0.50 41
60129105 0.00 48
60130101 0.00 17
60130102 0.50 18
60130103 0.00 41
60130104 0.50 42
60130105 0.00 48
60131101 0.00 18
60131102 0.50 19
60131103 0.00 42
60131104 0.50 43
60131105 0.00 48
60132101 0.00 19
60132102 0.50 20
60132103 0.00 43
60132104 0.50 44
60132105 0.00 48
60133101 0.00 20
60133102 0.50 21
60133103 0.00 44
60133104 0.50 45
60133105 0.00 48
60134101 0.00 21
60134102 0.50 22
60134103 0.00 45
60134104 0.50 46
60134105 0.00 48
60135101 0.00 22
60135102 0.50 23
60135103 0.00 46
60135104 0.50 47
60135105 0.00 48
60136101 0.00 23
60136102 0.50 24
60136103 0.00 47
60136104 0.50 48
* ROD 001 SET 1 GROUP 4
60137101 0.50 1
60137102 0.00 24
60137103 0.50 25
60137104 0.00 48
60138101 0.00 1
60138102 0.50 2
60138103 0.00 25
60138104 0.50 26
60138105 0.00 48
60139101 0.00 2
60139102 0.50 3
60139103 0.00 26
60139104 0.50 27
60139105 0.00 48
60140101 0.00 3
60140102 0.50 4
```

```
60140103 0.00 27
60140104 0.50 28
60140105 0.00 48
60141101 0.00 4
60141102 0.50 5
60141103 0.00 28
60141104 0.50 29
60141105 0.00 48
60142101 0.00 5
60142102 0.50 6
60142103 0.00 29
60142104 0.50 30
60142105 0.00 48
60143101 0.00 6
60143102 0.50 7
60143103 0.00 30
60143104 0.50 31
60143105 0.00 48
60144101 0.00 7
60144102 0.50 8
60144103 0.00 31
60144104 0.50 32
60144105 0.00 48
60145101 0.00 8
60145102 0.50 9
60145103 0.00 32
60145104 0.50 33
60145105 0.00 48
60146101 0.00 9
60146102 0.50 10
60146103 0.00 33
60146104 0.50 34
60146105 0.00 48
60147101 0.00 10
60147102 0.50 11
60147103 0.00 34
60147104 0.50 35
60147105 0.00 48
60148101 0.00 11
60148102 0.50 12
60148103 0.00 35
60148104 0.50 36
60148105 0.00 48
*
*
*
*
*
*
```

Author's Note: The remainder of the fuel rods are modelled in the same manner as Rod 1. They are not included here for the sake of brevity, but are available on the accompanying DVD.

```
*
*
*
*
* MATERIAL TABLES
*
* List of materials
* 1 Nichrome
* 2 Boron Nitride
* 3 Inconel
* 4 Water
*
```

```
20100100 tbl/fctn 1 1
20100200 tbl/fctn 1 1
20100300 tbl/fctn 1 1
20100400 tbl/fctn 1 1
*
* serpentine Inconel conductivity (W/(m*K))
20100101 303.0 29.14
20100102 333.0 29.29
20100103 363.0 29.43
20100104 393.0 29.58
20100105 423.0 29.72
20100106 453.0 29.87
20100107 483.0 30.01
20100108 513.0 30.16
20100109 543.0 30.30
20100110 573.0 30.45
20100111 603.0 30.59
20100112 633.0 30.74
20100113 663.0 30.88
20100114 693.0 31.03
20100115 723.0 31.17
20100116 753.0 31.32
20100117 783.0 31.46
20100118 813.0 31.61
20100119 843.0 31.75
20100120 873.0 31.90
20100121 903.0 32.04
20100122 933.0 32.18
20100123 963.0 32.33
20100124 993.0 32.47
20100125 1023.0 32.62
20100126 1053.0 32.76
20100127 1083.0 32.91
20100128 1113.0 33.05
20100129 1143.0 33.20
20100130 1173.0 33.34
20100131 1203.0 33.49
20100132 1233.0 33.63
20100133 1263.0 33.78
20100134 1293.0 33.92
20100135 1323.0 34.07
20100136 1353.0 34.21
20100137 1383.0 34.36
20100138 1413.0 34.50
20100139 1443.0 34.65
20100140 1473.0 34.79
20100141 1503.0 34.94
20100142 1523.0 35.03
*
* serpentine Inconel heat capacity (j/(m3*K))
20100151 303.0 2326692.74
20100152 333.0 2574258.60
20100153 363.0 2754542.42
20100154 393.0 2898540.21
20100155 423.0 3019479.23
20100156 453.0 3124326.99
20100157 483.0 3217238.49
20100158 513.0 3300905.46
20100159 543.0 3377178.62
20100160 573.0 3447388.92
20100161 603.0 3512527.88
20100162 633.0 3573355.34
20100163 663.0 3630467.37
20100164 693.0 3684340.80
20100165 723.0 3735363.45
20100166 753.0 3783855.28
20100167 783.0 3830083.60
```

```
20100168 813.0 3874274.17
20100169 843.0 3916619.50
20100170 873.0 3957285.18
20100171 903.0 3996414.77
20100172 933.0 4034133.54
20100173 963.0 4070551.58
20100174 993.0 4105766.12
20100175 1023.0 4139863.53
20100176 1053.0 4172920.90
20100177 1083.0 4205007.32
20100178 1113.0 4236185.02
20100179 1143.0 4266510.18
20100180 1173.0 4296033.80
20100181 1203.0 4324802.24
20100182 1233.0 4352857.85
20100183 1263.0 4380239.35
20100184 1293.0 4406982.30
20100185 1323.0 4433119.44
20100186 1353.0 4458680.94
20100187 1383.0 4483694.70
20100188 1413.0 4508186.58
20100189 1443.0 4532180.56
20100190 1473.0 4555698.98
20100191 1503.0 4578762.63
20100192 1523.0 4593895.39
*
* Boron Nitride conductivity (W/(m*K))
20100201 303.0 25.15
20100202 333.0 25.08
20100203 363.0 25.01
20100204 393.0 24.93
20100205 423.0 24.86
20100206 453.0 24.78
20100207 483.0 24.71
20100208 513.0 24.64
20100209 543.0 24.56
20100210 573.0 24.49
20100211 603.0 24.42
20100212 633.0 24.34
20100213 663.0 24.27
20100214 693.0 24.19
20100215 723.0 24.12
20100216 753.0 24.05
20100217 783.0 23.97
20100218 813.0 23.90
20100219 843.0 23.83
20100220 873.0 23.75
20100221 903.0 23.68
20100222 933.0 23.60
20100223 963.0 23.53
20100224 993.0 23.46
20100225 1023.0 23.38
20100226 1053.0 23.31
20100227 1083.0 23.24
20100228 1113.0 23.16
20100229 1143.0 23.09
20100230 1173.0 23.02
20100231 1203.0 22.94
20100232 1233.0 22.87
20100233 1263.0 22.79
20100234 1293.0 22.72
20100235 1323.0 22.65
20100236 1353.0 22.57
20100237 1383.0 22.50
20100238 1413.0 22.43
20100239 1443.0 22.35
20100240 1473.0 22.28
```

```
20100241 1503.0 22.20
20100242 1523.0 22.16
*
* Boron Nitride heat capacity (j/(m3*K))
20100251 303.0 1819200.34
20100252 333.0 1992795.21
20100253 363.0 2157046.31
20100254 393.0 2312254.32
20100255 423.0 2458719.90
20100256 453.0 2596743.71
20100257 483.0 2726626.42
20100258 513.0 2848668.70
20100259 543.0 2963171.21
20100260 573.0 3070434.63
20100261 603.0 3170759.60
20100262 633.0 3264446.82
20100263 663.0 3351796.92
20100264 693.0 3433110.60
20100265 723.0 3508688.50
20100266 753.0 3578831.30
20100267 783.0 3643839.66
20100268 813.0 3704014.25
20100269 843.0 3759655.73
20100270 873.0 3811064.78
20100271 903.0 3858542.05
20100272 933.0 3902388.21
20100273 963.0 3942903.94
20100274 993.0 3980389.89
20100275 1023.0 4015146.72
20100276 1053.0 4047475.12
20100277 1083.0 4077675.74
20100278 1113.0 4106049.25
20100279 1143.0 4132896.31
20100280 1173.0 4158517.60
20100281 1203.0 4183213.77
20100282 1233.0 4207285.50
20100283 1263.0 4231033.45
20100284 1293.0 4254758.28
20100285 1323.0 4278760.67
20100286 1353.0 4303341.27
20100287 1383.0 4328800.76
20100288 1413.0 4355439.79
20100289 1443.0 4383559.05
20100290 1473.0 4413459.18
20100291 1503.0 4445440.87
20100292 1523.0 4446440.87
*
* Inconel conductivity (W/(m*K))
20100301 303.0 14.57
20100302 333.0 15.03
20100303 363.0 15.49
20100304 393.0 15.97
20100305 423.0 16.44
20100306 453.0 16.91
20100307 483.0 17.38
20100308 513.0 17.85
20100309 543.0 18.31
20100310 573.0 18.78
20100311 603.0 19.25
20100312 633.0 19.72
20100313 663.0 20.20
20100314 693.0 20.68
20100315 723.0 21.17
20100316 753.0 21.66
20100317 783.0 22.17
20100318 813.0 22.69
20100319 843.0 23.22
```

```
20100320 873.0 23.75
20100321 903.0 24.30
20100322 933.0 24.85
20100323 963.0 25.41
20100324 993.0 25.98
20100325 1023.0 26.54
20100326 1053.0 27.09
20100327 1083.0 27.63
20100328 1113.0 28.14
20100329 1143.0 28.62
20100330 1173.0 29.07
20100331 1203.0 29.45
20100332 1233.0 29.77
20100333 1263.0 30.00
20100334 1293.0 30.13
20100335 1323.0 30.14
20100336 1353.0 30.01
20100337 1383.0 29.71
20100338 1413.0 29.21
20100339 1443.0 28.49
20100340 1473.0 27.52
20100341 1503.0 26.27
20100342 1523.0 25.25
*
* Inconel heat capacity (j/(m3*K))
20100351 303.0 3697554.53
20100352 333.0 3767503.70
20100353 363.0 3832810.82
20100354 393.0 3892799.02
20100355 423.0 3946968.43
20100356 453.0 3995189.80
20100357 483.0 4037803.76
20100358 513.0 4075639.76
20100359 543.0 4109968.85
20100360 573.0 4142403.80
20100361 603.0 4174760.39
20100362 633.0 4208893.32
20100363 663.0 4246520.06
20100364 693.0 4289045.81
20100365 723.0 4337402.69
20100366 753.0 4391916.05
20100367 783.0 4452210.52
20100368 813.0 4517168.61
20100369 843.0 4584954.10
20100370 873.0 4653112.69
20100371 903.0 4718761.87
20100372 933.0 4778882.14
20100373 963.0 4830721.43
20100374 993.0 4872324.18
20100375 1023.0 4903196.93
20100376 1053.0 4925121.47
20100377 1083.0 4943127.01
20100378 1113.0 4966632.26
20100379 1143.0 5010768.43
20100380 1173.0 5097893.77
20100381 1203.0 5259310.35
20100382 1233.0 5537193.43
20100383 1263.0 5986743.66
20100384 1293.0 6678572.30
20100385 1323.0 7701329.27
20100386 1353.0 9164583.94
20100387 1383.0 11201968.15
20100388 1413.0 13974590.98
20100389 1443.0 17674734.54
20100390 1473.0 22529839.87
20100391 1503.0 28806791.98
20100392 1523.0 33932925.04
```

```
*
* water conductivity (W/(m*K))
20100401 500.0 0.6488
20100402 505.0 0.6443
20100403 510.0 0.6395
20100404 515.0 0.6344
20100405 520.0 0.6289
20100406 525.0 0.6231
20100407 530.0 0.6169
20100408 535.0 0.6103
20100409 540.0 0.6033
20100410 545.0 0.5958
20100411 550.0 0.5878
20100412 555.0 0.5794
20100413 560.0 0.5704
20100414 565.0 0.06289
20100415 570.0 0.0621
20100416 575.0 0.06149
20100417 580.0 0.06103
20100418 585.0 0.06068
20100419 590.0 0.06043
20100420 595.0 0.06026
20100421 600.0 0.06015
*
* water heat capacity (j/(m3*K))
20100451 500.0 3864187.50
20100452 505.0 3863865.60
20100453 510.0 3864925.40
20100454 515.0 3867380.90
20100455 520.0 3871003.50
20100456 525.0 3877430.40
20100457 530.0 3884269.50
20100458 535.0 3894702.20
20100459 540.0 3907240.60
20100460 545.0 3923458.80
20100461 550.0 3943545.00
20100462 555.0 3968888.00
20100463 560.0 4000698.00
20100464 565.0 185104.00
20100465 570.0 166466.18
20100466 575.0 152215.84
20100467 580.0 140848.74
20100468 585.0 131458.50
20100469 590.0 123585.51
20100470 595.0 116841.44
20100471 600.0 110944.08
*
* * * * * * * * * * * * *
* POWER GENERATION
*
* power in the NiChrome
20210000 power 420
20210001 -1.0 0.00
20210002 0.0 0.00
20210003 10.00 4620000.00
20210004 180.00 4620000.00
20210005 181.00 4620000.00
20210006 182.00 4620000.00
20210007 183.00 4620000.00
20210008 184.00 4620000.00
20210009 185.00 4620000.00
20210010 186.00 4620000.00
20210011 187.00 4620000.00
20210012 188.00 4620000.00
20210013 189.00 4620000.00
20210014 190.00 4620000.00
20210015 191.00 4620000.00
```

```
20210016 192.00 4620000.00
20210017 193.00 4620000.00
20210018 194.00 4620000.00
20210019 195.00 4620000.00
20210020 196.00 4620000.00
20210021 197.00 4620000.00
20210022 198.00 4620000.00
20210023 199.00 4620000.00
20210024 200.00 4620000.00
20210025 201.00 4620000.00
20210026 202.00 4620000.00
20210027 202.20 4620000.00
20210028 202.40 4620000.00
20210029 202.60 4620000.00
20210030 202.80 4620000.00
20210031 203.00 4620000.00
20210032 203.20 4620000.00
20210033 203.40 4620000.00
20210034 203.60 4620000.00
20210035 203.80 4620000.00
20210036 204.00 4620000.00
20210037 205.00 4620000.00
20210038 206.00 4620000.00
20210039 207.00 4620000.00
20210040 208.00 4620000.00
20210041 209.00 4620000.00
20210042 210.00 4620000.00
20210043 211.00 4620000.00
20210044 212.00 4620000.00
20210045 213.00 4620000.00
20210046 214.00 4620000.00
20210047 215.00 4620000.00
20210048 216.00 4620000.00
20210049 217.00 4620000.00
20210050 218.00 4620000.00
20210051 219.00 4620000.00
20210052 220.00 4620000.00
20210053 221.00 4620000.00
20210054 222.00 4620000.00
20210055 223.00 4620000.00
20210056 224.00 4620000.00
20210057 225.00 4620000.00
20210058 226.00 4620000.00
20210059 227.00 4620000.00
20210060 228.00 4620000.00
20210061 229.00 4620000.00
20210062 230.00 4620000.00
20210063 231.00 4620000.00
20210064 232.00 4620000.00
20210065 233.00 4620000.00
20210066 234.00 4620000.00
20210067 235.00 4620000.00
20210068 236.00 4620000.00
20210069 237.00 4620000.00
20210070 238.00 4620000.00
20210071 239.00 4620000.00
20210072 240.00 4620000.00
20210073 241.00 4620000.00
20210074 242.00 4620000.00
20210075 243.00 4620000.00
20210076 244.00 4620000.00
20210077 245.00 4620000.00
20210078 246.00 4620000.00
20210079 247.00 4620000.00
20210080 248.00 4620000.00
20210081 249.00 4620000.00
20210082 250.00 4620000.00
```

```
20210083 251.00 4620000.00
20210084 252.00 4620000.00
20210085 253.00 4620000.00
20210086 1.00E+06 4620000.00
* * * * * * * * * * * * *
* CONTROL VARIABLES
* * * * * * * * * * * * *
*
*20500100 tu_420 tripunit 1.0 0.0 0
*20500101 420
*
*20500200 tdly_420 tripdlay 1.0 0.0 0
*20500201 420
*
*20500300 t-t0 sum 1.0 0.0 0
*20500301 -20.0 1.0 time 0 * Set initiation time of trip 420 as additive term of
cntrlvar!!!
*
*20500400 powtime mult 1.0 0.0 0
*20500401 cntrlvar 1
*20500402 cntrlvar 3
*
*20500500 ap_pow function 1.0 0.0 0
*20500501 cntrlvar 4 100
*
* * * * * * *
* END
* * * * * * *
.
```

APPENDIX I ASSERT INPUT DECK

```
****************************************
*
*BFBT Bundle
*ASSERT-PV v3R1
*K. Leung
*
*
*
*
****************************************
*Record i
****************************************
*MAXT
*10I5
9999
*
*
*
*
****************************************
*Record ii
****************************************
*KASEUNINUNOUTJ1TEXT
*I52A2I1A
10000SISI1BFBT Base Case
*
*
*
*
****************************************
*Group 1
****************************************
*NGROUPNPROPNPACKNPLOOKNFLUID
*12I5
    1    0    1    0    0
*
*
*
*
****************************************
*Group 2
****************************************
*NGROUPNOPTNNFRICNMULTNVISCWLAMNFN6NGRAVNURELNVRELNKMULT
*12I5
    2    1    2    6    0    0    0    1    1    3    0
*
*Record 2.2Active since NFRIC>0
*RUFHGT
*6F10.0
0.0002
*
*Record 2.8HT & CHF Options
*NHTCNCHFNHFWNCK1NCK2NCK3NCK4NCK5
*I5I5I5I5I5I5I5I5
    1    0    1    0    0    0    0    0
*
*
*
*
****************************************
*Group 3
```

```
****************************************
*NGROUPNQXOPTNAX
*12I5
    3    0   44
*
*Record 3.1Axial Profile
*YAXIALYAXIALYAXIALYAXIALYAXIALYAXIAL
*F5.0F5.0F5.0F5.0F5.0F5.0F5.0F5.0F5.0F5.0F5.0F5.0F5.0
.00001.000.00001.000.04171.000.04171.000.08331.000.08331.000
.12501.000.12501.000.16671.000.16671.000.20831.000.20831.000
.25001.000.25001.000.29171.000.29171.000.33331.000.37501.000
.37501.000.41671.000.45831.000.45831.000.50001.000.54171.000
.54171.000.58331.000.62501.000.62501.000.66671.000.70831.000
.70831.000.75001.000.75001.000.79171.000.79171.000.83331.000
.83331.000.87501.000.87501.000.91671.000.91671.000.95831.000
.95831.0001.0001.000
*
*
*
*
****************************************
*Group 4
****************************************
*NGROUPNCHANLNRODAXVOPT
*I5I5I5I5
    4   81   60   0
*
*Record 4.1
*
*
*>>>>ROW 1<<<<
*NTYPEIAREASCWPERIMHPERIMLCGAPWDSGAPDSSGAPANGLCGAPWDSGAPDSSGAPANG
*I1I4F5.2F5.2F5.2I5F5.2F5.2F5.2I5F5.2F5.2F5.2
1   1.47762.423.9660    20.3401.32885.59   100.3401.328184.4
1   2.95303.5521.932    30.3401.62090.00   110.3901.426180.0
1   3.95303.5521.932    40.3401.62090.00   120.3901.426180.0
1   4.95303.5521.932    50.3401.62090.00   130.3901.426180.0
1   5.95303.5521.932    60.3401.62090.00   140.3901.426180.0
1   6.95303.5521.932    70.3401.62090.00   150.3901.426180.0
1   7.95303.5521.932    80.3401.62090.00   160.3901.426180.0
1   8.95303.5521.932    90.3401.32894.41   170.3901.426180.0
1   9.47762.423.9660   180.3401.328175.6
*>>>>ROW 2<<<<
*NTYPEIAREASCWPERIMHPERIMLCGAPWDSGAPDSSGAPANGLCGAPWDSGAPDSSGAPANG
*I1I4F5.2F5.2F5.2I5F5.2F5.2F5.2I5F5.2F5.2F5.2
1  10.95303.5521.932   110.3901.42690.00   190.3401.620180.0
1  111.4363.8643.864   120.3901.62090.00   200.3901.620180.0
1  121.4363.8643.864   130.3901.62090.00   210.3901.620180.0
1  131.4363.8643.864   140.3901.62090.00   220.3901.620180.0
1  141.4363.8643.864   150.3901.62090.00   230.3901.620180.0
1  151.4363.8643.864   160.3901.62090.00   240.3901.620180.0
1  161.4363.8643.864   170.3901.62090.00   250.3901.620180.0
1  171.4363.8643.864   180.3901.42690.00   260.3901.620180.0
1  18.95303.5521.932   270.3401.620180.0
*>>>>ROW 3<<<<
*NTYPEIAREASCWPERIMHPERIMLCGAPWDSGAPDSSGAPANGLCGAPWDSGAPDSSGAPANG
*I1I4F5.2F5.2F5.2I5F5.2F5.2F5.2I5F5.2F5.2F5.2
1  19.95303.5521.932   200.3901.42690.00   280.3401.620180.0
1  201.4363.8643.864   210.3901.62090.00   290.3901.620180.0
1  211.4363.8643.864   220.3901.62090.00   300.3901.620180.0
1  221.4363.8643.864   230.3901.62090.00   310.3901.625179.6
1  231.4363.8643.864   240.3901.62090.00   320.3901.334180.0
1  241.4363.8643.864   250.3901.62090.00   330.3901.625180.4
1  251.4363.8643.864   260.3901.62090.00   340.3901.620180.0
1  261.4363.8643.864   270.3901.42690.00   350.3901.620180.0
1  27.95303.5521.932   360.3401.620180.0
*>>>>ROW 4<<<<
```

```
*NTYPEIAREASCWPERIMHPERIMLCGAPWDSGAPDSSGAPANGLCGAPWDSGAPDSSGAPANG
*I1I4F5.2F5.2F5.2I5F5.2F5.2F5.2I5F5.2F5.2F5.2
1  28.95303.5521.932   290.3901.42690.00   370.3401.620180.0
1  291.4363.8643.864   300.3901.62090.00   380.3901.620180.0
1  301.4363.8643.864   310.3901.62590.35   390.3901.620180.0
1  311.4533.8802.898   320.3201.64179.79   400.3201.641190.2
1  32.69663.6211.932   330.3201.641100.2
1  331.4533.8802.898   340.3901.62589.65   420.3201.641169.8
1  341.4363.8643.864   350.3901.62090.00   430.3901.426180.0
1  351.4363.8643.864   360.3901.42690.00   440.3901.426180.0
1  36.95303.5521.932   450.3401.620180.0
*>>>>ROW 5<<<<
*NTYPEIAREASCWPERIMHPERIMLCGAPWDSGAPDSSGAPANGLCGAPWDSGAPDSSGAPANG
*I1I4F5.2F5.2F5.2I5F5.2F5.2F5.2I5F5.2F5.2F5.2
1  37.95303.5521.932   380.3901.42690.00   460.3401.620180.0
1  381.4363.8643.864   390.3901.62090.00   470.3901.620180.0
1  391.4363.8643.864   400.3901.33490.00   480.3901.620180.0
1  40.69663.6211.932   490.3201.641169.8
1  410.0010.0010.001
1  42.69663.6211.932   430.3901.33490.00   510.3201.641190.2
1  431.4363.8643.864   440.3901.62090.00   520.3901.620180.0
1  441.4363.8643.864   450.3901.42690.00   530.3901.620180.0
1  45.95303.5521.932   540.3401.620180.0
*>>>>ROW 6<<<<
*NTYPEIAREASCWPERIMHPERIMLCGAPWDSGAPDSSGAPANGLCGAPWDSGAPDSSGAPANG
*I1I4F5.2F5.2F5.2I5F5.2F5.2F5.2I5F5.2F5.2F5.2
1  46.95303.5521.932   470.3901.42690.00   550.3401.620180.0
1  471.4363.8643.864   480.3901.62090.00   560.3901.620180.0
1  481.4363.8643.864   490.3901.62589.65   570.3901.620180.0
1  491.4533.8802.898   500.3201.641100.2   580.3901.625180.4
1  50.69663.6211.932   510.3201.64179.79   590.3901.334180.0
1  511.4533.8802.898   520.3901.62590.35   600.3901.625179.6
1  521.4363.8643.864   530.3901.62090.00   610.3901.620180.0
1  531.4363.8643.864   540.3901.42690.00   620.3901.620180.0
1  54.95303.5521.932   630.3401.620180.0
*>>>>ROW 6<<<<
*NTYPEIAREASCWPERIMHPERIMLCGAPWDSGAPDSSGAPANGLCGAPWDSGAPDSSGAPANG
*I1I4F5.2F5.2F5.2I5F5.2F5.2F5.2I5F5.2F5.2F5.2
1  55.95303.5521.932   560.3901.42690.00   640.3401.620180.0
1  561.4363.8643.864   570.3901.62090.00   650.3901.620180.0
1  571.4363.8643.864   580.3901.62090.00   660.3901.620180.0
1  581.4363.8643.864   590.3901.62090.00   670.3901.620180.0
1  591.4363.8643.864   600.3901.62090.00   680.3901.620180.0
1  601.4363.8643.864   610.3901.62090.00   690.3901.620180.0
1  611.4363.8643.864   620.3901.62090.00   700.3901.620180.0
1  621.4363.8643.864   630.3901.42690.00   710.3901.620180.0
1  63.95303.5521.932   720.3401.620180.0
*>>>>ROW 7<<<<
*NTYPEIAREASCWPERIMHPERIMLCGAPWDSGAPDSSGAPANGLCGAPWDSGAPDSSGAPANG
*I1I4F5.2F5.2F5.2I5F5.2F5.2F5.2I5F5.2F5.2F5.2
1  64.95303.5521.932   650.3901.42690.00   730.3401.328175.6
1  651.4363.8643.864   660.3901.62090.00   740.3901.426180.0
1  661.4363.8643.864   670.3901.62090.00   750.3901.426180.0
1  671.4363.8643.864   680.3901.62090.00   760.3901.426180.0
1  681.4363.8643.864   690.3901.62090.00   770.3901.426180.0
1  691.4363.8643.864   700.3901.62090.00   780.3901.426180.0
1  701.4363.8643.864   710.3901.62090.00   790.3901.426180.0
1  711.4363.8643.864   720.3901.42690.00   800.3901.426180.0
1  72.95303.5521.932   810.3401.328184.4
*>>>>ROW 8<<<<
*NTYPEIAREASCWPERIMHPERIMLCGAPWDSGAPDSSGAPANGLCGAPWDSGAPDSSGAPANG
*I1I4F5.2F5.2F5.2I5F5.2F5.2F5.2I5F5.2F5.2F5.2
1  73.47762.423.9660   740.3401.32894.40
1  74.95303.5521.932   750.3401.62090.00
1  75.95303.5521.932   760.3401.62090.00
1  76.95303.5521.932   770.3401.62090.00
1  77.95303.5521.932   780.3401.62090.00
```

```
1  78.95303.5521.932   790.3401.62090.00
1  79.95303.5521.932   800.3401.62090.00
1  80.95303.5521.932   810.3401.32885.60
1  81.47762.423.9660
*
*Record 4.2
*
*IDFUELIRODDIARODFLXLRPHILRPHILRPHILRPHI
*I2I3E5.2E5.2I5E5.2I5E5.2I5E5.2I5E5.2
 1  11.2301.150    10.250    20.250   100.250   110.250
 1  21.2301.300    20.250    30.250   110.250   120.250
 1  31.2301.150    30.250    40.250   120.250   130.250
 1  41.2301.300    40.250    50.250   130.250   140.250
 1  51.2301.300    50.250    60.250   140.250   150.250
 1  61.2301.150    60.250    70.250   150.250   160.250
 1  71.2301.300    70.250    80.250   160.250   170.250
 1  81.2301.150    80.250    90.250   170.250   180.250
 1  91.2301.300   100.250   110.250   190.250   200.250
 1 101.2300.450   110.250   120.250   200.250   210.250
 1 111.2300.890   120.250   130.250   210.250   220.250
 1 121.2300.890   130.250   140.250   220.250   230.250
 1 131.2300.890   140.250   150.250   230.250   240.250
 1 141.2300.450   150.250   160.250   240.250   250.250
 1 151.2301.150   160.250   170.250   250.250   260.250
 1 161.2301.300   170.250   180.250   260.250   270.250
 1 171.2301.150   190.250   200.250   280.250   290.250
 1 181.2300.890   200.250   210.250   290.250   300.250
 1 191.2300.890   210.250   220.250   300.250   310.250
 1 201.2300.890   220.250   230.250   310.250   320.250
 1 211.2300.890   230.250   240.250   320.250   330.250
 1 221.2300.890   240.250   250.250   330.250   340.250
 1 231.2300.450   250.250   260.250   340.250   350.250
 1 241.2301.150   260.250   270.250   350.250   360.250
 1 251.2301.300   280.250   290.250   370.250   380.250
 1 261.2300.890   290.250   300.250   380.250   390.250
 1 271.2300.890   300.250   310.250   390.250   400.250
 1 281.2300.890   330.250   340.250   420.250   430.250
 1 291.2300.890   340.250   350.250   430.250   440.250
 1 301.2301.150   350.250   360.250   440.250   450.250
 1 311.2301.300   370.250   380.250   460.250   470.250
 1 321.2300.890   380.250   390.250   470.250   480.250
 1 331.2300.890   390.250   400.250   480.250   490.250
 1 341.2300.890   420.250   430.250   510.250   520.250
 1 351.2300.890   430.250   440.250   520.250   530.250
 1 361.2301.150   440.250   450.250   530.250   540.250
 1 371.2301.150   460.250   470.250   550.250   560.250
 1 381.2300.450   470.250   480.250   560.250   570.250
 1 391.2300.890   480.250   490.250   570.250   580.250
 1 401.2300.890   490.250   500.250   580.250   590.250
 1 411.2300.890   500.250   510.250   590.250   600.250
 1 421.2300.890   510.250   520.250   600.250   610.250
 1 431.2300.450   520.250   530.250   610.250   620.250
 1 441.2301.150   530.250   540.250   620.250   630.250
 1 451.2301.300   550.250   560.250   640.250   650.250
 1 461.2301.150   560.250   570.250   650.250   660.250
 1 471.2300.450   570.250   580.250   660.250   670.250
 1 481.2300.890   580.250   590.250   670.250   680.250
 1 491.2300.890   590.250   600.250   680.250   690.250
 1 501.2300.450   600.250   610.250   690.250   700.250
 1 511.2301.150   610.250   620.250   700.250   710.250
 1 521.2301.300   620.250   630.250   710.250   720.250
 1 531.2301.150   640.250   650.250   730.250   740.250
 1 541.2301.300   650.250   660.250   740.250   750.250
 1 551.2301.150   660.250   670.250   750.250   760.250
 1 561.2301.150   670.250   680.250   760.250   770.250
 1 571.2301.150   680.250   690.250   770.250   780.250
 1 581.2301.150   690.250   700.250   780.250   790.250
```

```
 1 591.2301.300   700.250   710.250   790.250   800.250
 1 601.2301.150   710.250   720.250   800.250   810.250
*
*Record 4.3
*
*THETANBNDLSBNDLTLBNDLHL
*****
    0    1  370  370
*
*
*
*
****************************************
*Group 7
****************************************
*NGROUPJ6N2NGRIDNGRIDT
*I5I5I5I5I5
    7    2    0   30    2
*
*Record 7.1
*
*GRIDXLIGRIDGRIDXLIGRIDGRIDXLIGRIDGRIDXLIGRIDGRIDXLIGRIDGRIDXLIGRID
*E5.0I5E5.0I5E5.0I5E5.0I5E5.0I5E5.0I5E5.0I5
.0000  1  .1230  1  .1230  2  .1341  2  .1341  1  .2614  1
.2614  2  .2724  2  .2724  1  .3997  1  .3997  2  .4108  2
.4108  1  .5381  1  .5381  2  .5492  2  .5492  1  .6765  1
.6765  2  .6876  2  .6876  1  .8149  1  .8149  2  .8259  2
.8259  1  .9532  1  .9532  2  .9643  2  .9643  1 1.000  1
*
*Record 7.2-1
*
*NGRIDC
*I5
   81
*
*Record 7.3
*
*Type 1
*JCDPSP
*I5E5.2E5.2
    10.00050.00
    20.00050.00
    30.00050.00
    40.00050.00
    50.00050.00
    60.00050.00
    70.00050.00
    80.00050.00
    90.00050.00
   100.00050.00
   110.00050.00
   120.00050.00
   130.00050.00
   140.00050.00
   150.00050.00
   160.00050.00
   170.00050.00
   180.00050.00
   190.00050.00
   200.00050.00
   210.00050.00
   220.00050.00
   230.00050.00
   240.00050.00
   250.00050.00
   260.00050.00
   270.00050.00
```

```
   280.00050.00
   290.00050.00
   300.00050.00
   310.00050.00
   320.00050.00
   330.00050.00
   340.00050.00
   350.00050.00
   360.00050.00
   370.00050.00
   380.00050.00
   390.00050.00
   400.00050.00
   410.00050.00
   420.00050.00
   430.00050.00
   440.00050.00
   450.00050.00
   460.00050.00
   470.00050.00
   480.00050.00
   490.00050.00
   500.00050.00
   510.00050.00
   520.00050.00
   530.00050.00
   540.00050.00
   550.00050.00
   560.00050.00
   570.00050.00
   580.00050.00
   590.00050.00
   600.00050.00
   610.00050.00
   620.00050.00
   630.00050.00
   640.00050.00
   650.00050.00
   660.00050.00
   670.00050.00
   680.00050.00
   690.00050.00
   700.00050.00
   710.00050.00
   720.00050.00
   730.00050.00
   740.00050.00
   750.00050.00
   760.00050.00
   770.00050.00
   780.00050.00
   790.00050.00
   800.00050.00
   810.00050.00
*
*Record 7.2-2
*
*NGRIDC
*I5
    81
*Type 2
*JCDPSP
*I5E5.2E5.2
    11.20050.00
    21.20050.00
    31.20050.00
    41.20050.00
```

```
  51.20050.00
  61.20050.00
  71.20050.00
  81.20050.00
  91.20050.00
 101.20050.00
 111.20050.00
 121.20050.00
 131.20050.00
 141.20050.00
 151.20050.00
 161.20050.00
 171.20050.00
 181.20050.00
 191.20050.00
 201.20050.00
 211.20050.00
 221.20050.00
 231.20050.00
 241.20050.00
 251.20050.00
 261.20050.00
 271.20050.00
 281.20050.00
 291.20050.00
 301.20050.00
 311.20050.00
 321.20050.00
 331.20050.00
 341.20050.00
 351.20050.00
 361.20050.00
 371.20050.00
 381.20050.00
 391.20050.00
 401.20050.00
 411.20050.00
 421.20050.00
 431.20050.00
 441.20050.00
 451.20050.00
 461.20050.00
 471.20050.00
 481.20050.00
 491.20050.00
 501.20050.00
 511.20050.00
 521.20050.00
 531.20050.00
 541.20050.00
 551.20050.00
 561.20050.00
 571.20050.00
 581.20050.00
 591.20050.00
 601.20050.00
 611.20050.00
 621.20050.00
 631.20050.00
 641.20050.00
 651.20050.00
 661.20050.00
 671.20050.00
 681.20050.00
 691.20050.00
 701.20050.00
 711.20050.00
```

```
   721.20050.00
   731.20050.00
   741.20050.00
   751.20050.00
   761.20050.00
   771.20050.00
   781.20050.00
   791.20050.00
   801.20050.00
   811.20050.00
*
*Record 7.6
*
*KIJ
**
  0.5
*
*
*
*
****************************************
*Group 8
****************************************
*NGROUPNRODNCLADNCNFUELTNAXLCNQAXN7NRODTP
*I5I5I5I5I5I5I5I5I5I5
    8   60    0   4    1    0    0    0    0
*
*Record 8.1
*--All properties referenced at 270 CAssume =k/dx
*KFUELCFUELRFUELDFUELKCLADCCLADRCLADTCLADHGAP
*E5.2E5.2E5.2E5.2E5.2E5.2E5.2E5.2E5.2E5.2
3.0E1.40238.4E30.7301.8E1.49438.3E30.1302.0E5
*30.30.4023 83930.73018.31.4943 83150.13020469
*
*Record 8.4.1
*
*INNFNNGNNSNARCTILTTHANG
*I5I5I5I5I5F10.0F10.0
    1    2    3    3    3       0.0       0.0
    2    2    3    3    3       0.0       0.0
    3    2    3    3    3       0.0       0.0
    4    2    3    3    3       0.0       0.0
    5    2    3    3    3       0.0       0.0
    6    2    3    3    3       0.0       0.0
    7    2    3    3    3       0.0       0.0
    8    2    3    3    3       0.0       0.0
    9    2    3    3    3       0.0       0.0
   10    2    3    3    3       0.0       0.0
   11    2    3    3    3       0.0       0.0
   12    2    3    3    3       0.0       0.0
   13    2    3    3    3       0.0       0.0
   14    2    3    3    3       0.0       0.0
   15    2    3    3    3       0.0       0.0
   16    2    3    3    3       0.0       0.0
   17    2    3    3    3       0.0       0.0
   18    2    3    3    3       0.0       0.0
   19    2    3    3    3       0.0       0.0
   20    2    3    3    3       0.0       0.0
   21    2    3    3    3       0.0       0.0
   22    2    3    3    3       0.0       0.0
   23    2    3    3    3       0.0       0.0
   24    2    3    3    3       0.0       0.0
   25    2    3    3    3       0.0       0.0
   26    2    3    3    3       0.0       0.0
   27    2    3    3    3       0.0       0.0
   28    2    3    3    3       0.0       0.0
   29    2    3    3    3       0.0       0.0
```

```
    30    2    3    3    3        0.0        0.0
    31    2    3    3    3        0.0        0.0
    32    2    3    3    3        0.0        0.0
    33    2    3    3    3        0.0        0.0
    34    2    3    3    3        0.0        0.0
    35    2    3    3    3        0.0        0.0
    36    2    3    3    3        0.0        0.0
    37    2    3    3    3        0.0        0.0
    38    2    3    3    3        0.0        0.0
    39    2    3    3    3        0.0        0.0
    40    2    3    3    3        0.0        0.0
    41    2    3    3    3        0.0        0.0
    42    2    3    3    3        0.0        0.0
    43    2    3    3    3        0.0        0.0
    44    2    3    3    3        0.0        0.0
    45    2    3    3    3        0.0        0.0
    46    2    3    3    3        0.0        0.0
    47    2    3    3    3        0.0        0.0
    48    2    3    3    3        0.0        0.0
    49    2    3    3    3        0.0        0.0
    50    2    3    3    3        0.0        0.0
    51    2    3    3    3        0.0        0.0
    52    2    3    3    3        0.0        0.0
    53    2    3    3    3        0.0        0.0
    54    2    3    3    3        0.0        0.0
    55    2    3    3    3        0.0        0.0
    56    2    3    3    3        0.0        0.0
    57    2    3    3    3        0.0        0.0
    58    2    3    3    3        0.0        0.0
    59    2    3    3    3        0.0        0.0
    60    2    3    3    3        0.0        0.0
*
*Record 8.4.2
*
*NMATNPROPP
*I5I5
    3    3
*
*Record 8.4.3
*Material 1 - NiChrome
*NPT
*I5
   13
*
*Record 8.4.3.1
*NiChrome Conductivity (W/mK)
*TEMPPROPTTEMPPROPTTEMPPROPT
*F10.0F10.0F10.0F10.0F10.0F10.0
   0.00000   28.9976 125.00000   29.6012 250.00000   30.2049
 375.00000   30.8086 500.00000   31.4123 625.00000   32.0159
 750.00000   32.6196 875.00000   33.22331000.00000   33.8270
1125.00000   34.43061250.00000   35.03431375.00000   35.6380
1500.00000   36.2417
*
*Record 8.4.3
*Material 1 - NiChrome
*NPT
*I5
    3
*
*Record 8.4.3.2
*NiChrome Density (kg/m3)  [CONSTANT]
*TEMPPROPTTEMPPROPTTEMPPROPT
*F10.0F10.0F10.0F10.0F10.0F10.0
     0.000  8393.400   750.000  8393.400   1500.00  8393.400
*
*Record 8.4.3
```

```
*Material 1 - NiChrome
*NPT
*I5
   13
*
*Record 8.4.3.3
*NiChrome Heat Capacity (kJ/kg.K)
*TEMPPROPTTEMPPROPTTEMPPROPT
*F10.0F10.0F10.0F10.0F10.0F10.0
   0.00000    0.2258 125.00000    0.3479 250.00000    0.3964
 375.00000    0.4292 500.00000    0.4545 625.00000    0.4754
 750.00000    0.4932 875.00000    0.50891000.00000    0.5229
1125.00000    0.53571250.00000    0.54731375.00000    0.5581
1500.00000    0.5681
*
*Record 8.4.3
*Material 2 - Boron Nitride
*NPT
*I5
   13
*
*Record 8.4.3.1
*Boron Nitride - Conductivity (W/mK)
*TEMPPROPTTEMPPROPTTEMPPROPT
*F10.0F10.0F10.0F10.0F10.0F10.0
   0.00000   25.2263 125.00000   24.9192 250.00000   24.6121
 375.00000   24.3049 500.00000   23.9978 625.00000   23.6907
 750.00000   23.3836 875.00000   23.07641000.00000   22.7693
1125.00000   22.46221250.00000   22.15511375.00000   21.8479
1500.00000   21.5408
*
*Record 8.4.3
*Material 2 - Boron Nitride
*NPT
*I5
    3
*
*Record 8.4.3.2
*Boron Nitride Density (kg/m3)  [CONSTANT]
*TEMPPROPTTEMPPROPTTEMPPROPT
*F10.0F10.0F10.0F10.0F10.0F10.0
       0.0    2002.0     750.0    2002.0    1500.0    2002.0
*
*Record 8.4.3
*Material 2 - Boron Nitride
*NPT
*I5
   13
*
*Record 8.4.3.3
*Boron Nitride Heat Capacity (kJ/kg.K)
*TEMPPROPTTEMPPROPTTEMPPROPT
*F10.0F10.0F10.0F10.0F10.0F10.0
   0.00000    0.8172 125.00000    1.1675 250.00000    1.4424
 375.00000    1.6528 500.00000    1.8096 625.00000    1.9235
 750.00000    2.0056 875.00000    2.06661000.00000    2.1173
1125.00000    2.16881250.00000    2.23181375.00000    2.3172
1500.00000    2.4358
*
*Record 8.4.3
*Material 3 - Inconel
*NPT
*I5
   13
*
*Record 8.4.3.1
*Inconel - Conductivity (W/mK)
```

```
*TEMPPROPTTEMPPROPTTEMPPROPT
*F10.0F10.0F10.0F10.0F10.0F10.0
   0.00000   14.1163 125.00000   16.0437 250.00000   18.0017
 375.00000   19.9596 500.00000   22.0018 625.00000   24.2085
 750.00000   26.5372 875.00000   28.70351000.00000   30.0624
1125.00000   29.48911250.00000   25.26041375.00000   14.9354
1500.00000    0.0001
*
*Record 8.4.3
*Material 3 - Inconel
*NPT
*I5
   13
*
*Record 8.4.3.2
*Inconel Density (kg/m3)
*TEMPPROPTTEMPPROPTTEMPPROPT
*F10.0F10.0F10.0F10.0F10.0F10.0
   0.00000 8420.4260 125.00000 8371.8094 250.00000 8322.9991
 375.00000 8273.9951 500.00000 8224.7974 625.00000 8175.4059
 750.00000 8125.8208 875.00000 8076.04191000.00000 8026.0694
1125.00000 7975.90311250.00000 7925.54311375.00000 7874.9894
1500.00000 7824.2421
*
*Record 8.4.3
*Material 3 - Inconel
*NPT
*I5
   13
*
*Record 8.4.3.2
*Inconel Heat Capacity (kJ/kg.K)
*TEMPPROPTTEMPPROPTTEMPPROPT
*F10.0F10.0F10.0F10.0F10.0F10.0
   0.00000    0.4303 125.00000    0.4661 250.00000    0.4911
 375.00000    0.5109 500.00000    0.5388 625.00000    0.5759
 750.00000    0.6034 875.00000    0.62181000.00000    0.7708
1125.00000    1.56541250.00000    4.28151375.00000   11.5267
1500.00000   28.0298
*
*Record 8.4.4
*
*EPSSALFISNINSIPROPS
*F10.5F10.5I5I5
       1.0       0.5   50    0
*
*
*
*
****************************************
*Group 9
****************************************
*NGROUPNSKIPXNSKIPTN3N4N5NDXOPTN7MFLOWXMFLOWYREINIT
*I5I5I5I5I5I5I5I5I5I5I5I5
    9    1    5    0    0    0    0    0    0    0    0
*
*Record 9.1
*
*IELIMTMAXINRNTRIESIREBALHERROREERRORMERRORTERRORAXEROR
*I5I5I5I5F10.0F10.0F10.0F10.0F10.0F10.0
   80   50  100    1  0.000001    0.0001  0.000001     0.001     0.001
*
*Record 9.2
*
*SSDTNSSSTTDTNDT
*F10.0I5F10.0I5
   10.0E15    1    0.0001    0
```

```
*
*Record 9.3
*
*WRELAXFRELAXRRELAXHRELAX
*E5.0E5.0E5.0E5.0
 0.6 0.65 0.80 0.45
*
*Record 9.4
*
*NHTDX
**
20
*
*
*
*
*****************************************
*Group 10
*****************************************
*NGROUPNAMIXNALFAQNSPMIXNINMIXNOBFACNGPFACNROWVMNASSVMNRWEQV
*I5I5I5I5I5I5I5I5I5I5
   10    1    1    0    0    0    0    0    0    0
*
*Record 10.1
*
*ATRBTRASQBTR
*E5.0E5.0E5.0E5.0
*.0018 -0.40.0050.106
*
*
*
*
*****************************************
*Group 11
*****************************************
*NGROUPIHIGNPNHNGNQNDPTBLNHXPLENINPRENEXODVMAX
*I5I5I5I5I5I5I5I5I5I5I5I5
   11    1    0    0    0    0    0    0    0    1    1    0
*
*Record 11.1
*
*PEXITTHXINGINAFLUXTHXOUTDPSIREFINIREFEX
*F10.0F10.0F10.0F10.0F10.0F10.0F10.0I5I5
8.63000000292.0000001.550625360.52118822298.8000000.00000000    1    1
*7.16000000277.8000000.567994600.20262177284.80000030.0000000    1    1
*
*
*
*****************************************
*Group 12
*****************************************
*NGROUPNPAXLNPCHANNPRODNPNODENPGAPNPLOTNMARKNPCRSNSCHFXPRMIDNPRODL
*I5I5I5I5I5I5I5I5I5I5I5I5
   12    0   -1   -1    0   -1    0    0    0    0    0    0
*
*
*
*
*****************************************
*Group 18
*****************************************
*NGROUPITSCTLINTFLGNINTSCITRMINNPRINTPRTFLGNREDO
*I5I5I5I5I5I5I5I5
*   18    0    0    0    0    3    1   10
*
*Record 18.1
*
```

```
*DTBINDTBAXTBMAXMSSERRNRGERRRATDECRATINC
*F5.0F5.0F5.0F5.0F5.0F5.0F5.0
*1.E-51.000 10.01.0D-61.0D-62.0001.200
*
*Record 18.3
*
*TIMPRTTIMPRTTIMPRTTIMPRTTIMPRT
*F5.0F5.0F5.0F5.0F5.0
*1.0005.00010.00
****************************************
*END OF CASE
****************************************
*
    0
    0
```

APPENDIX J 1071-XX RESULT SUMMARY

Case	Planar Average			Sample Standard Deviation (Scatter)			Average Absolute Deviation	
	RELAP	ASSERT	EXP	RELAP	ASSERT	EXP	RELAP	ASSERT
1071-1	47.59	-----	38.79	13.94	-----	13.49	16.91	-----
1071-2	63.61	-----	57.27	7.49	-----	14.81	13.95	-----
1071-3	71.47	69.87	66.41	1.60	2.62	13.97	11.63	10.45
1071-4	34.29	85.39	81.83	44.54	1.60	8.10	56.44	5.90
1071-5	55.97	50.29	48.86	2.73	4.45	9.99	10.80	6.87
1071-6	73.46	69.25	68.51	0.44	2.87	7.87	6.62	5.69
1071-7	48.45	77.14	76.04	47.69	2.50	6.08	48.86	4.70
1071-8	90.02	89.43	86.36	0.65	1.50	4.37	3.92	3.73
1071-9	-----	23.90	19.81	-----	11.88	13.61	19.90	5.49
1071-10	67.73	62.47	59.80	1.12	5.07	7.78	8.70	3.90
1071-11	74.44	75.43	72.91	1.28	3.31	5.27	4.34	3.69
1071-12	87.91	79.55	77.34	7.67	2.62	4.33	10.74	3.36
1071-13	92.05	91.97	84.80	1.32	1.51	3.44	7.25	7.17
1071-14	29.54	27.09	28.20	2.85	2.03	7.88	7.27	6.25
1071-15	48.70	44.44	46.04	8.92	3.22	8.82	10.51	5.62
1071-16	-----	54.44	57.07	-----	3.41	8.97	57.07	5.57
1071-17	67.43	65.05	66.26	3.02	3.18	8.59	7.42	4.92
1071-18	76.70	74.60	73.88	0.22	2.57	6.76	5.61	4.04
1071-19	83.66	81.90	79.98	0.12	1.98	5.07	4.55	3.19
1071-20	38.85	34.55	36.15	0.30	3.50	6.90	5.87	4.43
1071-21	58.23	53.04	54.60	1.69	3.31	6.50	5.99	3.66
1071-22	68.13	63.98	64.13	0.42	3.12	5.43	5.01	2.75

Case	Planar Average			Sample Standard Deviation (Scatter)			Average Absolute Deviation	
	RELAP	ASSERT	EXP	RELAP	ASSERT	EXP	RELAP	ASSERT
1071-23	75.31	72.71	70.81	0.49	2.69	5.12	5.13	3.25
1071-24	82.16	81.03	78.07	0.61	2.16	4.76	4.81	3.60
1071-25	86.59	86.42	82.73	0.68	1.81	3.94	4.36	4.01
1071-26	41.21	37.02	37.62	0.94	4.14	6.55	6.16	3.48
1071-27	60.08	55.96	56.06	1.14	3.47	6.00	6.21	2.79
1071-28	70.03	67.14	66.18	1.32	3.06	5.19	5.55	2.70
1071-29	-----	75.17	74.57	-----	2.65	4.54	74.57	2.51
1071-30	83.14	82.65	80.59	1.66	2.19	4.17	4.61	2.80
1071-31	87.65	87.52	85.88	1.65	1.87	3.73	4.01	2.46
1071-32	87.68	87.50	85.51	1.63	1.87	3.68	4.13	2.59
1071-33	17.61	15.00	18.17	2.11	1.46	4.79	4.42	4.47
1071-34	35.69	31.48	34.27	3.90	2.54	6.58	6.34	4.43
1071-35	44.82	40.09	44.09	4.62	3.17	6.99	6.86	4.76
1071-36	55.97	51.47	54.97	0.06	3.64	6.99	6.18	4.18
1071-37	65.05	61.75	64.15	2.82	3.53	6.69	6.69	3.59
1071-38	73.01	71.02	70.81	9.77	2.93	5.73	10.20	2.75
1071-39	17.66	14.70	17.70	0.16	2.79	4.20	3.46	3.86
1071-40	37.50	32.66	35.93	0.18	2.86	6.67	5.52	4.94
1071-41	51.62	45.95	49.21	0.19	3.34	6.51	5.59	4.29
1071-42	61.73	57.78	60.25	16.36	3.41	5.05	13.95	3.00
1071-43	71.56	68.46	69.37	0.27	3.00	4.34	3.80	2.46
1071-44	78.66	76.67	75.79	0.27	2.48	4.17	3.92	2.44
1071-45	25.81	22.39	25.19	0.35	2.97	5.15	4.32	4.41
1071-46	43.68	38.71	41.34	0.37	3.19	5.55	4.82	4.02
1071-47	55.03	49.84	51.13	0.40	3.41	5.27	5.22	2.98
1071-48	64.31	60.13	61.54	3.68	3.30	4.57	5.49	2.85
1071-49	72.80	70.34	69.49	0.50	2.88	4.33	4.68	2.70
1071-50	79.22	78.09	77.76	0.57	2.43	3.88	3.48	2.61
1071-51	46.30	42.00	43.31	1.18	3.14	5.53	5.41	4.12
1071-52	65.74	63.09	63.83	1.45	3.15	5.70	5.93	4.29
1071-53	26.75	23.65	25.44	1.10	3.43	5.17	4.83	3.77
1071-54	26.38	23.50	25.36	1.08	3.45	5.24	4.94	3.90
1071-55	-----	41.16	43.17	-----	3.50	5.96	-----	4.59
1071-56	56.09	52.34	54.20	1.26	3.49	5.98	5.86	4.45
1071-57	56.33	52.51	53.58	1.24	3.48	5.92	5.94	3.62
1071-58	65.55	62.69	63.93	1.50	3.26	5.74	6.06	4.14
1071-59	73.71	72.47	72.53	1.66	2.86	5.64	5.91	4.11
1071-60	73.71	72.36	72.18	1.66	2.86	5.60	5.91	4.03

Case	Planar Average			Sample Standard Deviation (Scatter)			Average Absolute Deviation	
	RELAP	ASSERT	EXP	RELAP	ASSERT	EXP	RELAP	ASSERT
1071-61	80.37	79.69	79.40	1.65	2.48	4.98	5.32	3.72
1071-62	46.27	41.57	43.24	1.06	5.00	7.67	7.27	4.66
1071-63	65.22	62.27	62.46	1.36	3.77	6.61	6.74	4.27
1071-64	27.05	24.08	25.48	1.78	3.56	4.99	5.14	3.37
1071-65	45.74	41.89	43.21	1.87	3.62	5.88	6.16	4.13
1071-66	56.41	53.08	54.84	1.97	3.54	6.39	6.85	4.93
1071-67	65.60	63.28	64.41	2.30	3.28	6.34	7.07	4.87
1071-68	73.94	73.01	73.84	2.53	2.88	5.83	6.58	4.42
1071-69	17.24	15.17	16.90	1.75	1.37	4.19	3.78	3.36
1071-70	32.30	28.75	32.63	4.61	2.38	5.88	6.14	4.67
1071-71	42.66	38.22	42.77	2.52	3.12	6.00	5.44	4.86
1071-72	51.50	46.70	51.59	2.54	3.55	6.15	5.73	5.03
1071-73	61.88	58.14	61.80	0.07	3.74	5.48	4.67	3.89
1071-74	70.87	67.79	69.72	10.80	3.50	4.85	10.94	2.57
1071-75	22.65	19.82	22.17	0.43	2.65	4.16	3.85	3.42
1071-76	41.25	36.53	39.02	0.39	3.08	4.98	4.47	3.79
1071-77	50.80	45.54	47.74	0.40	3.38	5.00	4.77	3.53
1071-78	60.21	56.03	56.70	4.60	3.41	4.88	5.89	2.92
1071-79	69.42	66.76	66.65	0.50	3.09	4.76	4.78	3.30
1071-80	76.36	74.93	73.95	0.62	2.65	4.81	4.64	3.45
1071-81	27.34	24.77	26.68	1.21	2.99	4.65	4.46	3.74
1071-82	41.17	37.55	40.12	1.20	3.36	5.59	5.13	4.64
1071-83	51.27	47.81	50.77	1.27	3.50	6.30	6.07	5.53
1071-84	60.62	57.87	60.07	1.46	3.40	6.49	6.32	5.25
1071-85	-----	68.37	69.65	-----	3.08	6.29	-----	4.63
1071-86	69.97	68.54	69.42	1.58	3.06	6.18	6.02	4.70